Effects of near surface ocean gradients upon shelf sea air–sea gas exchange estimates

Submitted by Richard Peter Sims to the University of Exeter

as a thesis for the degree of

Doctor of Philosophy in Geography

In May 2018

Supervised by Dr Thomas Bell, Dr Ute Schuster and Professor Andrew Watson

The design and construction of NSOP, the cruise and seasonal study fieldwork, all of the writing, and data analysis for this thesis were completed by me.

I certify that all material in this thesis which is not my own work has been identified and that no material has previously been submitted and approved for the award of a degree by this or any other University.

All data from this thesis are freely available from the British Oceanographic Data Centre (BODC) https://www.bodc.ac.uk/

Signature: Richard Sims

Abstract

The seawater CO_2 partial pressures (pCO_2) which are used in flux calculations are measured in the mixed layer at ~5m. If the surface ocean is not mixed, the pCO_2 measured at 5m is not representative of the interfacial value and the calculated flux is incorrect. The objective of this work was to measure near surface pCO_2 gradients in the mixed layer to discern their occurrence, size and effect on the flux. A Near Surface Ocean Profiler (NSOP) was designed to precisely measure vertical gradients in the top 5 m of the ocean. Vertical profiles of pCO_2 were possible due to a fast equilibrating membrane equilibrator. Vertical profiles of temperature, salinity and pCO_2 were collected with NSOP during 4 research cruises at different times of the year in Shelf Seas and as part of a seasonal study at the Western Channel Observatory Site L4. Differences in pCO_2 of <2.5µatm and <5µatm over the surface 5m of the ocean were calculated using the near surface profiles made in the Shelf Seas and at L4 respectively. The largest differences in interfacial and subsurface CO_2 were >4µatm and were observed only when there were strong temperature gradients (> 0.05°C) and low wind speeds ($<6ms^{-1}$). There was no apparent relationship between the local meteorology and differences in the interfacial and subsurface pCO_2. Theoretical calculations of the formation of near surface layers with distinctly different pCO_2 to the subsurface pCO_2 indicate that the air–sea flux, biological production and rainfall could change the pCO_2 in a surface layer equal to the magnitude of the pCO_2 changes observed during the cruises. The largest differences in interfacial and subsurface CO_2 were observed when the wind speeds were low, this means that they have a relatively large effect on a small air sea fluxes over short periods of time but do not substantially alter the absolute size of flux which is dominated by strong winds over long timescales.

Table of Contents

List of Figures 8

List of Tables 11

1 Introduction 14

- 1.1 Introduction 14
- 1.2 The global and oceanic carbon cycles 14
- 1.3 Carbonate equilibria in seawater 15
- 1.4 Oceanic carbon parameters 17
  - 1.4.1 pH 17
  - 1.4.2 Dissolved inorganic carbon 17
  - 1.4.3 fCO_2 18
  - 1.4.4 Total Alkalinity 19
- 1.5 Determining other carbon parameters using carbon equilibria 19
- 1.6 Equations for the conversion of measured xCO_2 to in situ fCO_2 20
- 1.7 Surface ocean CO_2 climatologies 21
- 1.8 Shelf Seas 23
  - 1.8.1 Hydrography of the European shelf 23
  - 1.8.2 Biogeochemical seasonality in Shelf Seas and the coastal ocean 25
    - 1.8.2.1 Winter 26
    - 1.8.2.2 Spring 27
    - 1.8.2.3 Summer 28
    - 1.8.2.4 Autumn 29
  - 1.8.3 Export of carbon from shelf seas 30
  - 1.8.4 The carbon budget of shelf seas 32
- 1.9 Gas Exchange 32
  - 1.9.1 The flux equation 32
  - 1.9.2 Conceptual basis of gas exchange 33
  - 1.9.3 Wind speed control on gas exchange 34
  - 1.9.4 Other controls on gas exchange 35
    - 1.9.4.1 Bubbles 35
    - 1.9.4.2 Breaking waves 36
    - 1.9.4.3 Surfactants 36
    - 1.9.4.4 Rain 36
  - 1.9.5 Equations used to calculate the flux 37
- 1.10 CO_2 flux using climatologies 38
- 1.11 The vertical temperature structure of the surface ocean 38
  - 1.11.1 The thermal skin 39

1.11.2 The surface mixed layer/ Diurnal Warm layer 40
1.11.3 Measurement of upper ocean temperature 40
1.11.3.1 Measurements of the thermal skin temperature 40
1.11.3.2 Measurements of the mixed layer temperature 41
1.11.4 Numerical models of heating and turbulence 42
1.11.4.1 Diffusion models 42
1.11.4.2 Bulk layer models 42
1.11.4.3 Empirical models 43
1.12 Temperature dependencies in calculating the CO_2 flux 43
1.13 CO_2 sensitivity to temperature 44
1.14 Salinity structure of the upper ocean 45
1.15 Salinity dependencies in equations used to calculate flux 45
1.16 The effect of temperature and salinity skin effects on the CO_2 flux 46
1.17 Near Surface CO_2 Gradients 46
1.17.1 CO_2 gradients associated with temperature and salinity 46
1.17.2 CO_2 gradients associated with changes in surface carbon 47
1.18 Thesis hypothesis and overview 48
2 Theoretical basis for the formation of near surface CO_2 gradients 49
2.1.1 Surface carbon budget calculation 49
2.2 Processes that could drive the formation of near surface CO_2 gradients 50
2.2.1 Net primary production 50
2.2.2 Air to sea flux of CO_2 51
2.2.3 Dilution by rainfall 52
2.2.4 Calcification 52
3 Methods– A measurement system for vertical seawater profiles close to the air–sea interface 53
3.1 Introduction 53
3.2 The near surface ocean profiler 54
3.2.1 Near Surface Ocean Profiler (NSOP) description 54
3.2.2 NSOP deployment 56
3.3 CO_2 analysis 58
3.4 Equilibrator 59
3.5 DMS analysis 61
3.6 NSOP delay and response time 61
3.7 Data processing 62
3.8 Seawater sample collection using NSOP 63
3.9 Field Measurements / Observations 63

3.9.1 Open ocean deployment ... 64
3.9.2 Coastal deployment ... 67
3.10 Summary ... 69
4 NSOP deployments in UK shelf seas ... 70
4.1 Introduction ... 70
4.2 Cruise sampling considerations ... 70
4.3 SSB Cruise Programme ... 70
4.3.1 Pelagic cruises ... 71
4.3.2 Benthic cruises ... 72
4.3.3 North West European shelf cruise ... 72
4.4 Justification for choosing the SSB programme ... 72
4.5 Underway and Meteorological measurements on board RRS Discovery ... 72
4.5.1 Underway supply measurements ... 72
4.5.2 Meteorological measurements ... 73
4.5.3 Underway surface CO_2 system ... 73
NSOP ... 75
4.6 Deployments overview ... 75
4.7 Data description conventions for salinity, temperature and CO_2 ... 80
4.8 AUG14 ... 80
4.8.1 AUG 14 Cruise meteorology ... 80
4.8.2 AUG14 Salinity profiles ... 81
4.8.3 AUG14 Temperature profiles ... 81
4.8.4 AUG14 CO_2 profiles ... 82
4.8.5 AUG14 profile interpretation ... 86
4.9 OCT14 ... 87
4.9.1 OCT 14 Cruise meteorology ... 87
4.9.2 OCT14 Salinity profiles ... 88
4.9.3 OCT14 Temperature profiles ... 88
4.9.4 OCT14 CO_2 profiles ... 89
4.9.5 OCT14 profile interpretation ... 93
4.10 MAY15 ... 93
4.10.1 MAY15 Cruise meteorology ... 93
4.10.2 MAY15 Salinity ... 94
4.10.3 MAY15 Temperature profiles ... 94
4.10.4 MAY15 CO_2 profiles ... 95
4.10.5 MAY15 TA and DIC profiles ... 95
4.10.6 MAY15 Profile interpretation ... 102

4.11 JULY15 103
4.11.1 JULY15 Cruise meteorology 103
4.11.2 JULY15 Salinity profiles 104
4.11.3 JULY15 Temperature profiles 104
4.11.4 JULY15 CO_2 profiles 104
4.11.5 JULY15 TA and DIC profiles 105
4.11.6 JULY15 profile interpretation 112
4.12 Explaining TA and DIC noise 113
4.13 Summary 114
5 A seasonal study of horizontal and vertical near surface variability in surface seawater CO_2 at the Western Channel Observatory 114
5.1 Introduction 114
5.2 The Western Channel Observatory as the seasonal study location 115
5.3 Local hydrography 116
5.4 Time series measurements at the L4 mooring during the seasonal study 119
5.4.1 Meteorology 119
5.4.2 In water variables 121
5.4.3 Underway fCO_2 at L4 126
5.4.4 Tidal height and stage of the tidal cycle during NSOP deployments 127
6 Horizontal variability in surface seawater CO_2 close to the Western Channel Observatory 129
6.1 Introduction 129
6.2 Response times and spatial resolution of the “liqui–cel” and “showerhead” systems 129
6.3 Dates and locations of underway measurements made on transit to and from station L4 129
6.4 “liqui–cel” and “showerhead” underway measurement comparison 130
6.5 Surface salinity trends from the Breakwater to L4 134
6.6 Surface temperature trends from the Breakwater to L4 135
6.7 Horizontal CO_2 trends from the Breakwater to L4 136
6.8 Tidal influences on fCO_2 between the Breakwater and Penlee 138
6.9 Implications of horizontal differentials 143
6.10 Conclusions 144
7 A seasonal study of vertical variability in surface seawater CO_2 at the Western Channel Observatory 144
7.1 Introduction 144
7.2 NSOP deployments overview 144
7.3 Data description conventions for salinity, temperature and CO_2 151

7.4 Salinity profiles ... 151
7.5 Temperature profiles ... 151
7.6 CO_2 profiles ... 151
7.7 Profile interpretation ... 159
7.8 Advection of water masses at L4 ... 160
7.9 Summary ... 161
8 A synthesis of near surface gradients ... 162
8.1 Introduction ... 162
8.2 Standardising profiles ... 162
8.3 Salinity differences (ΔS) ... 162
8.4 Temperature gradients ... 166
8.5 NSOP derived ΔfCO_2 relative to showerhead CO_2 ... 176
8.6 CO_2 and temperature gradients ... 178
8.7 Classifying profile shapes ... 180
8.7.1 Comparing cruise profile shapes ... 181
8.7.2 Identifying common profile shapes during the SSB cruises ... 182
8.7.3 Insights from profile shapes ... 187
8.8 Gradients by region ... 188
8.9 Correction to in situ temperature ... 190
8.10 Which scenarios can feasibility explain observed gradients in a shelf sea environment? ... 197
8.11 Conclusions ... 198
9 Gradient modification on the air–sea flux ... 199
9.1 Introduction ... 199
9.2 Fluxes calculated using measurements from 5m ... 200
9.3 Percentage change in flux using surface temperature and salinity ... 201
9.4 Percentage change in the flux using surface salinity, temperature and CO_2 203
9.5 Conclusions ... 204
10 Implications for Shelf Seas globally ... 205
10.1 Implications of this work on the air sea flux of CO_2 in other Shelf Seas ... 205
10.2 Global coverage of shelf seas ... 205
10.3 Shelf sea surface irradiance ... 206
10.4 Shelf sea wind speed ... 209
10.5 Modelled wind and irradiance scenarios for diurnal warming events ... 213
10.6 Climatological diurnal warming ... 215
10.7 Shelf sea rainfall rate ... 218
10.8 Sea ice melt rate ... 222

10.9 Shelf sea atmosphere ocean ΔpCO_2 222
10.10 Shelf sea productivity rate 225
10.11 Synthesising disparate data – a theoretical approach 234
10.12 Shelf by shelf analysis 234
10.12.1 European Shelf 234
10.12.2 Scotian Shelf 234
10.12.3 Polar Shelf Seas 235
10.12.4 Caribbean Sea 235
10.12.5 Tunisian-Libya continental shelf and Adriatic Sea 235
10.12.6 Continental shelf off the West coast of Australia 236
10.12.7 East China Shelf 236
10.12.8 Shelf region Malaysia and the Sundra Shelf 236
10.12.9 Patagonian Shelf 236
10.12.10 Gulf of Carpentaria 237
10.12.11 The Great Barrier Reef 237
10.12.12 Tasmanian shelves 237
10.13 Summary - In which shelf seas are near surface gradients important 237
11 Conclusions and future recommendations 238
12 Appendix 240
12.1 RRS Discovery 240
12.2 Deployment location from RRS Discovery 241
12.3 Changes to methodology between cruises 242
12.3.1 Instrument Changes 242
12.3.2 Methodological Improvements 243
12.3.3 RV Plymouth Quest 244
12.3.4 Sampling considerations and methodological changes specific to RV Quest 244
13 References 245

List of Figures

Figure 1.1 The global carbon cycle 15
Figure 1.2 Bjerrum plot of carbon species 17
Figure 1.3 Variability in the fugacity coefficient for CO_2 19
Figure 1.4 Schematic of a non-dispersive infrared analyser 20
Figure 1.5 SOCAT surface fCO_2 climatology 22
Figure 1.6 The European shelf 24
Figure 1.7 Seawater fluxes across the European Continental shelf break 25
Figure 1.8 Seasonal climatology of the atmosphere–ocean ΔpCO_2 in the North Sea .. 27

Figure 1.9 Stratification and cross–slope exchange processes at the shelf break 30
Figure 1.10 Schematic of the continental shelf pump 32
Figure 1.11 Kinetic and thermodynamic forcing controls on air–sea CO_2 flux............. 37
Figure 1.12 Global climatological mean air sea fluxes of CO_2 38
Figure 1.13 Idealised temperature structure schematics 39
Figure 1.14 The relationship between temperature and CO_2 fugacity 45
Figure 2.1 Near surface gradient scenarios 49
Figure 3.1 NSOP deployment schematic 55
Figure 3.2 NSOP depth stability at different depths... 56
Figure 3.3 Photographs of the crew deploying NSOP on RRS Discovery 57
Figure 3.4 CO_2 system schematic.. 59
Figure 3.5 Liqui–cel efficiency.. 61
Figure 3.6 Liqui–cel system delay and response times 62
Figure 3.7 NSOP TA profile from an NSOP deployment on 19th July 2015................. 63
Figure 3.8 Meteorology preceding an NSOP deployment 30th July 2015..................... 64
Figure 3.9 Time series measurements from an NSOP deployment 30th July 2015...... 65
Figure 3.10 Salinity and temperature in the Central Celtic Sea on 30th July 2015........ 66
Figure 3.11 NSOP density and fCO_2 profiles in the Celtic Sea on 30th July 2015 67
Figure 3.12 Time series measurements from a NSOP deployment 15thApril 2014 68
Figure 3.13 NSOP profiles collected in Plymouth Sound on 15th April 2014 69
Figure 4.1 Field sites and NSOP deployment locations.. 77
Figure 4.2 AUG14 Cruise meteorology 81
Figure 4.3 AUG14 Salinity profiles 83
Figure 4.4 AUG14 Temperature profiles 84
Figure 4.5 AUG14 CO_2 profiles.. 85
Figure 4.6 OCT14 Meteorology from Stornoway airport 88
Figure 4.7 OCT14 Salinity profiles 90
Figure 4.8 OCT14 Temperature profiles.. 91
Figure 4.9 OCT14 CO_2 profiles 92
Figure 4.10 MAY15 Cruise meteorology 94
Figure 4.11 MAY15 Temperature profiles 97
Figure 4.12 MAY15 CO_2 profiles.. 98
Figure 4.13 MAY 15 TA profiles... 99
Figure 4.14 MAY 15 DIC profiles... 100
Figure 4.15 MAY 15 Measured and derived (TA/DIC) CO_2....................................... 101
Figure 4.16 JULY15 Cruise meteorology 104
Figure 4.17 JULY15 Salinity Profiles.. 106
Figure 4.18 JULY15 Temperature Profiles 107
Figure 4.19 JULY15 CO_2 Profiles.. 108
Figure 4.20 JULY15 TA Profiles.. 109
Figure 4.21 JULY15 DIC Profiles 110
Figure 4.22 JULY 15 Measured and derived (TA/DIC) CO_2..................................... 111
Figure 5.1 Western Channel Observatory Sites 116
Figure 5.2 Surface currents at the Western Channel Observatory 118
Figure 5.3 Surface salinity fields for the Western Channel Observatory 119
Figure 5.4 Meteorology at the L4 mooring... 121
Figure 5.5 Climatological wind speed and direction for station L4 121
Figure 5.6 Surface temperature and salinity at the L4 mooring 123
Figure 5.7 Surface temperature measurements at the L4 mooring........................... 123

Figure 5.8 Surface temperature differential at the L4 mooring 124
Figure 5.9 Surface L4 temperature and salinity climatology 124
Figure 5.10 Surface fluorescence and turbidity at the L4 mooring 125
Figure 5.11 River Tamar flowrate recorded daily at Gunnislake 126
Figure 5.12 Surface fCO_2 at the L4 mooring 127
Figure 5.13 Devonport tidal height 128
Figure 6.1 Ship tracks during the seasonal study 130
Figure 6.2 Comparison of coincident measurements from liqui–cel and showerhead CO_2 systems 131
Figure 6.3 Measurement overlap between the showerhead and liqui–cel CO2 systems 133
Figure 6.4 Surface salinity versus distance from L4 135
Figure 6.5 Temperature versus distance from L4 136
Figure 6.6 Temperature difference relative to L4 versus distance from L4 136
Figure 6.7 fCO_2 versus distance from L4 138
Figure 6.8 fCO_2 relative to L4 versus distance from L4 138
Figure 6.9 Surface CO_2 tracts on voyages between L4 and the breakwater 141
Figure 6.10 Surface salinity tracts on voyages between L4 and the breakwater 142
Figure 7.1 Sampling tracks around the L4 mooring 146
Figure 7.2 Station L4 salinity profiles (1 of 2) 153
Figure 7.3 Station L4 salinity profiles (2 of 2) 154
Figure 7.4 Station L4 temperature profiles (1 of 2) 155
Figure 7.5 Station L4 temperature profiles (2 of 2) 156
Figure 7.6 Station L4 CO_2 profiles (1 of 2) 157
Figure 7.7 Station L4 CO_2 profiles (2 of 2) 158
Figure 8.1 Magnitude of ΔS from NSOP profiles 164
Figure 8.2 ΔS occurrence with irradiance and wind speed 165
Figure 8.3 Magnitude of ΔT from NSOP profiles 167
Figure 8.4 Occurrence of ΔT in the Celtic Sea and at L4 168
Figure 8.5 Comparison ΔT measured by NSOP and the NSTS at L4 169
Figure 8.6 ΔT occurrence with irradiance and wind speed 171
Figure 8.7 ΔT occurrence with time of day 172
Figure 8.8 Magnitude of ΔCO_2 from NSOP profiles 174
Figure 8.9 ΔCO_2 occurrence with irradiance and wind speed 176
Figure 8.10 CO_2 differential with the underway system 178
Figure 8.11 ΔT versus ΔCO_2 179
Figure 8.12 Delta temperature and delta CO_2 relationship by cruise 180
Figure 8.13 Schematic representation of profile shapes 181
Figure 8.14 CO_2 profiles referenced against a surface value of 0 182
Figure 8.15 Profiles shapes - Linear Profiles 183
Figure 8.16 Profiles shapes - Change in the gradient near the surface above 2m 184
Figure 8.17 Profiles shapes - Change in the gradient below 2m 185
Figure 8.18 Profiles shapes - Linear with deviation around 3m depth 186
Figure 8.19 Profiles shapes - Linear with deviation at the surface around 1m 187
Figure 8.20 Topographic map of the Celtic Sea region 188
Figure 8.21 Topographic map of the Hebridean Shelf region 189
Figure 8.22 ΔT and ΔCO_2 by region 190
Figure 8.23 Temperature correction and ΔCO_2 relationship 192
Figure 8.24 Temperature and fCO_2 derived fractional CO_2 constants 194

Figure 8.25 MAY15 and JULY15 CO_2 profiles using calculated fractional constant... 196
Figure 9.1 CO_2 fluxes calculated using NSOP parameters from different depths 201
Figure 9.2 Percentage change in flux using surface salinity and temperature 202
Figure 9.3 Percentage change in flux using surface NSOP values........................... 204
Figure 10.1 Global map showing the spatial extent of shelf seas 206
Figure 10.2 Meridional averages of the ocean heat flux 207
Figure 10.3 Clear sky days 208
Figure 10.4 Global average solar irradiance.. 209
Figure 10.5 Maximum surface insolation values... 209
Figure 10.6 Global wind speed distribution 211
Figure 10.7 Latent and Sensible heat flux controls... 212
Figure 10.8 Diurnal warming as a function of peak radiation and wind speed 213
Figure 10.9 Peak solar radiation and wind speed control on diurnal warming 214
Figure 10.10 Probability difference for diurnal SST formation 214
Figure 10.11 Modelled average diurnal warming.. 216
Figure 10.12 Satellite derived diurnal warming... 217
Figure 10.13 Global map of the percentage of days where diurnal warming exceeds 0.1°C 217
Figure 10.14 Global map of daily rainfall 218
Figure 10.15 Global map of precipitation incidence.. 219
Figure 10.16 Global zonal mean seasonal cycle of precipitation 220
Figure 10.17 Figure legend 221
Figure 10.18 Global annual average ΔpCO_2 (seawater – air) climatology 223
Figure 10.19 Peak differences in seasonal amplitude 223
Figure 10.20 Global ΔpCO_2 (seawater – air) monthly climatology 225
Figure 10.21 Biological drawdown of CO_2 226
Figure 10.22 Satellite derived global annual column NPP inferred from surface chlorophyll concentrations... 227
Figure 10.23 Satellite derived global seasonal column NPP inferred from surface chlorophyll concentrations... 228
Figure 12.1 RRS Discovery propulsion and handling systems 241
Figure 12.2 Crane deployment schematic.. 243
Figure 12.3 Plymouth Quest schematic.. 244

List of Tables

Table 1 Key features of specialised surface ocean profilers....................................... 41
Table 2 Relative change in DIC and CO_2 from different processes in Shelf Seas........ 52
Table 3 RRS Discovery underway and meteorological measurements 74
Table 4 NSOP cruise deployments overview 78
Table 5 NSOP seasonal study overview table.. 147

Acknowledgements

I could never have got to this stage without the help of my mum Jane who strived to get me the best schooling possible, something she never had. I'm so grateful for all the little things you did to encourage me to learn when I was younger, whether it was helping with my spellings or nurturing my love of science. To ensure I went to a good school you literally fought the rest of the family, even though it risked jeopardising your marriage. Knowing you always supported me even when I was disappointed in my own performance was so important and gave me the confidence to be the first in the family to go to university, thanks Mum.

To my PhD cohort old and new, you have had my back the whole way. Thanks to Debs, Kylie, Steph, Becca and Jackie who showed me that writing poetry on Fridays and going to the beach in the afternoon is an alternate path to victory and PhD success. To Kristian the office guru, your mantra of not stressing about work led to some incredibly fun and often stupid times like transporting moon jellies in a crisp packet. I'm hugely appreciative of the afternoon tea club, Emily, Bianca, Paul and Frankie who got me through the analysis stage; we made a great chancel pub quiz team. Dan, Zara, Francesco and Emilie, thanks for making me feel like a PML OAP and making me realise I needed to knuckle down and finish my thesis.

To the other friends I made along the way, you will be stuck with me forever. To my bike gang, the porky from Yorkie, the shins from Shrewsbury, and my bike wife the legs from Lewisham, I owe you three so much for encouraging me to start cycling again, it changed my outlook and brought me great joy and relaxation at the weekends. I'll always remember Mads passing out in France and Antony cracking open the port wine in the Eden project. To my hiking friends Charlie, Will, Giulia, Woody and Mike thanks for trouncing about with me on our many hiking trips. A huge thank you to Silvana for always organising fun things to do and making me fall in love with Plymouth.

To all my SSB friends, thank you for the great memories, I'll never forget trying to listen to Dr Dre over the sound of the filter rig with Lucie, chasing after dolphins, dancing about the rosette, making toilet paper bats, flying a kite on the bow of Discovery, guessing the deep chlorophyll maximum and of course emptying the waste tank. Truly the cruise never ends.

It's only fitting I commit a paragraph to my PhD brother Kieran as we took this journey together. We were likened to Bert and Ernie for a reason, I don't think there is another person alive who I could have lived and worked with for three years without going completely mad. We definitely kept each other on track, whether it was riding rhinos, chomping cashews, photographing pyramids, unlocking Netflix achievements, or going to the lab at 9pm.Truly fun times, so say we all.

Thanks to everyone who has offered guidance and helped along the way. A big thank you to Ming and Vas for always being happy to listen and give advice, at times you've both felt like extra supervisors. Thanks to Rob and Paul for agreeing to be my examiners, I really appreciate the thought you put in to your feedback, it has been invaluable and really improved the thesis. Thanks to the crews of the Discovery and Quest who went above and beyond to accommodate me in deploying NSOP.

My greatest thanks are reserved for my PhD supervisors Tom, Ute and Andy who have been brilliant. I am immensely grateful that I always felt like I was deciding the direction of the project as this always made it feel like it was mine. I see now that the reason for this was that I was never led, I was guided which in retrospection is indicative of the excellent supervision I was given. I made countless mistakes along the way, yet you were all always so patient with me. I always knew I wanted to be a scientist and thanks to your help I am now one. You only get one primary supervisor and I made such a good choice with you Tom, always pushing me, encouraging me, watching out for me, fighting for me and making so much time for me on a daily basis. You have been more than a supervisor; you are a mentor, role model and friend. I'm eternally grateful, thank you so much.

1 Introduction

1.1 Introduction

Exchange between the ocean and atmosphere is an important process for many gases. Important examples include carbon dioxide (CO_2), for which the oceans account for 25% of the sink for anthropogenic emissions (Le Quéré et al., 2016), and dimethylsulfide (DMS), which has an oceanic source and influences cloud properties with implications for the global energy balance (Quinn and Bates, 2011). The magnitude and direction of air–sea gas transfer is typically represented by $Flux=k\Delta C$ (Liss and Slater, 1974), where ΔC is the concentration difference across the air–sea interface and k ($54ms^{-1}$) is the gas transfer velocity. Direct flux measurements (Bell et al., 2013, Yang et al., 2013, Miller et al., 2010) are only possible for a small number of gases and are not made routinely. Most flux estimates use a wind speed–based parameterisation of k (e.g. Wanninkhof, 2014) coupled with measurements of ΔC.

CO_2 is the most well–observed trace gas in the surface ocean, with 14.5 million measurements compiled into a global database, the Surface Ocean CO_2 Atlas (SOCAT), http://www.socat.info/ (Bakker et al., 2016). Global trace gas databases also exist for gases such as methane and nitrous oxide https://memento.geomar.de/ (Bange et al., 2009), dimethylsulfide http://saga.pmel.noaa.gov/dms/ (Lana et al., 2011) and halocarbons https://halocat.geomar.de/ (Ziska et al., 2013). Accurate estimation of air–sea flux requires concentration measurements that are representative of the interfacial concentration difference. Surface seawater samples are often collected from the underway seawater intake of research vessels, typically at 5–7 m depth. A source of potential error in air–sea flux calculations arises from the assumption of vertical homogeneity within the mixed layer (Robertson and Watson, 1992b). If vertical concentration gradients exist in the mixed layer, then underway seawater is not representative of the interfacial layer, which could create a global sampling bias (McNeil and Merlivat, 1996).

Vertical gradients in trace gas concentrations have been observed under conditions that are favourable for near surface stratification (Royer et al., 2016). At low wind speeds, high solar irradiance can suppress the depth of shear–induced mixing to create a near surface layer several degrees warmer than the water below (Ward et al., 2004a, Fairall et al., 1996). Near surface stratification in the marine environment can also be induced by freshwater inputs such as rain (Turk et al., 2010) and riverine discharge. Changes in surface seawater temperature and salinity alter the solubility of dissolved gases and thus the amount available for air–sea exchange (Woolf et al., 2016). Dissolved gases isolated in the upper few metres of the ocean may additionally be modified by physical process such as air–sea exchange and photochemistry. Marine biota confined within the stratified layer (Durham et al., 2009), may also alter trace gas concentrations. For the purposes of this thesis, near surface gradients are defined as physical and/or chemical gradients in the upper 5 m of the ocean.

1.2 The global and oceanic carbon cycles

The global carbon cycle is a fundamental biogeochemical cycle that encompasses the exchange of carbon between its reservoirs on earth. The four primary carbon reservoirs are the atmosphere, biosphere, hydrosphere and lithosphere (Figure 1.1). The amounts and residence times of carbon in these reservoirs range by orders of magnitude as do the gross and net fluxes between them (Figure 1.1). The global carbon budget defines the size of the reservoirs and the exchange rates between the reservoirs (Le Quéré et al., 2016). The size of a reservoir is in a steady state if the inputs of carbon match the outputs. An imbalance between the inputs and outputs will result in the reservoir growing or shrinking. Humans have perturbed the natural carbon cycle by the rapid release of CO_2 into the atmosphere via the combustion of fossil fuels since the industrial revolution (Solomon et al., 2007). To understand human perturbations of the carbon cycle it is necessary to have measurements of the sizes of and the fluxes between reservoirs. As the oceanic reservoir is a sink for ~25% of anthropogenic CO_2, understanding the air– sea flux of CO_2 is of paramount importance in understanding changes in the carbon cycle today and into the future (Sabine et al., 2004).

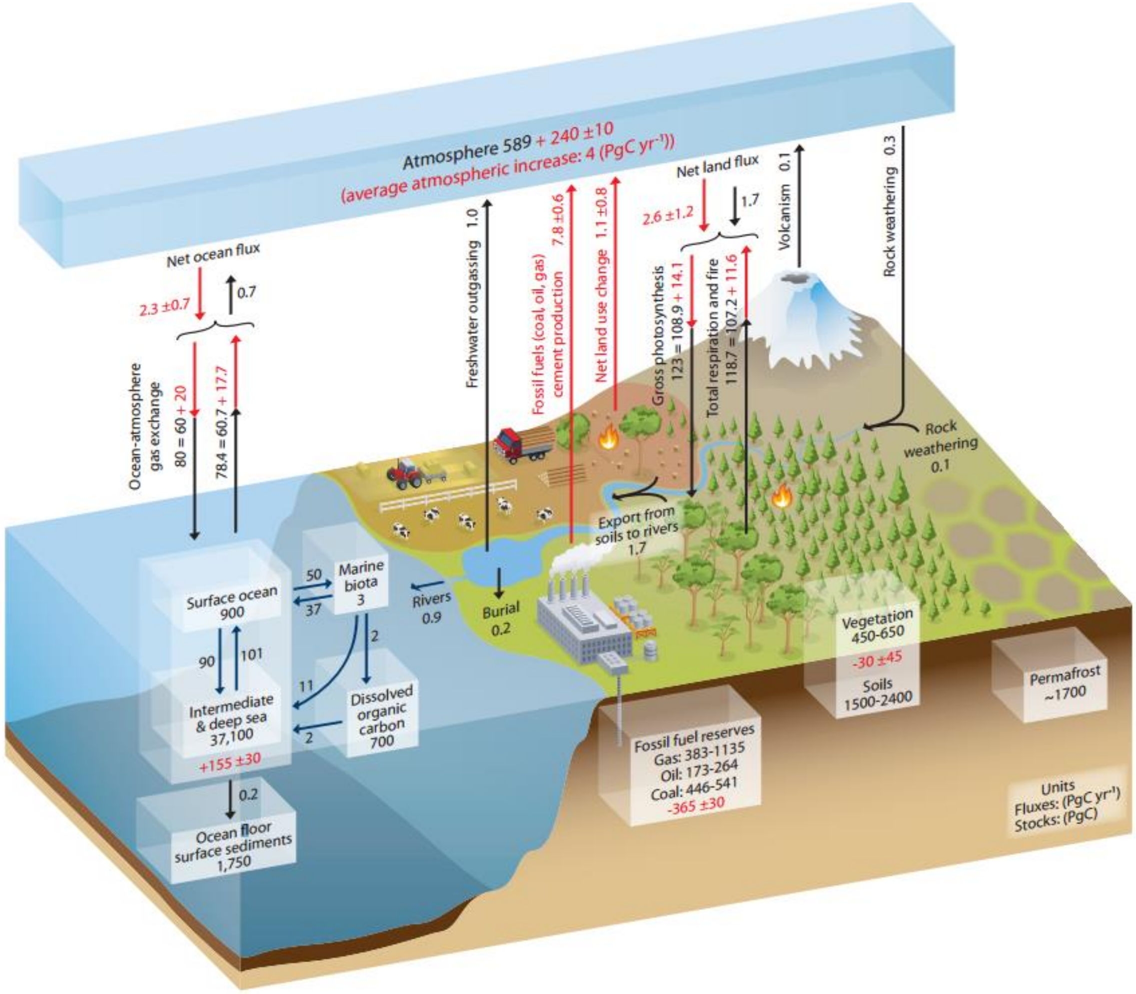

Figure 1.1 The global carbon cycle

Schematic of the global carbon cycle as at 2011. Carbon reservoirs are represented by boxes. Reservoir sizes in Peta grams of carbon (Pg C) are given just below the name of each box. Pre industrial fluxes (Pg C a^{-1}) are indicated by black arrows. Changes to the size of reservoirs and fluxes between 1750 and 2011 are marked separately in red (Ciais et al., 2014).

1.3 Carbonate equilibria in seawater

Atmospheric carbon dioxide ($CO_{2\,(g)}$) dissolves in seawater becoming the aqueous form ($CO_{2\,(sw)}$) (equation 1). $CO_{2\,(sw)}$ is then hydrolysed to form carbonic acid (H_2CO_3) in seawater (equation 2). H_2CO_3 undergoes two further dissociation reactions (equations 3 & 4) to form hydrogen (H^+), bicarbonate (HCO_3^-) and carbonate (CO_3^{-2}) ions (Millero, 1995). As the concentration of H_2CO_3 greatly exceeds that of $CO_{2\ (sw)}$, the concentrations of both dissolved species are often aggregated as $[CO_2]$. Equation 5 summarises the sequence of CO_2 dissociation in seawater.

$$CO_{2(g)} \rightleftarrows CO_{2(sw)} \qquad \text{Equation (1)}$$

$$CO_{2(aq)} + H_2O \rightleftarrows H_2CO_3 \qquad \text{Equation (2)}$$

$$H_2CO_3 \rightleftarrows HCO_3^- + H^+ \qquad \text{Equation (3)}$$

$$HCO_3^- \rightleftarrows H^+ + CO_3^{-2} \qquad \text{Equation (4)}$$

$$CO_{2(g)} \rightleftarrows CO_{2(aq)} + H_2O \rightleftarrows H_2CO_3 \rightleftarrows HCO_3^- + H^+ \rightleftarrows 2H^+ + CO_3^{-2} \qquad \text{Equation (5)}$$

The solubility constant for the dissolution of CO_2 as in equation (1) is given by the aqueous phase solubility coefficient for CO_2 (k_0) (mol m^{-3} Pa^{-1}). Measurements of k_0 as a function of both temperature (T) and salinity (S) were made by (Li and Tsui, 1971) and (Murray and Riley, 1971) and later validated by (Weiss, 1974).

The Ostwald solubility coefficient (α) is the volume of gas that dissolves in a solvent at the temperature of the solvent, in this case seawater at a specified temperature (T_{sw}). k_0 is directly linked to the Ostwald solubility coefficient (equation 6), where R (m^3 Pa K^{-1} mol^{-1}) is the ideal gas constant.

$$k_0 = \alpha\ (RT_{(sw)})^{-1} \qquad \text{Equation (6)}$$

The dissociation constants for (equations 2 & 3) can be combined and simplified to give the first dissociation constant for CO_2 in seawater (pK_1) (equation 7). The dissociation constant for equation 4 is the second dissociation constant for CO_2 in seawater (pK_2) (equation 8) (Dickson and Millero, 1987).

$$pK_1 = [HCO_3^-][H^+][CO_2]^- \qquad \text{Equation (7)}$$

$$pK_2 = [CO_3^{-2}][H^+][HCO_3^-]^- \qquad \text{Equation (8)}$$

Values of both pK_1 and pK_2 have been determined by potentiometric titrations (Mehrbach et al., 1973, Hansson, 1973b, Hansson, 1973a). Reanalysis of previously published studies by Dickson and Millero (1987) showed agreement between the calculated dissociation constants. pK_1 and pK_2 are estimated in seawater using temperature and salinity relationships such as those in equations 9 and 10 (Goyet and Poisson, 1989). The dissociation constants of Mehrbach et al. (1973) and Dickson and Millero (1987) have been adopted as the community standard and by the Joint Panel of

Oceanographic Standards for UNESCO 1987 over the more precise dissociation constants given by Goyet and Poisson (1989) and Roy et al. (1993). [HCO_3^-] and [CO_2] are equal when pH=pK_1 whereas [HCO_3^-] and [CO_3^{-2}] are in equal abundance when pH=pK_2 (Figure 1.2).

$$pK_1 = 812.27T^{-1} + 3.356 - 0.00171S\ln(T) + 0.000091S^2$$ Equation (9)

$$pK_2 = 140.87T^{-1} + 4.604 - 0.00385S\ln(T) + 0.000182S^2$$ Equation (10)

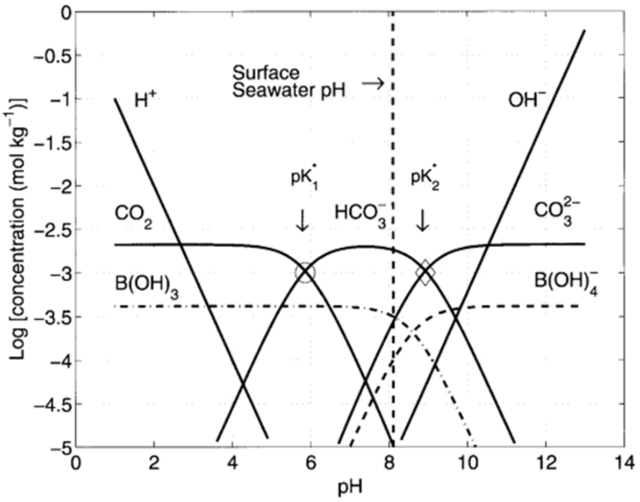

Figure 1.2 Bjerrum plot of carbon species

Bjerrum plot showing pH as a function of carbon speciation in seawater. In the plot above the dissolved organic carbon (DIC) content is 2100 µmol kg^{-1}, the salinity is 35 and temperature 25°C. The circle and diamond indicate pK1=5.86 and pK2=8.92 of carbonic acid. Boric acid $B(OH)_3$ dissociates to form borate $B(OH)_4^-$, the dissociation constant for boric acid in seawater has a pKa=9.24 (Zeebe and Wolf-Gladrow, 2001).

1.4 Oceanic carbon parameters

1.4.1 pH

pH is the negative logarithm of the hydrogen ion concentration [H^+] (equation 11)

$$pH = -\log(H^+)$$ Equation (11)

In natural seawaters the hydrogen ion concentration can be approximated as (equation 12)

$$[H^+] = [H^+]_F + [HSO_4]^-$$ Equation (12)

Where $[H^+]_F$ is the free ion concentration and $[HSO_4]^-$is the sulphate concentration

1.4.2 Dissolved inorganic carbon

The sum of the inorganic carbon species in seawater (equation 13) are collectively referred to as the dissolved inorganic carbon (DIC) (Emerson and Hedges, 2008).

$$DIC = [HCO_3^-] + [CO_3^{-2}] + [CO_2]$$ Equation

(13)

DIC is a total quantity and is not affected by temperature or pressure. By substitution it is possible to express DIC as a product of an individual species, the first and second dissociation constants and the hydrogen ion concentration (equations 14, 15 and 16) (Wolf-Gladrow et al., 2007).

$$[CO_2] = DIC / (1 + pK_1/[H^+] + pK_1pK_2/[H^+]^2) \qquad \text{Equation (14)}$$

$$[HCO_3^-] = DIC / (1 + [H^+]/pK_1 + pK_2/[H^+]) \qquad \text{Equation (15)}$$

$$[CO_3^{-2}] = DIC / (1 + [H^+]^2/pK_1pK_2 + [H^+]/pK_2) \qquad \text{Equation (16)}$$

1.4.3 fCO_2

Dalton's law states that in a mixture of ideal gases the total pressure is the sum of the partial pressures (p) of each gas. The mole fraction (x) of a gas is the number of moles of that gas (mol_g) per total moles of the atmospheric gases (mol_a). The mole fraction of a gas is technically dimensionless as the units cancel. The more commonly used notation for small values of trace gases is the parts–per notation. The parts–per notation gives the number of particles of the trace gas relative to a fixed number of particles of every gas in the mixture. The parts–per notation is dimensionless, parts per million (ppm) and parts per billion (ppb) commonly used.

For all non–ideal gases such as CO_2, the fugacity (f) of a gas is its effective pressure. The fugacity of a gas can be determined using the CO_2 mole fraction (xCO_2) and pressure (p) in the equation of state (equation 17). The fugacity coefficient of a gas is the fugacity of that gas divided by the total pressure of all the gases in the gas mixture. fCO_2 can be given in Pascals or atmospheres, to make the values of fCO_2 comparable to the PPM of pCO_2; units of µatm are typically used for fCO_2. An ideal gas has the same fugacity and partial pressure and thus a fugacity coefficient of 1. The fugacity coefficient and xCO_2 vary by <0.5% under natural oceanic conditions (Figure 1.3). CO_2 can be reported as either a fugacity or partial pressure in seawater, this had led to both values being used interchangeably despite being incorrect.

$$fCO_2 = xCO_2\ p\ \exp[1/RT\int_0^p \ (V\ (CO_2) - RT/p\ dp] \qquad \text{Equation (17)}$$

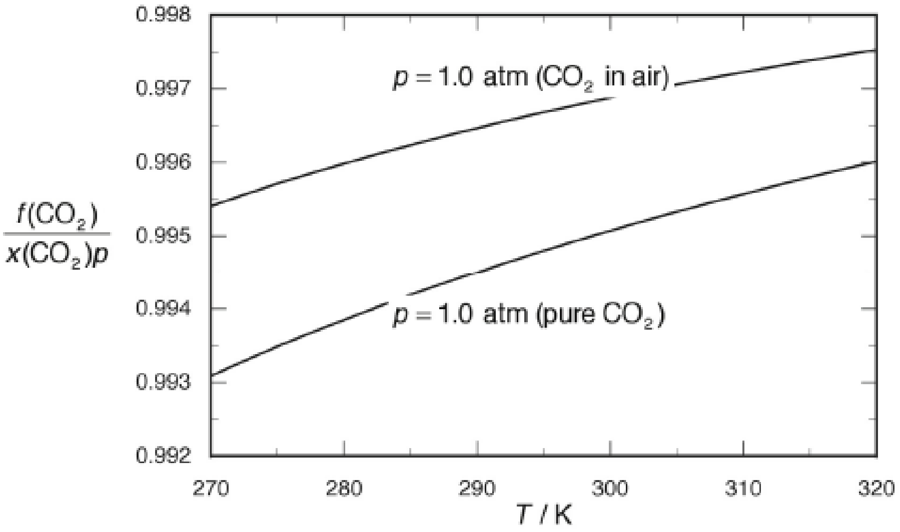

Figure 1.3 Variability in the fugacity coefficient for CO_2
Variability in the fugacity coefficient of CO_2 with changes in temperature at a fixed pressure of 1 atmosphere, for both pure CO_2 and CO_2 in air from Dickson et al. (2007).

1.4.4 Total Alkalinity

For there to be charge balance in the ocean, the anion and cation species must balance. The majority of cation and anion species do not exchange protons in the pH range of seawater. The total sum of cations that do not exchange in the pH range of seawater slightly exceeds the total sum of anions that do not exchange protons in the pH range of seawater. The difference is made up of the anion species that significantly exchange protons in the pH range of seawater. These anions make up the alkalinity. Total alkalinity (TA) measured in micro equivalents per kilogram (eq kg^{-1}) is defined as

'The number of moles of hydrogen ion equivalent to the excess of proton acceptors (bases formed by weak acids with a dissociation constant $K \leq 10^{4.5}$ at 25°C and zero ionic strength) over the proton donors (acids with $K \geq 10^{-4.5}$) in 1kg of sample' (Dickson, 1981).

The species that make up TA are given in equation (18). The two carbonate species make up the majority (96%) of alkalinity; once borate is included 99% of alkalinity is accounted for. For practical purposes a practical alkalinity (PA) can be used as an approximation for TA in natural seawaters (equation 19).

$$TA = HCO_3^- + 2CO_3^{-2} + B(OH)_4^- + H_3SiO_4^- + HPO_4^{-2} + 2PO_4^{-3} + OH^- - H^+ - HSO_4^- - HF - H_3PO_4 \qquad \text{Equation (18)}$$

$$PA = HCO_3^- + 2CO_3^{-2} + B(OH)_4^- + OH^- - H^+ \qquad \text{Equation (19)}$$

1.5 Determining other carbon parameters using carbon equilibria

Using two of the four measureable carbon quantities (TA, DIC, fCO_2 and pH) discussed in section 1.4 it is possible to calculate the remaining two parameters at equilibrium. When the remaining parameters are calculated this way, their accuracy is within the analytical uncertainty error of the measurement technique except when DIC and TA are used to calculate pH and fCO_2 (Millero, 1995). The low accuracy (±1.2%) of fCO_2 derived from DIC and TA is due to the uncertainties in pK1 (Lee et al., 1996). By equilibrating seawater samples with known gas mixtures Lueker et al. (2000) found that the fCO_2 values determined using the equilibrium constants of Mehrbach et al. (1973) agreed with equilibrated values to 0.07 ±0.5% (the 95% confidence limit). When equilibrating seawater samples with gases with fCO_2 >500 µatm, the fCO_2 was overestimated by 3.35 ±1.22% (Lueker et al., 2000), this overestimation was attributed to systematic errors in the equilibrium constants determined by Mehrbach et al. (1973).

1.6 Equations for the conversion of measured xCO_2 to in situ fCO_2

In the gas phase, CO_2 absorbs in the infrared part of the spectrum with the two main absorption bands at 15µm and 4.3µm, a third minor band exists at 2.7µm (Martin and Barker, 1932). Non–dispersive infrared (NDIR) gas analysers have an infrared source that emits at the wavelength of CO_2 and an infrared detector measures the infrared radiation coming from the source (Figure 1.4). Using the intensity of the source, the measured intensity at the detector and the distance between the source and detector, the beer–lambert law can be used to determine the absorption by CO_2 and thus amount of CO_2 in the measurement cell. NDIR analysers report the mole fraction of CO_2 (xCO_2) in the measurement cell after correcting for the interference from water vapour not removed by the dryer.

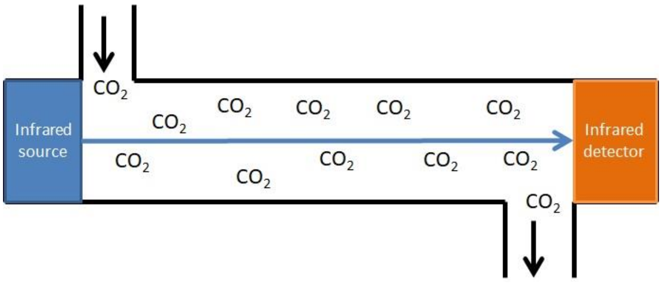

Figure 1.4 Schematic of a non-dispersive infrared analyser
Schematic representation of a non–dispersive infrared (NDIR). The infrared source and infrared detector are at opposite ends of the measurement cell which is filled with the sample gas. The direction of the infrared radiation emitted by the source is indicated by the blue arrow, the length of the arrow is the distance between the source and detector. Absorption of some of the infrared radiation by CO_2 is indicated by the CO_2 in the path of the infrared radiation. The sample gas flows through the cell, the inlet and outlet are indicated by black arrows.

There are a number of necessary equations required to convert this to the in–situ seawater fugacity ($fCO_{2\ sw}$).

To account for the drift in the analyser, three CO_2 standards are analysed before and after measurements. A linear fit is used to calculate the actual xCO_2 at different points between the standards (Dickson et al., 2007).

To measure seawater xCO_2, seawater is put into contact with a small volume of air in what is known as an equilibrator. In the equilibrator the small volume of air equilibrates with the seawater until it has the same xCO_2 as the seawater.

xCO_2 needs to be converted to the partial pressure of CO_2 in the equilibrator ($pCO_{2\ equ}$) using the measured pressure in the equilibrator (p_{eq}). From the definition of xCO_2 this simply requires multiplication with the equilibrator pressure (equation 20).

$$pCO2_{equ} = xCO_2 * p_{eq} \qquad \text{Equation (20)}$$

Water vapour alters the total pressure; in the presence of water vapour the water vapour pressure (p_{H2O}) must be subtracted from the total pressure (equation 21).

$$pCO2_{equ} = xCO2 * (p_{eq} – p_{H2O}) \qquad \text{Equation (21)}$$

It is assumed that the equilibrator headspace is at 100% humidity and the vapour pressure is given as a function of temperature (equation 22) (Cooper et al., 1998).

$$p_{H2O} = 0.981 * \exp (14.32602 – (5306.83/ (273.15 +T))) \qquad \text{Equation (22)}$$

Other versions of the equation for the water vapour pressure exist including one given by Dickson et al. (2007) and Weiss and Price (1980) that includes salinity (equation 23).

$$p_{H2O} = \exp(24.4543 - 67.4509(100/T) - 4.8489 \ln(T/100) - 0.000544S) \qquad \text{Equation (23)}$$

The conversion from pCO_2 to fCO_2 is made using (equation 24)

$$fCO_{2\ equ} = pCO_{2\ equ} * \exp (((B_{CO2} + 2*\delta_{CO2})*p_{atm})/ R*T_{equ}) \qquad \text{Equation (24)}$$

Where B_{CO2} is the first viral coefficients of CO_2 (equation 25)and δ_{CO2} is a cross viral coefficient (equation 26) for the binary mixture of CO_2–air , both are given in the temperature range of natural seawaters by Weiss (1974). R is the specific gas constant.

$$B_{CO2} = -1636.75 +12.0408 (T+273.15) - 0.0327957(T+273.15)^2 + 0.0000316528(T+273.15)^3 \qquad \text{Equation (25)}$$

$$\delta_{CO2} =57.7 -0.118(T+273.15) \qquad \text{Equation (26)}$$

The final step involves correcting for the in situ water temperature using the in situ temperature and the equilibrator temperature (equation 27) (Takahashi et al., 1993).

$$fCO_{2\ sw =} fCO_{2\ equ}* (\exp 0.0423 (T_{sw} – T_{equ}) \qquad \text{Equation (27)}$$

1.7 Surface ocean CO_2 climatologies

Many laboratories are measuring surface ocean CO_2 in different parts of the global ocean. Considerable international coordination lead to the establishment of a global carbon observing system (Monteiro et al., 2010) and the creation of standard operating procedures for measuring CO_2 (Dickson et al., 2007). Standardisation of the measurement methodologies and data logging is important as it minimises measurement errors and ensures all necessary data and metadata are logged. In order to make accurate assessents of the atmosphere ocean CO_2 flux it is necessary to compile all measurements of surface ocean CO_2 into a large global database.

Two primary databases exist, the freely accessible SOCAT (Surface Ocean Carbon Atlas) database (Pfeil et al., 2012) and the LDEO database kept by Takahashi et al. (2009). Both databases are continuously being expanded with each database iteration (Bakker et al., 2014).

SOCAT is the largest of the two databases with over 23 million measurements in v6, this is substantially more than the 10 million measurements found in v3. The increase in the number of measurements reflects the increase in the number of autonomous measurement systems on research ships. The spatial and temporal distribution of the measurements in SOCAT v3 can be seen in (Figure 1.5). Measurement frequency increased dramatically in the 90s, 00s and into the 10s as did the number of measurements in the Southern hemisphere particularly around Antarctica. There remain regions that are completely under sampled such as in the South Pacific, Southern Ocean and Indian Ocean and there are regions with seasonal variability such as the shelf seas which are also under sampled.

All the corrections listed in section 1.6 are completed by the SOCAT community to remove systematic errors that might occur by using different equations or using the equations incorrectly. The SOCAT community also perform independent quality control on all the data to detect any erroneous measurements. The SOCAT quality control involves automated data checks using WOCE flags and manual checks by quality controllers using the extensive guidelines detailed in Bakker et al. (2016).

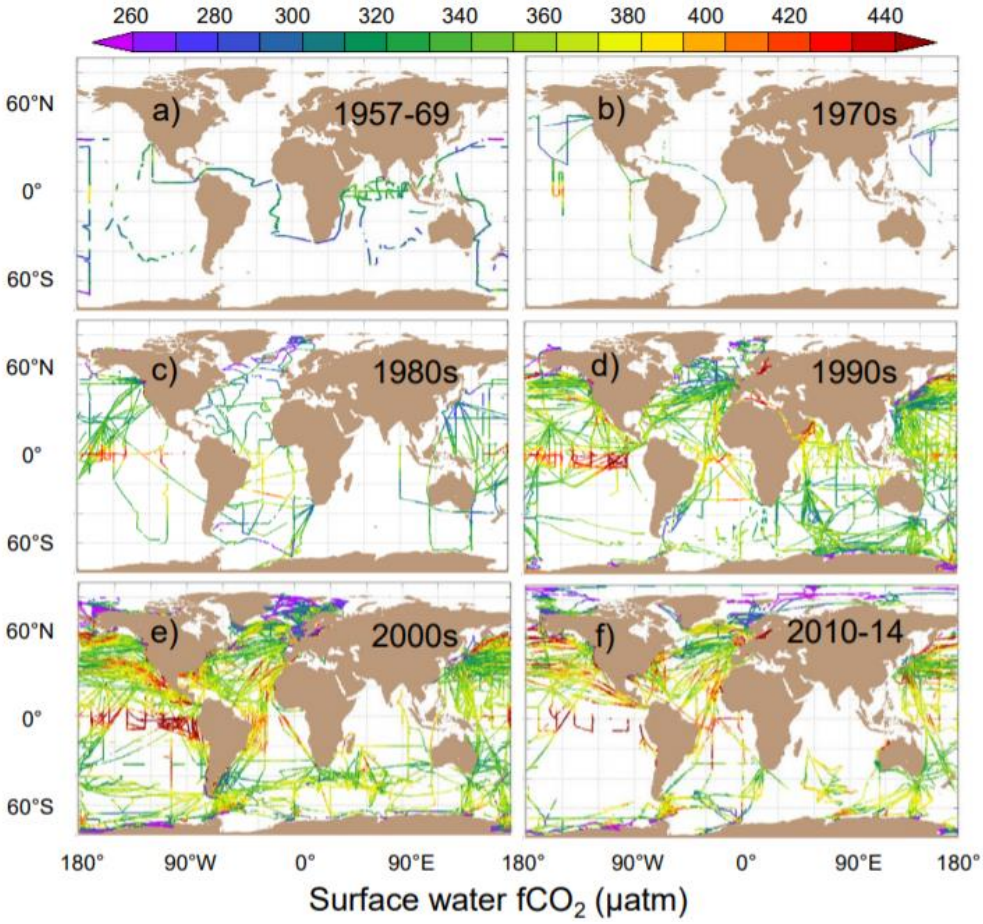

Figure 1.5 SOCAT surface fCO_2 climatology

Global measurements coverage of surface fCO_2 data in SOCAT v3 split into broadly decade time periods (Bakker et al., 2016).

1.8 Shelf Seas

All of the field observations in this thesis were either made in the Celtic Sea, Hebrides Shelf and the English Channel near Plymouth; all these regions are UK Shelf waters and are part of the European Shelf. A broad introduction to the physics and biogeochemistry of shelf seas is given in the context of the European Shelf to provide some background to the measurements discussed later in sections 4, 5 and 6. Whilst this introduction to shelf seas is focused heavily around the European shelf, the European shelf is considered a typical shelf sea so the description of the physics and biogeochemistry is also relevant to other shelf seas and the coastal ocean.

Shelf seas are defined as regions of the sea surrounding continents up to the boundary between the open ocean which is marked by the 200m isobaths (Laruelle et al., 2013). The continental slope is the region between the shallow shelf waters and deep ocean waters. Globally, shelf seas are relatively small in extent 2.6 X 10^7 km^2 (Walsh, 1991).

1.8.1 Hydrography of the European shelf

The Northeast Atlantic is one of the largest with a surface area of 1.11 X 10^6 km^2 (Laruelle et al., 2014). The width of the European Shelf varies substantially between Norway and Portugal (Figure 1.6). The width of the shelf changes considerably over small spatial extents, in the Celtic Sea it is 500km whereas in the Shelf Sea west of Ireland it is between 50 and 150km. The continental slope is steep between Portugal and North West Scotland except across the Porcupine Bank off the West Coast of Ireland where the shelf drops off more gradually (Figure 1.6) (Huthnance et al., 2009).

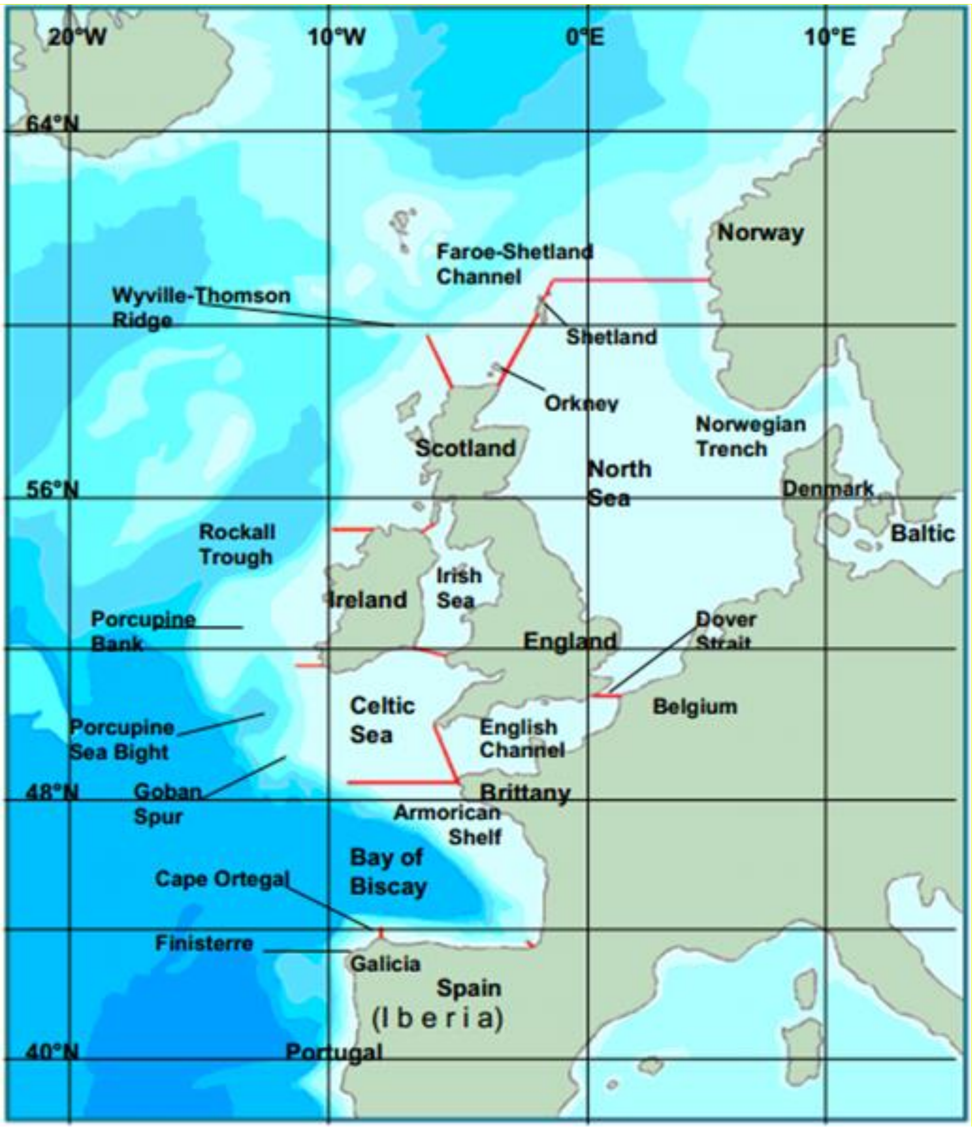

Figure 1.6 The European shelf

Map of the European Shelf. Different regions of the shelf are broken up by red lines, the 200m and 100m contours are given as the colour change from white, light blue to dark blue (Huthnance et al., 2009)

The movement of water in shelf seas is driven by adjacent slope currents, winds, tides and buoyancy sources such as freshwater inputs and heating and cooling. In the Northwest European Shelf, North Atlantic water flows northwards past Ireland Scotland and Norway whereas waters formed by convection in Northern Biscay flow Southwards (Pingree and New, 1989). The net flux of seawater that is transferred from the shelf to the Atlantic Ocean along the edge of the shelf between Brittany to Norway is 2.5 sverdrups (Sv, $1x10^6$ ms^{-1}); this is balanced by input from rainfall and rivers. Rivers in the Baltic Sea feed the largest freshwater source in the shelf sea and are incorporated into the Norwegian Coastal Current.

The influence of the tide and freshwater input will be greatest in the nearshore region and the shelf exchange processes will have a greater impact close to the shelf. The semidiurnal North Atlantic tides are large (tidal speeds exceed 0.1m/s across the shelves) and are predominantly barotropic stimulators of turbulence and mixing. In the near shore region a freshwater lens might be expected whereas the central shelf is beyond the tidal mixing front and thus less subjected to the influence of tides (Huthnance et al., 2009). Where bottlenecked in straits and around headlands tidal speeds can exceed 0.5m/s. Complex dynamics at the shelf break mean that the influence of internal waves and slope currents can manifest themselves at the surface at the shelf break (Sharples et al., 2007).

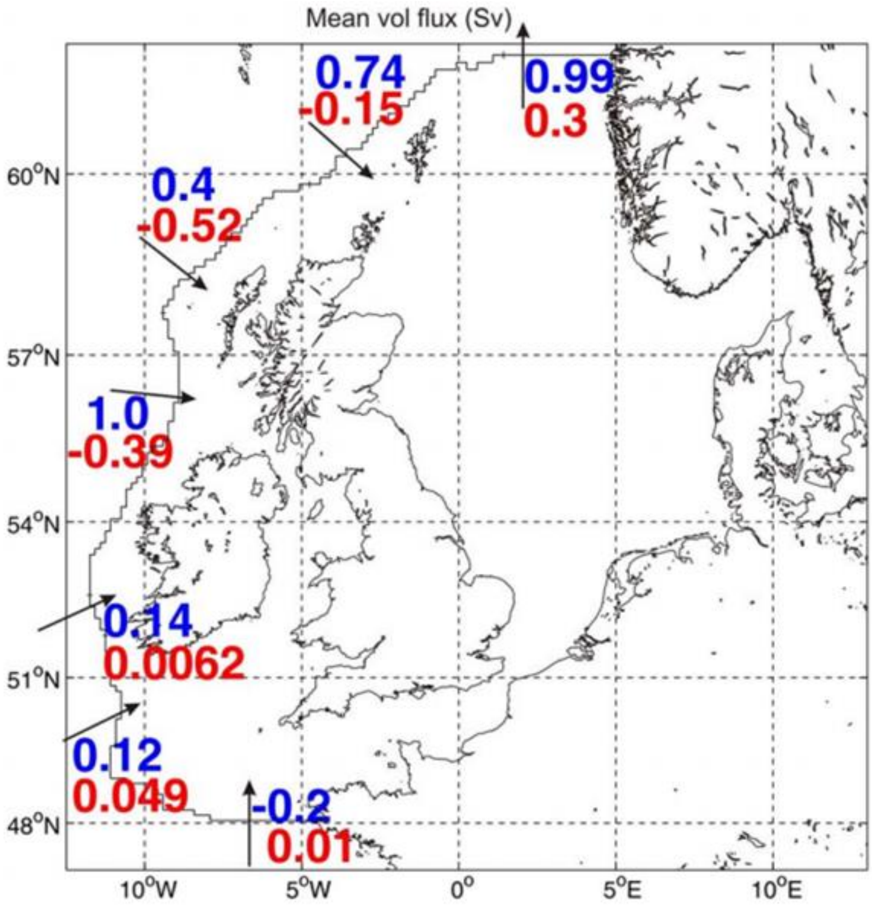

Figure 1.7 Seawater fluxes across the European Continental shelf break

Fluxes in sverdrups (Sv,1x10^6 ms^{-1}) on the European Shelf, fluxes above 150m (blue) and below (red). All fluxes are given at the 200m contour, positive numbers indicate the flux is onto the shelf except the flux closest to Norway (Huthnance et al., 2009).

1.8.2 Biogeochemical seasonality in Shelf Seas and the coastal ocean

Biological production by marine phytoplankton can alter the pCO$_2$ in seawater via photosynthesis and respiration; both of these processes alter the inorganic carbon pool. Net community production (NCP) is given as the excess of gross primary production (GPP) over community respiration (R),NCP= GPP-R (Calleja et al., 2005). During growth and cell division, GPP outstrips R resulting in a reduction of pCO$_2$ and DIC (Robertson et al., 1994). Shelf sea surface water CO$_2$ in the North East Atlantic is very seasonal with values ranging between 100 and 670ppm primarily due to temporal and spatial variability in biological production (Frankignoulle et al., 1996).

1.8.2.1 Winter

Between the breakdown of thermal stratification in mid–October and the rest ratification in early April the water column is well mixed. Nutrients are readily available but a combination of a lack of light and grazing by zooplankton prevents phytoplankton growth. Depending on location, the water column pCO_2 falls between slight under saturation (-20µatm) and slight oversaturation (+20µatm) relative to the atmosphere between mid–October and the beginning of winter (Figure 1.8d). Throughout January and February the water column pCO_2 approaches equilibrium with the atmospheric pCO_2 which is reached by March (Figure 1.8a) (Thomas et al., 2004). Despite being close to equilibrium during the winter, faster wind speeds mean the flux is still large at this time of year.

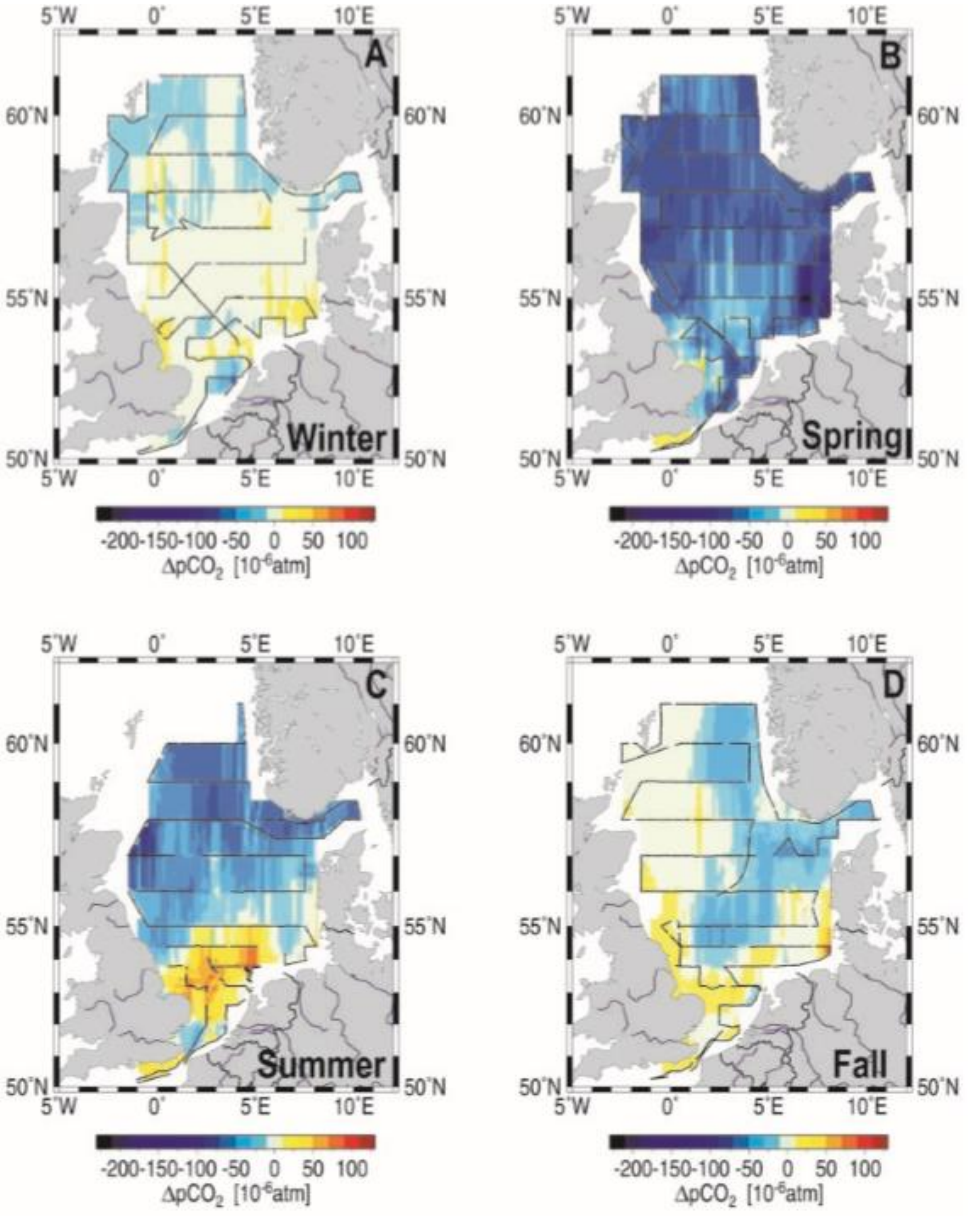

Figure 1.8 Seasonal climatology of the atmosphere–ocean ΔpCO_2 in the North Sea

Seasonal climatological maps of the difference between the atmosphere and ocean pCO_2 in the North Sea based on data from 4 cruises in August–September 2001, November 2001, March 2002 and May 2002. This delta (Δ) is expressed as the oceanic pCO_2 – atmospheric pCO_2 (Thomas et al., 2004).

1.8.2.2 Spring

In the spring increased surface heating and reduced wind stress results in the shoaling of the light determined critical depth for net algal growth down to the base of the mixed layer (Figure 1.9) (Pingree et al., 1976). The net heat flux inversion from negative to positive reduces turbulence and vertical mixing and allows phytoplankton to congregate in the euphotic zone where there is access to light. The resultant increase in phytoplankton abundance is termed the spring bloom and typically occurs in April a month after the inversion of the net heat flux (Smyth et al., 2010b). Strong tidal and wind mixing can increase the suspended sediment load, this can delay the timing of the spring bloom as the suspended sediment may limit the amount of light available to phytoplankton (Tett et al., 1993). Fresh water inputs on the other hand can advance the bloom as they shallow the surface layer. The North Atlantic Oscillation (NAO) determined the location of the north-west European summer storm track and is thus a controlling factor in the variability of vertical mixing of nutrients and primary production rates (Rippeth et al., 2009).

Another source of nutrients to shelf seas is by rivers (Nixon et al., 1996). The riverine nutrient flux on the European shelf is 1000-1800 kT yr^{-1} for nitrogen and 50-90 kT yr^{-1} for phosphorus (Brion et al., 2004). The riverine nutrient flux and the flux of colour dissolved organic matter and suspended particulate material can result in high production light limited regimes in coastal zones(Holt et al., 2012). The nitrogen riverine input is much smaller than that from shelf exchange 7700 kT yr^{-1} (Jickells, 1998).

The spring bloom concludes when the nutrient supply in the surface ocean becomes depleted. The diatoms are the first phytoplankton group to bloom, with abundance rapidly increasing in early April; the diatom bloom is short lived spanning 2 weeks with the peak in mid–April and rapid decline occurring in late April. The decline in the diatoms coincides with the increases in the phaeocystis and Coccolithophores which occur in early May, with the phaeocystis dominating this part of the bloom (Widdicombe et al., 2010)**.** Coccolithophores are a group of phytoplankton that build layers of calcite (calcium carbonate, $CaCO_3$) plates around their cells called coccoliths (Robertson et al., 1994). The precipitation of calcite shells reduces alkalinity (Suykens et al., 2010). The equation for calcification is given by equation where Ca^{+2} is the calcium ion concentration (Calleja et al., 2013).

$$Ca^{+2} + 2HCO_3^- \rightleftarrows CaCO_3 + H_2O + CO_2 \qquad \text{Equation (28)}$$

The CO_2 produced by calcification is generated intra–cellularly and may be used preferentially for photosynthesis; this slows down the uptake of extra cellular CO_2 for photosynthesis. This effect should make calcifying organisms less effective at taking up CO_2 compared to other species and may be important in calculating CO_2 drawdown during the summer when Coccolithophores are most prevalent.

As the number of phytoplankton increases there is a coincident increase in the number of cilate microzooplankton during the spring bloom whereas the dinoflagellate microzooplankton do not increase until after the bloom (Atkinson et al., 2015)**.** During the bloom the increased production removes CO_2 from the water column making the water column undersaturated at the surface (Kitidis et al., 2012).

The depletion of nutrients in the euphotic zone is responsible for the sharp declines in phytoplankton abundance marking the end of the spring bloom.

1.8.2.3 Summer

Thermal stratification in shelf seas during the summer produces a thermocline that penetrates down to tens of meters. The tidal mixing front separates the summer stratified region from the tidally mixed areas (Figure 1.9). In the North West European Shelf the tidal mixing front is located inshore of the shelf edge (Figure 1.1) (Simpson et al., 1981). Phytoplankton productivity in the summer is limited by how much nitrogen is biologically regenerated as ammonia and how much nitrate is entrained through the thermocline by winds, surface waves, internal waves and Ekman suction from the wind stress curl (Figure 1.9) (Pingree et al., 1978). Biogenic reduction in sediments is an additional source of essential nutrients such ammonia and nitrate (Rowe et al., 1975). Tidal mixing can also supply nutrients into the euphotic zone (Sharples et al., 2007). The fronts between the summer stratified and mixed waters are a hotspot for phytoplankton growth (Pingree et al., 1976).

Photosynthesis by phytoplankton removes CO_2 from the water leaving the surface ocean undersaturated in CO_2 throughout the summer, meaning that there is a large net flux into the ocean during this time (Frankignoulle et al., 1996). In the summer of 1992 the whole English channel was undersaturated by 0 to 30 ppm relative to the atmosphere (~355 ppm) except for a small area near Calais, in the spring of the following year all the waters were heavily undersaturated and then oversaturated in the Autumn of the same year (Frankignoulle et al., 1996).

As the temperature of the surface ocean increases in the summer, solubility declines, this increases the pCO_2 in the water, this effect reduces uptake by the atmosphere and this reduction is enhanced by the presence of calcification. During a phytoplankton bloom it has been calculated that the coccolithophore species Emiliania Huxleyi reduced the air sea pCO_2 differential by 15µatm (Robertson et al., 1994) . Coccolithophore blooms can reduce the air sea pCO_2 flux in a localised area of the North Atlantic by 55% (Shutler et al., 2013).

Despite the lower production the surface water column does not finish equilibrating with the atmosphere before the end of the summer suggesting there is poor ventilation, this is supported by the 5 – 6 month post spring bloom equilibration time estimation for the Western Channel Observatory made by Kitidis et al. (2012) for a 15m turnover using the local gas transfer velocity estimated using the wind speed. This summer equilibration is much slower than seen in the English Channel which equilibrates by mid – July (Borges and Frankignoulle, 2003). The breakdown of stored matter by heterotrophs means that respiration exceeds photosynthesis (Borges et al., 2006). The euphotic zone remains nutrient depleted until the breakdown of stratification in late September.

1.8.2.4 Autumn

Nutrient entrainment into the mixed layer in autumn can be enough to initiate a second smaller bloom in early September (Garcia-Soto and Pingree, 1998). Autumn blooms are characterised by dinoflagellates (Siemering et al., 2016). The triggering of autumn blooms is linked to the erosion of the thermocline as changes in the vertical temperature structure drive mixing and nutrient and light availability (Pingree et al., 1976).

In mid–autumn the thermocline is completely eroded by mixing from tidal currents, winds and waves (surface and internal) (Figure 1.9). This mixing extends down to the shelf floor across the whole of the European shelf. Winter mixing redistributes nutrients in the water column, with the nutrient rich bottom waters replenishing the surface waters which were depleted during the spring bloom and the summer season. Upon the breakdown of stratification there is increased turbulence and vertical mixing and the shelf returns to the regime where phytoplankton population is controlled by grazing. Following the stratification breakdown over the winter months the nutrient concentrations slowly begin to increase and the light availability decreases. Similarly, the water below the thermocline high in dissolved inorganic carbon (DIC) from the mineralisation of organic matter is mixed throughout the water column making the water oversaturated (~20 μatm) during September and October before reaching equilibrium in November (Kitidis et al., 2012).

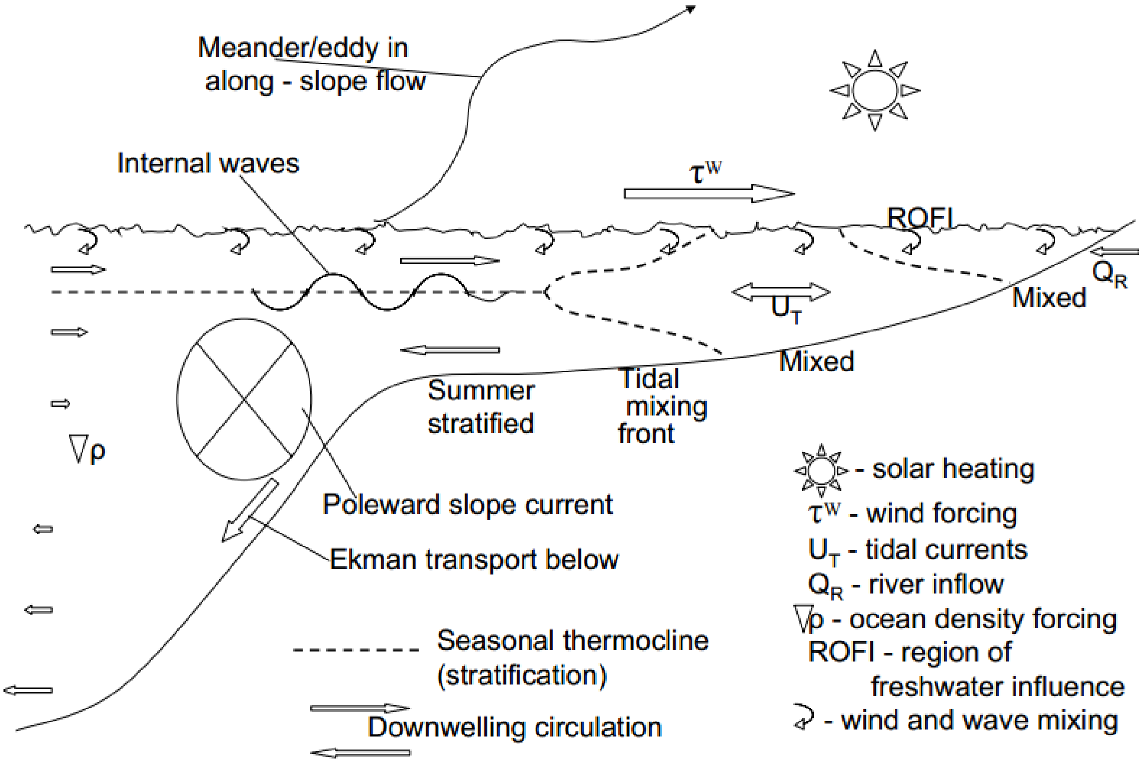

Figure 1.9 Stratification and cross–slope exchange processes at the shelf break
Schematic of the physical processes occurring between the coast, across the shelf and down the shelf edge to the deep ocean (Huthnance et al., 2009).

1.8.3 Export of carbon from shelf seas

In shelf seas, the process by which carbon is exported off the shelf by the solubility and biological carbon pumps and is replaced by the input from the atmosphere is termed the Continental Shelf Pump (CSP) (Figure 1.10). It has been proposed that the removal of carbon off the shelf by the CSP is balanced by the air–sea CO_2 flux (Tsunogai et al., 1999). If organic carbon burial in sediments is small as suggested by de Haas et al. (2002) then the CSP will balance the net flux to the ocean from air sea gas exchange. In theory drawdown is most efficient over an annual cycle if carbon taken up by phytoplankton in spring and summer sinks below the seasonal thermocline (before it can be respired) and into the deep ocean past the permanent thermocline. Assuming the solubility pump is a negligible component of the CSP; stoichiometry demands that for an off–shelf flux of carbon there must be a corresponding flux of nutrients (N, P and Si) that reflects the productivity in the surface ocean. Terrestrial nutrient sources (rivers, groundwater) and atmospheric sources in the case of nitrogen are important as they prevent shelf seas becoming nutrient depleted (Jickells, 1998).

Total global export to depth via the solubility and biological pumps is estimated as 16 Pg C a^{-1} which is equivalent to a third of global oceanic production (Falkowski et al., 1998), this carbon is remineralized to DIC and is returned to the surface by the global overturning circulation.

In temperate shelf seas dense waters with a high DIC content are generated by winter cooling and flow off the shelf into the ocean interior, this has been called cascading (Ivanov et al., 2004). Waters with an enriched DIC content are exported off the shelf and do not re–equilibrate with the atmosphere in the short term. Steep topography at the shelf edge may inhibit export off the shelf. Other transport mechanisms for particulate organic material (POM) besides cascading include downwelling, filaments, eddy exchange or transport through a slope current Ekman layer (Figure 1.9) (Simpson and Sharples, 2012, Huthnance, 1995). As slope sediments are physically closer to the surface than deep ocean sediments, it is intuitive to assume there is less time for remineralisation or dissolution resulting in increased carbon burial.

Due to the shallow depth of shelf seas, a large amount of particulate organic matter (POM) including particulate organic carbon (POC) settles below the thermocline and is sequestered in sediments, this is equivalent to >40% of global oceanic sequestration of carbon (Muller-Karger et al., 2005). Using satellite derived productivity and an empirical model for particulate organic carbon (POC) flux. Muller-Karger et al. (2005) estimate the amount of carbon settling below the thermocline in shelf seas to be 0.68 Pg C a^{-1}. 0.62 Pg C a^{-1} settles to the seafloor and 0.06 Pg C a^{-1} is buried in sediments. The settled component of the POC flux of 0.62 Pg C a^{-1} is bigger than the 0.31 Pg C a^{-1} in the deep ocean. The estimate of 6 Pg C $a^{-}1$ is also supported by modelling studies (Yool and Fasham, 2001).

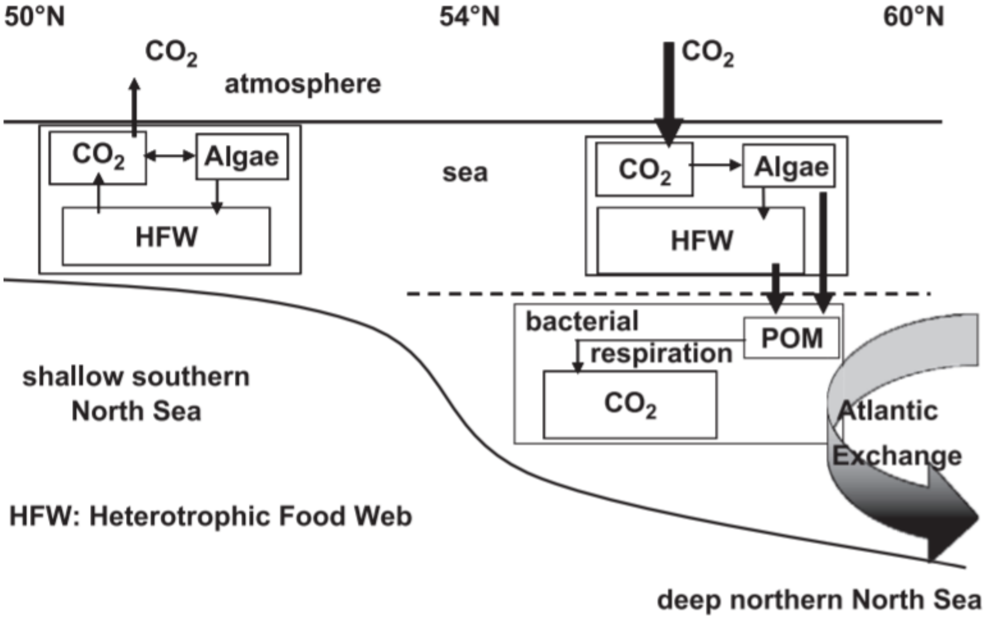

Figure 1.10 Schematic of the continental shelf pump

Cross section schematic of the South-North section in the North Sea (Bozec et al., 2005) after (Thomas et al., 2004). The sizes of the arrows indicate the relative sizes of the carbon fluxes. The dashed line indicates the depth of the thermocline and the darkening of the arrow indicates increasing dissolved inorganic carbon (DIC) with depth, which is transported off the shelf into the North Atlantic Ocean.

1.8.4 The carbon budget of shelf seas

For the annual carbon budget of Shelf Seas to be neutral the losses must equal inputs. Exchange of carbon happens with the atmosphere by air sea gas exchange, via riverine input, by exchange with the open ocean and by deposition and regeneration in the sediments. The carbon budget of Shelf seas varies substantially between seasons.

Averaged over the year global shelf seas are a strong net sink for CO_2 0.4 Pg C a^{-1}(Frankignoulle and Borges, 2001, Thomas et al., 2004). Borges (2005) suggests that continental shelves act as a net sink for CO_2 but speculates that this flux is negated by an opposing estuarine flux. Laruelle et al. (2014) use measurements from the SOCAT database to make flux estimate for the global shelf seas and estimate shelf uptake as 0.19 ± 0.05 Pg C yr^{-1}.

Shelf seas are small in size but due to their high productivity shelf seas are responsible for a large proportion of CO_2 uptake by the oceans. Estimates suggest that shelf seas account for 29% (Boyd and Trull, 2007) or as much as 40% (Thomas et al., 2004) of the net global CO_2 drawdown by the oceans.

1.9 Gas Exchange

1.9.1 The flux equation

The flux (F , mol m^{-2} s^{-1}) of slightly soluble gases across the air–sea interface is defined at the product of the gas transfer velocity (k , ms^{-1}) and the difference in the gas concentrations between the sea surface (C_0 , mol m^{-3}) and the bottom of the liquid boundary layer (C_w , mol m^{-3}) (equation 29) (Wanninkhof et al., 2009). The concentration difference between the sea surface and liquid boundary layer (ΔC) is also called the thermodynamic forcing function.

$$F=k\,(C_w - C_0) \qquad \text{Equation (29)}$$

When there is no chemical gradient across the atmospheric boundary layer, C_0 is equal to the product of the dimensionless Ostwald solubility (α) and the concentration of the gas in the air C_a (equation 30).

$$F= k(C_w - \alpha C_a) \qquad \text{Equation (30)}$$

The thermodynamic forcing function may be written in terms of the partial pressure of the gas in air and water, for CO_2 this is given by equation 31, where k_0 (mol m^{-3} Pa^{-1}) is the aqueous phase solubility of CO_2 introduced in equation 6.

$$F=k\,k_0\,(pCO_{2(sw)} - pCO_{2(a)}) \qquad \text{Equation (31)}$$

1.9.2 Conceptual basis of gas exchange

Conceptual models of slightly soluble gases with α<5 indicate that k is controlled by hydrodynamics at the interface. Liss and Slater (1974) proposed a stagnant film model where transfer is constrained by molecular diffusion (D, m^2 s^{-1}) across a thin layer of water of constant thickness (z) (equation 32).

$$F= d\,\frac{dc}{dz} \qquad \text{Equation (32)}$$

$$k= D/z \qquad \text{Equation (33)}$$

Changes in thickness affect the transfer velocity. The best agreement between modelled values of k and those measured using the dual tracer technique has been found to occur when D is raised to a power between a 1/2 and 2/3 (Upstill-Goddard et al., 1990, Nightingale et al., 2000). z is poorly represented as a stagnant layer with a constant thickness and is better modelled as a dynamic surface layer, where the thickness is modulated by impinging eddies, flow divergence or mixing via surface renewal events. These models predict the thickness of the layer z is proportional to $D^{2/3}$ or $D^{1/2}$ thus k is scaled as observed (Wanninkhof et al., 2009).

The performance of conceptual models depends on their treatment of hydrodynamics at the surface aqueous layer and whether they use an eddy diffusion boundary layer or eddy structure approach such as surface renewal or penetration (Wanninkhof et al., 2009). In all these cases, k is given as a function of the hydrodynamics and the molecular diffusivity (equation 34).

$$k= aD^n g\,(Q, L, v) \qquad \text{Equation (34)}$$

Where a is a model dependent constant, g is a model dependent function based on the velocity scale Q governed by the intensity of the turbulence and water side friction velocity (u^*_w), the length scale L governed by the turbulence integral length scale and boundary length scale and kinematic viscosity of water v. This equation can be rewritten in terms of the dimensionless Schmidt Number (Sc) where Sc = v/D, a function of temperature and salinity and referenced at 20°C (equation (35).

$$k=aSc^{-n}f\ (Q, L, v) \qquad \text{Equation (35)}$$

It is assumed that the wind stress supplies the kinetic energy which drives gas exchange at the interface. The energy input from the wind does not scale linearly with the wind speed due to wave generation and wave breaking.

For reactive gases whose solubilities exceed $\alpha \geq 100$ or which react in water, air–side processes rather than aqueous phase hydrodynamics control gas exchange. Such gases include ammonia, ozone and sulphur dioxide. Transfer velocities for these gases are around two to three orders of magnitude higher than less soluble gases at a given wind speed; the transfer velocity also scales linearly with the wind speed. Gases like dimethylsulfide (DMS) with an intermediate solubility α=10 are controlled by a combination of air and water side processes, for DMS this is 10% air phase and 90% water phase.

In the depiction of their two layer model Liss and Slater (1974) state that whether air or water phase dynamics dominated the transfer velocity was controlled by the sum of the air and water resistances (equation 36).

$$k^{-1}= (k_a/\alpha)^{-1} +(\varepsilon k_w)^{-1} \qquad \text{Equation (36)}$$

Where k_a/α and εk_w are the gas transfer velocities through the diffusive sublayer for the air and water side interfaces respectively. $k_a/\alpha = 1/R_{air}$ and $\varepsilon k_w = 1/R_{water}$ where R_{air} and R_{water} are the air and water side resistances respectively. The ratio of D for the air and water is proportional to k_a and k_w in the two layer model such that $k_a \approx 100kw$.

An equation for k for a flat surface was given by Deacon (1977) equation (37), where β is a numerical constant from boundary layer theory.

$$k= \beta^{-1}\ u_{*w}\ Sc^{-n} \qquad \text{Equation (37)}$$

There is an implicit assumption in equation (37) that all the processes that effect k are encompassed by the wind speed alone but this neglects other drivers of gas exchange from net stress including breaking and non–breaking waves and other factors like bubble entrainment, rain and buoyancy generated turbulence. Other formulations such as given by Hare et al. (2004) are more encompassing and consider other drivers (equation 38) .

$$k= u_{*a}\ [(\rho_w/\rho_a)^{-1/2}\ (b_w Sc_w^{1/2} + \ln(z_w/d_w)/k)]^{-1} \qquad \text{Equation (38)}$$

Where subscripts are water and air, and ρ_w and ρ_a the density of water and air and $b_w = \Lambda R_r^{1/4}/\ \varphi$ where Λ is an adjustable parameter, R_r is roughness Reynold number and φ is an empirical function that accounts for buoyancy and turbulence.

1.9.3 Wind speed control on gas exchange

Wind speed is the dominant physical forcing over the ocean. The wind speed at 10m (u_{10}) is related to u_{w*} and thus k from (equation 39), where c_d is the drag coefficient and $u_{w*} = (\rho_w/\rho_a)^{½}$

$$u_{10} =(\rho_w/\rho_a)^{½}\ u_{w*}\ c_d^{-1/2} \qquad \text{Equation}$$

(39)

The large majority of wind speed relationships are based on empirical studies. The first of these were performed in wind tunnels over 3 distinct surface types, smooth, undulating and one with breaking waves (Liss and Merlivat, 1986, Liss et al., 1988).

The first widely utilized wind speed parametrisation of k was given by Wanninkhof (1992) where u_{10} is the wind speed at 10m (equation 40).

$$k=0.31u_{10}^{2}(Sc/Sc_{660})^{-1/2}$$ Equation (40)

A larger dataset was later used to refit these data and a cubic dependence was found to provide the best fit for k (Wanninkhof and McGillis, 1999). A reanalysis of the ocean bomb radiocarbon C^{14} inventory by Sweeney et al. (2007) showed that it had been previously overestimated by 25% and the flux had subsequently been overestimated by 33% in Wanninkhof (1992). There have been numerous other wind speed parameterisations (Ho et al., 2006, McGillis et al., 2001, Wanninkhof et al., 2013). Another widely used relationship was developed by Nightingale et al. (2000) using tracer release experiments (equation 41), this relationship has proven to be extremely robust and is the parameterisation used for all future calculations in this thesis. k_{600} and k_{660} (cm hr^{-1}) are gas transfer velocities normalised to the Schmidt number of CO_2 at 20°C in fresh water and saltwater respectively.

$$k_{660} = 0.222u^{2}_{10} + 0.333u_{10}$$ Equation (41)

All wind speed relationships struggle to account for the discontinuity at low wind speeds, as k will not reach zero at low wind speeds due to buoyancy effects and chemical enhancement for gases like CO_2. McGillis et al. (2004) suggest that a strong diurnal heating cycle enhances buoyancy driven gas exchange at low wind speeds.

It is necessary to use a consistently compiled wind speed product (e.g. NCEP reanalysis or QuikScat) for calculating fluxes as wind speeds can vary substantially depending on the origin of the data and the methodology used to derive the wind speed. Due to the quadratic dependence on the flux, small differences in the wind speed can this can substantially affect the flux estimate (Wanninkhof et al., 2009).

1.9.4 Other controls on gas exchange

As well as the wind speed a number of other factors affect the flux, these can be visualised as in (Figure 1.11).

1.9.4.1 Bubbles

Bubbles enhance air–sea gas exchange (Woolf, 1997). Bubbles can increase the flux in three ways, as turbulence created by breaking waves (Woolf, 1995), by transfer across their surface (Memery and Merlivat, 1985) and via disruption of the thin surface microlayer of the ocean by bursting bubbles (Woolf et al., 2007). For trace gases, the gas flux through bubbles is linearly related to the concentration difference and has a steeper relationship the lower the solubility of the gas (Memery and Merlivat, 1985). The effect of bubbles is often considered separately and given as an additional flux term (Keeling, 1993, Woolf, 1997) and has been argued to scale with the percentage whitecap cover (Anguelova and Webster, 2006, Goddijn-Murphy et al., 2011, Monahan and Spillane, 1984).

1.9.4.2 Breaking waves

Wallace and Wirick (1992) suggest that gas exchange parameterisations underestimate gas exchange and suggest breaking waves account for the large majority of gas exchange at high wind speeds, this was demonstrated by more extensive measurements by Farmer et al. (1993). Breaking waves have been shown to induce significant bubble mediated gas transport at high wind speeds (D'Asaro and McNeil, 2007, Asher et al., 1996, Zappa et al., 2001, Zappa et al., 2004). Gas exchange is enhanced by wave breaking at low wind speeds and short wavelengths (Melville and Matusov, 2002). Long waves have been shown to suppress near surface water turbulence and decreases gas transfer at higher wind speeds (Bell et al., 2013).

1.9.4.3 Surfactants

Organic surfactants found at the surface of the ocean have been shown to reduce air sea gas exchange by acting as a barrier to gases. Calleja et al. (2009) suggest that this impact is most significant at wind speeds below $5ms^{-1}$ and suggest total surface organic matter concentration (TOC) is a good proxy for organic surfactants. Frew et al. (1990) determined the extent of surfactants for 7 common phytoplankton species. Surfactant release experiments have shown that the air sea flux of He and SF_6 is inhibited by as much as 5–55% at wind speed of 7.2–10.7 ms^{-1}(Salter et al., 2011). Similarly measurements from a gas exchange tank indicate surfactants reduce the gas transfer coefficient between 14 to 51% (Pereira et al., 2016). Recent measurements of surfactants have shown them to be ubiquitous across the surface ocean and present at wind speeds as high as $13ms^{-1}$ (Sabbaghzadeh et al., 2017), in the Atlantic regions of surfactant activity reduce the air sea flux by up to 32% (Pereira et al., 2018).

1.9.4.4 Rain

Rain has two effects on gas exchange, the first is by dilution of the surface layer, which decreases CO_2 (Turk et al., 2010), the second is by turbulent mixing near the surface which enhances k (Komori et al., 2007). The effect of rain on the gas exchange rate is determined by the kinetic energy supplied to the water by the raindrops (Ho et al., 1997). It has been suggested that the turbulent mixing affect may even outstrip the wind effect during heavy rain events (Komori et al., 2007). The net effect of rain depends on whether the region is a net source or sink; in sink regions more CO_2 is drawn down whereas in source regions the source is either enhanced or reduced depending on the increased turbulence or dilution effect. Wet deposition of DIC and DOC in rainwater is a minor additional input of carbon as rainwater has no buffering capacity.

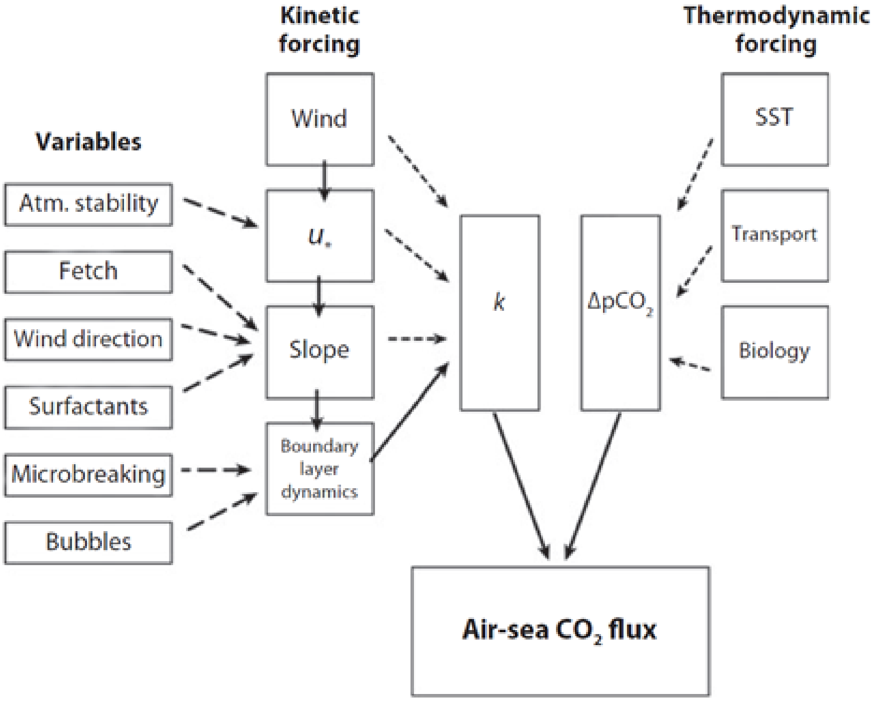

Figure 1.11 Kinetic and thermodynamic forcing controls on air–sea CO_2 flux

A schematic of the factors controlling air sea gas exchange. SST is the sea surface temperature, k the gas transfer coefficient, ΔpCO_2 is the oceanic partial pressure of CO_2 minus the partial pressure of atmospheric CO_2 and u* is the friction velocity(Wanninkhof et al., 2009).

1.9.5 Equations used to calculate the flux

The flux F (gC m^{-2} hr^{-1}) is calculated following Johnson (2010) using (equation 42)

$$F = k_w\, k_0\, \Delta pCO_2 = TR\, \Delta pCO_2 \qquad \text{Equation (42)}$$

TR is the transfer coefficient (g C m^{-2} hr^{-1} μatm^{-1}) (equation 43)

$$TR = (k_w)\,(k_0)\,(12\,)(1000/10^{-6})(0.01) \qquad \text{Equation (43)}$$

where ((12)(1000/10^{-6}) is a scaling factor to convert from mol L^{-1} atm^{-1} to gC m^{-3} μatm^{-1} and 0.01 is a scaling factor to convert cm hr^{-1} to m hr^{-1}

k_w is water side transfer velocity (cm hr^{-1}) (equation 44)

$$k_w = (k_{660})\,(Sc/Sc_{660})^{-1/2} \qquad \text{Equation (44)}$$

K_{660} in (cm hr^{-1}) is from (Nightingale et al., 2000) (equation 45)

$$k_{660} = 0.222u^2_{10} + 0.333u_{10} \qquad \text{Equation (45)}$$

Sc is the dimensionless Schmidt number temperature dependence from (Wanninkhof, 1992) (equation 46).

$$Sc = 2073.1 - 125.62(T) + 3.6276(T)^2 - 0.04321(T)^3 \qquad \text{Equation (46)}$$

The solubility of CO_2 (k_0, mol L^{-1} atm^{-1}) is from (Weiss, 1974) (equation 47). Note that the units of k_0 used here are approximately the same as introduced previously as L^{-1} atm^{-1} can be converted to Pa^{-1} m^{-3}.

$$k_0 = \exp(-60.2409 + 93.4517(100/T + 273.15) + 23.3585(\log(T+273.15/100)) + S(0.023517 - 0.023656(T+273.15/100) + 0.0047036((T+273.15/100)^2))) \qquad \text{Equation (47)}$$

1.10 CO_2 flux using climatologies

Flux estimates based on data from the SOCAT and LDEO databases have been shown to broadly agree (Sabine et al., 2012).

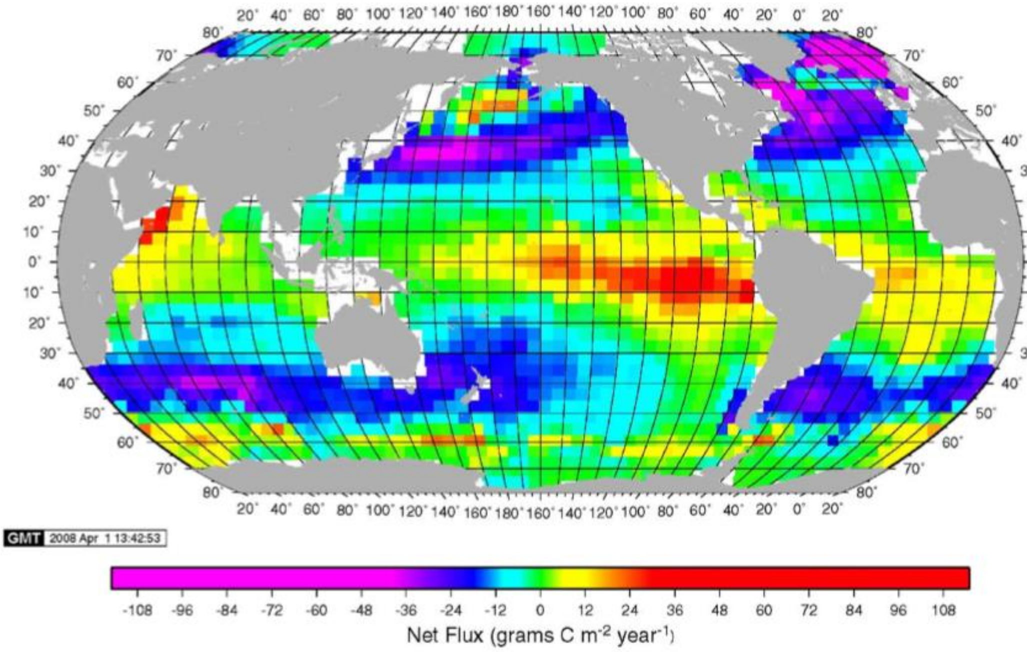

Figure 1.12 Global climatological mean air sea fluxes of CO_2

Annual mean air sea flux of CO_2 for the reference year 2000 (Takahashi et al., 2009).

1.11 The vertical temperature structure of the surface ocean

Sea surface temperature (SST) is commonly used to refer to the temperature in the upper surface ocean (<5m). The use of a broad term like SST to define surface temperature implies that there is no structure in the vertical surface temperature in the near surface ocean but this is not the case. A schematic of the near surface temperature structure is given for two scenarios, with and without diurnal warming (Figure 1.13). The temperature profile can be thought of as always having a cool skin at the surface and under the right conditions a diurnal warm layer in the surface of the ocean. The SST should be quoted at a specific depth due to the occurrence of diurnal warming.

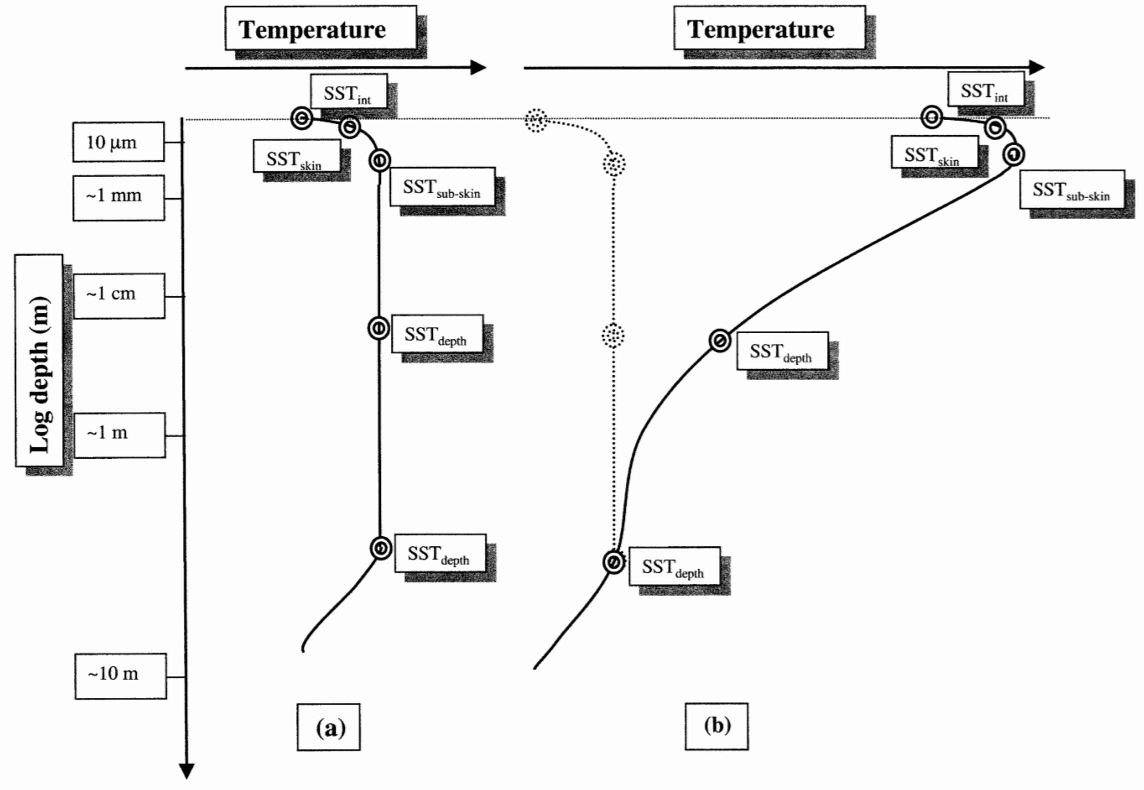

Figure 1.13 Idealised temperature structure schematics
Schematic representation of the upper ocean temperature structure at night and in the presence of diurnal warming (Donlon et al., 2002).

1.11.1 The thermal skin

The upper 1mm of the ocean's surface has a cold thermal skin which suppresses turbulence towards the interface, globally the surface is an average of 0.3°C cooler than the bulk temperature (Robertson and Watson, 1992a). Other estimates of the cool skin suggest it is 0.14±0.1°C cooler (Donlon et al., 1999). In the model by Fairall et al. (1996) once solar heating exceeds cooling by turbulent scalar heat transport by net longwave radiation the layer is cut off from its source of turbulence. The cool skin is present both day and night (Gentemann et al., 2009) and a strong temperature gradient is maintained by the magnitude and direction of the ocean–atmosphere heat flux (Donlon et al., 2002). Temperature gradients are present in the skin layer; the penetration depth of the emitted radiation is a function of the wavelength of the radiation such that it is necessary to reference skin temperatures with an associated wavelength. Not accounting for the wavelength dependency means that over the small infrared wavelength band measured by radiometers the wavelength specific values vary by 0.01°C (Donlon et al., 2002).

A distinction between the upper skin layer and the bottom of the skin layer called the subskin is made by Donlon et al. (2002) as the region where molecular and viscous heat transfer processes are most important. The subskin varies on the timescale of the order of minutes and is influenced by solar warming. A distinction is also made for the skin interface, an extremely thin layer (10µm) at the true air–sea interface that cannot be accurately measured with profiling instruments due to its thickness and the movement of the oceans surface.

1.11.2 The surface mixed layer/ Diurnal Warm layer

Below the cool skin is the ‘surface mixed layer’ where turbulence is assumed to maintain a well–mixed unstratified layer. In reality both thermal heating and precipitation can create stratification in the mixed layer. Thermally induced stratification of the mixed layer leads to what is called the ‘diurnal warm layer’. The temperature difference between the skin and the bulk temperature is often substantial and can be as high at 4.6°C (Ward, 2006). It has been shown that surface heat and momentum fluxes vary with the skin layer thickness and diurnal thermocline (Ward and Donelan, 2006). The vertical diffusion of heat, vertical stratification, the rate of turbulent mixing and changing absorption with depth (which is itself controlled by the absorptivity of the water) control vertical temperature gradients,

In low wind speed conditions the depth of the diurnal warm layer will be confined to the upper few meters (Gemmrich et al., 2008). Turbulence from wind induced shear and convection is cut off and heating of these layers by insolation enhances stratification and creates a positive buoyancy flux that prevents the warm layer deepening (Soloviev and Lukas, 1997). Diurnal stratification begins to deteriorate when heat loss exceeds heat gain, this leads to the accumulation of cooler water near the surface that drives free convection and the gradual breakdown of the diurnal warm layer by overturning (Gentemann et al., 2009). A number of other physical processes can break the thermal stratification including wind induced mixing of the upper ocean, shear flow instabilities, breaking surface waves or breaking internal waves. Wind speed is the fundamental driver of these processes.

1.11.3 Measurement of upper ocean temperature

1.11.3.1 Measurements of the thermal skin temperature

The thermal skin of the ocean is very difficult to sample in–situ, so measurements are made using remote sensing technologies.

Measurements of the sea surface temperature are made by multichannel infrared radiometers on orbiting satellites such as the Advanced Very High Resolution Radiometer (AVHRR), Tropical Rainfall Measuring Mission (TRMM) and Moderate Resolution Imaging Spectro–radiometer (MODIS) (Donlon et al., 2002). These space based observations have accuracies better than 1°C but are not accurate to the 0.3°C needed to characterise the thermal skin, for this reason these satellite measurements need field validation (Minnett and Ward, 2000, Wimmer et al., 2012).

Validation of satellite measurements is made by relatively few ship based infrared radiometers such as the Marine-Atmospheric Emitted Radiance Interferometer (MAERI) (Minnett et al., 2001) and the infrared sea surface temperature autonomous radiometer (ISAR) (Donlon et al., 2008). Measurements made by microwave radiometers in the 6–10GHz wavelength band penetrate to just below 1mm (Donlon et al., 2002). Radiometers have also been permanently installed at fixed ocean sites such as oil rigs (Niclòs et al., 2004). Radiative transfer models are used to account for the thermal skin effect and are used to correct the satellite derived SST (Horrocks et al., 2003). Donlon et al. (1999) have shown using measurements with radiometers at wind speeds <6ms^{-1} that the temperature differential between the skin and bulk is large (~1.5°C) and declines as the wind speed increases, this was also seen by Horrocks et al. (2003). These in situ measurements of the skin are extremely difficult due to the high instrument cost and the need for continuous calibrations.

1.11.3.2 Measurements of the mixed layer temperature

Turbulence at the ocean's surface means that finely resolved temperature profiles can not be made using the CTD during a rosette deployment from a research vessel. There have been very few oceanographic field campaigns (Maske et al., 2014) that have focused solely on measuring near surface temperature profiles (Ward et al., 2004b). Unfortunately many autonomous profilers such as the Argo profiling floats do not sample the top 5m due to the risk of the build–up of biological contaminants on sensors(Kawai and Wada, 2007). Ocean gliders can be repurposed to sample at a higher resolution near the oceans surface (Matthews et al., 2014). Specialist instruments have been purposefully designed to take measurements of near surface temperature profiles, the Skin Depth Experimental Profiler (SkinDEeP) (Ward et al., 2004b), the Air Sea Interface Profiler (ASIP)(Ward et al., 2014), the Skin Temperature Profiler (STEP) (Mammen and von Bosse, 1990) and the emergent profiler developed by (Soloviev and Vershinsky, 1982, Soloviev et al., 1988). These profilers are equipped with high accuracy temperature, salinity, depth and turbulence sensors and are designed to break through the air–sea interface (Table 1). Reliable long term measurements of the temperature structure of the surface ocean can also be acquired using multiple CTD devices fixed to moorings (Prytherch et al., 2013, Yokoyama et al., 1995) or by drifters (Reverdin et al., 2013).

Table 1 Key features of specialised surface ocean profilers

Key instrument specifications of a number of recent surface ocean profilers. Note that this is a synthesis of available information from a number of journals, in some cases the numbers are directly from the journal whilst others have been inferred given other information.

Instrument name	Ocean gliders	ASIP	SkinDEep	Step	Emergent
Length	~1.8m	2.5 m	1.36 m	2.00 m	0.8 m
Mass	50 kg	82 kg	29.5 kg	25.5 kg	
Temperature Resolution	0.01°C	0.0001°C	0.001°C	0.01°C	0.0006 °C
Conductivity resolution	NA – slow response time of conductivity sensor	0.00001Sm^{-1}	0.001 Sm^{-1}	NA	0.00005 S m -1
Shear resolution	NA	10^{-4} s^{-1}	NA	NA	? (Soloviev et al., 1988)
Measurement depth resolution	1m	0.002%	0.0005 m	0.0005 m for temperature	0.003m for temperature and 0.001m for salinity
Acceleration	?	0.098 ms^{-1}	?	NA	NA
Profiling speed	0.15 –0.25 ms^{-1}	~0.5 m s^{-1}	~0.3 – 0.5 m s^{-1}	1 – 2.5 ms^{-1}	1.06 ms^{-1}
Surface sampling	~0.5m	Within 0.01m of the surface	Penetrates the surface	Penetrates the surface	Penetrates the surface
Maximum	130 days	6000m	Up to several	1 profile	1 profile from

deployment length		equivalent to 3.2 hours continuous sampling	days with reduced measurement frequency	from a depth of 50m	a depth of 50m
Maximum deployable sea state	At least 11 ms^{-1}	At least 15 ms^{-1}	At least 5.8 ms^{-1}	At least 10 ms^{-1}	At least 5 ms^{-1}

1.11.4 Numerical models of heating and turbulence

Numerical models can predict the occurrence of temperature gradients and can identify the conditions required to form them. This information can then be used to infer temperature gradients on a wider scale by using other measured environmental parameters like wind speed and incoming solar irradiance. Numerical models of diurnal variations in the upper ocean can be broadly categorized into three groups, diffusion type, bulk/slab type and empirical models (Karagali and Høyer, 2013).

1.11.4.1 Diffusion models

Diffusion models that parameterize turbulent mixing and eddy diffusion empirically are based on Kondo et al. (1979). This 1D–model reproduces the surface current and sea temperature in the top 10m of the ocean and performs well at simulating the surface boundary layer. Diffusion models that parameterize turbulent mixing and eddy diffusion by estimating turbulence quantities using turbulent closure schemes are based on Mellor and Yamada (1982). By combining a modified version of the Kondo et al. (1979) model with the second order turbulence closure scheme used by Mellor and Yamada (1982) it is possible to replicate field measurements that show a sharp 4°C diurnal thermocline in the surface metre (Kawai and Kawamura, 2000).

1.11.4.2 Bulk layer models

For bulk models the initial conditions are constant profiles of temperature, salinity and current within a mixed layer.

Multi–layer models estimate turbulent kinetic energy in every vertical layer of the model (typically <0.25m). Multi–layer models like The ‘Price–Weller–Pinkel’ (PWP) model (Price et al., 1986) have frequently been used to study diurnal SST variations. The numerical scheme used is a reworked version of the dynamic instability model (DIM) used by (Price et al., 1978) that incorporates a mixing process in the stratified region of the mixed layer. In the DIM when the mixed layer deepens the rate of change of potential energy matches the rate of energy released from the mean flow by the reduction in vertical shear. The PWP model overestimates diurnal SSTs, it is suggested that this is because of insufficient vertical mixing caused by not accounting for Langmuir circulation and breaking waves (Large et al., 1994). These processes are beginning to be accounted for in mixed layer models (Noh et al., 2004). Scanlon et al. (2012) used a 1D mixed layer model incorporating a parameterisation of turbulence using wave breaking as well as validating a solar absorption model. Their results showed considerable variability in stratified waters. Fairall et al. (2003) created a model with improved wave breaking. In general, models with improved wave breaking underestimate the temperature profile whereas coarse baseline models agree better with *in situ* observations (Large et al., 1994).

Single layer models avoid excessive model calculations and specialize in simulating diurnal variation near the surface. Fairall et al. (1996) (F96) created a simpler version of the PWP model that overlooks the full mixed layer dynamics to focus solely on temperature. This single layer makes several assumptions, firstly that the temporal integrals of surface heat and momentum fluxes are isolated in the warm layer, secondly linearity in the temperature profile is assumed. If the bulk Richardson number in the model is smaller than a critical number it is possible to determine the depth of the warm layer. The linear temperature profile in the F96 model does not always agree with observations and consistently overestimates the warm layer (Ward et al., 2004a). Gentemann et al. (2009) created a model for Profiles of Surface Ocean Heating (POSH) which they showed agreed with in situ measurements. Zeng and Beljaars (2005) propose an improved temperature profile for the F96 model which due to the fact it is not computationally intensive it can be coupled to global climate models to determine global seasonal distributions of diurnal warming (Large and Caron, 2015).

1.11.4.3 ***Empirical models***

Empirical models use external data such as surface wind speed and insolation to estimate diurnal warming. Many of these models are designed to account for the fact that often there is insufficient input data to initialise the models (Gentemann et al., 2009). Price et al. (1987) developed an empirical model that was capable of calculating the temperature at 0.6 m. (Webster et al., 1996) also incorporated rainfall into their empirical model but their model was unable to replicate the observed warming. The empirical models mentioned previously only define a daily temperature range but more recent models have estimated the change in diurnal SST every hour. One of these models by Gentemann et al. (2003) used a least squares fit with their model to reduced variability in diurnal SSTs made from satellite retrieval.

1.12 Temperature dependencies in calculating the CO_2 flux

There are five equations in which temperature is applied to raw xCO_2 before it is possible to calculate the CO_2 flux, these are the correction for water vapour (equation 23), the correction to fugacity using the viral coefficient of CO_2(equations 25 and 26) ,the correction to in situ temperature (equation 27), in the calculation of the solubility (equation 47) and the calculation of the Schmidt number (equation 46) (Woolf et al., 2016).

Woolf et al. (2016) note that their temperature and gas flux are also linked through irreversible thermodynamics but in light of previous work Ward et al. (2004a) consider the effect of irreversible thermodynamics to be very small and thus ignore it. They also note that vertical gradients in the atmospheric boundary layer may exist but again ignore them.

The equation to calculate the water vapour pressure is temperature dependent (equation 23). The interfacial temperature should be used to obtain the saturation water vapour. This effect is the smallest of the temperature effects and is estimated at 0.2% $°C^{-1}$ (McGillis and Wanninkhof, 2006).

The conversion to fugacity utilises the first and the viral coefficients of CO_2, these are both temperature dependent (equations 25 and 26)(Ward et al., 2004a).

The correction to in situ temperature accounts for repartitioning of carbonate species at different temperatures (equation 27). This effect is thought to give a sensitivity of 1.5% $°C^{-1}$ of the concentration at the marine boundary layer due to the incorrectly assumed temperature (McGillis and Wanninkhof, 2006). To reduce the sensitivity to the in–situ temperature, the equilibrator fCO_2 should be corrected directly to the skin temperature rather than the in situ measurement (Woolf et al., 2016).

The equation to calculate solubility k_0 has a temperature dependency (equation 47). The equations for calculating solubility are imprecise and vary by as much as 2% in warm waters (McGillis and Wanninkhof, 2006). The miscalculation of the solubility of CO_2 is the largest of the temperature effects 2.5% $°C^{-1}$. A better calculation would involve taking the derivative of the solubility with respect to temperature using the solubility equation given by (Weiss, 1974).

Temperature is also required to calculate the Schmidt number dependency (equation 46).

1.13 CO_2 sensitivity to temperature

There are two ways to derive the CO_2 sensitivity to temperature changes; the first is to calculate the effect on the concentration directly and the second involves inferring it by calculating the temperature effect on fugacity. The isochemical effect of temperature on fugacity is calculated by taking the contributions from the repartitioning and from changes in solubility. Using only temperature and salinity errors for this equation are reduced to <0.04 $\Delta T\%$.(Copin-Montegut, 1988). For a 4% δT, solubility accounts for a change of 2.5% δT meaning repartitioning of carbonate species accounts for the remaining 1.5% δT (Hare et al., 2004).

Takahashi et al. (1993) took measurements of North Atlantic seawater and from these developed a widely utilized relationship (equation 48).

$$\partial \ln CO_2/\partial T = 0.0433 - 0.000087(T) \qquad \text{Equation (48)}$$

The simpler form (equation 48) is almost identical and whilst less precise is still commonly used (Pfeil et al., 2012), Takahashi et al. (2009) note the difference between the two equations is small.

$$\partial \ln CO_2/\partial T = 0.0433 \qquad \text{Equation (49)}$$

McGillis and Wanninkhof (2006) note that the temperature sensitivity varies substantially (3.7% $°C^{-1}$ to 5.3% $°C^{-1}$) from 0°C –30°C (Figure 1.14) and that the Takahashi correction is based only on measurements taken on a single cruise in the North Atlantic and is not done under the same conditions as TA, DIC, salinity, silicate and phosphate changed along the cruise track. Goyet et al. (1993) propose a temperature correction that encompasses other measured carbonate variables TA and DIC. McGillis and Wanninkhof (2006) also suggest that the equations for the carbonate system should be used to directly correct the concentrations but this requires DIC and TA measurements.

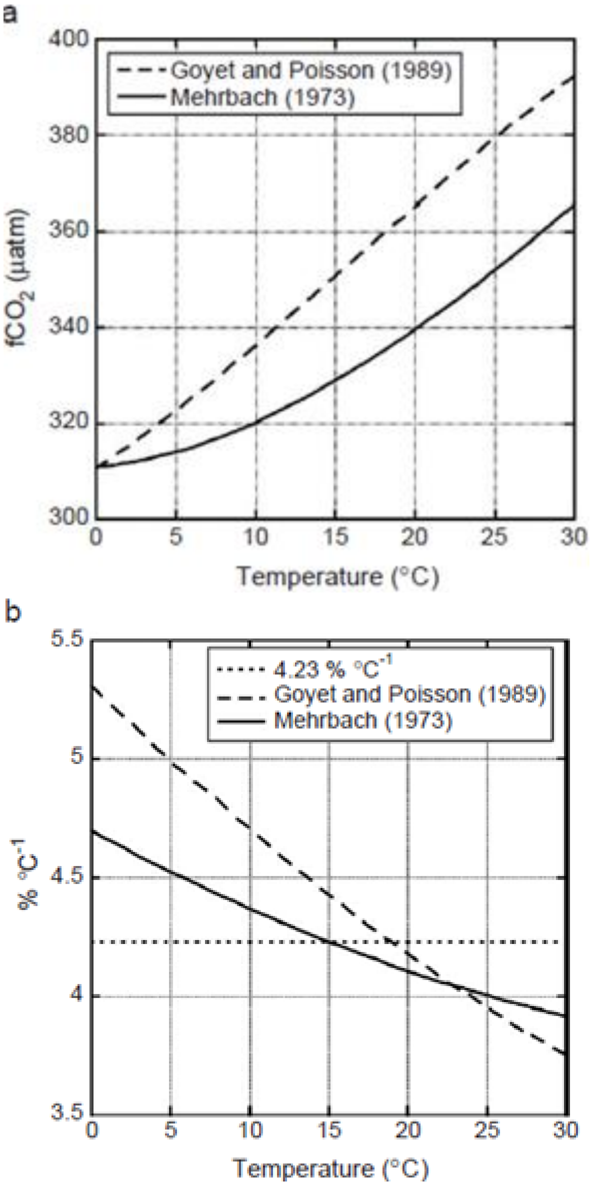

Figure 1.14 The relationship between temperature and CO_2 fugacity

(a) The change in the fugacity of CO_2 as a function of temperature for 0–30℃, with a fixed alkalinity of 2300μmol kg^{-1} and a decreasing DIC from 2150–1940 μmol kg^{-1}mimicking changes from high to low latitudes. (b) The fractional change in the fugacity of CO_2 with temperature (McGillis and Wanninkhof, 2006).

1.14 Salinity structure of the upper ocean

Evaporation at the surface of the ocean is thought to result in a salty skin (Drushka et al., 2016). Unlike the thermal boundary layer which can extend much deeper the salinity effect is expected to be isolated to the skin layer (Woolf et al., 2016). The saline skin was shown to be ubiquitous in the tropics with an average value of 0.40 ± 0.41 (Wurl et al., 2018).

1.15 Salinity dependencies in equations used to calculate flux

It is necessary to account for salinity in many of the same stages as it is for temperature, accounting for the effect of salinity on the solubility (equation 47) the water vapour equation (equation 23) and in the in situ correction if using a temperature relationship with a salinity dependency (Goyet et al., 1993).

Zhang and Cai (2007) give a theoretical expression for the salty skin and show it to be approximately 70% the size of the thermal skin. The size of the salty skin is not well known as there is still uncertainty in the equations used to model it(Asher et al., 2014). The calculation by (Zhang and Cai, 2007) only include the solubility effect and not the role of salinity on vapour pressure and the in situ correction. Salinity reduces the solubility of CO_2, this means that a salty skin will lower the pCO_2 at the surface which is the opposite effect to thermal skin (Woolf et al., 2016). The most recent estimate of the saline skin on the CO_2 flux suggests that it is much smaller than previous estimates, approximately 1/6 the size of the effect of the thermal skin and in the opposing direction (Woolf et al., 2016)

1.16 The effect of temperature and salinity skin effects on the CO_2 flux

Several studies have explored the effect of the thermal skin on the CO_2 flux. A reduction in the sea surface temperature of 0.3°C due to a cold thermal skin causes the carbonate species repartitioning and reduces the fCO_2 by 2.5 – 4 µatm (Robertson and Watson, 1992a, Sarmiento and Sundquist, 1992). The size of the cool thermal skin (0.3°C) has been validated by numerical modelling by Fairall et al. (1996) who used the model of Price et al. (1986) to get an average noon value of 0.18°C. Minnett et al. (2011) observed a more modest skin effect but noted the persistence of the skin effect at high winds.Van Scoy et al. (1995) revised the estimate of the skin effect on annual ocean uptake of CO_2 made by (Robertson and Watson, 1992a) using a more complete dataset from 0.7Gt a^{-1} to 0.48Gt a^{-1}.

McGillis and Wanninkhof (2006) have stated that the CO_2 flux occurs over a layer much smaller than 1mm, they state that only 10% of the temperature gradient over the thermal skin occurs over the mass molecular boundary layer. By taking the thermal skin temperature gradient to be an order of magnitude smaller, Zhang and Cai (2007) estimate the effect to be much smaller (0.05Gt a^{-1}). Woolf et al. (2016) are critical of the methodology used by Zhang and Cai (2007) as only solubility was accounted for whereas the temperature and salinity effects on saturated vapour pressure and on the pressure fugacity relationship were completely neglected.

Using measurements from the equatorial Pacific Ward et al. (2004a) show that the skin effect is cancelled by the warm layer affect but do not suggest this is true everywhere as the insolation in this region is strong and the cool skin effect is found globally.

1.17 Near Surface CO_2 Gradients

1.17.1 CO_2 gradients associated with temperature and salinity

For air sea fluxes it is necessary to have the CO_2, temperature and salinity at the oceans interface, the majority of these measurements are made at 5m below the interface. Sections 1.11 and 1.14 show that diurnal warm layers can form in the surface meters of the ocean and at the ocean interface there is a ubiquitous cold salty skin. Diurnal warm layers and the cold salty skin are temperature and salinity changes between the ocean interface and the surface mixed layer. Sections 1.12 and 1.15

demonstrate that temperature and salinity affect the calculation of CO_2 which means that using surface mixed layer temperature and salinity to derive interfacial CO_2 in the presence of diurnal warm layers and the cold salty skin will produce errors in the derived CO_2. Similarly using the surface mixed layer temperature and salinity to calculate the air sea flux of CO_2 in the presence of diurnal warm layers and the cold salty skin will introduce errors in the flux.

Temperature gradients in diurnal warm layer (~0 – 4.6°C) and the thermal skin have been observed in the surface ocean (Ward et al., 2004a). Radiometers give accurate measurements of the oceans skin (Woolf et al., 2016). An array of moored temperature instruments provides substantially more information about the surface ocean temperature structure (Prytherch et al., 2013). Modelling studies have shown that diurnal warm layers can develop under clear sky and low wind speed conditions (Jeffery et al., 2008). As temperature has a large effect on CO_2 these temperature gradients have a substantial effect on the CO_2 flux (Robertson and Watson, 1992a). Woolf et al. (2016) point out that there is interplay between the thermal skin and the diurnal warm layer with the former increasing solubility and drawdown and the later increasing temperature and decreasing solubility and thus flux.

Whilst the temperature and salinity skin effects on the flux have been investigated, there has been no comprehensive analysis which has quantified their combined effect on the global flux due to the fact local measurements of temperature and salinity gradients can not be extrapolated to wider regions.

These temperature and salinity effects on CO_2 are important and are discussed throughout this thesis but the main focus of the thesis is CO_2 gradients arising from changes in surface carbon.

1.17.2 CO_2 gradients associated with changes in surface carbon

In addition to physically induced changes (temperature and salinity), CO_2 in the near surface ocean may also change due to chemical changes in near surface carbon. Surface mixing by wind and waves would mean that the change in CO_2 due to a chemical process would be unobservable. Therefore chemical changes in CO_2 will only have an effect on the surface CO_2 if stratification is present. Stratification in the near surface is predominantly driven by surface warming and by surface freshwater inputs from rivers, rain and ice melt. This intricately links the physical processes to the chemical ones as stratification is the theoretical prerequisite for chemical CO_2 gradients. Chemical gradients in near surface CO_2 could be caused by changes in net primary production, an air sea flux, calcification or rainfall, the theoretical basis for this is discussed in greater detail in chapter 2.

There have been very few *in situ* measurements of vertical CO_2 profiles with coincident temperature and salinity data. Measurements of pCO_2 from moored instruments are difficult as the apparatus is not appropriate for small, low power installations. Attempts have been made at attaching sensors to moorings however these sensors have an accuracy of 2–3 µatm which is not sufficient to make detailed measurements near the surface (Fiedler et al., 2013). Hales et al. (2004) used a towed profiler to measure CO_2 from 15 and 100m but due to the setup were unable to take measurements of the near surface, they noted significant difference between their underway CO_2 and that of their instrument between 5 and 15m which they attribute to temperature gradients in the surface layer.

The only study to measure vertical chemical gradients in CO_2 in the open ocean was by (Calleja et al., 2013) who observed large 13±1 µatm vertical CO_2 gradients between the surface and 5m, they attributed these gradients to changes in net primary production. Calleja et al. (2013) do not show whether primary production can realistically stimulate gradients of this size over a set timeframe. These CO_2 gradients were much larger than expected by the trace gas community and have been met with scepticism. There have been no other independent repeat measurements in the open ocean to validate their magnitude until this thesis. There is evidence that meltwater and river runoff in polar regions can create vertical CO_2 gradients (Murata et al., 2008). Measurements made from a small boat above stratified meltwater ponds shows that the ΔCO_2 can be between -180 and +140 µatm different to the mixed layer below (Miller et al., 2018). Unpeerreviewed work of measurements of surface N_2O similarly points to the presence of near surface gradients (Fischer et al., 2018).

In addition to producing inaccurate surface fCO_2 and flux measurements, physical and chemical CO_2 gradients can also produce erroneous derivations of k when measuring the flux directly during dual tracer and eddy covariance experiments. Near surface gradients have been suggested as an explanation for a 10–25% error in k (Jacobs et al., 2002).

1.18 Thesis hypothesis and overview

The main questions that need to be answered are,

What is the expected frequency and magnitude of CO_2 gradients based on theory?

How can near surface CO_2 gradients be measured?

How frequent are near surface CO_2 gradients?

How large are near surface gradients in CO_2?

Can near surface CO_2 gradients be predicted with meteorological variables?

Does horizontal variability in CO_2 impact vertical gradients?

What effect do near surface CO_2 gradients have on the air sea flux?

This thesis attempts to answer these questions. In chapter 2 a theoretical framework for the formation of near surface CO_2 gradients is outlined. Chapter 3 introduces the near surface ocean profiler (NSOP), a novel instrument designed to measure near surface gradients. Chapter 4 presents profiles of salinity, temperature and CO_2 taken in different seasons from four cruises in UK shelf waters. Chapter 5 introduces the Western Channel Observatory which was the site for the seasonal study measurements detailed in chapters 6 and 7. Chapter 6 examines the spatial variability of CO_2 in the coastal zone based on horizontal CO_2 transects. Chapter 7 presents further profiles of salinity, temperature and CO_2 as part of a summer time series at the Western Channel Observatory station L4. Chapter 8 is a synthesis of all the profiles from the research cruises and the Western Channel Observatory and explorers the size and occurrence of ΔS, ΔT and ΔCO_2. Chapter 9 reveals how the flux of CO_2 changes when using surface measurements recorded with NSOP. The general conclusions of this work are outlined in chapter 11.

2 Theoretical basis for the formation of near surface CO_2 gradients

2.1.1 Surface carbon budget calculation

A simple model system is constructed here that approximates the stratified surface as a single layer and assumes that thermal stratification creates a near surface thermocline at 5m. In this model there is no exchange with water in the subsurface layer below, this is based on the estimates in p265 Soloviev and Lukas (2006) that imply that entrainment at the bottom of the diurnal warm layer is negligible. The processes (inputs/outputs) that can alter the inorganic carbon pool above 5 m are air–sea gas exchange, rain, photosynthesis, respiration and calcification. Each process adds or removes carbon from the DIC pool (μ mol kg^{-1}). Four scenarios are discussed that would result in positive or negative near surface gradients (Figure 2.1).

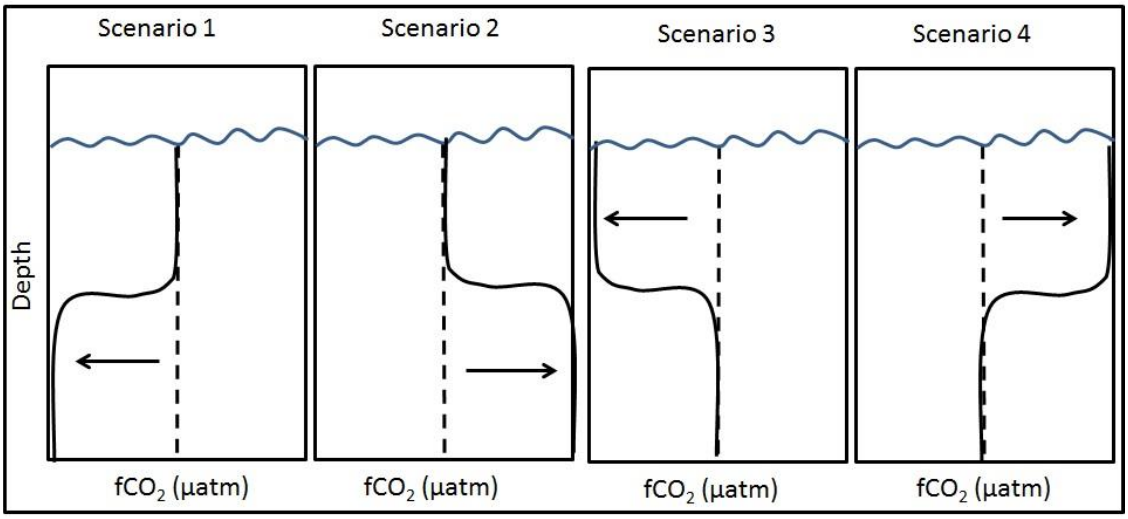

Figure 2.1 Near surface gradient scenarios

4 different theoretical scenarios leading to near surface gradient in fCO_2. The wavy blue line represents the air sea interface, the dashed line represents the pre gradient CO_2 baseline, the solid black line represents a formed ΔCO_2 and the arrow indicates the direction of change.

Scenario 1 – DIC depletion at depth (>5m) giving apparent enhancement in the surface layer. This could be created by enhanced photosynthesis or reduced respiration compared with the surface layer.

Scenario 2 –DIC production at depth (>5m) giving apparent depletion in the surface layer. This could be created by increased respiration, decreased photosynthesis or by increased calcification in the subsurface layer.

Scenario 3 –DIC depletion in the surface layer. This could be caused by increased photosynthesis or reduced respiration at the surface, CO_2 flux out of the ocean or by DIC dilution due to rainfall.

Scenario 4 – DIC accumulation in the surface layer. This could be created by enhanced respiration, decreased photosynthesis or calcification relative to the underlying layer or an air–sea CO_2 flux into the surface layer.

Without a pre gradient baseline it is impossible to distinguish whether the gradient has formed due to changes in the DIC pool in the surface layer or below it. For example scenarios (1 and 4) and (2 and 3) both show gradients of the same magnitude and direction between the surface and subsurface.

A number of additional assumptions were made to calculate the necessary rate for ΔCO_2 of 0.1, 1 and 10 µatm. These three CO_2 values are used indicatively as they span two orders of magnitude from what would be considered a small to a large gradient. Model initial conditions were set to salinity = 35, seawater density = 1.025 kg L^{-1}, seawater temperature = 15°C, silicate = 15 µmol kg^{-1}, phosphate = 1 µmol kg^{-1}, atmosphere fCO_2 = 410µatm, ocean fCO_2 = 400µatm, and TA and DIC concentrations of 2300 and 2080.25 µmol kg^{-1}.

Calculations using CO2SYS (Lewis et al., 1998) infer that DIC needs to increase to 2080.3, 2080.71 and 2084.70 µmol kg^{-1} to create ΔCO_2 of 0.1, 1 and 10 µatm respectively. Isolating each of the processes altering the DIC pool enables an estimate of the necessary rate/flux required to create the gradient over a given length of time.

It is important to note that air–sea CO_2 fluxes and dilution by rainfall only alter the DIC pool in the surface layer. In contrast, the processes of calcification, respiration and photosynthesis occur throughout the upper water column. For these processes to create a ΔCO_2 there needs to be a difference in the rates of these processes between the surface layer and >5m.

2.2 Processes that could drive the formation of near surface CO_2 gradients

2.2.1 Net primary production

Shelf seas are considered net autotrophic, with positive net primary production (NPP =Production - respiration) year round. The average (NPP) rates for the Central Celtic Sea from April and July 2015 were 201.32 and 35.4 mmol C m^{-2} d^{-1} respectively (Poulton et al., 2017). These estimates are from 24 hour incubations and agree with previous production measurements made in summer in the Celtic Sea (64.17 mmol C m^{-2} d^{-1}) (Moore et al., 2003) and with the satellite estimates of NPP (~ 25mmol C $m^{-2}d^{-1}$) (Field et al., 1998).

Primary production also alters seawater alkalinity. Production of hydroxide ions during nitrate assimilation increases alkalinity and hydrogen ion production decreases the alkalinity during ammonium assimilation (Brewer and Goldman, 1976). Based on nutrient concentrations measured in shelf seas (Mayers et al., 2018), the surface was deplete of ammonium so the autotrophs were utilizing nitrate. The effect on TA by primary production is also accounted for in the following calculations.

The NPP data are from the mixed layer shelf sea waters. In April 2015 and July 2015 the mixed layer was 30m and 26m respectively (Poulton et al., 2017). Using the assumed density of seawater 1.025 kgL^{-1}, the volume of water (L) in the column the average production rate can be calculated per kg per day (6.547 and 1.330 mmol C kg^{-1} d^{-1} for April and July respectively).

Using the April and July production rates, it would be expected that the DIC content would fall by 0.273 and 0.048 µmol kg^{-1}. The DIC change equates to a drop in CO_2 of 0.7 and 0.13 µatm respectively. Assuming stratification were to last from the morning through to the mid–afternoon (10am – 4pm) then the DIC content would drop by 1.64 and 0.288 µmol kg^{-1}. Changing the fCO_2 by 4.08 and 0.78 µatm in April and July respectively.

Whilst NPP is positive in all seasons in the Central Celtic Sea (Poulton et al., 2017), the balance between primary production and plankton respiration can vary substantially (García-Martín et al., 2017). In different regions of the European Shelf net heterotrophy (negative NPP) has been inferred when the respiration rate was 2.4 mmol O_2 m^{-3} d^{-1} and the production rate was very low(Garcia-Martin et al., 2014).

In the open ocean (e.g. in the oligotrophic gyres), respiration can exceed photosynthesis resulting in net heterotrophy (Duarte and Agustí, 1998, Williams, 1998). Other studies have shown the oligotrophic gyres to be ‘functionally diverse’ and both auto and heterotrophic(Serret et al., 2015). It is feasible that a respiration induced gradient could exist in a heterotrophic region such as the oligotrophic ocean during daylight hours. Assuming the net respiration rate of ~2 mmol O_2 m^{-3} d^{-1} is accurate and using mole balance to convert to an equivalent release of CO_2 equates to a release of carbon of 0.08µmol C kg^{-1} hr^{-1}, the same order of magnitude as the net production rates. Net heterotrophy also occurs at night as photosynthesis stops. In this scenario the cessation of photosynthesis coincides with the breakdown of thermal stratification so it is unlikely that a gradient would form.

2.2.2 Air to sea flux of CO_2

The flux is calculated using equations 42 to 47 (section 1.9.5), using wind speed (U_{10}) =6ms^{-1}, ΔpCO_2=10 µatm, salinity = 35 and SST =15 °C. Increasing wind speed increases the flux exponentially, a wind speed of 6ms^{-1} was chosen for these calculations as near surface temperature stratification has been shown to break down at wind speeds greater than this(Matthews et al., 2014).

Under these conditions and using these equations, the flux out of the ocean is 32.80 µmol C m^{-2} hr^{-1}. If the CO_2 comes from within a 5m surface layer with a density of 1.025kgL^{-1} then the DIC content decreases by 0.0064 µmol kg^{-1} hr^{-1} and the CO_2 by 0.0241µatm. The air sea flux does not alter the alkalinity. For these calculations it is assumed that the change in pCO_2 does not alter the flux.

A change in DIC of 0.46 µmol kg^{-1} equates to a CO_2 change of 1 µatm; it is clear that a moderate air sea flux (Takahashi et al., 2009) can stimulate a 1 µatm gradient in a 1m surface layer. If the carbon from the air sea flux was confined to a much shallower layer more representative ~2.0m then the increase in DIC in that layer would be 150% greater and would increase the CO_2 by 0.0454 µatm in 1 hour.

The atmosphere ocean pCO_2 difference of 10 µatm is a realistic estimate for the average open ocean which is close to equilibrium. The high productivity throughout the Spring and Summer means Shelf seas are up to an order of magnitude more undersaturated than the open ocean. After the spring bloom and in the summer on the European shelf the ΔpCO_2 were ~100 and 40 µatm respectively (Humphreys et al., 2018). Assuming the same values for all other variables including TA at (2300 µmol kg^{-1}) and using fCO_2 of 310 and 370 µatm, DIC was calculated to be 2032.2 and 2066.0 µmol kg^{-1} respectively for each scenario. Recalculating the flux with a ΔCO_2 of 100 and 40 µatm over a layer of 1m would create ΔC of 0.550 and 0.317 µatm within an hour.

2.2.3 Dilution by rainfall

When rain water mixes with the seawater in the stratified layer it reduces the TA, salinity and DIC by dilution (Drushka et al., 2016). Rainwater has no buffering capacity and is much lower in DIC, alkalinity and salinity. A DIC concentration of 13 µmol kg^{-1} and salinity and TA concentrations of 0 are used following (Turk et al., 2010). Rainfall can be classified by its intensity as light (<2mm hr^{-1}), moderate 2–15 mm hr^{-1} ,heavy (15–30mm hr^{-1}), very heavy (30–60mm hr^{-1}) and torrential (>60mm hr^{-1}) (Llasat, 2001). Rainfall rates of 100mm hr^{-1} can change the sea temperature by as much as 0.2°C but for light and moderate rain this is more likely to be between 0 and 0.05°C depending on cloud height, as this effect is likely small we ignore temperature here (Gosnell et al., 1995).

Over the course of 1 hour with a moderate rain intensity of 10mm hr^{-1}, the seawater in the surface 5m will be diluted by ~0.2%. The salinity would be reduced to 34.93, DIC to 2076.12 µmol kg^{-1}, alkalinity to 2295.40 µmol kg^{-1} and CO_2 to 398.81 µatm. This would equate to a drop in CO_2 of 1.19 µatm. If the stratified layer is only 1m deep in the tropics as shown to be a more realistic approximation by Henocq et al. (2009) then the dilution would be ~1% and thus reduce salinity to 34.65, alkalinity to 2277.22 µmol kg^{-1}, DIC to 2059.78 µmol kg^{-1} and CO_2 to 394.2 µatm, a drop in CO_2 of 5.8 µatm. With vertical observations of salinity it is possible to infer the timing and intensity of rain (Turk et al., 2010).

2.2.4 Calcification

Average calcification rates for the North West European shelf were observed as between 0.6 to 9.6 mmol C m^{-2} d^{-1} in June 2011 (Poulton et al., 2014). Measurements during the spring bloom suggest that the calcification rate does not vary substantially between spring and summer (Mayers et al., 2018). Using the assumed density of seawater 1.025 kgL^{-1}, the volume of water (L) in the column assuming a euphotic depth of 30m, and calcite production rate is estimated as between 0.0195 and 0.313 µmol C kg^{-1} d^{-1}. Calcification decreases the DIC content and the TA by twice that amount, producing CO_2. Assuming the maximum calcification rate of 0.313 µmol C kg^{-1} d^{-1}, calcification would increase the fCO_2 by 0.011µatm in 1 hour. This is a negligible effect on the CO_2 even when scaled up over several hours.

Under certain specific conditions with freshwater from ice melt and river runoff, surface waters can become undersaturated with aragonite(Chierici and Fransson, 2009). However, as calcite and aragonite are both supersaturated in the surface there will be no net calcium carbonate dissolution at the surface(Feely et al., 2009). UK shelf seas are oversaturated in both minerals (Ostle et al., 2016) and at L4 (Kitidis et al., 2012). Calcite dissolution is not included in these calculations.

Table 2 Relative change in DIC and CO_2 from different processes in Shelf Seas

Shaded processes directly alter the flux in a confined layer.

Process	Change in DIC	Rate of CO_2 change	Change in CO_2 in 6 hours	Relative surface:subsurface ratio required for process to create a vertical gradient (*)
Calcification	-0.013 µmol kg^{-1}hr^{-1}	+0.011 µatm hr^{-1}	+0.077 µatm	9000

NPP	April	-0.273 μmol kg^{-1} hr^{-1}	-0.70μatm hr^{-1}	-4.08 μatm	2.4
	July	-0.048 μmol kg^{-1} hr^{-1}	-0.13 μatm hr^{-1}	-0.78 μatm	8.70
Air Sea flux (ocean sink)	April (ΔpCO_2 = 100 μatm) 1m layer	0.320 μmol kg^{-1} hr^{-1}	0.550 μatm hr^{-1}	3.30 μatm	-
	July (ΔpCO_2 = 40 μatm) 1m layer	0.128 μmol kg^{-1} hr^{-1}	0.317 μatm hr^{-1}	1.90 μatm	-
Moderate Rainfall (10mm hr^{-1}) 1m layer		-4.12 μmol kg^{-1} hr^{-1}	-1.19 μatm hr^{-1}	-7.14 μatm	-

*to create a 1 μatm gradient in 1 hour.

3 Methods– A measurement system for vertical seawater profiles close to the air–sea interface

This chapter is a reworked version of a previously published methods paper that described the NSOP used to sample near surface gradients (Sims et al., 2017).

3.1 Introduction

Identifying and quantifying near surface gradients in trace gas concentrations is challenging. Ship motion often inhibits near surface measurements made with the standard oceanographic approach of sampling with Niskin bottles mounted on a CTD rosette. Substantial vertical movement of the rosette limits how close to the surface a sample can be taken. For example, a crane arm 4 m above the sea surface and 11 m from the centreline of a ship that is rolling by ±4 degrees will induce ~1.5 m sample depth variation every few seconds. CTD/Niskin bottle sampling requires that the rosette is kept below the sea surface. Sampling within 2 m of the sea surface is often impossible, even under relatively calm conditions.

This chapter focuses primarily on the Near Surface Ocean Profiler (NSOP), which has been designed to precisely measure vertical gradients in the top 10 m of the ocean. Variations in the depth of seawater collection are minimised when using the profiler compared to conventional CTD/rosette deployments. The profiler consists of a remotely operated winch mounted on a tethered yet free floating buoy, which is used to raise and lower a small frame housing sensors and inlet tubing. Seawater at the inlet depth is pumped back to the ship for analysis. The profiler can be used to make continuous vertical profiles or to target a series of discrete depths. The profiler has been successfully deployed during wind speeds up to 10 m s^{-1} and significant wave heights up to 2 m. The potential of the profiler is demonstrated by presenting measured vertical profiles of the trace gases carbon dioxide and dimethylsulfide. Trace gas measurements use an efficient microporous membrane equilibrator to minimise the system response time.

3.2 The near surface ocean profiler

3.2.1 Near Surface Ocean Profiler (NSOP) description

The design principles for NSOP were:

(1) Platform diameter less than the wavelength of most open ocean waves, allowing it to ride the swell;

(2) Short sampling arm close to the sea surface to reduce vertical movements induced by platform motion;

(3) Capable of deployment close to the ship (to retrieve water for trace gas analysis), but away from major turbulence and motion due to the ship itself.

NSOP is a repurposed ocean buoy (1.6 m diameter) with a central lifting eyelet (Figure 3.1). The top of the buoy is 0.5 m above the sea surface. Mounted on top of the buoy are a line of sight, remotely operated winch (Warrior Winch, model C8000) and a gel battery (Haze, model HZY–S112–230). The winch feeds Kevlar rope through a block and tackle with a 3:1 ratio to reduce rope pay–out speed to ~0.05 m s^{-1}. The block and tackle is attached to the end of an outstretched arm 0.25 m from the outer edge of the buoy. The winch line is attached to an open frame (0.35 m diameter, 0.8 m height) with the capacity to house multiple sensors. Desired sampling depth is targeted using knowledge of the winch pay–out speed. Rope pay–out is then timed with a stopwatch. This approach only approximately regulates the sampling depth because: (i) winch pay–out varies slightly depending on the amount of rope on the spool; and (ii) variable horizontal current strength affects the vertical versus horizontal position of the sampling frame. To minimise horizontal movement of the sampling frame a 10 kg weight was attached to the base of the frame.

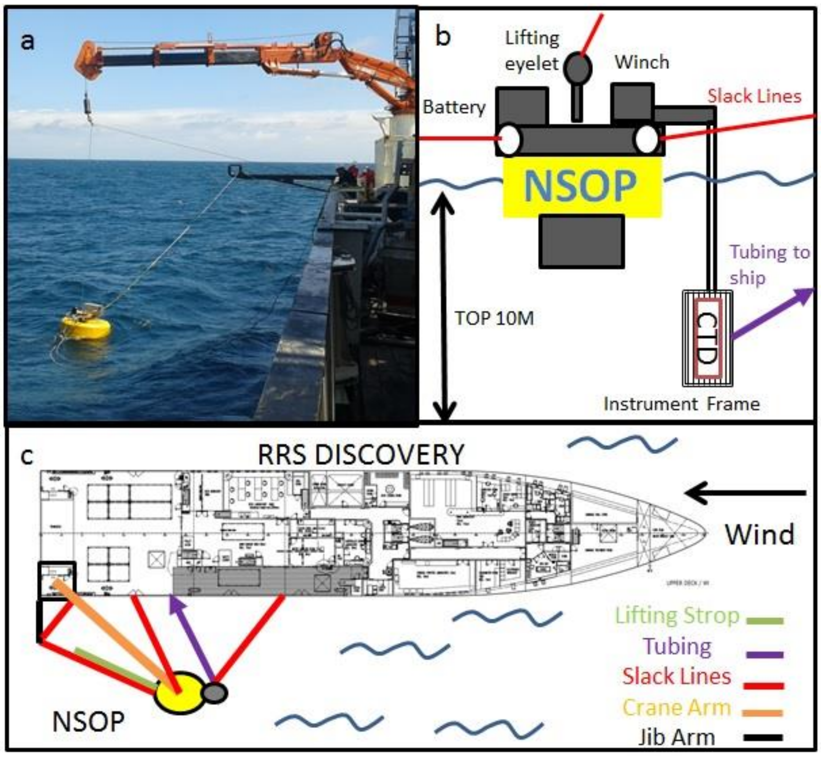

Figure 3.1 NSOP deployment schematic

Different points of view of an NSOP deployment: (a) Image from a deployment on *RRS Discovery* in May 2015 (Cruise DY030); (b) Schematic cross section of NSOP including tubing back to ship (purple) and slack lines (red); and (c) Top down schematic from a research ship including ship orientation. Not to scale.

The primary sensor on the sampling frame is a small CTD (Valeport miniCTD) set to sample at a high frequency (>1 Hz). Under calm conditions it is possible to sample as close as 0.1 m from the air–sea interface when the miniCTD and tubing are mounted near the top of the frame. Rougher conditions demand that the frame be kept deeper (~0.5 m) as motion can momentarily bring the sensors and tubing out of the water. An emergency tag line was attached to the sampling frame in case the winch line failed. Seawater for trace gas analysis was pumped back to the ship at 3.5 L min^{-1} through a 50 m PVC hose (0.5 in inner diameter). A heavy duty peristaltic pump (Watson Marlow, model 701IB/R), primed with water from the ship's underway supply was used to overcome the large hydraulic head (~4 m). The open end of the tubing was located at the same depth as the miniCTD. Water arriving to the ship's laboratory was divided, with ~3.0 L min^{-1} for flow–through analysis (e.g. equilibrator for trace gases) and ~0.5 L min^{-1} for discrete samples (e.g. total alkalinity).

The depth resolution capability of NSOP at a particular depth was assessed by looking at pressure variations under calm conditions with a fixed amount of winch rope paid out. In calm to moderate conditions (<2.5 m significant wave height) the amount of vertical movement indicated by the standard deviation (SD) in the depth is ±0.18 m (Figure 3.2). During four deployments in rough conditions (>2.5 m significant wave height), the depth variability increased as the sampling frame was lowered (at 5 m, SD was ±0.275 m).

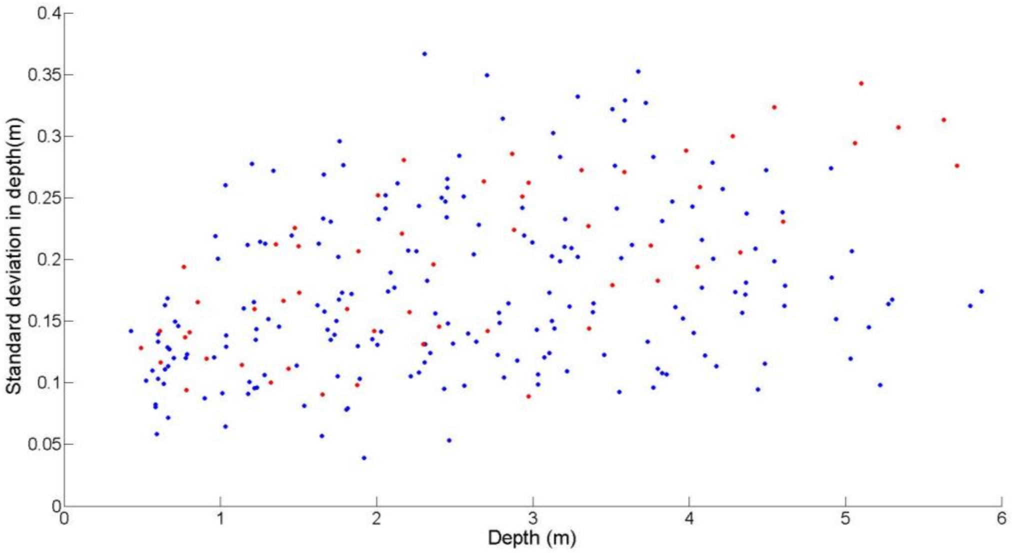

Figure 3.2 NSOP depth stability at different depths

Changes in the standard deviation of the NSOP frame depth as the frame is lowered in the water column. The dataset is comprised of 17 NSOP deployments in the Central Celtic Sea. Data from deployments where the significant wave height exceeded 2.5 m are coloured in red whereas those in blue are for wave heights below 2.5 m.

3.2.2 <u>NSOP deployment</u>

On a large research vessel such as *RRS Discovery*, the deployment and recovery of NSOP requires close coordination between the bridge and three personnel on deck. NSOP was always deployed while the ship was on station and not at the same time as other overboard deployments. Ship orientation during deployments was typically with bow into the wind but also accounted for swell and current direction/speed. NSOP was lifted by the aft crane (Figure 3.3). Once NSOP was lowered to the surface it was detached from the crane via a quick release. Two slack lines were looped through eyelets on the free–floating NSOP to maintain its position close to the ship. A third slack line was connected to the top of the buoy and passed through a block on a fully extended crane arm of 7 m to maintain this distance between NSOP and the ship. The slack lines successfully inhibited the tendency of NSOP to drift horizontally without disrupting its ability to ride the swell. The instrument frame acted like a sea anchor and minimised rotation of NSOP. A 4 m lifting strop used for recovery was connected to the lifting eyelet and loosely lashed to the aft slack line. During retrieval, the slack lines were hauled in and the crane and jib arms brought towards the ship to bring NSOP alongside. The lifting strop was then parted from the slack line and attached to the crane to lift NSOP back on deck (Figure 3.3).

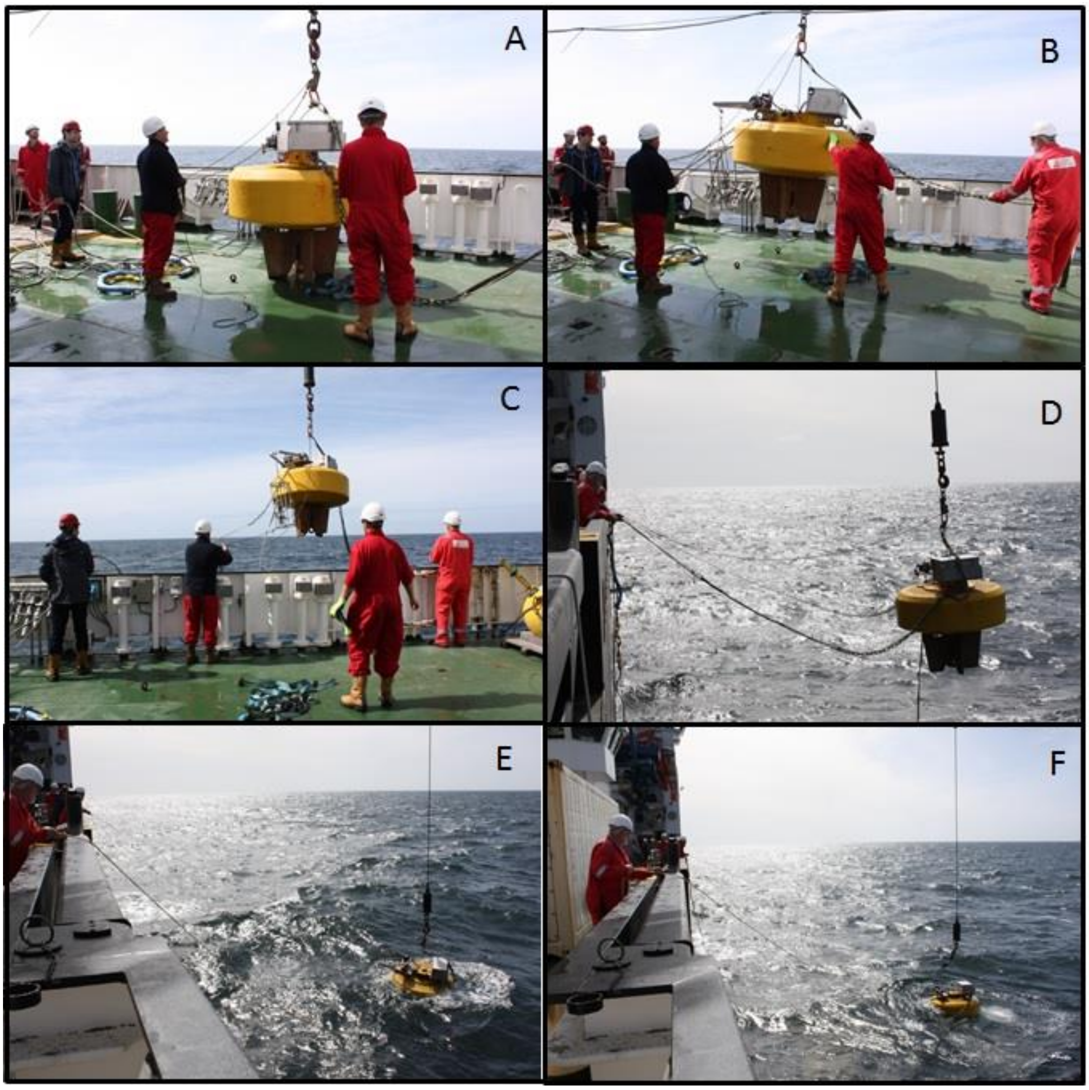

Figure 3.3 Photographs of the crew deploying NSOP on RRS Discovery

Photographs of a Near Surface Ocean Profiler deployment. Panels indicate, the system setup before lifting (a), lifting and steadying with slack lines (b), lifting and deployment over the balwark of the ship (c), lowering to the sea surface (d), contact with the sea surface (e) and quick release activation and seperation from the crane (f).

Turbulence from the ship's propellers has the potential to mix the water column and destroy any near surface gradients. The ship did not use the aft thrusters whenever conditions were suitable (mild sea state, weak currents and no local hazards). Keeping NSOP away from the ship limited disruption of near surface gradients by the thrusters and reduced the risk of line entanglement in the aft propellers. Our winch did not have a groove bar to feed the rope onto the winch drum, leading to an increased likelihood of snagging during spooling. To minimize snagging, the rope was manually fed onto the winch spool before deployments. Visual monitoring of the NSOP frame, slack lines and winch spool is important during deployment.

NSOP has been successfully deployed in 'moderate' sea states up to Beaufort force 5 (~10 m s^{-1} wind speed and wave heights of ~2.0 m). Deployment length typically varied from 1–3 hours.

NSOP can be used in two profiling modes: ‘continuous’ and ‘discrete’. Continuous profiling maximises vertical coverage and involves the winch continuously paying rope in and out at ~0.05 m s^{-1}. A complete down/up profile to 10 m can be conducted in approximately 7 minutes. The depth resolution during continuous profiling is determined by the measurement response time. Instruments with rapid response times such as the miniCTD temperature and conductivity sensors (0.15 s and 0.09 s) have theoretical depth resolutions of 0.75 cm and 0.45 cm respectively. Actual depth resolution will also be affected by the sampling depth variability of the NSOP instrument frame. A measurement setup with a longer response time (such as for seawater CO_2) requires a different approach (see Section 3.6).

During discrete profiling, the winch pays out a fixed amount of rope (typically 0.5 m) and the sampling frame is left at a fixed depth. After a fixed sampling period, more rope is paid out. The process is repeated down and then up such that a set of discrete depths are sampled in a ‘stepped’ profile. The discrete profiling depth resolution is determined by the depth fluctuations when sampling at a fixed depth (see Section 3.2). Discrete profiles are a more appropriate approach for measurement systems with a longer response time. A discrete profile with 0.5 m steps down to 5 m and back to the surface using a 2.5 min sampling period takes about an hour. The sampling period at each depth and frequency/distribution of depths within the profile can be adjusted to suit sampling priorities.

The maximum deployment time is limited by the capacity of the winch battery. When under no load, the battery allows for approximately 3 hours of operation in the continuous mode. Discrete profiling requires substantially less winch usage such that battery drainage is even less of a concern.

3.3 CO_2 analysis

The CO_2 measurement system (Figure 3.4) is a modified version of the system described by Hales et al. (2004). Seawater from the NSOP inlet was passed through the equilibrator (Section 3.4) at ~3 L min^{-1} and the flow rate monitored (Cynergy ultrasonic flow meter, model UF25B). A compressed nitrogen gas supply, maintained at a constant flow rate of 100 mL min^{-1} (Bronkhurst mass flow controller, model F–201–CV–100) flows through the equilibrator in the opposite direction to the seawater flow. The gas has high water vapour content after equilibration and is dried (Permapure nafion dryer, model MD–110–48S–4). The dried sample then enters the analytical cell of a NDIR Licor 7000, which is protected with a 0.2 µm filter (Pall, Acro 50).

CO_2 measurements at atmospheric pressure as recommended by Dickson et al. (2007) were not possible due to the nature of the experimental setup. The continuous gas flow through the system caused a small 0.4 kPa pressure increase in the Licor measurement cell, this was in good agreement with a similar observation by Burke Hales (0.5kpa > ambient pressure; Personal communication). The elevated pressure was taken to be representative of the equilibrator pressure and was used to obtain the partial pressure of CO_2 in the equilibrator ($pCO_{2(eq)}$).

The Licor was calibrated using three CO_2 standard gases before and after each NSOP deployment. The partial pressures of the standard gases (BOC Ltd.) were determined by referencing against US National Oceanic and Atmospheric Administration certified standards (244.91, 388.62, 444.40 ppm) in the laboratory. The seawater temperature at the entry and exit ports of the equilibrator was recorded at 1 Hz (Omega ultra–

precise 1/10 DIN immersion RTD) using stackable microcontrollers (Tinkerforge master brick 2.1 and PTC bricklet). Equilibrator temperature probes and the miniCTD temperature sensor were calibrated before and after each cruise against an accurate reference sensor (Fluke, model 5616–12, ±0.011°C) in a stable water bath (Fluke 7321).

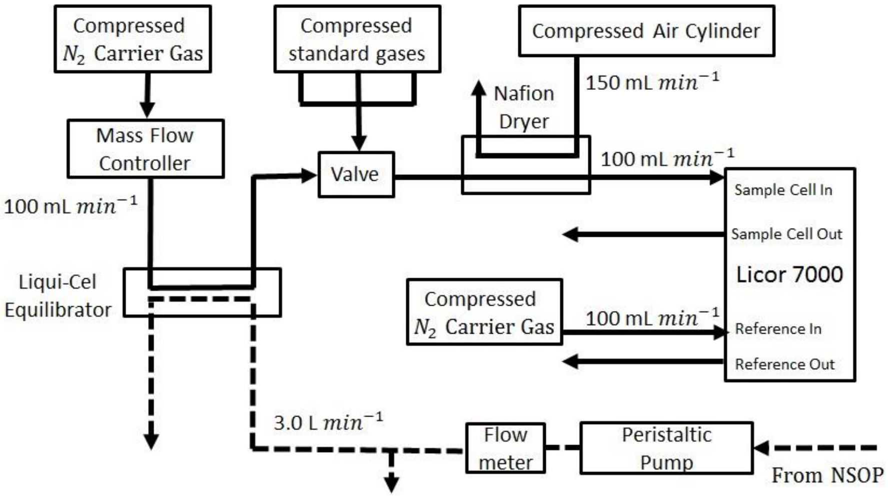

Figure 3.4 CO_2 system schematic

Solid and dashed arrows correspond to gas and water flows respectively. The Licor reference cell is flushed with equilibrated gas at 100 mL min^{-1}. A manual selection valve was used to switch between equilibrated gas and the CO_2 standards.

3.4 Equilibrator

The showerhead equilibrator is the most commonly–used equilibrator for CO_2 but takes ~100 s to equilibrate (Dickson et al., 2007, Kitidis et al., 2012, Körtzinger et al., 2000, Webb et al., 2016). This equilibration time is too slow for effective use during NSOP deployments. A polypropylene membrane equilibrator (Liqui–Cel, model 2.5x8) was used with liquid and gas volumes of 0.4 L and 0.15 L and a surface area of 1.4 m^2. Due to its large surface area to volume ratio and membrane porosity (50%), the Liqui–Cel expedites gas transfer and efficiently achieves equilibration (Loose et al., 2009), with a 3s response time for CO_2 (Hales et al., 2004). Membrane equilibrators have been used by others for trace gas analysis (Hales et al., 2004, Marandino et al., 2009).

Fugacity of seawater CO_2 is calculated from the Licor gas phase CO_2 measurement. This approach assumes that the gas phase sample has equilibrated fully with the seawater. Equilibration efficiency experiments were performed in a seawater tank using a showerhead equilibrator as a reference. Liqui–Cel equilibration efficency declined after prolonged exposure to seawater, likely due to biofouling of the membranes. In a fouled equilibrator, equilibration efficency was a function of the flow rate on both the water and gas side of the membrane. An increased gas flow rate reduces the residence time inside the Liqui–Cel and allows less time to equilibrate (Figure 3.5). Increasing the waterside flow rate moves the gas phase closer to equilibrium because the transfer coefficent in the membrane increases (Figure 3.5b).

Cleaning with an acid – base sequence restored the efficiency of a fouled equilibrator. It was necessary to actively pump chemicals through the Liqui–Cel to achieve a full recovery in efficiency.

Laboratory experiments were conducted with two Liqui–Cel 2.5 x 8 units before and after cleaning. In a relatively new Liqui–Cel (< 2 years old) that had been infrequently used and repeatedly cleaned, the efficiency was flow rate dependent prior to cleaning. In the gas phase, an increase in gas flow from 10 to 100 ml reduced the efficiency to 98.9%. In the water phase, reducing the water flow from 4 L min^{-1} to 1 L min^{-1} reduced the efficiency to 99.6%. These efficiency reductions are smaller than those reported for the older unit but are still significant.

As recommended in the Liqui–Cel cleaning guide (biological fouling section), the unit was cleaned in sequence using 3% HCl and 5% W/W NaOH solutions. The Liqui–Cel was drained and rinsed with fresh water after each cleaning solution was used. Capping the bench–side (lower) liquid port and pouring acid or base solution into the upper port until overflow was ineffective as the solution did not fully drain through the membrane. In order for chemicals to flush through the Liqui–Cel, each solution was circulated with a peristaltic pump for 2 hrs in the opposite direction to the usual seawater flow. Based on this it is recommended that the efficiency is assessed regularly and cleaned as appropriate.

Efficiency reductions in membrane equilibrators like the Liqui–Cel have not been reported by previous studies. Some authors have used 5–50 µm filters to minimise biofouling (Hales et al., 2004) but this was not possible with the NSOP experimental design. If filtering seawater is not possible, It is recommended that the liqui–cel is flushed with freshwater after use, regular cleaning of the Liqui–Cel and daily tests to quantify equilibration efficiency. Trace gas measurement systems that use an internal liquid phase standard (e.g. dimethylsulfide,section 3.5) account for any changes in equilibrator efficiency.

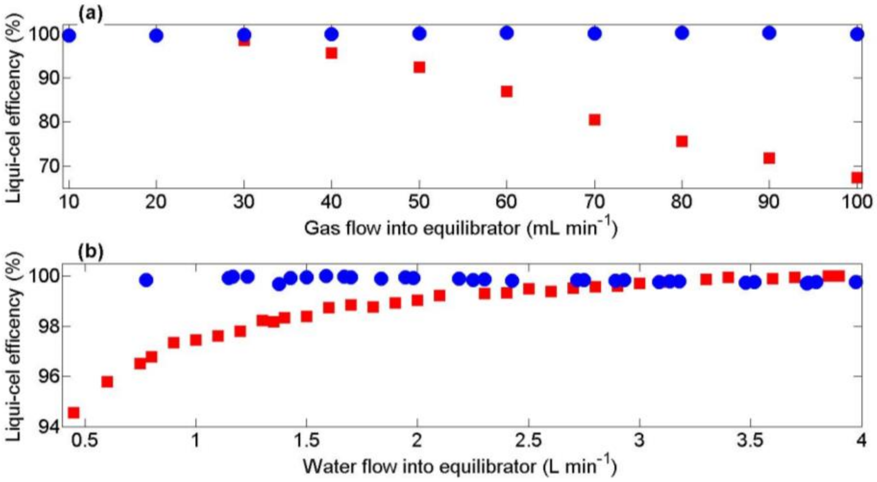

Figure 3.5 Liqui–cel efficiency

Liqui–Cel CO_2 equilibration efficiency (Liqui–Cel mixing ratio / showerhead mixing ratio) for: changing gas flow at a fixed water flow rate of 4 L min^{-1}(a); and changing water flow at a fixed gas flow of 100 mL min^{-1}(b). Blue = unfouled equilibrator. Red = fouled equilibrator.

3.5 DMS analysis

DMS was measured with Atmospheric Pressure–Chemical Ionisation Mass Spectrometry (API–CIMS), using a system modified following Saltzman et al. (2009). Measurements were calibrated using an isotopic liquid standard of tri–deuterated DMS (see Bell et al., 2013 for details). Isotopic standard was injected at 120 µL min^{-1} into the 3 L min^{-1} seawater flow from NSOP before it entered the Liqui–Cel equilibrator. Compressed nitrogen gas was passed through the equilibrator in the counter direction to the seawater flow at 1 L min^{-1}. The use of an internal standard meant that any incomplete equilibration of the ambient non–isotopic DMS was also true for the isotope. The gas stream exited the equilibrator and was dried (Permapure nafion dryer, model MD–110–48S–4) before entering the mass spectrometer for analysis. DMS was detected at m/z (mass/charge) 63 and the isotopic standard detected at m/z 66. The concentration of DMS was calculated using the ion signals and relevant flow rates (Bell et al., 2015). This approach has been shown to compare well with other analytical techniques for DMS (Royer et al., 2014, Walker et al., 2016).

3.6 NSOP delay and response time

Different approaches were used to assess the delay between instantaneous miniCTD measurements and water arriving to the ship for analysis. The delay between seawater entering the inlet and reaching the equilibrator was calculated as 114 s using the internal volume of NSOP tubing (0.5 in inner diameter, 54 m length) and a seawater flow rate of 4.15 L min^{-1}. Delay correlation analysis between the NSOP miniCTD temperature sensor and a second sensor positioned at the entrance to the equilibrator gives a similar delay of 112 s. Note that the total delay of the system is greater because it also includes the time that equilibrated gas takes to reach the Licor. The total delay was determined by quickly transferring the seawater inlet quickly between two buckets with distinctly different CO_2 concentrations and timing how long it took for the signal to be detected by the Licor (139 s; Figure 3.6).

The response time of the NSOP setup was determined by simulating step changes in gas concentrations. A model fit to the exponential change in signal was used to estimate the response time (Figure 3.6). The response time of the system (e–folding time) for CO_2 is estimated as 24 s, which is slightly faster than the 34 s reported by Webb et al. (2016). The e–folding time in the DMS signal is estimated as 11 s, which is consistent with the rapid gas flow rate through the analytical system.

Continuous profiling with the CO_2 system and a 24 s response time yields a depth resolution of 1.2 m, which is greater than the required resolution to resolve near surface CO_2 gradients over the length scale of diurnal warm layers which is ~1-2m (Ward, 2006). DMS has a faster response time than CO_2, but in continuous profiling mode this only translates to a depth resolution of 0.6 m, slightly less than the 1.2–2 m reported by Royer et al. (2014). A depth resolution of < 0.5 m was desired to capture upper ocean vertical gradients in CO_2 and DMS so NSOP was operated in discrete profiling mode.

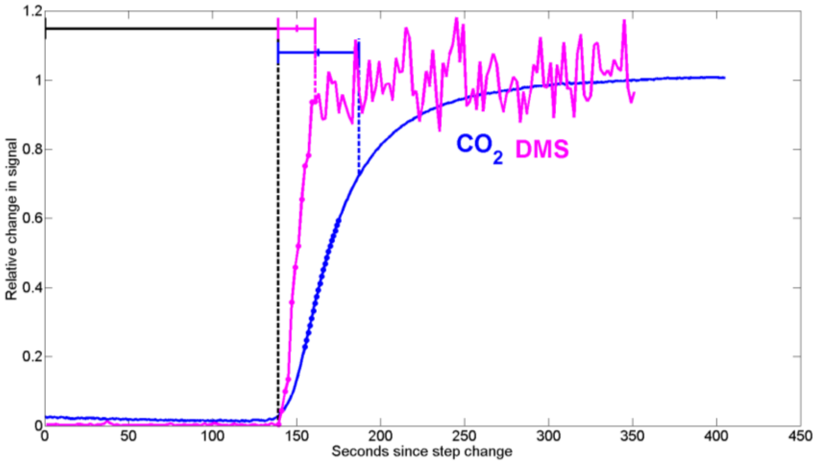

Figure 3.6 Liqui–cel system delay and response times

Instrument responses to step changes in seawater CO_2 (blue) and DMS (magenta). Step changes from 350 to 400 μatm for CO_2 and 0 to 2 nmol L^{-1} for DMS have been scaled down so that the initial and end concentrations are between 0 and 1. Time is referenced against the point when the step change was initiated. The response is seen in both instruments after a delay of 138 s (black dashed line). Two e-foldings are indicated by vertical dashed lines for CO_2 (blue) and DMS (magenta). The data points marked by circles were used to make an exponential fit to the data to determine the response time (Sect 2.5).

3.7 Data processing

During discrete profiling, distinct sample depths were identified from the rapid changes in pressure during depth transitions. Data were binned into discrete depth bins using CTD pressure measurements. Trace gas data were assigned to depth bins after adjusting for the calculated transit time through the NSOP tubing (Section3.6). CO_2 data from the beginning (2 e–foldings + 15 s buffer = 63 s) and end (15 s buffer) of each depth bin were excluded from analysis to account for the response time of the system and the transition time between sample depths. The same approach was taken for DMS, where the faster response time resulted in a smaller portion of data excluded at the beginning of each depth bin (2 e–foldings + 15 s buffer = 37 s).

The CO_2 mixing ratio (xCO_2) measured in the Licor is converted to equilibrator fugacity ($fCO_{2(eq)}$) using calibration standards, *in situ* seawater salinity, and the pressure and temperature in the equilibrator (SOP 5# Underway pCO_2 Dickson et al., 2007). Vertical profiles of seawater $CfsO_2$ fugacity ($fCO_{2(sw)}$) are calculated using average equilibrator fugacity ($fCO_{2(eq)}$), equilibrator temperature ($T_{(eq)}$) and *in situ* seawater temperature ($T_{(sw)}$) at each depth (Takahashi et al., 1993).

3.8 Seawater sample collection using NSOP

The NSOP setup enables vertical profiles of discrete seawater samples to be collected from upstream of the equilibrator, with a split in the tubing diverting ~0.5 L min^{-1} into a sink. For example, discrete seawater samples (250 ml) have been successfully collected and analysed for Total Alkalinity (TA). Samples were collected and poisoned following best practice recommendations (SOP#1, (Dickson et al., 2007). Bottle filling plus 1 overfill took ~60 s. Start and end times were recorded so that collection depth could be retrospectively determined from the CTD pressure data.

Samples were analysed for TA (cell potentiometric titration, SOP#3B; Dickson et al., 2007). Analysis was performed on a Versatile INstrument for the determination of Total Alkalinity (VINDTA) (Marianda: Vindta 3C; Schuster et al., 2014). Certified reference materials for TA (Scripps Institution of Oceanography; batch 142) were run every 12 hrs. Replicate samples were collected at the surface of each profile to determine the measurement accuracy as ±1.502 μmol^{-1} kg^{-1}. An example depth profile of TA collected with NSOP can be seen from July 19th (Figure 3.7).

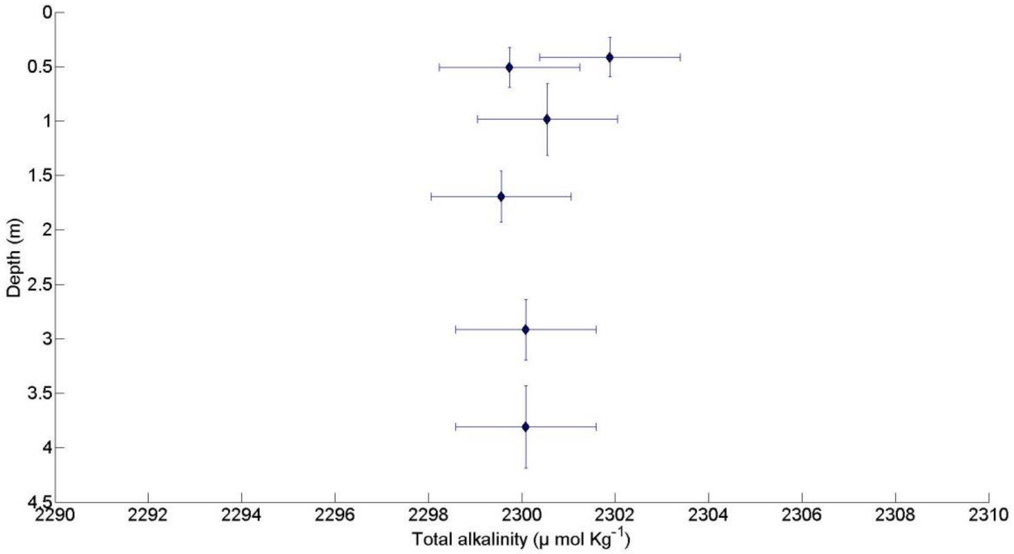

Figure 3.7 NSOP TA profile from an NSOP deployment on 19th July 2015

Total alkalinity profile determined using TA samples collected with NSOP in the Celtic Sea on the 19th July 2015. Water sample depth is calculated as described in section 3.7.

3.9 Field Measurements / Observations

Presented below are example profiles collected using NSOP. The first deployment was in the open ocean (July 30th 2015, Central Celtic Sea; 49.4213°N, -8.5783°E) from *RRS Discovery* (100 m length, 6.5 m draught). The second deployment was in coastal waters (15th April 2014, Plymouth Sound; 50.348°N, -4.126°E) from the *RV Plymouth Quest* (20 m length, 3 m draught).

3.9.1 Open ocean deployment

NSOP was deployed at 14:05 (UTC) on 30th July 2015. During the 6 hours preceding deployment, the ship was on station and encountered persistently strong solar radiance (> 600 W m^{-2}), mild winds (< 6 m s^{-1}) and calm sea state (significant wave height < 1.6 m). This combination of low wind speeds and high irradiance (Figure 3.8) is favourable for near surface stratification (Donlon et al., 2002).

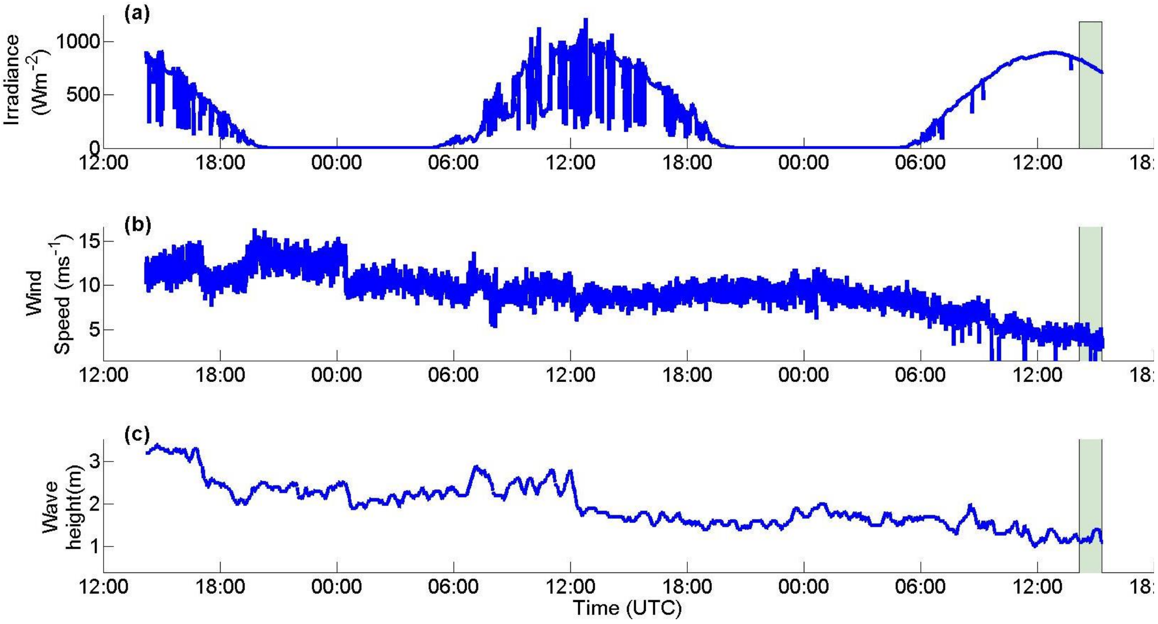

Figure 3.8 Meteorology preceding an NSOP deployment 30th July 2015

Timeseries of meteorology and sea state variables in the Celtic Cea in July 2015 while the ship was on station: irradiance(a); wind speed(b); and significant wave height(c). The data begin 48 h before the start of the profile at 14:05 hrs (UTC). The vertical grey bar indicates the period when NSOP was profiling.

Figure 3.9 presents the time series data collected by NSOP for depth, temperature, salinity and $fCO_{2(sw)}$. Discrete profiling began at 14:05 hrs (UTC) at 0.7 m depth, which was as close to the surface as the frame could be located without the possibility of breaking the surface. Depth bins were identified based on rapid depth transitions (Figure 3.9a). Bottles were filled for discrete samples during the downcast. Profiling lasted 75 minutes and finished back at the surface at 15:20 hrs (UTC). Seawater temperature was 16.61± 0.06 °C. At 14:20 hrs (UTC) $fCO_{2(atm)}$ was 398 µatm and $fCO_{2(sw)}$ was 389 µatm at 0.67 m meaning the ocean was undersaturated with respect to the atmosphere. The temperature and seawater CO_2 were the expected magnitude for summer in the Celtic Sea, ~16°C (James, 1977) and ~350 µatm (Frankignoulle and Borges, 2001). Salinity was 35.45 throughout the entire NSOP deployment, only varying by ±0.004, this was within the range of 35.5–35.0 previously observed in the Celtic Sea (Frankignoulle et al., 1996).

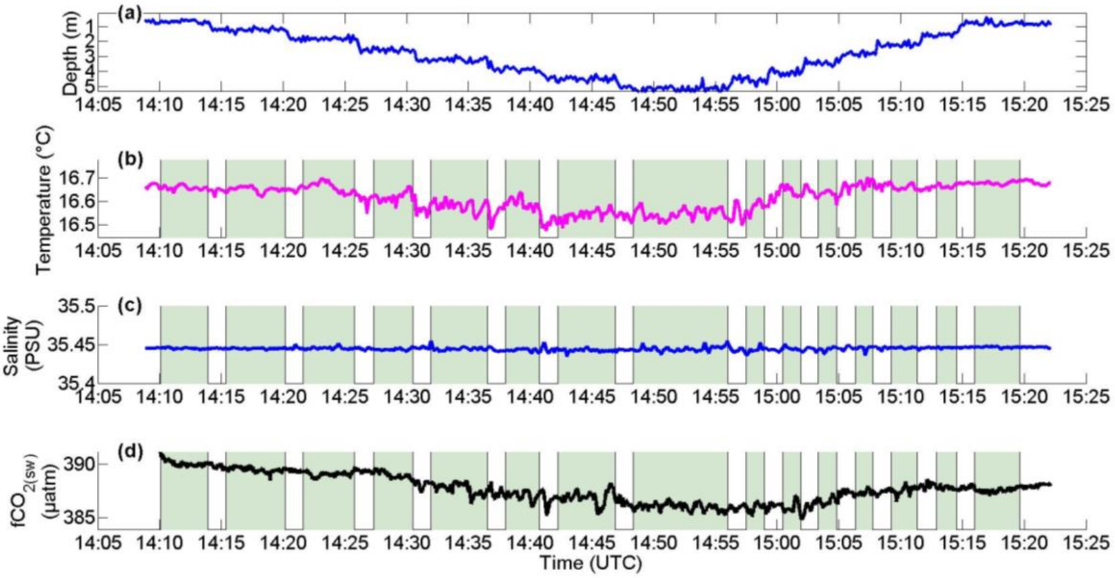

Figure 3.9 Time series measurements from an NSOP deployment 30th July 2015

Time series measurements made during an NSOP deployment in the Celtic Sea on 30th July 2015. Data are 1 Hz depth (a), seawater temperature (b), salinity (c) and fCO_2(sw) (d). Data used for depth bin analysis (Section3.7) is identified by a shaded background.

Depth–binned salinity and temperature data did not show any significant variability (Figure 3.10). A slight temperature gradient was observed, with 0.15°C difference between 5 m and the surface and a fairly constant reduction with depth (0.03°C per metre). The shape of the temperature profile was similar for down and up casts, although some continued warming of surface waters was evident in the up cast. The temperature measured by NSOP at 5.15 m depth agrees well with the coincident temperature measured by the bow thermistor at 5.5 m (< 0.02°C difference) (Figure 3.10c). There is no evidence that the ship's thrusters/propellers disrupted the near surface gradients.

The NSOP temperature profile is compared with thermistor readings from a series of Sea–Bird Scientific (SBE 56) sensors (0.3, 0.6, 1.5, 3.5 and 7 m depth) mounted on a nearby temperature chain moored ~2.8 km away (49.403°N, -8.606°E) from the deployment site . The vertical profile implied by the NSOP deployment agrees with the mooring data (Figure 3.10c), and corroborates the warming of the upper few metres of the ocean observed during the deployment. The agreement between these independent datasets suggests that it is unlikely that NSOP caused any significant localized warming of surface waters. The mean difference between NSOP temperature from discrete depths and the mooring sensors is 0.02°C. The surface data from the NSOP up cast show less agreement with the mooring, with NSOP temperatures ~0.05 °C lower than the 0.3 m and 0.6 m mooring sensors. During the profile the ship drifted ~1 km from the start position of the profile and a further 0.2 km from the mooring. The small offset between the NSOP surface temperatures and the mooring may be driven by horizontal variability between the deployment and mooring locations. It is also possible that turbulence mixed warm surface waters down into cooler sub–surface layers. Turbulence could have been generated around the NSOP sampling frame or by an increase in wave–driven mixing when the significant wave height increased at ~15:00 hrs UTC (Figure 3.8).

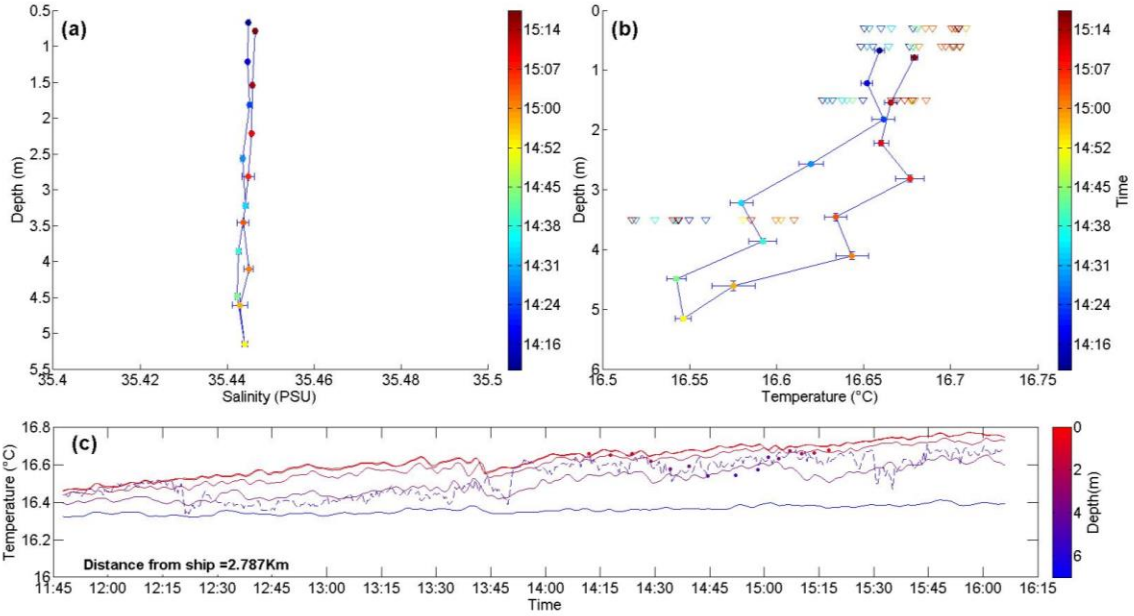

Figure 3.10 Salinity and temperature in the Central Celtic Sea on 30th July 2015

Salinity and temperature in the Central Celtic Sea on 30th July 2015. NSOP profiles of salinity (a) and temperature (b) were derived using depth bins as described in Section 3.7. Data points are coloured by sampling time. Vertical and horizontal error bars show two standard errors of the mean in each depth bin. Coloured triangles in (b) are time–averaged temperature for four depths 0.3, 0.6, 1.5 and 3.5 m at the nearby Central Celtic Sea temperature mooring (49.403°N, -8.606°E). (c) Timeseries of temperature at the mooring. Timeseries of temperature at depths (0.3, 0.6, 1.5 and 3.5 m) are solid lines whereas the dashed line is the underway temperature at 5.5 m from RRS Discovery (located 2.8 km from the mooring). The mooring and underway temperatures are coloured according to their sample depth, where red is the air–sea interface. The circles are binned temperature data from NSOP which have also been coloured to reflect the depth of collection.

Seawater density (Figure 3.11a) was calculated using the salinity and temperature profile data (Figure 3.10a and b) and the 1983 Unesco equation of state (Millero and Poisson, 1981). As expected with little variation in the salinity, changes in the density profile are dominated by temperature. The down and up casts for CO_2 show excellent agreement below 2.5 m. Surface water (< 2 m) CO_2 is 2–4 µatm higher than at 5 m (Figure 3.11b). Elevated surface CO_2 could be explained by a sustained flux from the atmosphere into a near surface stratified layer with inhibited deep water exchange. Under this assumption a vertical gradient in seawater CO_2 would need to be established shortly after the temperature gradient. A paired t–test showed that the fCO_2 measured in the surface bins on the downcast and upcast are were significantly different ($p = <0.001$) . The deepening of the surface stratified layer could explain the more homogeneous CO_2 during the upcast. It is worth noting that in addition to physical processes, plankton trapped within the surface layer could also modify the surface CO_2. Trace gas concentrations may also be different in the sea surface microlayer but sampling that close to the surface is beyond the capabilities of NSOP. Complimentary measurements of the sea surface microlayer could be made using other state of the art purpose built sampling platforms such as the Sea Surface Scanner (Ribas-Ribas et al., 2017).

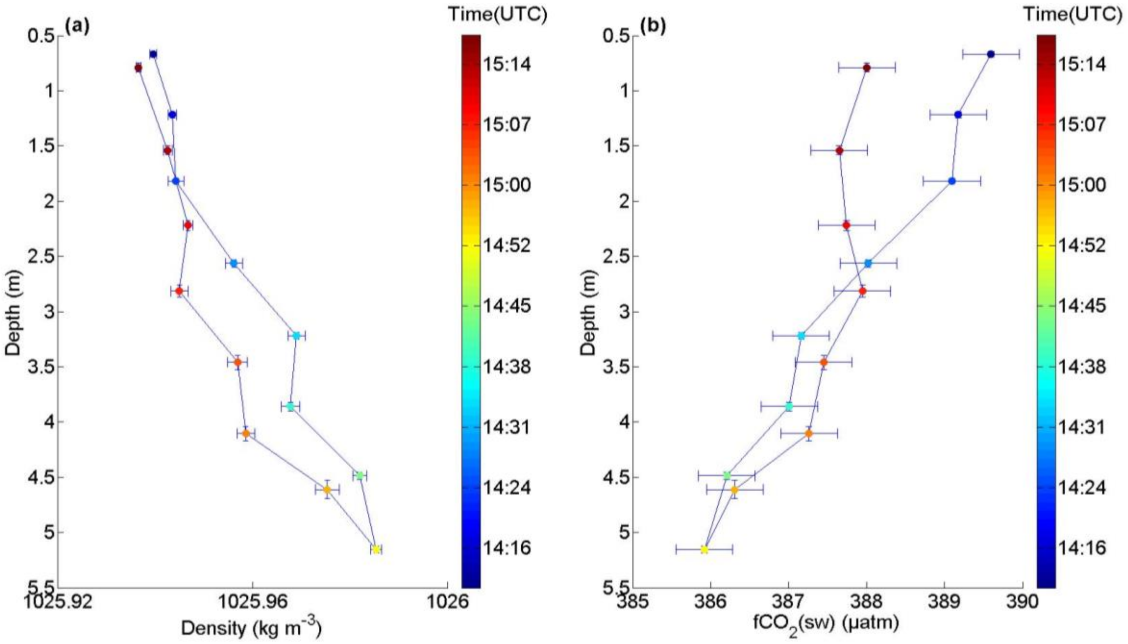

Figure 3.11 NSOP density and fCO_2 profiles in the Celtic Sea on 30th July 2015

NSOP density (a) and $fCO_{2(sw)}$ (b) profiles from the Celtic Sea on 30th July 2015. Data points are coloured by sample time. Vertical error bars correspond to two standard errors of the mean in each depth bin. The horizontal error bars in (a) are two standard errors of the mean, whereas in (b) they are the propogated error from the the binned measurements used to calculate $fCO_{2(sw)}$.

To assess measurement accuracy the NSOP Liqui–Cel CO_2 system was compared against an independent CO_2 system that had a showerhead equilibrator coupled to the ship's seawater supply pumped from 5.5 m below the sea surface (Hardman-Mountford et al., 2008, Kitidis et al., 2012). Technical issues meant that the underway CO_2 system installed on *RRS Discovery* was not functioning during the deployment detailed above. However during a deployment on the 19th July 2015, the $fCO_{2(sw)}$ measured by NSOP at 5 m agreed well with independent measurements from the underway system, (difference = 1.7+/- 4.18 µatm). The agreement between the two systems is in line with previous intercomparisons (Ribas-Ribas et al., 2014, Körtzinger et al., 2000).

3.9.2 Coastal deployment

DMS profiles were collected on a small research vessel on 15th April 2014. NSOP was deployed within Plymouth Sound at 12:00 hrs UTC and recovered 95 minutes later (Figure 3.12). In the sheltered environment behind the breakwater the standard deviation in depth was ±0.10 m, smaller than observed during open ocean profiling. Seawater temperature and salinity demonstrate clear structure, with lower temperatures and higher salinities associated with sub–surface water. Two river estuaries (Plym and Tamar) converge and flow out to the open ocean through Plymouth Sound. A freshwater surface lens was likely observed that was protected from wave–driven mixing and had been warmed over the course of the day. A different miniCTD was used during this deployment and was thus also able to collect fluorescence data (Figure 3.12d).

Temperature profiles (Figure 3.13a) show a sharp discontinuity in the downcast at ~5 m whereas in the upcast the thermocline had shoaled to ~3.5 m. The salinity profiles suggest similar mixing depths to the temperature profiles, with lower salinity water at the surface (Figure 3.13b). The increase in fluorescence with depth (Figure 3.13c) is either due to reductions in chlorophyll concentration close to the sea surface or because of quenching of the phytoplankton photosynthetic apparatus, which is often observed in surface waters that experience strong irradiance (Sackmann et al., 2008). DMS concentrations reduce steadily with depth (Figure 3.13d), which is likely explained by changes in DMS production and consumption rates by the biological community (Galí et al., 2013). The DMS profiles from the upcast and the downcast are very similar, with the largest difference at the very surface. A large difference in the surface–most data point can also be seen in the temperature data, and may reflect mixing with sub–surface waters due to the motion of NSOP or short time–scale variations in the physical environment.

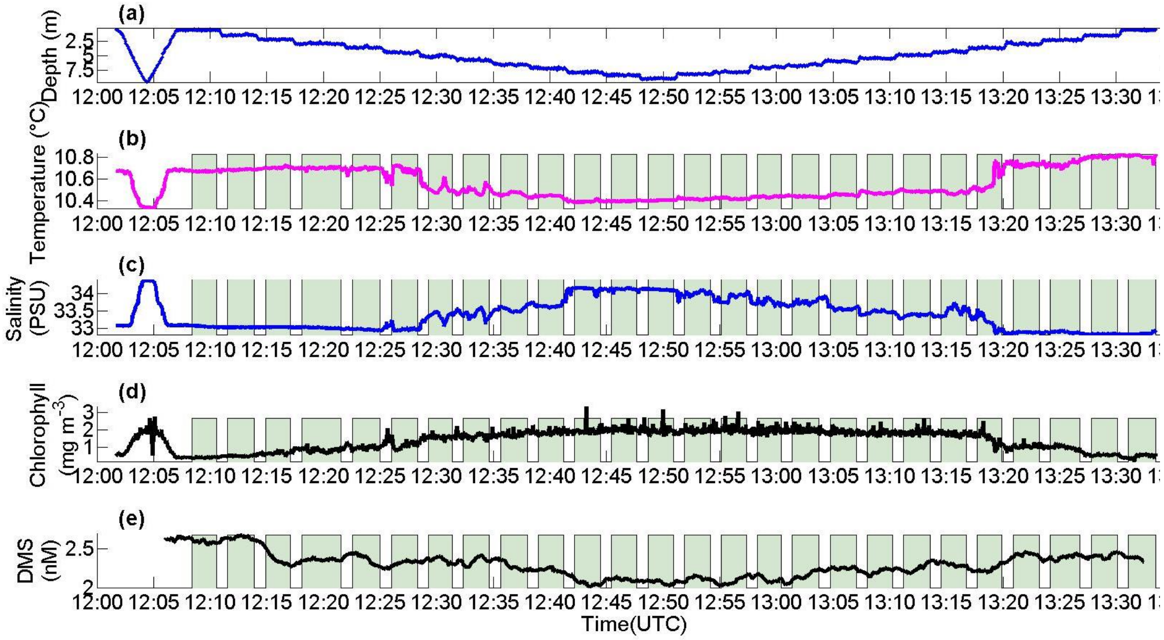

Figure 3.12 Time series measurements from a NSOP deployment 15thApril 2014

Time series measurements during an NSOP deployment in Plymouth Sound on 15th April 2014: depth (a), temperature (b), salinity (c), chlorophyll fluorescence (d) and $DMS_{(sw)}$ (e). Data used for depth bin analysis (Section3.7) is identified by a shaded background. The beginning of the time series is an example off a continuous profile (Section 3.2).

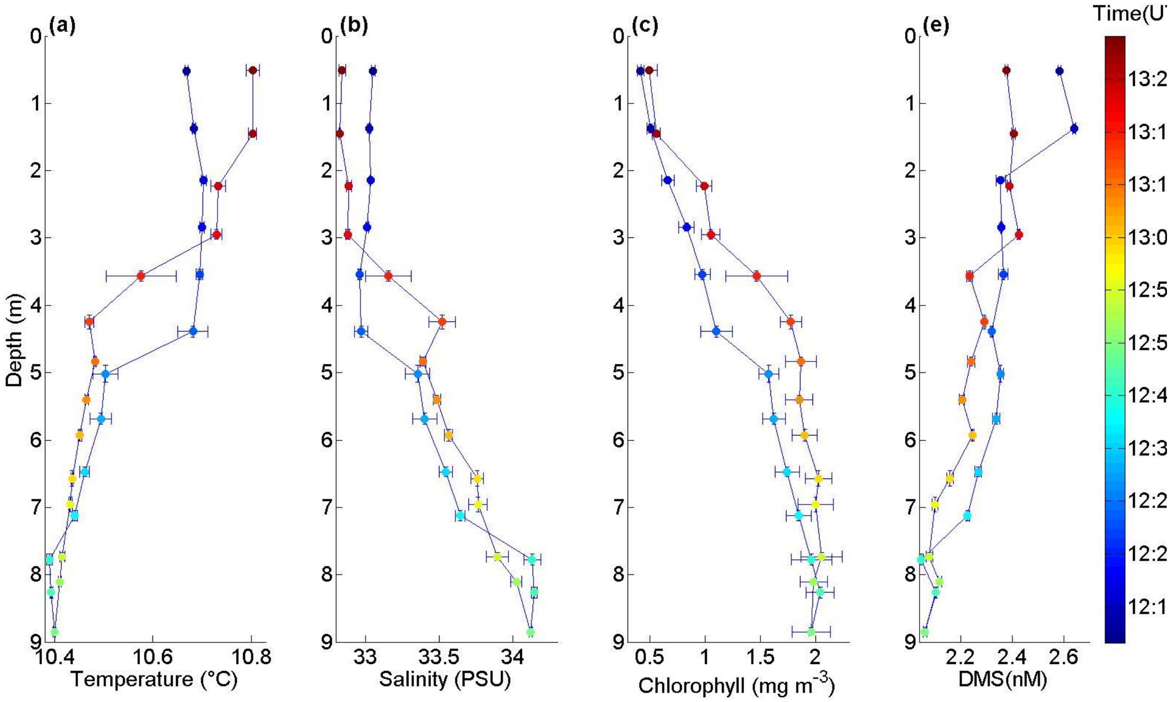

Figure 3.13 NSOP profiles collected in Plymouth Sound on 15th April 2014

NSOP profiles collected in Plymouth Sound on 15th April 2014: temperature (a), salinity (b), chlorophyll fluorescence (c), and $DMS_{(sw)}$ (d). Data are coloured by sample time. Vertical and horizontal error bars are two standard errors of the mean (SEM) in each depth bin.

3.10 Summary

This chapter describes a Near Surface Ocean Profiler (NSOP) designed to measure vertical trace gas profiles near the air–sea interface. NSOP is unique in approach as its sampling frame is lowered from a buoy that rides the ocean swell, reducing relative motion of the frame and hence fluctuations in sampling depth. The NSOP design facilitates near surface (< 0.5 m) sampling, significantly improving the capability to resolve vertical gradients. Other benefits include the ability to sample away from ship–driven turbulence and the flexibility to make a large range of near surface measurements. The NSOP sampling frame houses the miniCTD and also has the capacity to incorporate additional sensors (e.g. turbulence, dissolved oxygen and other measures of phytoplankton abundance and photosynthetic health). The ability to collect water from discrete depths facilitates the collection of near surface samples that require additional processing or take longer to analyse (e.g. TA, dissolved inorganic carbon, nutrients, the DMS–precursor DMSP, dissolved organic carbon). NSOP is highly versatile and can be used for continuous or discrete profiling. Further development could adjust winch pay out speed and enable continuous, high resolution depth profiles for slower response time measurements (e.g. $fCO_{2(sw)}$).

Near surface stratification in the upper few metres of the ocean due to temperature and salinity gradients is a well–documented phenomenon. The presence or absence of chemical and biological gradients within near surface stratified layers has been difficult to assess. NSOP is a platform with the capability to successfully resolve gradients in these near surface layers.

4 NSOP deployments in UK shelf seas

4.1 Introduction

To test a number of the hypotheses of this project (section 1.18**)**, specifically

How frequent are near surface CO_2 gradients?

How large are near surface gradients in CO_2?

Can near surface CO_2 gradients be predicted with meteorological variables?

What effect do near surface CO_2 gradients have on the air sea flux?

It was necessary to make observations of near surface gradients in the ocean. Research cruises offer the opportunity to make deployments in the open ocean for prolonged periods of time. Due to time limitations, NSOP could not be deployed for the entirety of cruises, instead each deployment represents a snapshot in time. As the ocean is large and non-homogeneous in both space and time, to attempt to characterise near surface gradients across the entire ocean it was necessary to make multiple deployments under varying conditions.

4.2 Cruise sampling considerations

As outlined in section 1.17, a number of variables may influence the occurrence and magnitude of near surface gradients; these are wind speed, solar irradiance, biological activity and ocean physics. These variables and processes dictated both the cruise programme chosen for this project and the sampling priorities during each cruise.

The main considerations for cruises on which to deploy NSOP are listed below.

- To observe a range of meteorological conditions (wind speeds and solar irradiances) the cruises would need to be conducted in regions with diverse meteorology or if sampling in one region that region would need to have diverse seasonal meteorology.
- To increase the chance of capturing a wide range of wind speeds and solar irradiances, the cruises needed to be long enough that the distribution of wind speed and solar irradiance would not be biased towards persistent large scale weather features.
- To observe the changes in biological communities over long periods of time, the cruises needed to return to the same sites during different seasons to observe gradients during periods of different biological abundance and production.
- Cruises in stormy seas needed to be avoided as the inability to deploy in rough seas would have severely reduced the number of deployments.

4.3 SSB Cruise Programme

The cruise programme for this project was the UK NERC Shelf Seas Biogeochemistry (SSB) programme https://www.uk-ssb.org/ .

The main objectives of the shelf seas biogeochemistry programme were to improve knowledge of nutrient and carbon dynamics in European Shelf seas, their wider biogeochemical cycles and their response to climate change and anthropogenic drivers. The scope of such a large programme meant it was split into several work packages, consisting of a pelagic (WP1), benthic (WP2), trace metal (WP3), modelling

(WP4) and blue carbon (WP5) components. The objectives of this thesis aligned with those of the pelagic work package 1.

The timeline for the SSB programme involved an intensive year of cruise fieldwork where both the pelagic and benthic work packages involved four dedicated cruises each in an attempt to cover the full seasonal cycle. The trace metal work package (WP3) worked alongside both WP1 and WP2. Once the cruises were completed the data were compiled for the modelling work package (WP4) to upscale the results and for the blue carbon module (WP5) to determine the carbon budget for the European shelf.

Eight cruises were conducted on RRS Discovery (v4 commissioned in 2014) in the Central Celtic Sea in the southwestern European shelf and on the Outer Hebridean shelf part of the Northwest European shelf. The two work packages leading the cruises had different objectives including which stations to visit, how long to spend at each station, what instruments to deploy and what to sample, hence compromises had to be made.

4.3.1 Pelagic cruises

During the four pelagic cruises, a significant amount (~50-60%) of time was spent on station to allow for process studies, the remainder of science time designated for across shelf and shelf break transects.

The SSB pelagic work package 1 had a key process station location in the Central Celtic Sea (CCS, Lat 49.403 °N, Long -8.606 E, depth 145.5m, Figure 4.1). CCS was chosen as the process site as it was deemed representative of the seasonally stratified open shelf region (Sharples and Holligan, 2006). Measurements of chemical rates (including respiration (García-Martín et al., 2017) and primary production (Mayers et al., 2018)) and biological and chemical abundances (including TA/DIC (Humphreys et al., 2018), trace metals (Birchill et al., 2017), zooplankton, (Giering et al., 2018), nutrients (Davis et al., 2018) and DOM (Carr et al., 2018)) were repeatedly made at CCS. A temperature chain mooring was deployed at CCS for 17 months between March 2014 and July 2015 covering the period of the cruise programme. The mooring consisted of combined temperature and salinity sensors at 10, 30, 45, 49, 69, 99, 129 and 145m, and additional temperature sensors at 0.3, 0.6, 1.5, 3.5, 7, 15, 20, 25, 35, 37, 40, 42, 47, 49, 54, 59, 64, 79, 89, 109 and 120m. Also located alongside the temperature chain mooring was the Meteorological Office ODAS buoy which recorded the air and sea temperature, wind speed and direction, air pressure, relative humidity and significant wave height and period 1.5m above the surface. Ocean gliders as well as a wire walker system were deployed during the three final pelagic cruises. A number of landers were also deployed at CCS.

A second pelagic site at the shelf edge/break (Lat 48.568°N,-9.515°E, 210m, Figure 4.1), was located in deeper water close to the edge of the Southwestern edge of the European shelf. Due to its proximity to the shelf break, the shelf edge was a key site for the deployment of ocean gliders.

Another station called the Celtic Deep was located further inland (99m, Lat 51.137°N, Long,-6.567°E, Figure 4.1). This site was chosen to represent the shallower and inland shelf regions.

4.3.2 Benthic cruises

On the four benthic cruises there were four key process stations representing different sediment types found across the shelf (Figure 4.1), mud (Benthic A, 106 m, 51.213 °N, -6.137 °E), sand (Benthic G, 104 m, 51.074 °N, -6.577 °E) , sandy mud (Benthic I, 108 m, 50.604 °N , -7.109°E) and muddy sand (Benthic H, 105 m, 50.519 °N , -7.033 °E). These sites were clustered together in the Central Celtic Sea and close to the Celtic Deep site. The majority of ship time on the benthic cruises was spent on station, for coring, trawling and seabed imaging, with some complimentary pelagic measurements of key parameters (mainly chemical abundances) also being made.

4.3.3 North West European shelf cruise

An additional UK NERC National Capability funded cruise to the Outer Hebrides in October 2014 provided added value to the SSB programme and complimented the other 8 cruises by providing information about the Outer Hebridean Shelf region (Painter et al., 2016). This cruise was comprised entirely of transects across the Hebridean shelf break. The Shelf Seas Biogeochemistry programme cruises were the first on RRS Discovery.

4.4 Justification for choosing the SSB programme

The sampling priorities for the SSB cruises overlapped with the considerations listed above for measuring near surface gradients. Access to berths on several cruises increased the opportunity to make more NSOP deployments. Four cruises spread throughout the year meant that a range of seasonal conditions were likely to be covered. Month long cruises meant there was a reduced chance of experiencing the weather for the entirety of the cruise as weather systems in the mid latitudes typically last around one week. The cruises were based in the Celtic Sea which has strong physical (8.61 – 13.33°C) and biological seasonality (Chlorophyll-a 0.3 – 1.1 mg m^{-3})(Pingree et al., 1976). As the cruise schedules included multiple repeat stations it meant there was some spatial variability in the deployment sites.

During a typical year in the Celtic sea, a large range of meteorological conditions occur with the net heat flux varying by 8 orders of magnitude between seasons (Pingree, 1980). Due to the limitations of long range forecasting there is no way to know in advance the weather conditions that will be observed on a cruise. Periods of low wind speed and high solar irradiance have been shown to be required for the development of thermal stratification (Fairall et al., 1996). As periods of coincident low wind and high solar irradiance are infrequent in the Celtic Sea (Pingree, 1980), sampling needed to be targeted towards them to ensure they were not missed if possible. There was a slight seasonal bias towards cruises in the summer months when solar irradiance is higher and wind speeds are lower (Huthnance et al., 2009). There was an additional bias towards deployments in the mid afternoon when solar irradiance is at its strongest.

4.5 Underway and Meteorological measurements on board RRS Discovery

All quality controlled underway measurements made on the ship are provided by the British Oceanographic Data Centre (BODC) at a frequency of 1/30Hz.

4.5.1 Underway supply measurements

The position of the ship (latitude and longitude), ship heading and the water column depth are routinely recorded on board (Table 3).

RRS Discovery is fitted with a nontoxic seawater supply, which supplies seawater throughout the laboratories. The exact depth of the nontoxic supply remains unverified by measurements and is not verifiable using the ships schematics. The depth of the intake is also subject to change as the ship heaves and the load of the ship changes. The nontoxic seawater intake depth has been approximated at 5.3–6 m by the National Marine Facilities (NMF) technicians who operate this ship and at 6m by the ships officers who observed the nontoxic inlet whilst RRS Discovery was in dry dock.

Sea temperature is measured by a temperature sensor (Table 3) mounted to the hull of the ship at the ships intake; this is calibrated against CTD deployment by the British Oceanographic Data Centre (BODC). Seawater is pumped up from the intake to the underway laboratory, the flow is then split so that 1.6 LPM is delivered to the thermosalinograph (to measure salinity and temperature a second time) and 20 litres per minute (LPM) is passed through a debubbler before supplying the Wetlabs transmissometer and fluorometer(chlorophyll and transmittance) at 10 LPM (Table 3). The remainder of the seawater and the fraction that is not passed through the debubbler is then distributed through the ship to supply the deck labs and the underway CO_2 system (Hardman-Mountford et al., 2008). The underway system was periodically (~between cruises) purged and cleaned to remove any biological deposits that have built up in the underway supply of the ship.

4.5.2 Meteorological measurements

The meteorological platform is located at the bow of the ship and is approximately 10 m above the sea surface. The meteorological platform was optimized when built to reduce wind flow distortion around the platform. All meteorological variables were recorded here including atmospheric temperature and humidity, wind speed and direction, significant wave height, barometric pressure, and irradiance (Table 3). An inlet is located on the meteorological platform and supplies air to the meteorology lab for atmospheric CO_2 analysis.

4.5.3 Underway surface CO_2 system

The autonomous underway pCO_2 system installed on RRS Discovery is described in detail in Hardman-Mountford et al. (2008), this system is located in the meteorology laboratory of the ship. The laboratory is supplied with seawater from the underway intake that has been pumped directly up to minimise heating in the ship. A showerhead equilibrator with a seawater flowrate of 1.6LPM is used to equilibrate the CO_2 in seawater with a small volume of air. The main showerhead equilibrator is connected to a small secondary equilibrator with a seawater flowrate of 1.3LPM; the secondary equilibrator is open to the atmosphere which allows the equilibrator to remain at atmospheric pressure without pulling in ambient air (Kitidis et al., 2012). The headspace air in the main equilibrator is then dried and analysed for CO_2 using a Licor infra–red detector. Three CO_2 standards with nominal partial pressures of (250, 380 and 450 ppm) supplied by BOC Ltd and calibrated against National Oceanic and Atmospheric Administration (NOAA) standards are intermittently run by the system to account for drift in the Licor detector. Atmospheric air is pumped to the laboratory from the meteorology platform at the bow of the ship. The system continuously cycles between the equilibrator headspace, the atmospheric sample and the standards (Hardman-Mountford et al., 2008). All the variables required to perform the calculations to determine sea surface pCO_2 are recorded, according to Dickson et al. (2007).

Table 3 RRS Discovery underway and meteorological measurements Variables recorded by the continuous measurement system on the ship, the units of each measurement and the manufacturer, make and model number of the instrument used for each measurement. Measurements are reported at 1/30 Hz.

Variable	Units	Instrument make and model number
Atmospheric temperature	°C	Vaisala HMP45A temperature and humidity sensor
Chlorophyll–a concentration	mg m^{-3}	Wetlabs wetstar QS3S through flow fluorometer connected to the non–toxic seawater supply (20LPM)
Water depth	m	Konsberg Maritime EM710 (70–100kHz) Multibeam echo sounder
Downwelling Irradiance as energy between 300–3000nm	W m^{-2}	Kipp and Zonen CM6B port and starboard mounted pyranometers
Downwelling vector irradiance as energy (PAR wavelengths)	W m^{-2}	Skye instruments SKE510 PAR(photosynthetic active radiation) port and starboard mounted pyranometers
Position (latitude and Longitude) and heading,	°	Applanix POS MV V3 – GNSS and attitude sensor
Atmospheric pressure	mbar	Vaisala BaroCap PTB100A barometric pressure sensor
Relative humidity	%	VaisalaHMP45A temperature and humidity sensor
Salinity	Non dimensionless number	Seabird 45 thermosalinograph connected to the non–toxic seawater supply and computed using UNESCO 1983 algorithm, calibrated against other measurements. (1.6LPM)
Significant wave height	m	WAMOS 2 X–band nautical radar for wind speeds >3m/s
SST (sea surface temperature)	°C	Seabird 45 thermosalinograph (Non–toxic supply temperature) and Seabird 38 remote thermometer (hull mounted at ships inlet and calibrated against other measurements).
Transmittance–attenuance (red light wavelength) per unit length of the water body by 25cm path length red light	m^{-1}	Wetlabs Wetstar CST transmissometer connected to the non–toxic seawater supply (20LPM)

Velocity above ground Northward and Eastward components	cm s^{-1}	Calculated from GPS data
Wind direction relative to a moving platform	°	Gill Windsonic in–situ anemometer
Wind speed relative to a moving platform	ms^{-1}	Gill windsonic in–situ anemometer

4.6 NSOP Deployments overview

NSOP deployments followed the methodology outlined in section 3 with minor related deployment information specific to RRS Discovery located in the appendix (section12).

NSOP was deployed on four SSB cruises between August 2014 and July 2015, three cruises were conducted in the Celtic Sea (AUG14, MAY15 and JULY15) and one on the Hebridean Shelf (OCY14), the cruise tracks for these four cruises is shown in Figure 4.1. Of the four cruises three were pelagic focused (AUG14, OCT14 and JULY15) and one was benthic focused (MAY15). The number of deployments made on each of the cruises AUG14, OCT14, MAY15 and JULY15 was 7, 6, 8 and 8 respectively (Table 4).

The route of the Discovery during both legs of AUG14 can be seen in Figure 4.1. During the first leg the ship visited the Shelf edge, CCS and the Benthic sites which were all important SSB sites. During the second leg, the ship visited Celtic A and CCS in order to turn around moorings. NSOP was deployed extensively on the first leg of the cruise and less frequently on the second leg with the only deployments on the 17th and 21st August.

The route of the Discovery during OCT14 can be seen in the cruise track Figure 4.1. The ship transited northwards to the Outer Hebrides and then performed across shelf transects down to the Malin Shelf. Due to the poor weather in this region during the first half of the cruise, NSOP was deployed infrequently and only where the weather permitted. Near the end of the cruise the weather improved making additional deployments possible. The locations of the deployments are located along the transect path between station CTDs.

The route of the Discovery during MAY15 can be seen in the cruise track Figure 4.1. The ship spent the majority of the cruise at the 4 benthic sites which are clustered together in the shallower region of the shelf sea; this is where six of the deployments for this cruise occurred. Near the end of the cruise, the ship went down to the CCS site where a further two NSOP deployments were made (21st and 23rd) before heading to the shelf edge and back to port.

The route of the Discovery during JULY15 can be seen in the cruise track Figure 4.1. The ship spent the large majority of the cruise at the CCS process station where 4 of the NSOP deployments for this cruise were made. The remaining 4 deployments were made at the shelf edge site or off the shelf break. Deployments in other sites were not possible during this cruise as commitments to the across shelf transects and process station work at the CCS site were the main focus of the cruise and thus took priority.

The time of day of all 29 NSOP deployments from the four cruises are shown in (Table 4). A one sample Kolmogorov –Smirnov test confirmed a normal distribution of deployments. The average deployment time was 15:00 (UTC) as desired in order to measure diurnal warm layers. All the deployments were made in the 12 hour window between 9:00 and 21:100 (UTC), whilst there were some deployments made during the twilight hours and in darkness, there were no deployments made overnight. The normal distribution seen across all the profiles was not seen during each of the individual cruises which showed biases to certain times of the day, for MAY15 this was the morning, AUG14 the evening and JULY15 the mid–afternoon, these biases were caused by trying to accommodate other cruise commitments.

As outlined in section 4.2, the purpose of sampling during different seasons was to increase the probability of observing different meteorological conditions. Whilst it was anticipated that the conditions would be different between cruises, this was not always the case as can be seen in the average wind speed, sea state and solar irradiance for the cruises, listed in Table 4. Instrument malfunction resulted in no in situ measurements of wind speed or solar irradiance from the Hebridean cruise (OCT14). Both variables are taken from closest Met Office Integrated Data Archive System (MIDAS) observation site located at Stornoway airport (MIDAS station code – SRC_ID 54) on the west coast of Scotland (58.213 °N, -6.317° W, Figure 4.1) for the corresponding time period as this was on average only 270 km away from the 6 NSOP deployment locations.

The wind speed varied between cruises with the average wind speeds during MAY15 and JULY15 being 9.28 ±4.10 ms^{-1} and 8.67 ±3.97 ms^{-1}, whereas AUG14 was the least windy of the Celtic Sea cruises with an average wind speed of 6.57 ±3.80 ms^{-1} (Table 4). The wind speed during each of the cruises varied substantially with large standard deviations in wind speed 5.22 ± 2.82 ms^{-1} (Table 4). The second leg of AUG14 had the lowest observed winds and the smallest variability in the wind speed. By far the strongest winds were observed during cruise OCT14 with average wind speed of 15.66 ± 7.85 ms^{-1}, more than twice those observed on the majority of the other cruises.

For the 3 cruises where data were directly recorded by the ship instrumentation there were only minor differences between the average solar irradiance AUG14a 225.06 ± 283.51 Wm^{-2}, AUG14b 253.02 ± 295.04 Wm^{-2}, MAY15 254.98 ± 307.20 Wm^{-2} and JULY15 202.84 ± 289.98 Wm^{-2}. The irradiance measurements have large standard deviations because the measurements are collected throughout the day which includes times of high irradiance at midday and extremely low irradiance at night. The lowest irradiances were seen in the winter during the OCT14 cruise (196.22±551.61 Wm^{-2}).

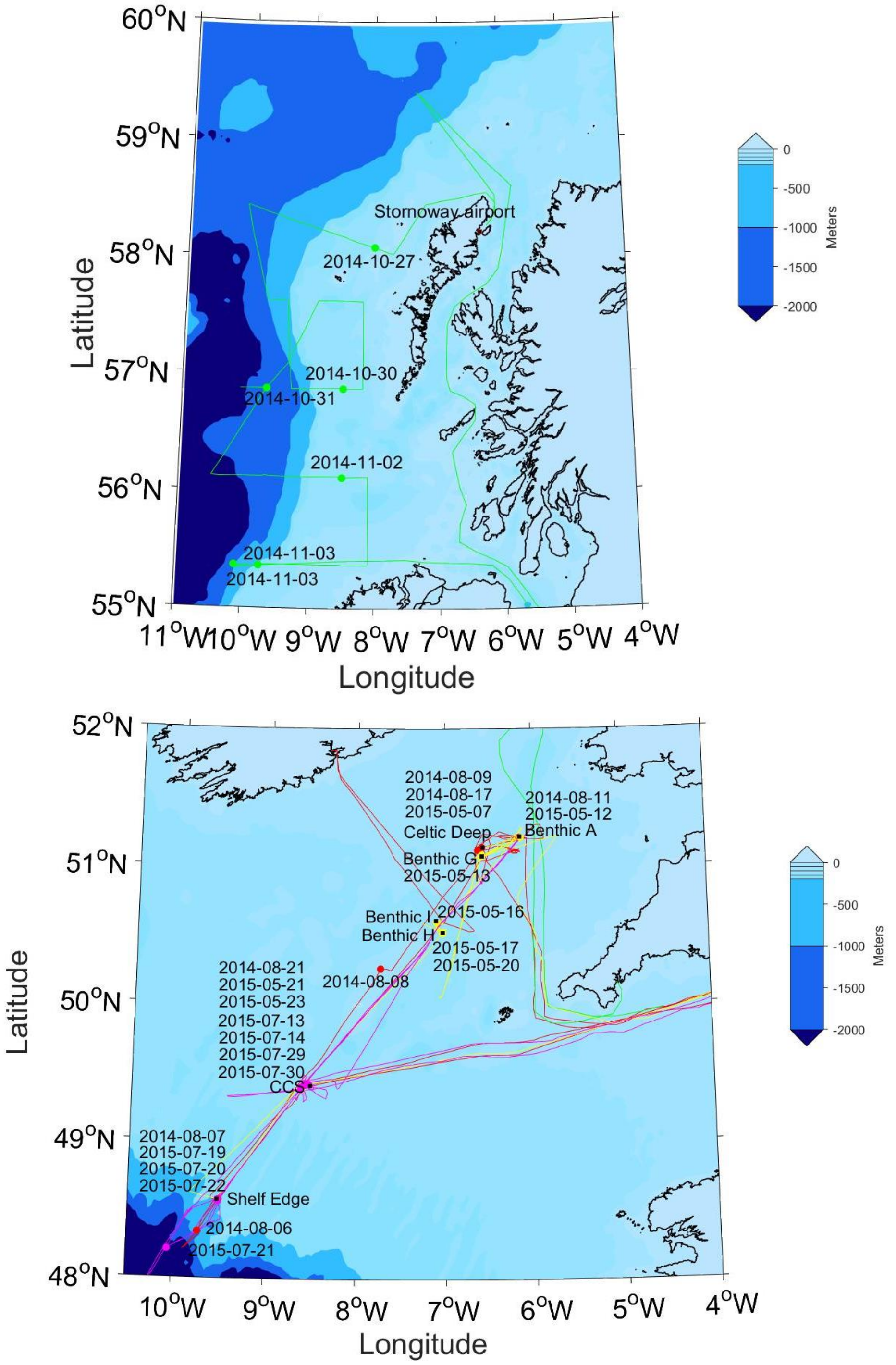

Figure 4.1 Field sites and NSOP deployment locations

NSOP deployment locations in the Celtic Sea and Outer Hebridean Shelf. Key pelagic (CCS, Shelf Edge and Celtic Deep) and benthic SSB stations (Benthic A, Benthic G, Benthic H and Benthic I), and the Stornoway Midas station are indicated by black square markers and a text labels. Cruise tracks for the 4 cruises AUG14, OCT14, MAY15 and JULY15 are indicated by red, green, yellow and magenta lines respectively. Deployment locations for AUG14 (7 deployments), OCT14 (6 deployments), MAY15 (8 deployments) and JULY15 (8 deployments) are indicated by text labels and filled markers whose colour matches that of the cruise tracks. Bathymetric depth is indicated by the colourbar. Coastline is outlined in black.

Table 4 NSOP cruise deployments overview

NSOP cruise deployments overview table gives the cruise identifier, the focus of the cruise, the location, the number of NSOP deployments, the dates and the abbreviation for all the cruises here NSOP was deployed.

Cruise name, code and dates	Deployment date	Deployment start and end times (UTC)	Geographical location	Name of deployment site if applicable	Location (latitude and longitude)	Distance drifted during deployment (km)	Average Wind Speed (ms^{-1})	Average Wind Speed (ms^{-1})	Beaufort wind speed classification and corresponding sea state description	Average irradiance (Wm^{-2})	Average irradiance (Wm^{-2})	Significant wave height (m)	Significant wave height (m)
AUG14 DY026 (legs A and B) August 3rd – August 22nd 2014	06-08-2014	16:34 – 16:43	Central Celtic Sea	–	48.3343°N -9.7294°W	0.0152	6.57±3.80 5.22±2.82	3.18352724248044	Smooth	225.06±283.51 253.02±295.04	428.138644752335	–	–
	07-08-2014	19:19 – 19:37		Shelf Edge	48.6639°N -9.4286°W	5.837		5.21875824802232	Slight		145.234889985120		–
	08-08-2014	14:45 – 15:05		–	50.3050°N -7.6200°W	7.3587		8.77067107833414	Slight - moderate		36.7729782540831		–
	09-08-2014	19:14 – 19:47		Celtic Deep	51.1239°N -6.6261°W	3.4062		5.61109370841887	Slight		8.62921671298349		–
	11-08-2014	09:45 – 10:09		Benthic A	51.2118°N -6.1415°W	0		6.79998183788703	Slight		410.474283191704		–
	17-08-2014	18:25 – 18:40		Celtic Deep	51.1373°N -6.5712°W	0.0044		6.73700248985565	Slight - moderate		198.442297174663		–
	21-08-2014	19:13 – 19:37		CCS	49.3976°N -8.5966°W	0		4.35922563651008	Slight		3.14650695340179		–
OCT14 DY017 October 19th – November 7th 2014	27-10-2014	14:10 – 14:30	Outer Hebridean shelf	–	58.1818°N -8.6093°W	0.3905	15.66±7.85	11	Moderate	196.22±551.61	0	–	–
	30-10-2014	13:02 – 13:25		–	56.8740°N -8.4536°W	1.3123		10	Moderate		37.2155465689536		–
	31-10-2014	17:05 – 17:41		–	56.8720°N -9.7804°W	1.6588		11	Moderate		33.4314214618482		–
	02-11-2014	14:26 – 14:37		–	56.1016°N -8.4762°W	1.2601		16	Rough – very rough		0		–
	03-11-2014	12:52 – 13:10		–	55.3644°N -9.7067°W	1.0633		13	Rough		369.690229815058		–
	03-11-2014	20:06 – 20:10		–	55.3624°N -10.0686°W	2.2641		11	Moderate		4.88163343254915		–
MAY15	07-05-2015	15:52 –	Central	Celtic	51.0795°N	2.1359	9.28±4.10	7.5799319	Slight -	254.98±30	608.34462		1.7139098

DY030 May 4th–May 25th 2015		16:11	Celtic Sea	Deep	-6.5796°W			6382867	moderate	7.20	1239065		0538771
	12-05-2015	12:58 – 13:23		Benthic A	51.1530°N -6.3149°W	0.4118		6.09101958605478	Slight - moderate		660.617499853648		2.00877679733436
	13-05-2015	10:47 – 11:05		Benthic G	51.0829°N -6.5831°W	0.8257		5.28826859103367	Slight		445.208457945369		1.51761033282569
	16-05-2015	11:11 – 11:39		Benthic I	50.5861°N -7.0891°W	2.1127		7.73404190442864	Slight - moderate		598.315943497110		2.53215627208450
	17-05-2015	13:55 – 14:17		Benthic H	50.5320°N -7.0170°W	4.5101		6.87519670067394	Slight - moderate		303.496163650835		3.23138812100789
	20-05-2015	14:21 – 14:54		Benthic H	50.1108°N -7.6370°W	3.2734		8.78796125509978	Moderate		412.996598088448		2.05608426289696
	21-05-2015	11:31 – 12:29		CCS	49.3883°N -8.5989°W	4.141		6.21709140639842	Slight - moderate		126.831928331878		1.55917386700183
	23-05-2015	11:41 – 12:04		CCS	49.6678°N -6.4990°W	3.6586		5.45256794049971	Slight		408.304192077652		1.14439380678611
JULY15 DY033 July 11th–August 3rd 2015	13-07-2015	17:17 – 17:35	Central Celtic Sea	CCS	49.3861°N -8.6106°W	1.7286	8.67±3.97 Range of 0 –24.36 m s^{-1}	10.1190971369015	Moderate	219.7599 ±284.6526 Range of 0 –1213.6	162.037453471004	2.1481 ± 1.0945 Range of 0.0411–6.3000	2.91985426336895
	14-07-2015	16:11 – 16:31		CCS	49.3865°N -8.6134°W	2.1516		7.85997703025856	Slight - moderate		663.597851215259		2.10809555983535
	19-07-2015	14:23 – 14:55		Shelf Edge	48.5716°N -9.5098°W	0.3478		6.10666080622482	Slight - moderate		821.079792816596		1.36948231734021
	20-07-2015	14:07 – 14:47		Shelf Edge	48.5677°N -9.5110°W	1.8404		7.59068505856572	Slight - moderate		679.466600709040		1.52116285873926
	21-07-2015	13:48 – 14:03		–	48.2088°N -10.0441°W	2.128		7.98373801619069	Moderate		815.065626086192		3.28281900614658
	22-07-2015	13:14 – 13:46		Shelf Edge	48.5541°N -9.4954°W	2.9997		5.82835524034336	Slight		81.4809457210047		1.70309705546827
	29-07-2015	15:08 – 15:22		CCS	49.4141°N -8.5367°W	3.0023		8.50324310596238	Slight - moderate		817.002044963872		1.79831598856842
	30-07-2015	14:58 – 15:17		CCS	49.4157°N -8.5742°W	1.2068		3.92260743115902	Smooth		799.593693588235		1.17471668470420

4.7 Data description conventions for salinity, temperature and CO_2

Profiles where a variable increases towards the surface are defined as having positive gradients and vice versa. For simplicity, deployments are referred to by the deployment date (dd/mm) format. Δ Salinity, temperature and CO_2 gradients are always referred to as occurring over ~4.5m between the maximum and minimum NSOP sampling depths of 0.5m and 5m.

4.8 AUG14

4.8.1 AUG 14 Cruise meteorology

The wind speed at the start of the cruise between the 3rd and 8th of August, remained relatively low (< 8 ms^{-1}) (Figure 4.2a). Two profiles on the 6th and the 7th were made in these conditions. Around midday on the 8th through to the end of the first leg on the 12th the wind speed increased substantially; two profiles were taken during this time. The average wind speed for the first leg of the cruise was 6.57±3.8 ms^{-1}. In contrast, the second leg of the cruise had a lower average wind speed of 5.22 ± 2.82 ms^{-1}, with almost all recorded wind speeds below 10 $m\ s^{-1}$. The two profiles measured on the second leg were made under these low wind speeds.

The solar irradiance during the cruise was relatively constant throughout (Figure 4.2b). The peak irradiance did not vary greatly and was between 800–1040 $W\ m^{-2}$ every day except the 9th where the peak irradiance was much lower (730 $W\ m^{-2}$). The strength of solar heating can be determined by integrating the solar irradiance over different time periods, therefore the area of the daily irradiance peaks represents the total energy input by solar irradiance. Whilst having similar maximum solar irradiances, the 4th of August will have received more energy than the 5th because the solar irradiance remained higher for a longer length of time. The average energy input by solar irradiance was 0.217±0.06 $kW\ m^{-2}\ d^{-1}$ during the first leg and 0.217±0.06 $kW\ m^{-2}\ d^{-1}$ during the second leg. The energy received on the 9th August 0.109 $kW\ m^{-2}\ d^{-1}$ was substantially lower than the daily average.

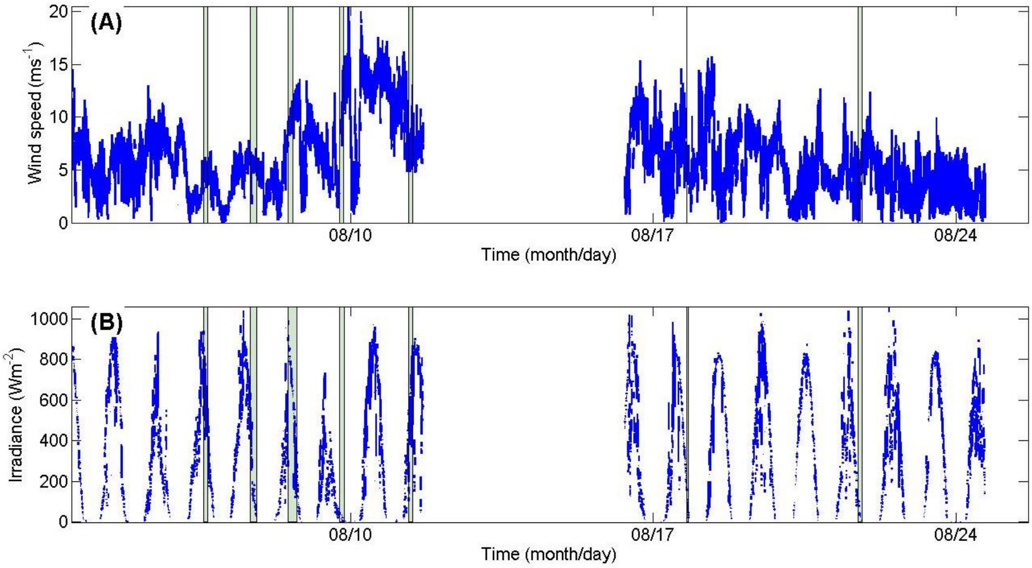

Figure 4.2 AUG14 Cruise meteorology

Timeseries of ship underway meteorological variables during AUG14: wind speed (a) and solar irradiance(b). The time during which the seven NSOP deployments for this cruise were made are indicated by solid transparent lines with widths equivalent to the period of the deployments.

4.8.2 AUG14 Salinity profiles

Seven salinity profiles were measured during the AUG14 cruise (Figure 4.3). Only the profile taken on the 9th August indicates strong salinity variability (> 0.02). The three profiles made on the 7th, 17th and 21st all show negligible variability <0.003, besides the anomalous surface value on the 17th and the mid profile outlier on the 7th all of these three profiles have statistically insignificant salinity gradients as indicated by a two sampled t-test using data from the 0.5 and 5m bins. In addition to the profile on the 7th, the other profile made at the shelf edge on the 6th also indicates negligible salinity gradient. The profiles on the 8th and 11th indicate negative salinity gradients towards the surface, these two deployments were both made in the more coastal region and during daylight hours. The surface salinity varies considerably between sites, with the shelf edge deployments on the 6th and 7th having ~0.6 higher salinity than further inland at the Benthic sites on the 9th.

4.8.3 AUG14 Temperature profiles

Seven temperature profiles were measured during the AUG14 cruise (Figure 4.4). Two of these made slightly off the shelf on the 6th and at the Shelf edge on the 7th of August show the largest temperature changes between 0.5 to 5m of 0.55°C and 0.08°C respectively. In the remaining profiles from the shallower part of the shelf, the temperature changes were much smaller <0.04°C. Despite the low temperature variations in the profiles made between the 8th and 21st August, all the profiles from the cruise were statistically significant as indicated by a two sampled t-test using data from the 0.5 and 5m bins. The strongest temperature gradient on the 6th occurred between the surface and 6m, with the majority of the warming between 6 and 2m. The profiles on the 8th, 17th and 21st have negative temperature gradient towards the surface with the surface temperature slightly colder than the rest of the profile. The profile made on the 11th during daylight hours had a slight positive temperature gradient of 0.022°C between 5m and 0.5m whereas the profiles made on the 17th and 21st in the early evening have slight negative temperature gradients of -0.004°C and -0.016°C between

5m and 0.5m. The temperature in the profile from the 9th August varies by 0.026°C between 17.883 and 17.908 °C but there is only a very small negative temperature gradient of -0.0043°C between the surface and 5m.

4.8.4 AUG14 CO_2 profiles

The CO_2 profiles (Figure 4.5) measured on the 7th, 8th, 9th, 11th, and 21st show that the near surface CO_2 does not change substantially in the surface 5m as there was very small variability within the profiles <1.5µatm. All the profiles were statistically significant when the surface partial pressures are compared to the deepest measurements of the profiles using a 2 paired t-test using data from the 0.5 and 5m bins. The CO_2 deployments on the 6th and 17th show strong 6.3 and 2.8 µatm gradients from the surface to 5 m respectively, the deployment on the 6th was the only deployment of the cruise where the surface ocean was saturated with respect to CO_2.

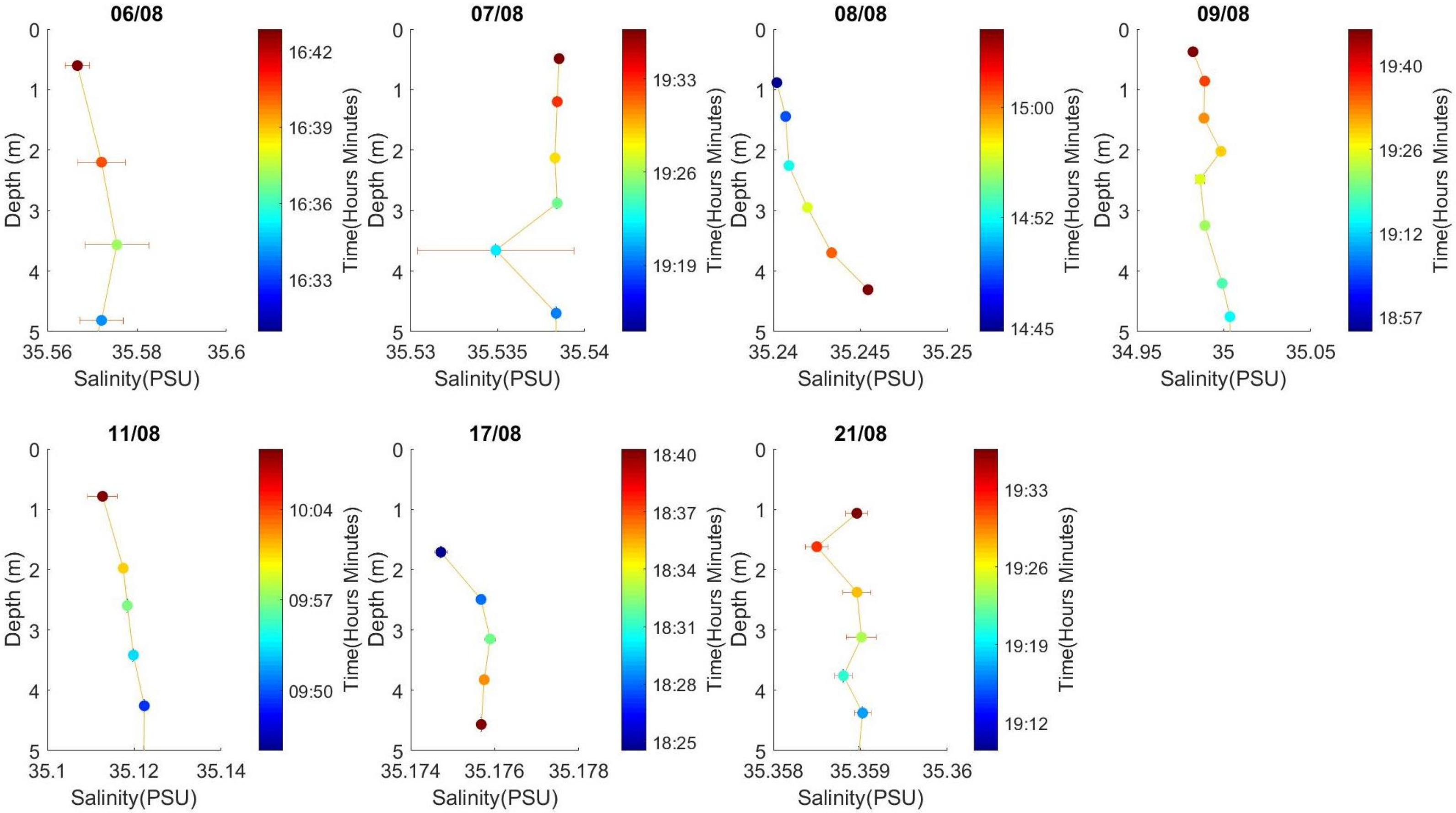

Figure 4.3 AUG14 Salinity profiles

Seven salinity profiles collected in the Central Celtic Sea during August 2014. NSOP profiles of salinity were derived using the depth bins determined in Chapter 2. Data points are coloured by sampling time. Vertical and horizontal error bars show two standard errors of the mean in each depth bin. The date of each profile is given above each subplot.

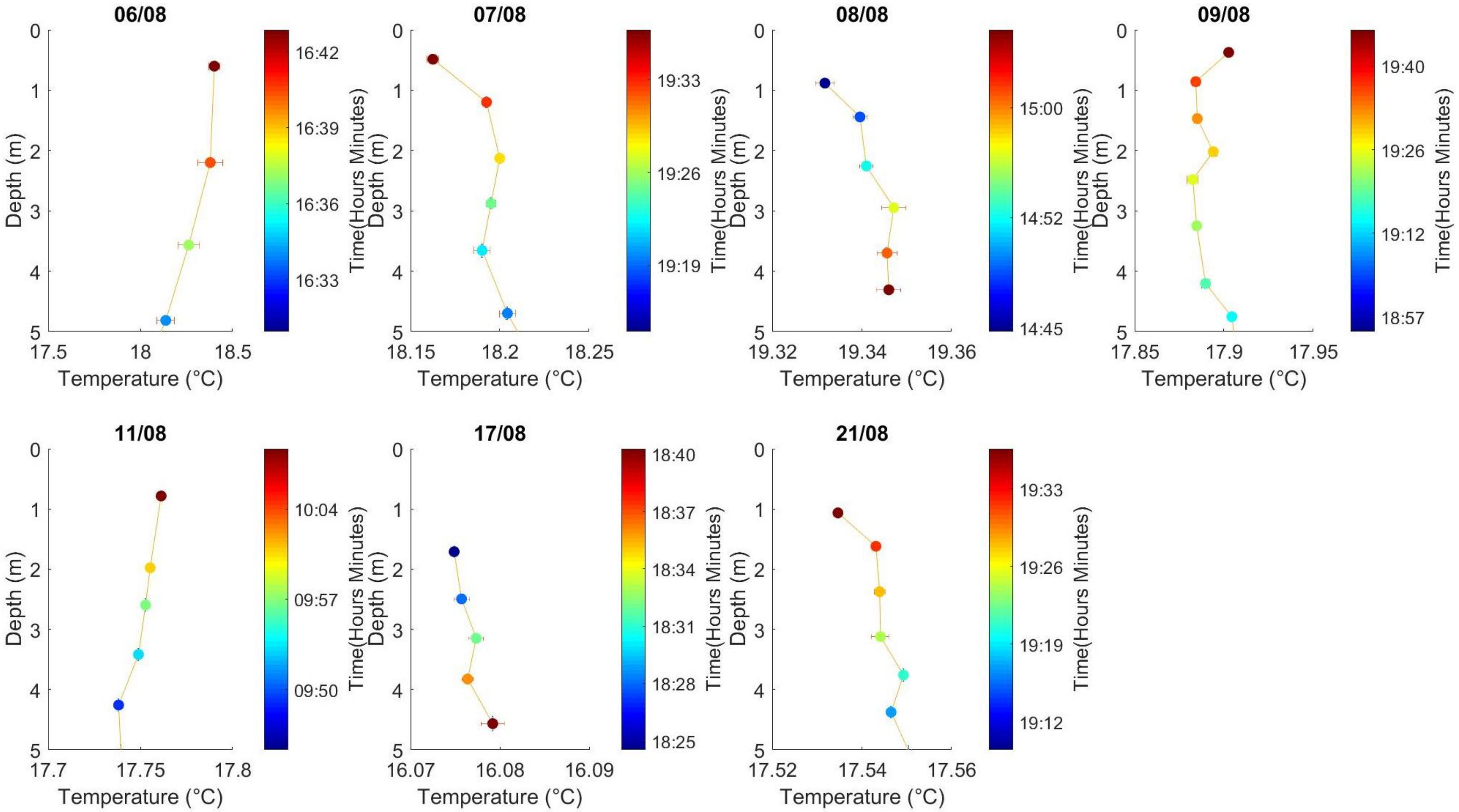

Figure 4.4 AUG14 Temperature profiles

Seven temperature profiles collected in the Central Celtic Sea during August 2014. NSOP profiles of temperature were derived using the depth bins determined in Chapter 2. Data points are coloured by sampling time. Vertical and horizontal error bars show two standard errors of the mean in each depth bin. The date of each profile is given above each subplot.

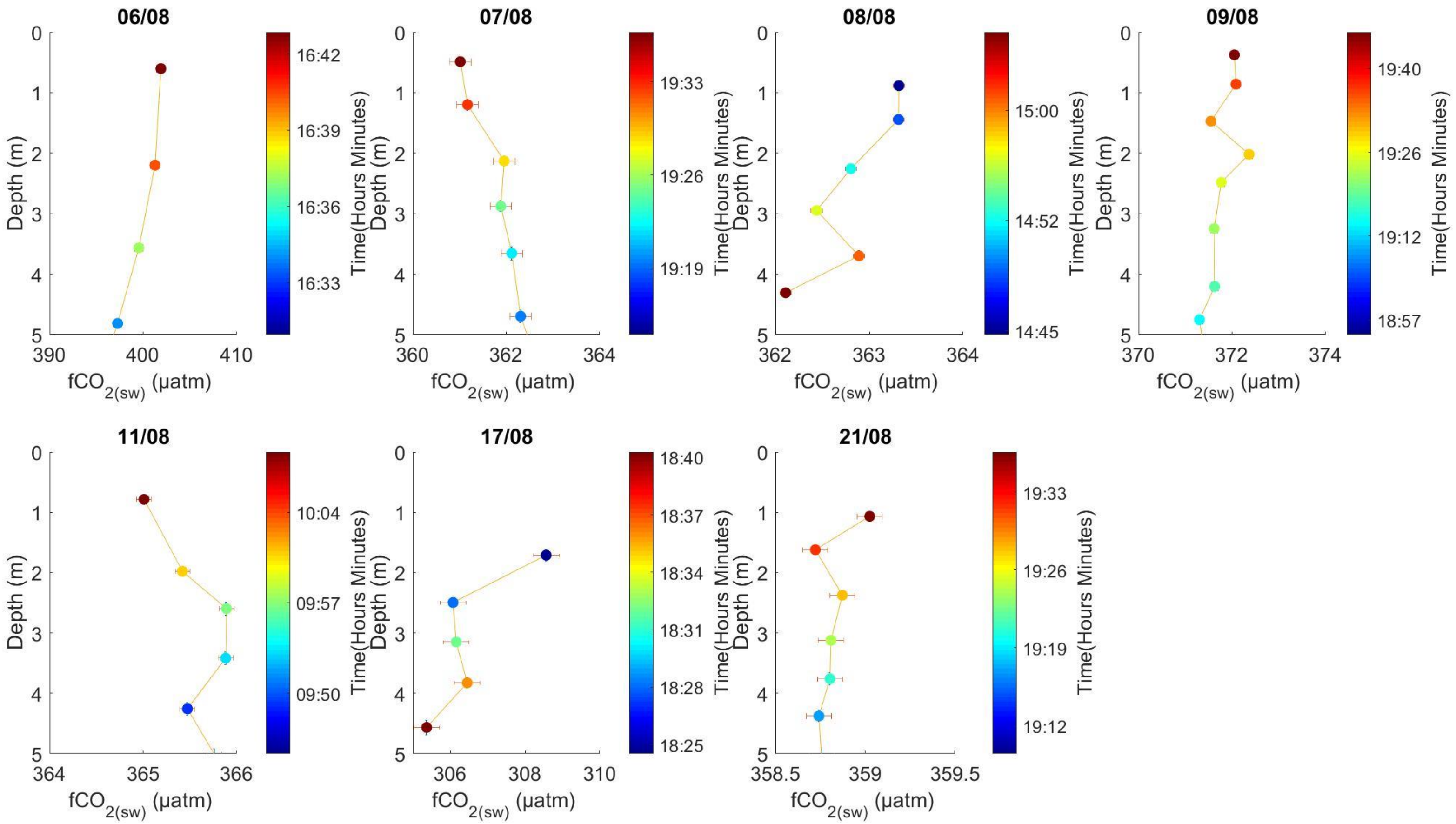

Figure 4.5 AUG14 CO_2 profiles

Seven CO_2 profiles collected in the Central Celtic Sea during August 2014. NSOP profiles ofCO_2 were derived using the depth bins determined in Chapter 2. Data points are coloured by sampling time. Vertical error bars show two standard errors of the mean in each depth bin. The horizontal errors are the propagated error using the averaged bin variable to calculate fCO_2. The date of each profile is given above each subplot.

4.8.5 AUG14 profile interpretation

The CO_2 deployment on the 6th shows a strong 8 µatm gradient from 0.5m to 5 m. There was no significant change in salinity during this profile as indicated by a two sampled t-test using data from the 0.5 and 5m bins. This large CO_2 gradient coincided with a strong near surface temperature gradient of 0.35°C between 0.5 and 5m, this temperature gradient was likely able to establish under the constant weak winds and high irradiance throughout the morning and early afternoon. This was one of only two profiles made off the shelf edge in deep waters, where there are weaker tidal currents (Wright et al., 1999) which may explain why the temperature gradients were established. The strength of the temperature gradient is expected to be highest at this time of the day as it lags the peak of incoming solar irradiance by 2 to 3 hours (p247 Soloviev and Lukas, 2006). If the temperature and CO_2 gradients were already established at the start of the profile it means they were formed in the morning or around midday and were maintained throughout the afternoon. Near surface stratification leads to a surface layer which is isolated from the water below. If there was no exchange with the water below then the confined layer would eventually reach equilibrium with the atmosphere depending on the ΔpCO_2 and the magnitude of the air sea flux. If the only waterside exchange is by the slow process of diapycnal mixing then a gradient would be established as was observed in this deployment. The fact that both the temperature and CO_2 gradients change sharply below 2m but were relatively homogeneous above 2m, is evidence that the temperature profile is determining the structure of near surface CO_2 gradients.

The CO_2 deployment on the 11th shows a small negative gradient towards the surface. This cast precedes a previous NSOP down cast which did not indicate the presence of a CO_2 gradient. At this early point in the morning (8–10am), there were moderate 10 ms^{-1} winds and the solar irradiance had peaked at $840Wm^{-2}$. The salinity and temperature profiles for this deployment show freshening in the salinity of 0.02 (mostly in the surface 1m) and a slight positive temperature gradient towards of 0.03°C between 0.5 and 5m. The lower salinity found in the upper meter of the profile indicates that there must have either been a source of fresh water from rainfall or there was a freshwater lens in the area that was transported by tides or the rivers that feed the nearby Bristol Channel. The increased temperature may have been driven by the increased irradiance (500 – 600 Wm^{-2} by 10:00) throughout the morning or by rainwater as it can be at a higher temperature than seawater. There were no measurements of rainfall made during the cruise but rainfall during this deployment is supported by a mention of ‘bad weather’ in the deployment. As rainwater has a lower density than seawater it forms a buoyant layer that remains at the surface facilitating surface stratification. If the observed salinity decrease and temperature increase were caused by rainfall then the reduced CO_2 in the top meter may also have been caused by dilution of the seawater by low CO_2 rainwater. On the two upper most bins at the end of the profile the CO_2 content is lower at the surface than their respective casts which mirror the two salinity bins that were also much lower. If the lower salinity leads to near surface stratification, it would be expected that the freshwater would be isolated at the surface and unable to mix, this would mean that the surface layer retained the lower CO_2 content of the rainwater. The dilution effect was modelled by Turk et al. (2010), they predicted that the dilution effect would be confined to the top 1.5 m as is observed here but would also be much larger (~30 µatm) than was observed by the very near surface measurements made with NSOP.

The profiles on the 7th, 8th, 9th, 17th and 21st showed that the near surface water column CO_2 gradients were small (<1.5 µatm) despite being statistically significant when a 2 paired t-test t was used on the date in the 0.5 and 5m bins. Similarly the salinity gradients for these five these profiles are either not significant or are negligibly small. These deployments excluding the one made on the 8th were all made in the evening across the central Celtic sea during low irradiance conditions and moderate wind speeds.

Of these profiles five profiles, only the profile on the 7th has a notable temperature gradient of -0.08°C between 5m and 0.5m, this may be due to latent heat loss throughout the near surface, this negative temperature gradient coincided with a slight negative CO_2 gradient of -1.4µatm from 0.5m to 5 m. The profile on the 8th was made during high irradiance and high wind speed conditions; this explains why there was no gradient present. On the 9th the salinity fluctuated upwards and downwards between 34.983 and 35.004 and is likely the result of transitioning backwards and forwards across a front and may reflect the stronger tidal currents present close to the benthic sites. The temperature recorded on the profile on the 9th changes at the same time as the salinity, these coincident changes suggest that the temperature and salinity changes are a result of different water masses mixing. The observed warming at the surface near the end of the profile was very unlikely to have been caused irradiance as this had dropped dramatically by the end of the profile. The salinity varied between 35.3585 and 35.3592 in the profile on the 21st, when excluding the second bin from the surface 35.3585 the variability drops to 0.0004 which is very low. As the upper bin is the same as the bins below this may reflect that the profile sampled a slightly different water mass before moving back to the original water mass. The large 2.8 µatm gradient between 5m and 0.5m measured on the 17th does not coincide with temperature or salinity gradients, as biological production can not account for this gradient on the timescale of the deployment then the only viable explanation for this observation is water mass advection .

4.9 OCT14

4.9.1 OCT 14 Cruise meteorology

Due to the malfunction on the underway system there were no meteorological data for the Hebridean cruise (OCT14). Wind speed and solar irradiance were taken from closest Met Office Integrated Data Archive System (MIDAS) observation site at Stornoway Airport (Midas station number – SRC_ID54), on the West coast of Scotland (58.214 °N, -6.325° W).

The wind speed was very high at the start of the cruise, on occasion exceeding $30ms^{-1}$ before any NSOP deployments (Figure 4.6).The wind speed subsequently dropped and three deployments were made in moderate to rough conditions. The wind speed slowly picked up in the final week of the cruise with the final three deployments being made in rough to very rough conditions.

The solar irradiance during the cruise was extremely inconsistent with peak irradiance varying from 200 to 900 Wm^{-2} (Figure 4.6). The low peak irradiance was caused by overcast conditions throughout the cruise. The extremely low irradiance seen throughout the middle of the cruise from October 26th through to November 2nd was caused by a persistent fog. There were a few days with higher irradiance but there were no NSOP deployments on these days as they largely coincided with wind speeds which would have prevented deployments.

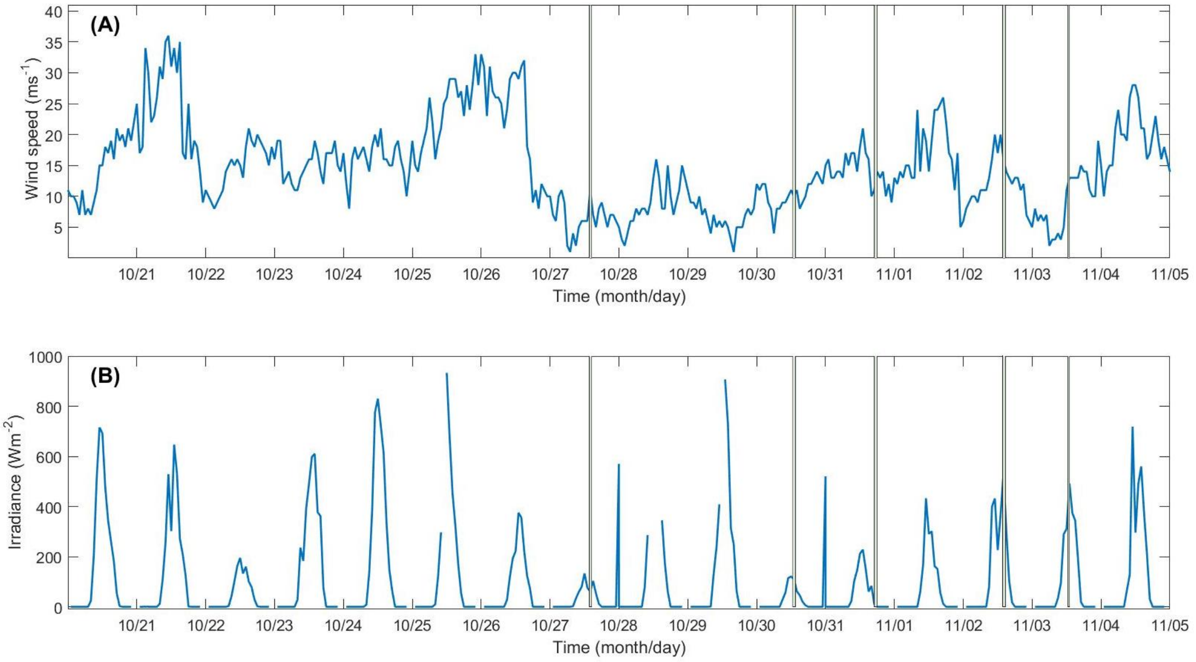

Figure 4.6 OCT14 Meteorology from Stornoway airport

Time series of ship underway meteorological variables during OCT14 from the Stornoway airport Midas station (SRC_ID54) , wind Speed (a) and solar irradiance (b). The time during which the 6 NSOP deployments for this cruise were made are indicated by solid transparent lines with widths equivalent to the lengths of the deployments.

4.9.2 OCT14 Salinity profiles

The salinity profiles measured by NSOP on OCT14 (Figure 4.7), show very little variability with the maximum salinity change observed in the profiles being 0.012. The profile made on the 27th shows the largest variability in salinity, the change was largely isolated to below 4m. The profile on the 30th had declining salinity towards the surface. The two profiles on the 31st October and 2nd November have a less saline surface layer, with the upper most bins being statistically different to the rest of the profiles, the majority of the change in the profile is in this top bin of the profile made on the 31st. The two profiles made on the 3rd show variability but the salinity changes were negligibly small <0.003.

4.9.3 OCT14 Temperature profiles

The temperature profiles measured using NSOP on OCT14 (Figure 4.8), show very little variability with the maximum temperature change over the profile being 0.016°C between 5m and 0.5m. These profiles indicate that the temperature gradients were negligible for this cruise. The absence of gradients is what was expected as the high winds at the time of year and the low irradiance and short day length mean the conditions are not favourable for near surface stratification Two of the profiles with the largest temperature variability (the 31st and the first deployments on the 3rd) were made in the mid afternoon when irradiance is usually higher. The other profile with a large temperature change was the second profile made on the 3rd. The profile on the 30th indicates a slightly cooler surface layer, as this is confined to the uppermost bin in these profiles it is likely that this cooling was caused by evaporative cooling at the surface or by conduction of less dense cold overlying rainwater. The temperatures during all 6 deployments fall with a small range of 12–12.5 °C, except for during the deployment on the 31st made off the shelf edge where the temperature was much lower (11.67 °C).

4.9.4 OCT14 CO_2 profiles

The CO_2 profiles measured using NSOP on OCT14 (Figure 4.9) all show statistically significant gradients as indicated by a two sampled t-test using data from the 0.5 and 5m bins. The profiles made on the 30th, 31st and both deployment on the 3rd show low variability in CO_2. There is a large difference between the surface and the lower two bins during the deployment on the 2nd, this created a large positive gradient of 2µatm between 5m and 0.5m. The CO_2 profiles on the 27th shows the CO_2 partial pressures to be decreasing towards the surface creating a large -1.9µatm gradient between 5m and 0.5m. The profile on the 27th is the only one of the six profiles to have a negative gradient.

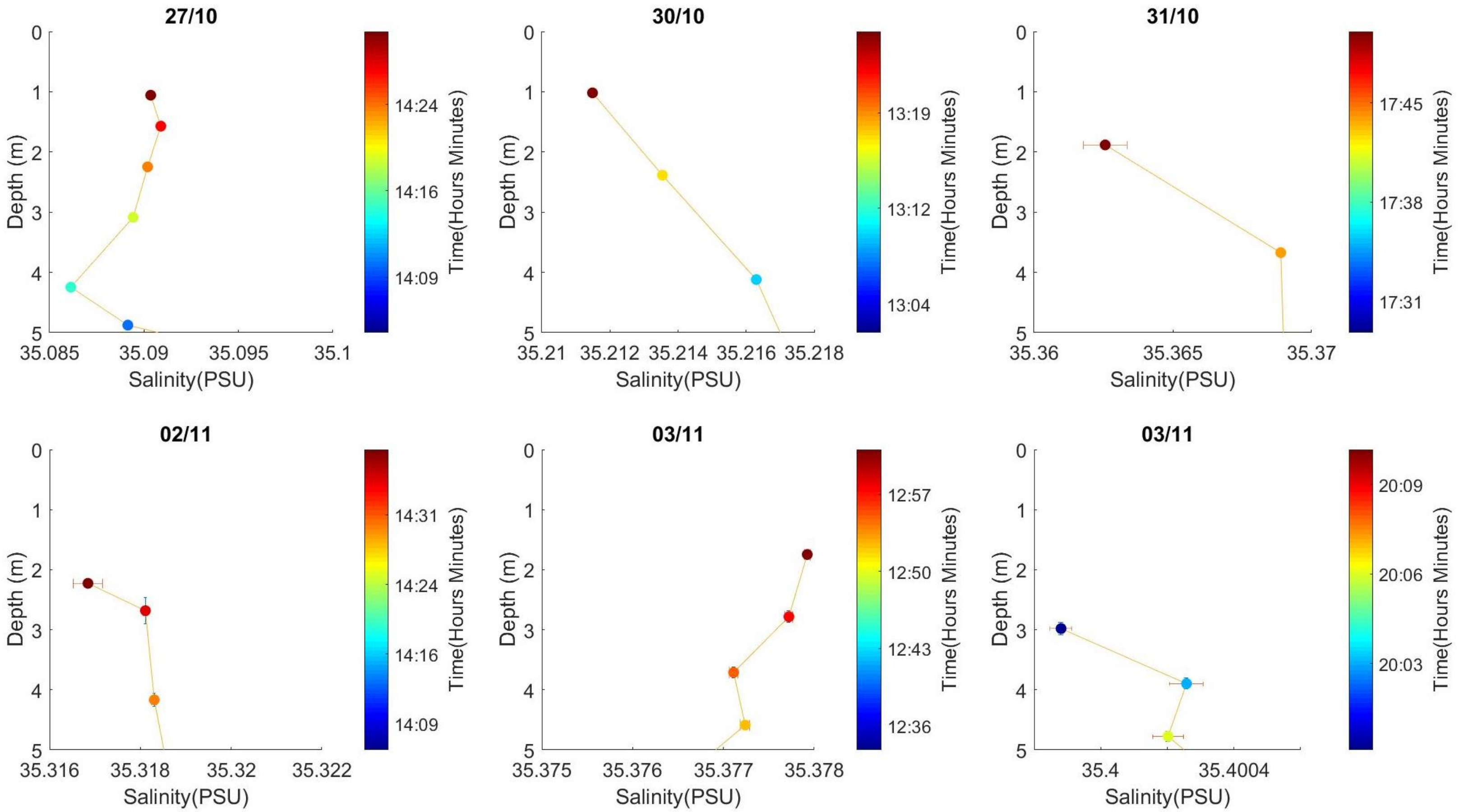

Figure 4.7 OCT14 Salinity profiles

6 salinity profiles collected in the Outer Hebrides during October and November 2014. NSOP profiles of salinity were derived using the depth bins determined in chapter 2. Data points are coloured by sampling time. Vertical and horizontal error bars show two standard errors of the mean in each depth bin. The date of each profile is given above each subplot.

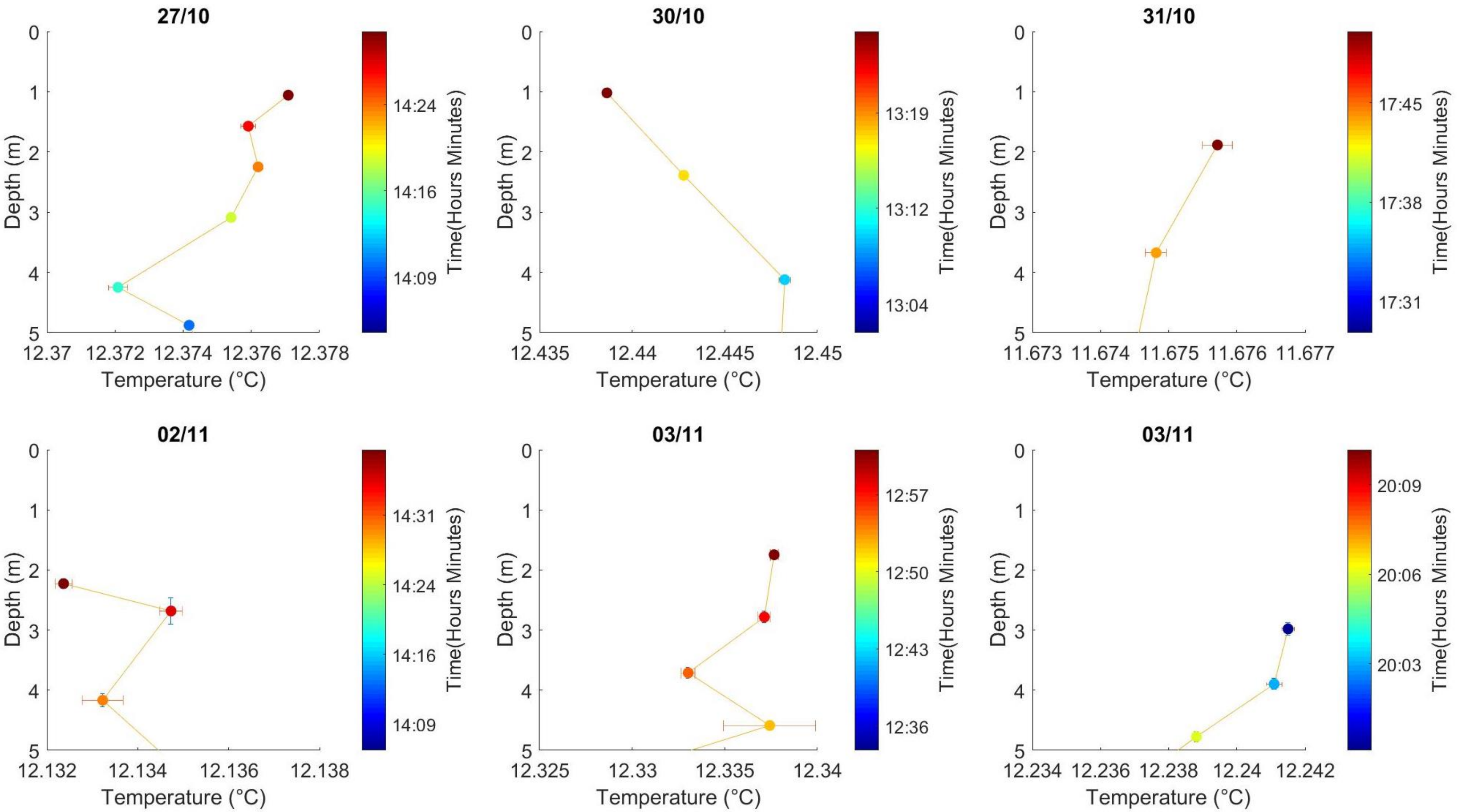

Figure 4.8 OCT14 Temperature profiles

6 temperature profiles collected in the Outer Hebrides during October and November 2014. NSOP profiles of temperature were derived using the depth bins determined in chapter 2. Data points are coloured by sampling time. Vertical and horizontal error bars show two standard errors of the mean in each depth bin. The date of each profile is given above each subplot.

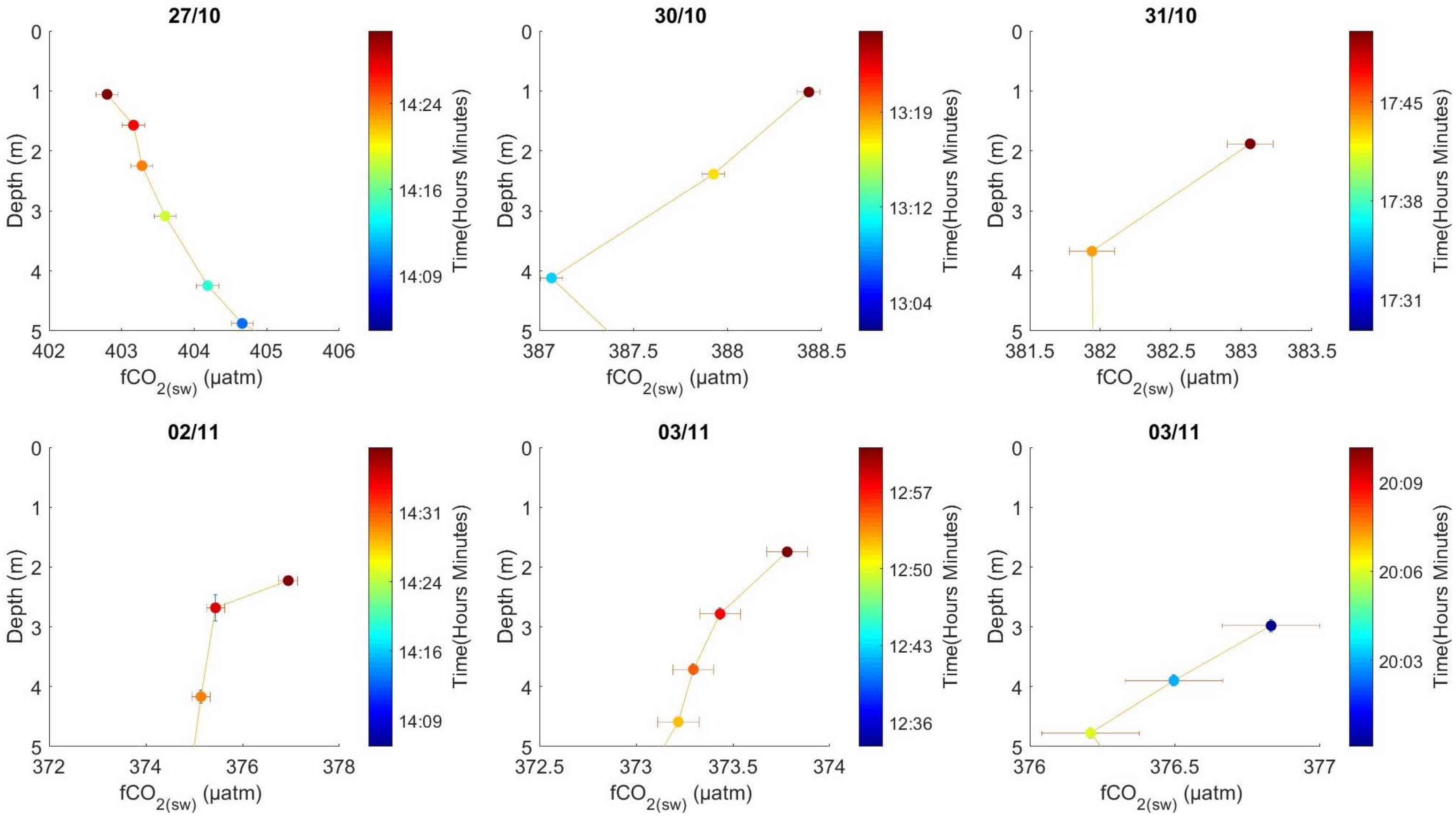

Figure 4.9 OCT14 CO_2 profiles

6 CO_2 profiles collected in the Outer Hebrides during October and November 2014. NSOP profiles of CO_2 were derived using the depth bins determined in chapter 2. Data points are coloured by sampling time. Vertical error bars show two standard errors of the mean in each depth bin. The horizontal errors are the propagated errors using the averaged bin variables to calculate fCO_2. The date of each profile is given above each subplot.

4.9.5 OCT14 profile interpretation

The profile on the 27th is the only profile from this cruise with a negative CO_2 gradient; it was also the only profile made in a region that was oversaturated with CO_2. This could be evidence to support the modelling in chapter 2 that the direction of the gradient tends to be the same as the direction of the flux. For this to be the case the evasive flux would then have to remove CO_2 more quickly than the mixing processes are able to replenish them in the surface, this seems improbable. There were no temperature or salinity gradients in the associated profiles for this deployment suggesting there were no water mass changes. The CO_2 declines quite steadily with time so it is possible what appears to be a gradient is in fact changes throughout the whole water column. As this deployment was made in a shallow part of the Hebridean Shelf it would be more productive than the open shelf (Mayers et al., 2018) and photosynthesis changes in time could account for this gradient. Whether the inferred profile reflects changes throughout the water column can not be inferred as the underway system of the ship was malfunctioning at this time.

The other large gradient measured on the 2nd was made when there were negligible temperature -0.0028°C and salinity gradients -0.0018 between 5m and 0.5m. It’s not clear why the surface would have 2.03 µatm higher pCO_2 here between 5m and 0.5m.

The remaining 4 profiles (30th, 31st and both deployments on the 3rd) had negligible/ very small salinity gradients (<0.012) and with the exception of the second deployment on the 3rd which had a gradient of 0.04°C, all the other profiles had temperature gradients <0.01 °C between 5m and 0.5m. For the profile on the 31st where the temperature change was very small (0.003°C), the change is below the resolution of the microCTD. Given the high wind speeds and very low irradiance it was expected that there would be no surface stratification in both salinity and temperature. The fact that all these profiles had small CO_2 gradients (<1.2 µatm between 5m and 0.5m) is strong evidence that they can not form under turbulent conditions. Despite the lack of stratification there still appears to be a slight positive CO_2 gradients in all 4 profiles. The cause of elevated surface CO_2 could not be due to biology as the affect would be throughout the water column as it is not stratified. It is not clear why there would be any change found exclusively at the surface as there is no stratification. The most probable explanation is that these small gradients reflect a change throughout the water mass during the sampling period which confounds the interpretation of the vertical gradients.

4.10 MAY15

4.10.1 MAY15 Cruise meteorology

During MAY15 the wind speed was 9.28 ± 4.10 ms^{-1} (Figure 4.10a). Despite large fluctuations in wind speed all 8 NSOP deployments for this cruise were made when the wind speed was below 10 $m\ s^{-1}$. Many of the NSOP profiles spanned a period of time when the wind was actively changing such as on the 20th May where the wind speed increased considerably from 6.83 to 9.71 ms^{-1} during sampling.

The daily solar irradiance seen during MAY15 was variable (Figure 4.10b). Peak solar irradiance during the cruise was upwards of 800 $W\ m^{-2}$ on every day of the cruise except on the 8th and 22nd Whilst the majority of the days saw high peak irradiance, on many of these days that intensity was not maintained for more than a few hours such as on the 15th, 21st and 24th which have very narrow irradiance peaks.

Significant wave height for MAY15 (c) mirrors the trends in wind speed (Figure 4.10a). The periods where wind speeds were highest 5th–7th, 10th–12th and 18th –20th are also the times where significant wave height was greatest. The trends in significant wave height lag behind those in wind speed as it takes ~4 hours for the wave field to mirror changes in the wind speed (Parvaresh et al., 2005). Most of the NSOP deployments occurred when the wave height was below 2 m except on the 16th and 17th where the wave height was 3–4 m.

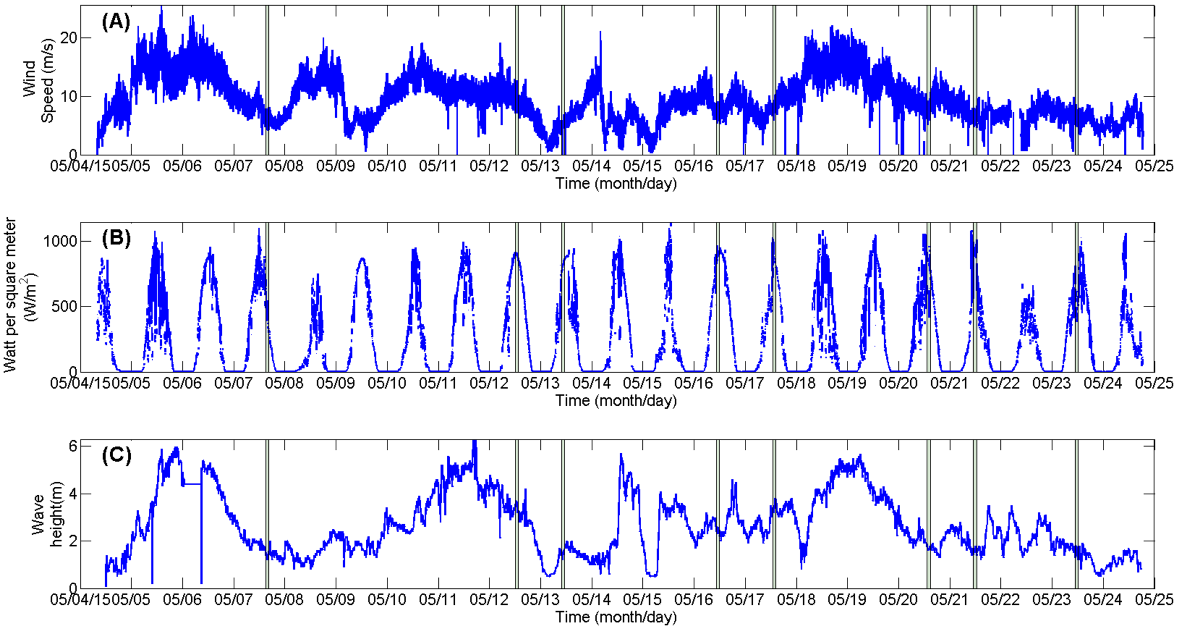

Figure 4.10 MAY15 Cruise meteorology

Timeseries of ship underway meteorlogical variables (wind Speed (a), solar irradiance (b) and Significant wave height(c)) during MAY15. The time during which the 8 NSOP deployments for this cruise were made are indicated by solid transparent lines with widths equivalent to the lengths of the deployments.

4.10.2 MAY15 Salinity

Unfortunately during MAY15, the salinity sensor on the Valeport MicroCTD was faulty and the salinity could not be reconciled with that measured by the underway system. The failure of the salinity sensor on the microCTD undermined the interpretation of the associated CO_2 profiles. Surface water column salinity was measured via the underway seawater supply on RRS Discovery during NSOP profiling and indicates salinity changes were small (<0.03) for all deployments. The fact that the salinity recorded by the underway system does not change by more than 0.03 suggests that the ship did not transit through new distinct water masses during the NSOP profiling. The largest changes in salinity over the course of the profiles was seen at the sites found in the northeast of the Celtic Sea on the 12th,16th, 17th and 20th. Small changes in salinity were observed on the 7th, 13th, 21st and 23rd around the benthic sites and CCS site.

4.10.3 MAY15 Temperature profiles

Eight temperature profiles were collected during MAY15 (Figure 4.11). The two profiles made at the shallower benthic sites had the strongest temperature gradients between 5m and 0.5m of 0.12 °C between 0.5 and 5m on the 7th and 0.21 °C on the 13th. The temperature gradient on the 13th was linear towards the surface above 4m whereas the temperature profile on the 7th was not linear and showed warmer water at intermediate depths and colder water at the surface, this meant that overall the surface to 4.5m gradient was much smaller at 0.04 °C. The other two strong temperature gradients between 5m and 0.5m were observed on the 17th and 21st at 0.09 °C and 0.13 °C respectively, both gradients were close to linear and trended positively towards the surface. The temperature change between 5m and 0.5m observed in the remaining four profiles on the 12th, 16th, 20th and 23rd was below 0.04 °C.

4.10.4 MAY15 CO_2 profiles

Eight CO_2 profiles were measured during the MAY15 cruise (Figure 4.12). The profiles taken on the 7th, 21st and 23rd show no statistically significant gradients in CO_2 based on a two sampled t-test using data from the 0.5 and 5m bins. The CO_2 profiles on the 16th and 17th show consistency in the lower part of the profile with significant higher CO_2 at surface, ~4 µatm in both cases. The profile on the 12th shows a slight negative CO_2 gradient of 2 µatm between 5m and 0.5m. The profile on the 13th identified a slight positive gradient towards the surface above 4 m with, no constant CO_2 below 4 m. The profile on the 20th showed a large 2.3 µatm increase in CO_2 between 3.5 to 2.5 m and a much smaller increase of 0.5 µatm between 2.5 and 0.5m.

4.10.5 MAY15 TA and DIC profiles

5 profiles of TA and DIC were measured during the MAY15 cruise (Figure 4.13 & Figure 4.14). Whilst 6 bottles were sampled for each profile with two replicates at the surface, a number of samples were lost due to instrument errors and software bugs in the new VINDTA 3Cs; this meant losing or removing ~8 samples including some surface replicates. The surface replicates are not true replicates as they were not in bottle replicates and they were collected over consecutive 2 minute periods each. In most cases where there were surface replicates, they do not agree any better than the values from the other sample.

The desired accuracy for TA as a carbonate system parameter is <1 µmol kg^{-1} but a more realistic estimate of measurement accuracy is 1–2 µmol kg^{-1}. The TA values for each profile were all within 15µmol kg^{-1} of each other which is much larger than the spread that might be expected if there no gradients. Based on the 2 surface replicates the accuracy was ~2 µmol kg^{-1}. There is no discernible distinctive structure in the TA profiles.

The DIC values for each profile were all within 20 µmol kg^{-1}, the desired accuracy is <2 µmol kg^{-1} but was much higher due to issues with the stability of the coulometer cell, 3 µmol kg^{-1} as was observed here, based on the 2 surface replicates the accuracy was ~3 µmol kg^{-1}. The profile on the 20th seems to indicate declining DIC towards the surface; the remaining profiles seem to show a random spread.

The measured and TA/DIC derived CO_2 are plotted together in Figure 4.15. The values show a large spread, this is partially expected due to the propagation of errors in the calculation but as the TA and DIC were much more variable than expected this spread is almost double that. There is a trend towards lower CO_2 towards the surface seen in the derived CO_2 values on the 16th and 20th, neither the magnitude nor structure of these trends are seen in the measured profile. In all 5 cases where there is comparable measured and derived CO_2, the measured CO_2 is substantially lower than the derived values. The overestimation may be due to errors in the acid based chemistry found in the near coastal region of shelf seas due to riverine organic acids (Fassbender et al., 2017), similar overestimation using TA and DIC was also observed by Hartman et al. (2018) at the same time of year in the shelf sea.

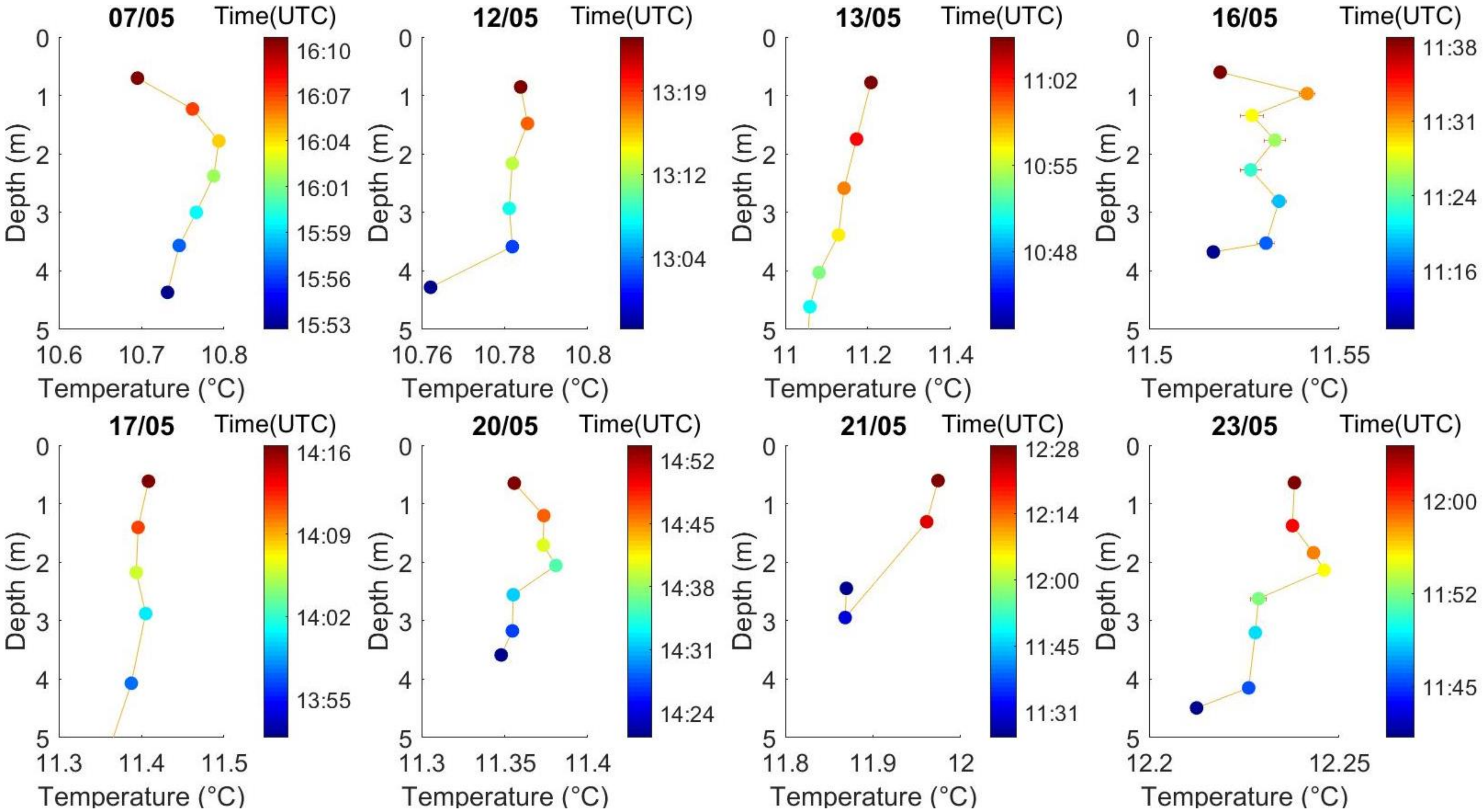

Figure 4.11 MAY15 Temperature profiles

8 temperature profiles collected in the Celtic Sea during May 2015. NSOP profiles of temperature were derived using the depth bins determined in chapter 2. Data points are coloured by sampling time. Vertical and horizontal error bars show two standard errors of the mean in each depth bin. The date of each profile is given above each subplot.

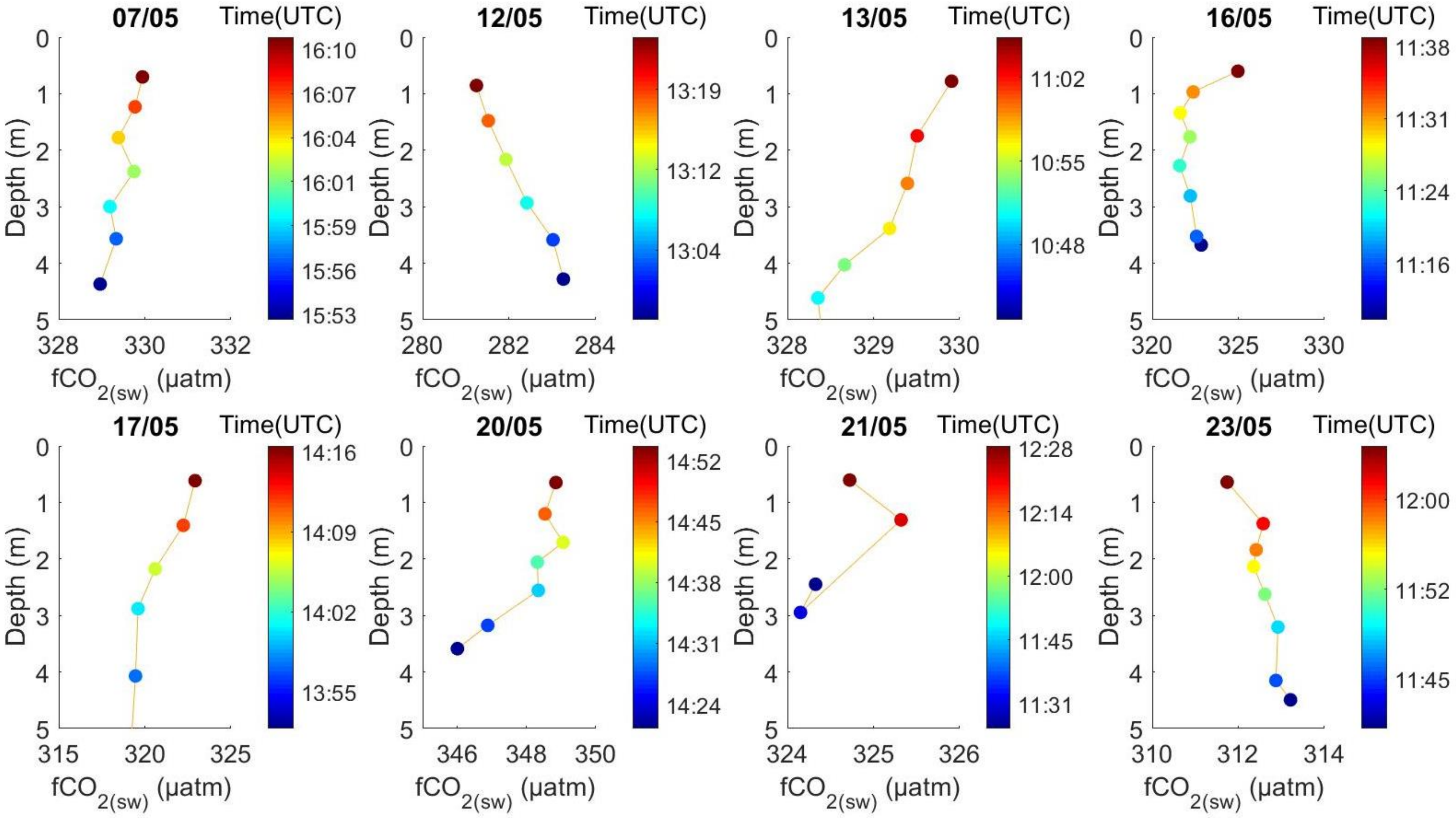

Figure 4.12 MAY15 CO_2 profiles

8 profiles collected in the Celtic Sea during May 2015. NSOP profiles of CO_2 were derived using the depth bins determined in chapter 2. Data points are coloured by sampling time. Vertical error bars show two standard errors of the mean in each depth bin. The horizontal errors are the propagated errors using the averaged bin variables to calculate fCO_2. The date of each profile is given above each subplot.

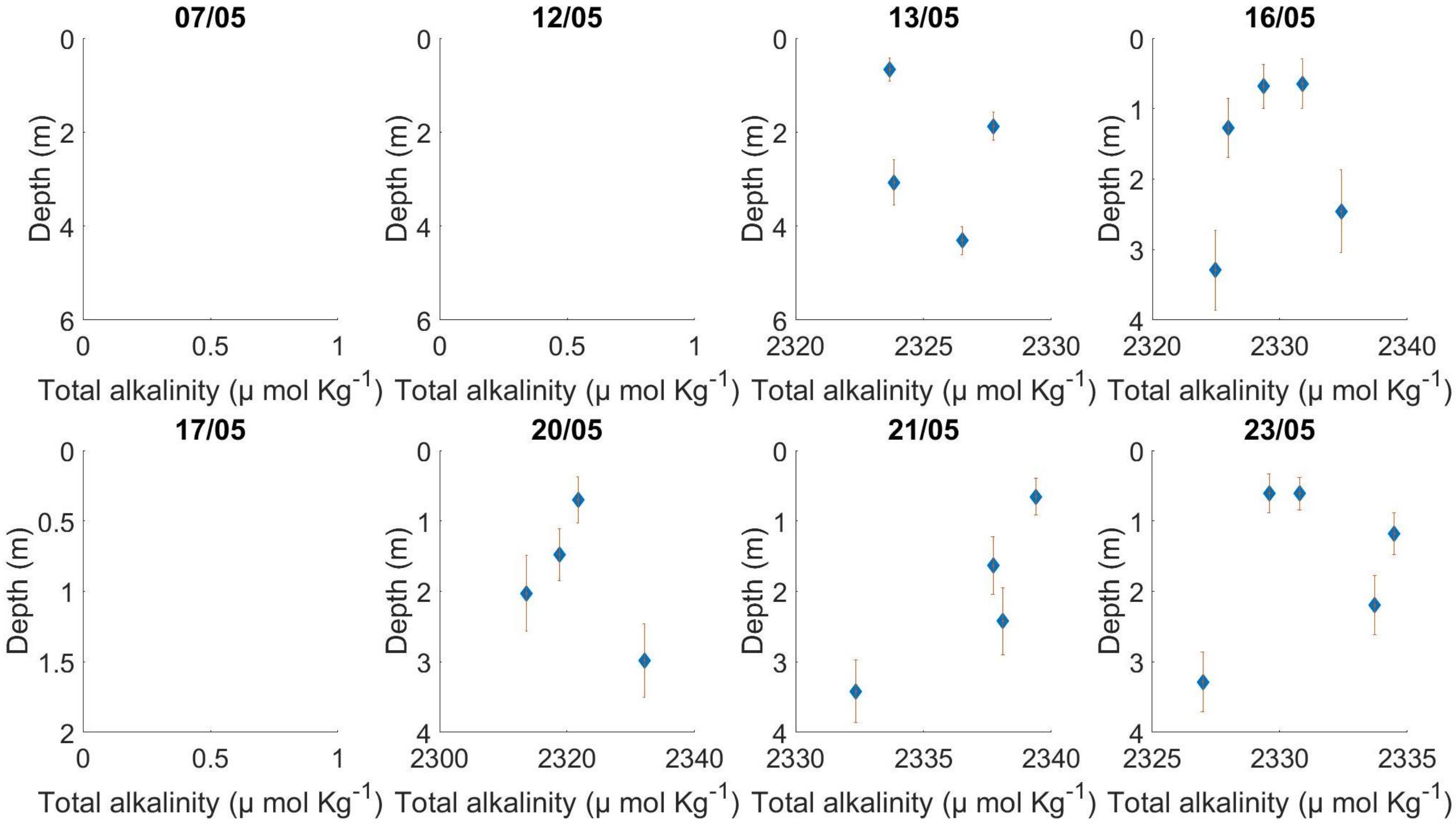

Figure 4.13 MAY 15 TA profiles

7 profiles of total alkalinity collected in the Celtic Sea during May 2015. Vertical error bars show two standard errors of the mean in each depth bin. The date of each profile is given above each subplot.

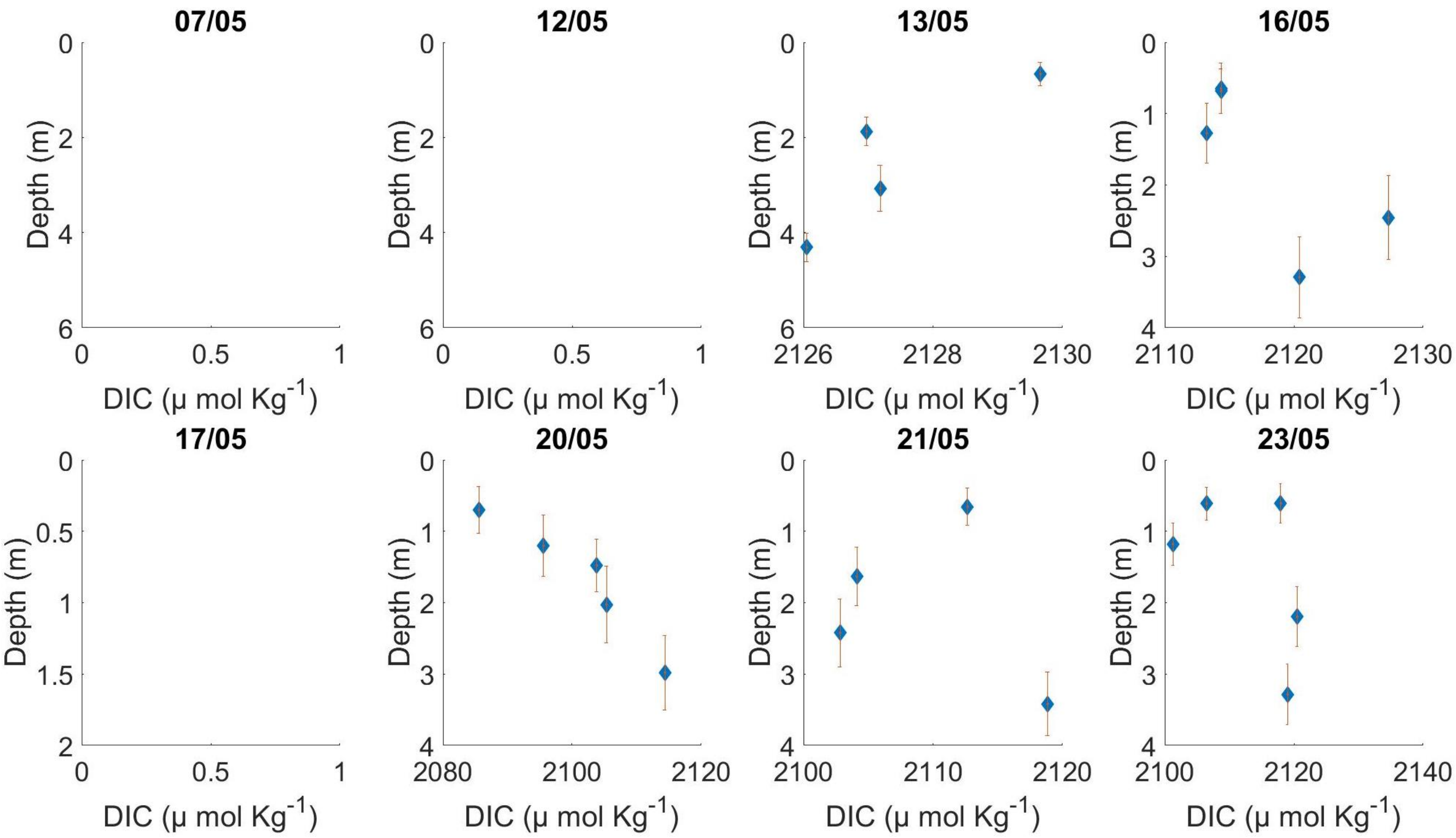

Figure 4.14 MAY 15 DIC profiles

7 profiles of DIC collected in the Celtic Sea during May 2015. Vertical error bars show two standard errors of the mean in each depth bin. The date of each profile is given above each subplot.

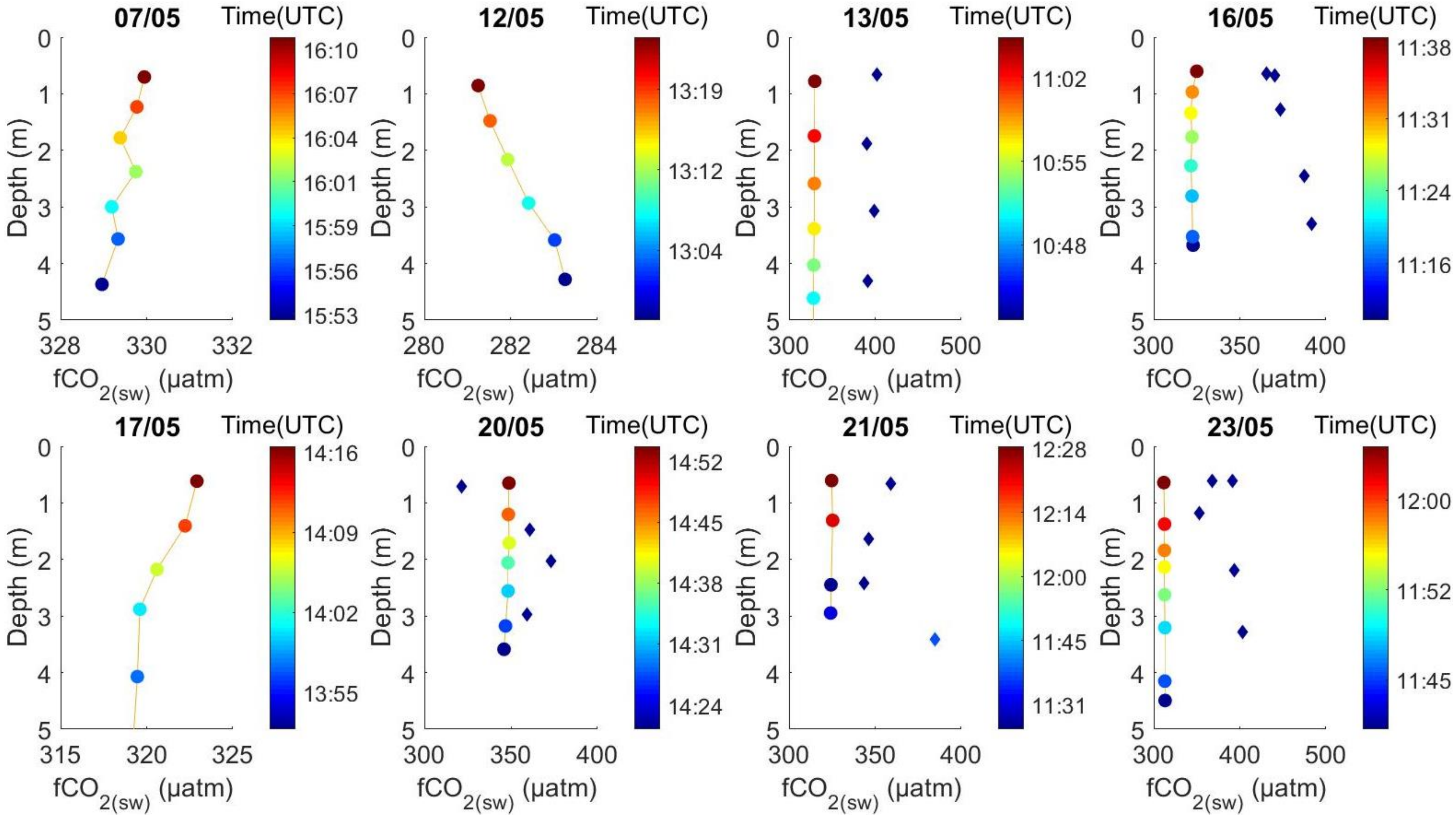

Figure 4.15 MAY 15 Measured and derived (TA/DIC) CO_2

8 CO_2profiles collected in the Celtic Sea during May 2015. NSOP profiles of CO_2 (circles) were derived using the depth bins determined in chapter 2. Vertical error bars show two standard errors of the mean in each depth bin. The horizontal errors are the propagated errors using the averaged bin variables to calculate fCO_2. The TA and DIC calculated fCO_2 are plotted as diamonds. Data points are coloured by sampling time. The date of each profile is given above each subplot.

4.10.6 MAY15 Profile interpretation

Three positive CO_2 gradients greater than 1.5µatm between 0.5 and 5 m were observed on the 20th,17th and 16th during MAY15.

On the deployment on the 20th the water column salinity varied by a small amount (0.01) during the deployment. There was some small temperature variability (0.04°C) between 0.5 and 5 m but overall there was only a small temperature gradient of 0.0079°C between 0.5 and 5m. Despite the absence of temperature gradients there was still a statistically significant CO_2 gradient between the measurements above and below 2.5m based on a two sampled t-test using data from each bin. The lower CO_2 in the bins below 2.5m corresponds to the largest change in the temperature profile at the same depth and the slight change in salinity recorded by the underway and at the same time and thus could reflect the ship transitioning through a different patch of water.

During the deployment on the 17th there was a strong positive CO_2 gradient of 3.8 µatm between 5m and 0.5m. There was a corresponding positive temperature gradient of 0.1 °C and a large salinity change in the water column of 0.04 as indicated by the salinity of the underway system. Temperature and CO_2 simultaneously increase in the top three bins located in the surface 2.5 m, the temperature changes are very slight and the changes in CO_2 below 3m are not significant based on a two sampled t-test using data from the bins. The greater temperature agreement below 3m suggests that the near surface warming does not extend below 3m here or alternatively as this profile was made early in the day solar irradiance had not peaked and the rest of the water column had not warmed yet.

During the profile on the 16th, only the CO_2 in the surface bin is significantly different from the rest of the profile based on a two sampled t-test using data from each bin, a large departure in temperature is not seen in the same bin which makes the cause of the change difficult to assess, it could be a possible outlier or reflect a water mass change as there is a coincident salinity change in the underway salinity at the same time.

The profile measured on the 12th shows a slight negative CO_2 gradient of 2 ppm between 5m and 0.5m, there was no change in salinity recorded by the underway system and there was also no accompanying temperature gradient. The lack of stratification is not surprising as despite the high irradiance 900 Wm^2 there were still moderate winds of $10ms^{-1}$. This is the only profile from this cruise with a negative CO_2 gradient <-1.5 µatm between 5m and 0.5m. The CO_2 measured by the underway system is very stable which suggests that this may reflect an issue with the instrumentation, possibly as the result of leak as the CO_2 slowly decreases over time. As the CO_2 from the underway is stable and for NPP changes to induce a gradient there needs to be stratification it does not seem likely this was caused by phytoplankton production.

The profiles on the 7th, 13th, 21st and 23rd have very small gradients in CO_2 (<1.5µatm). The salinity from the underway system was very stable over the course of all four of these deployments (<0.001). These 4 profiles show variable temperature in the near surface. The profile on the 7th showed temperature variability of 0.12°C in the water column but no net temperature gradient towards the surface, the changes during this profile may reflect cooling in the near surface due to the breakdown of stratification in the late afternoon. The temperature gradient between 5m and 0.5m on the 13th was the largest measured during this cruise at 0.21°C, this was likely able to be established under the moderate irradiance

(850Wm^2) and low wind speeds (< 5m s^{-1}) during and in the morning of the deployment. The shape of both the temperature and CO_2 profiles is very similar with a similar change in both at the same depths. The temperature gradient between 5m and 0.5m was 0.13°C on the 21st but as there was a pause in the deployment this temperature change may reflect warming of the water column during this time. There is a much smaller temperature gradient between 5m and 0.5m of 0.04°C on the 23rd. The absence of CO_2 gradients in all 4 of these profiles is probably due to the lack of strong and consistent stratification caused by moderate to weak solar irradiance on the days of the deployment.

4.11 JULY15

4.11.1 JULY15 Cruise meteorology

The wind speed during JULY15 (Figure 4.16) was 8.67±3.97 m s^{-1} (with a range of 0 –24.36 m s^{-1}); this is classified as moderate on the Beaufort wind force scale. The large variability from the mean is due to the persistently high wind speeds (>15 m s^{-1}) encountered between July 26th and 28th and the intermittently low wind (<5 m s^{-1}) speeds observed on July 15th, 18th, 20th, 22nd, 25th and between July 30th and August 1st. All 8 deployments from this cruise were made under wind speeds of 5–10 m s^{-1}, except for the deployment on the 30th which was made during wind speeds of <5 m s^{-1}. The wind speed during each deployment remained fairly constant.

The solar irradiance during JULY15 (Figure 4.16) was 219.7599 ±284.6526 Wm^{-2} with a range of 0 –1213.6Wm^{-2}. The magnitude of the solar irradiance was not consistent throughout the cruise and varied between days with some days receiving a maximum of 1200 Wm^{-2} whereas on the 23rd the maximum irradiance was 240 Wm^{-2}. The solar irradiance received was similar in the morning and afternoon most days (e.g. July 17th and 28th) but on several other days there was much higher irradiance in the morning (25th and 26th) or in the afternoon (12th and 13th). Despite irregular irradiances once integrated per day and averaged the total energy received per day of the cruise by solar irradiance barely varies (0.246 ± 0.04 kWm^{-2}d^{-1}).

The significant wave height measured during JULY15 was 2.1481 ± 1.0945 m with a range of 0.0411– 6.3000 m, it closely lags behind the trends in the wind speed. The highest wind speeds observed during the 24th – 28th are also the periods where significant wave height is highest. Similarly the lowest wind speeds on the 31st correspond to the lowest significant wave heights at the detection limit of the instrument. 7 of the 9 NSOP deployments occurred when the significant wave heights was between 1–2m, the remaining two deployments on the 13th and 21st were made at significant wave heights of 3.2 and 3.5m respectively.

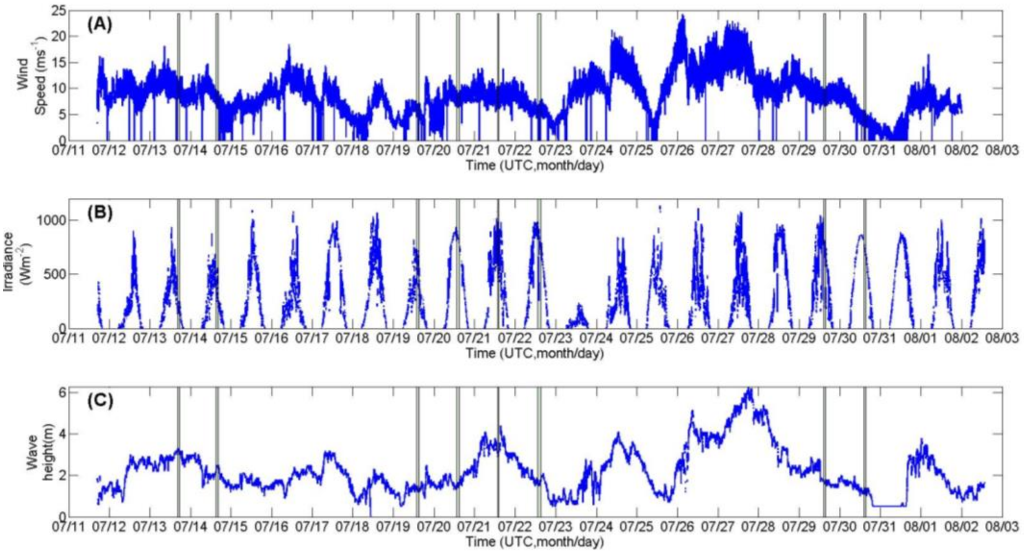

Figure 4.16 JULY15 Cruise meteorology

Timeseries of ship underway meteorlogical variables (wind Speed(a), solar irradiance (b) and Significant wave height (c)) during JULY15. The time during which the 8 NSOP deployments for this cruise were made are indicated by solid transparent lines with widths equivalent to the lengths of the deployments.

4.11.2 JULY15 Salinity profiles

Eight salinity profiles were measured during the JULY15 cruise (Figure 4.17). None of the measured profiles indicated strong salinity gradients (>0.02 between 5m and 0.5m). The four profiles measured on July 13th, 14th, 29th and 30th at the CCS site all show minute salinity variations of <0.004. The salinity remains stable at the CCS site for the month, only varying by 0.03 between the 13th and 30th of July. During the deployments at the shelf edge on July 19th, 20th and 22nd the waters were 0.15 more saline than found at the CCS site, the singular profile off the shelf on July 21st had the highest average salinity of all the profiles from this cruise (35.63). The shelf edge profiles on July 19th and 20th are the most variable and both indicate a negative gradient of ~0.02 between 5m and 0.5m. There was minimal variability in the salinity profiles made on July 21st and 22nd (< 0.006).

4.11.3 JULY15 Temperature profiles

Eight temperature profiles were measured during the JULY15 cruise (Figure 4.18). Of the four profiles made at the CCS sites, three of the profiles measured on July 13th, 14th and 29th indicate a minimal temperature change (<0.02 °C between 5m and 0.5m), the fourth profile made on July 30th revealed a gradient of 0.14 °C between 5m and 0.5m. The average temperature of these four indicates that the SST at the CCS was increasing slowly over the month of July. Two profiles made at the shelf edge and break on July 20th and 21st reveal only marginal temperature changes of <0.02 °C. In the profile on July 19th made at the shelf break there was large 0.48 °C temperature variability that reflects the temperature dropping from 16.49 °C to 16.01 °C from 5m to 2m and then back to 16.41 °C at 0.5m, overall there was a much smaller gradient of 0.0850°C between 5m and 0.5m. There was a positive gradient of 0.23 °C between 5m and 0.5m on July 22nd at the shelf edge.

4.11.4 JULY15 CO_2 profiles

Eight CO_2 profiles were measured during the JULY15 cruise (Figure 4.19). Six of the profiles had positive gradients from 5 m to 0.5 m. the profiles on the 19th and 20th had negative gradients of -0.39 and -0.29 from 5m to 0.5m. Of all eight profiles, only two profiles had statistically significant CO_2 gradients based on a two sampled t-test using data from the 5m to 0.5m bins. The two statistically significant profiles were made on July 22nd and 29th and had positive gradients of 5.2 and 2 µatm respectively between 5m and 0.5m. The remaining six profiles (13th,14th,19th, 20th, 21st and 30th) whilst all indicating small gradients (<1.5 µatm) between 5m and 0.5m and were not statistically significant.

4.11.5 JULY15 TA and DIC profiles

7 profiles of TA and DIC were measured during the JULY15 cruise (Figure 4.20 & Figure 4.21). Whilst six bottles were sampled for each profile with two replicates at the surface, a number of samples were lost due to instrument issues, this meant discarding the profile from the 13th of July and then removing ~10 outliers. The surface replicates are not true replicates as they were not in bottle replicates and they were collected over consecutive 2 minute periods each. In most cases where there were surface replicates, they do not agree any better than the values from the other sample

The TA values for each profile were all within 10 µmol kg^{-1}, the desired accuracy is <1 µmol kg^{-1} but is more realistically 1–2 µmol kg^{-1}. Based on the 3 surface replicates the accuracy was ~2 µmol kg^{-1}. Given this accuracy it would be expected that 95% of all the values would fall within a range of 4 standard deviations, so the spread is larger than this. There is no discernible structure in the TA profiles except for the 29th where it appears TA declines towards the surface.

The DIC values for each profile were all within 12 µmol kg^{-1}, the desired accuracy is <2 µmol kg^{-1} but was much higher due to issues with the stability of the coulometer cell, 3 µmol kg^{-1} as was observed here, based on the 3 surface replicates the accuracy was ~3 µmol kg^{-1}. The profile on the 14th seems to indicate declining DIC towards the surface whereas the profiles on the 21st and 30th point to an increase in DIC towards the surface, the remaining profiles seem to show a random spread.

The measured and TA/DIC derived CO_2 are plotted together (Figure 4.22). The values show a large spread, this is partially expected due to the propagation of errors in the calculation but as the TA and DIC were much more variable than expected this spread is almost double what is expected. There are no trends or structure in any of the derived CO_2 profiles, meaning that the noise in the measurements is masking it or there is no or a small trend. In contrast to the samples collected in MAY15, the derived CO_2 is substantially lower than the measured CO_2 in all but the profile on the 19th. The underestimation may also be explained by errors in the acid based chemistry found in Shelf Sea; as there is consistent overestimation in May and underestimation in July, this may relate to seasonal changes related to biological production.

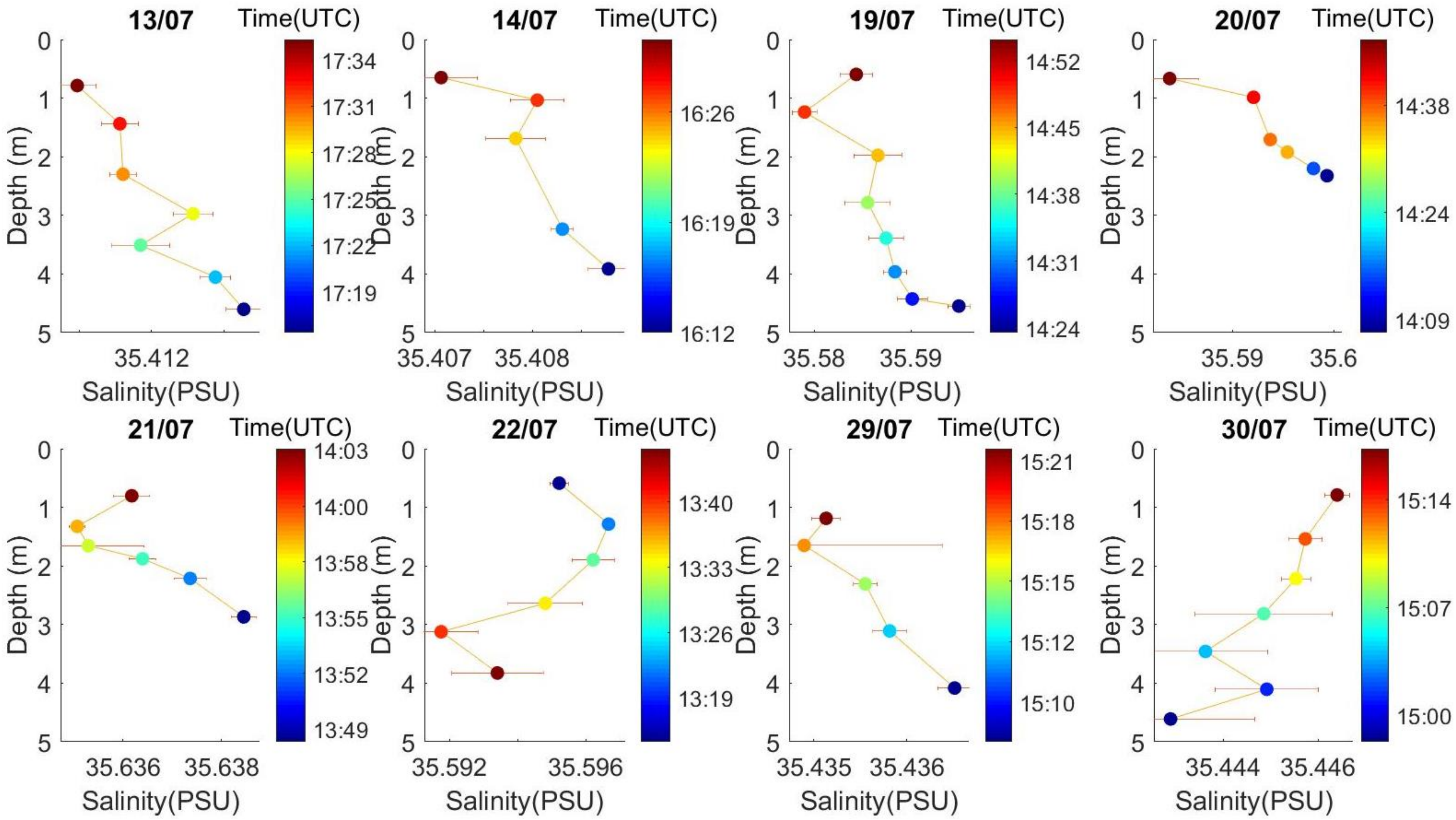

Figure 4.17 JULY15 Salinity Profiles

8 salinity profiles collected in the Celtic Sea during July 2015. NSOP profiles of salinity were derived using the depth bins determined in chapter 2. Data points are coloured by sampling time. Vertical and horizontal error bars show two standard errors of the mean in each depth bin. The date of each profile is given above each subplot.

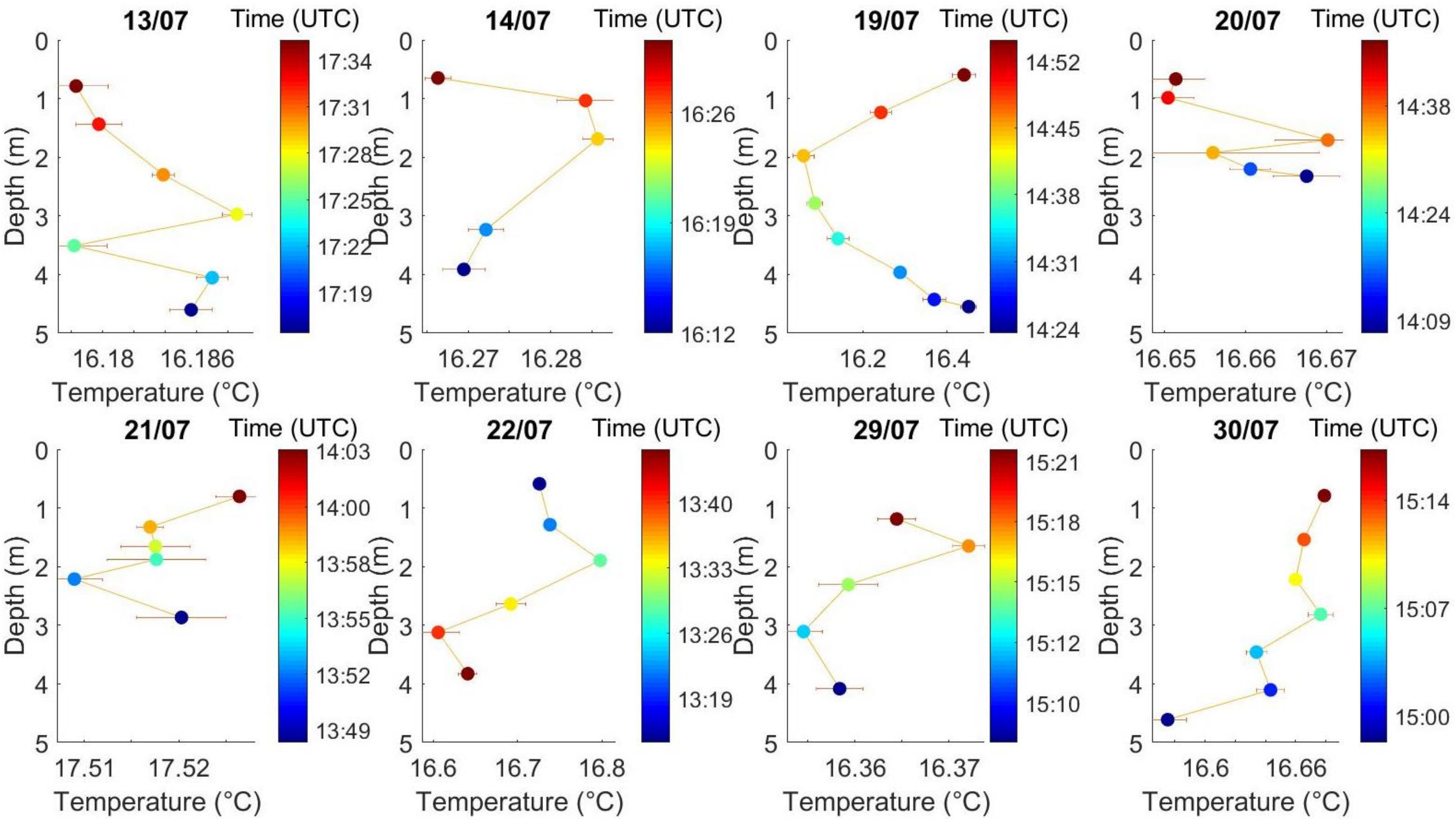

Figure 4.18 JULY15 Temperature Profiles

8 temperature profiles collected in the Celtic Sea during July 2015. NSOP profiles of temperature were derived using the depth bins determined in chapter 2. Data points are coloured by sampling time. Vertical and horizontal error bars show two standard errors of the mean in each depth bin. The date of each profile is given above each subplot.

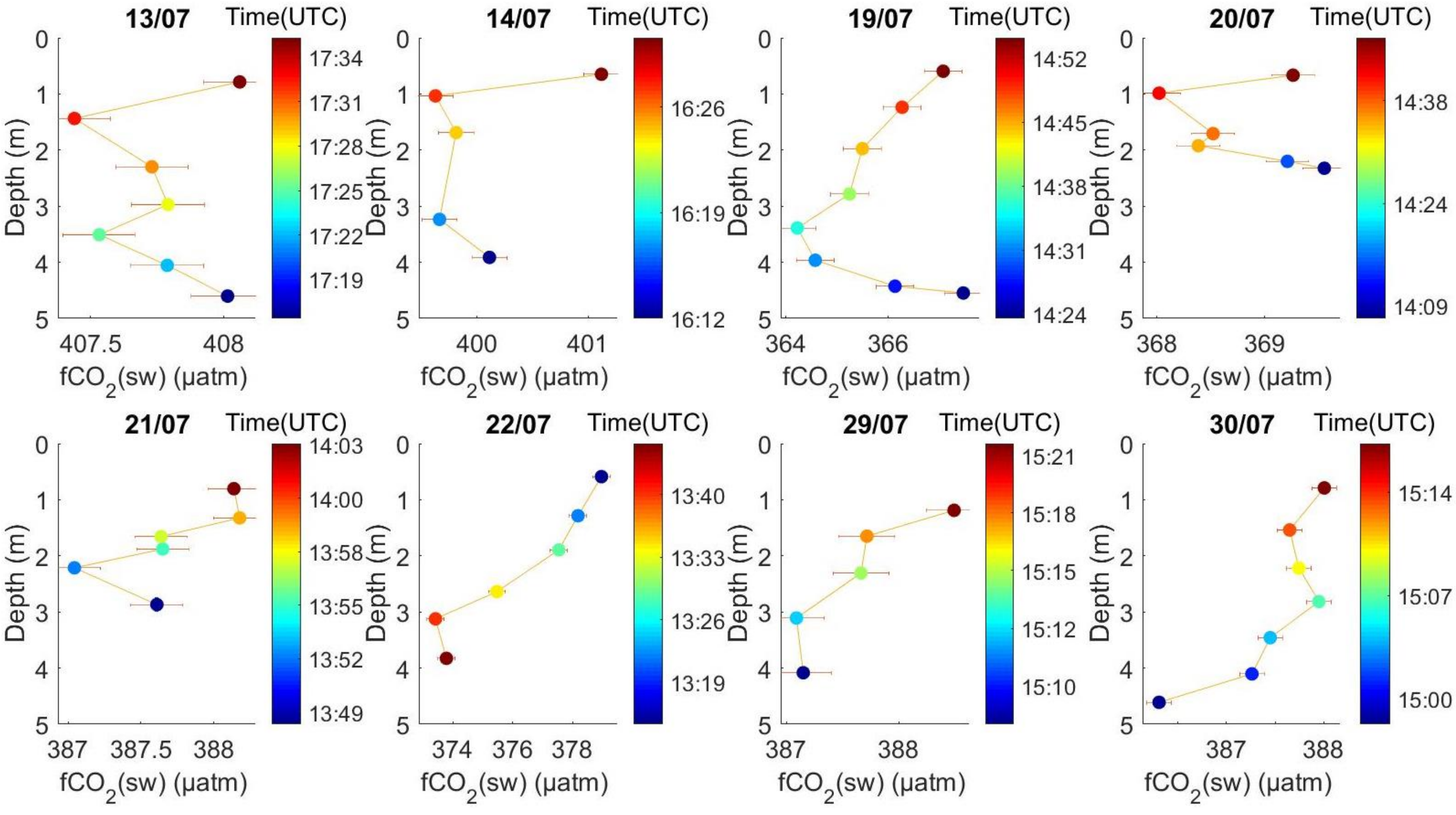

Figure 4.19 JULY15 CO_2 Profiles

8 profiles collected in the Celtic Sea during July 2015. NSOP profiles of CO_2 were derived using the depth bins determined in chapter 2. Data points are coloured by sampling time. Vertical error bars show two standard errors of the mean in each depth bin. The horizontal errors are the propagated errors using the averaged bin variables to calculate fCO_2. The date of each profile is given above each subplot.

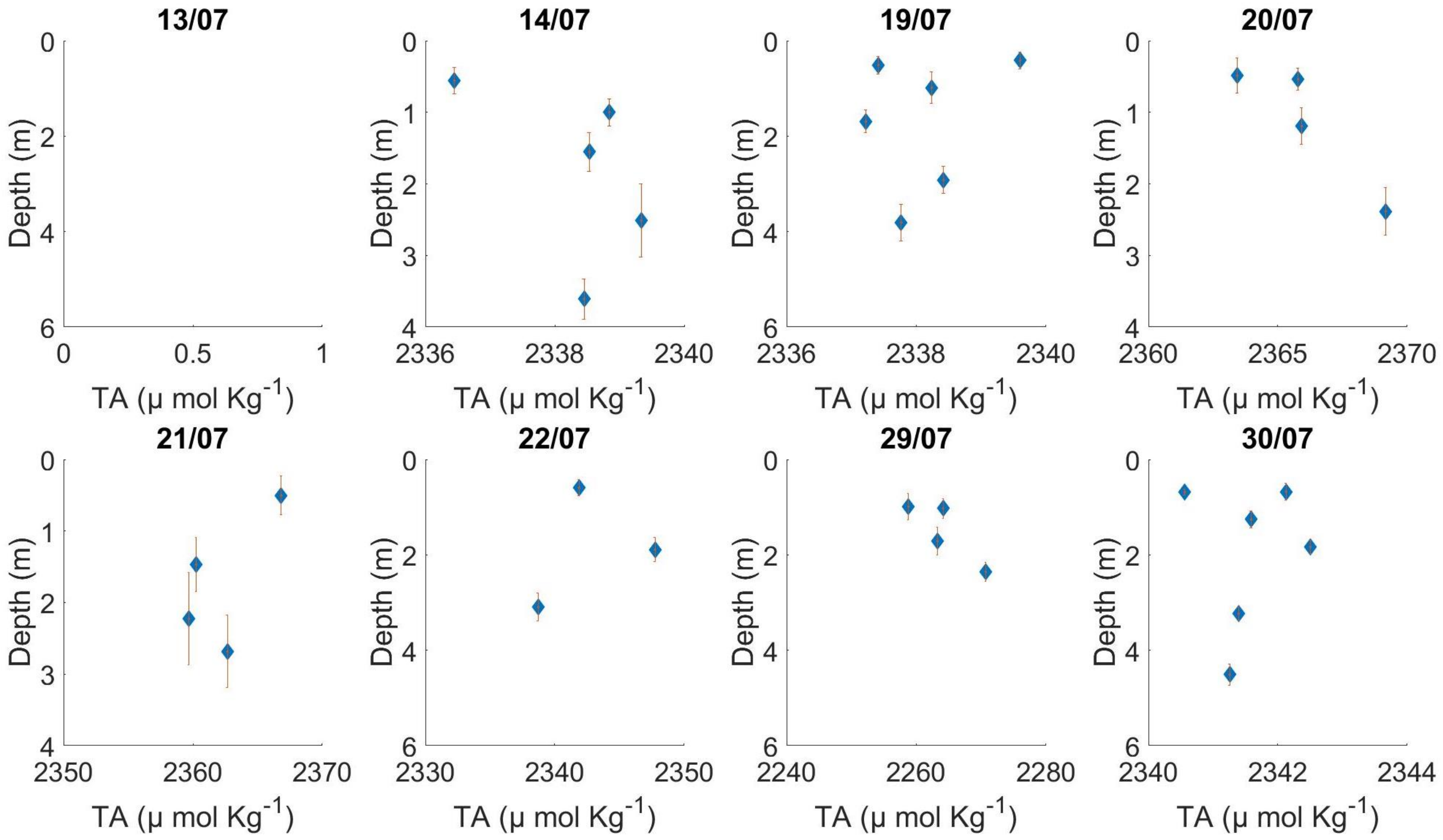

Figure 4.20 JULY15 TA Profiles

7 profiles of total alkalinity collected in the Celtic Sea during July 2015. Vertical error bars show two standard errors of the mean in each depth bin. The date of each profile is given above each subplot. Data points are coloured on the same sampling time at the profiles above.

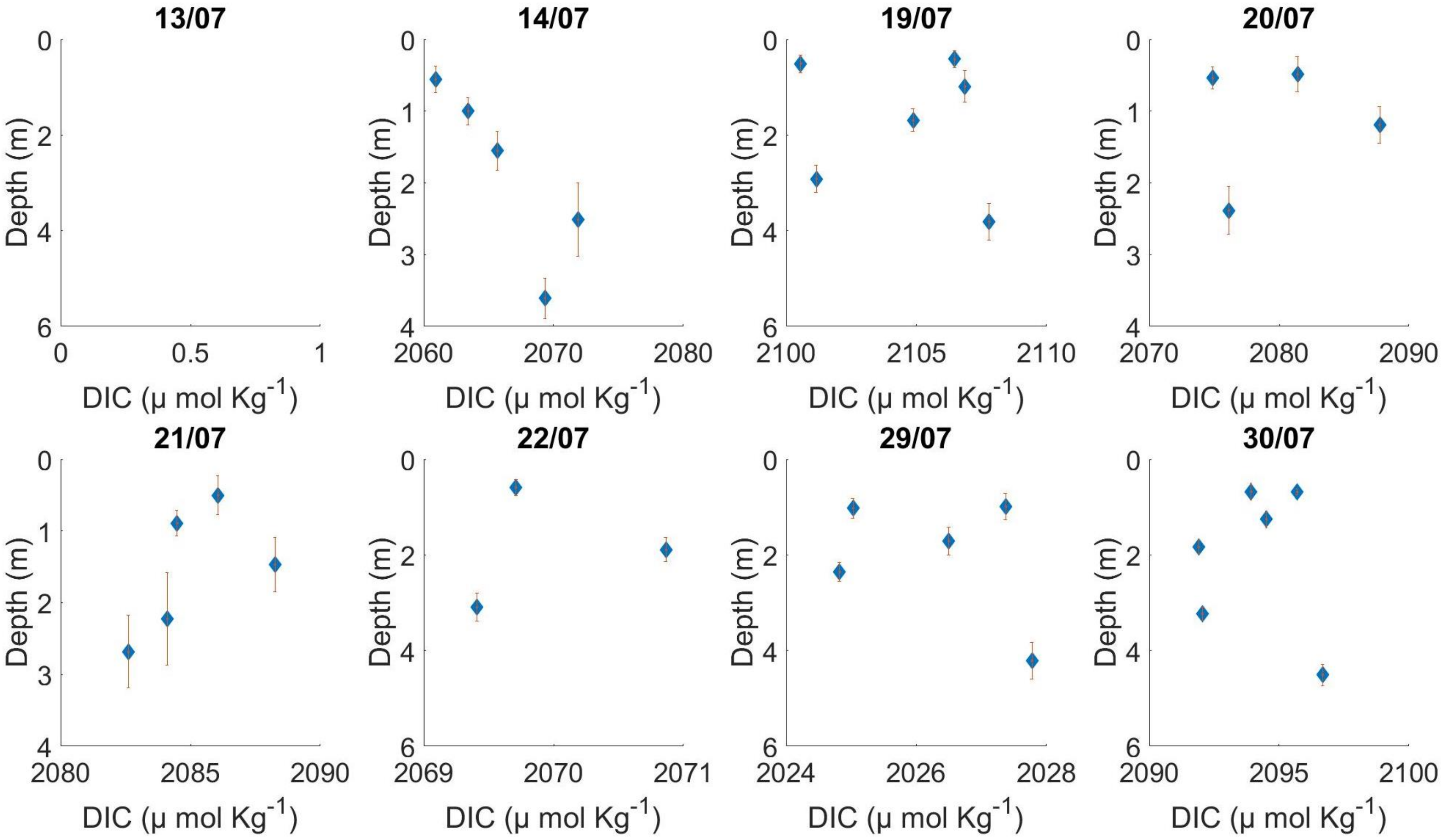

Figure 4.21 JULY15 DIC Profiles

7 profiles of dissolved inorganic carbon collected in the Celtic Sea during July 2015. Vertical error bars show two standard errors of the mean in each depth bin. The date of each profile is given above each subplot. Data points are coloured on the same sampling time at the profiles above.

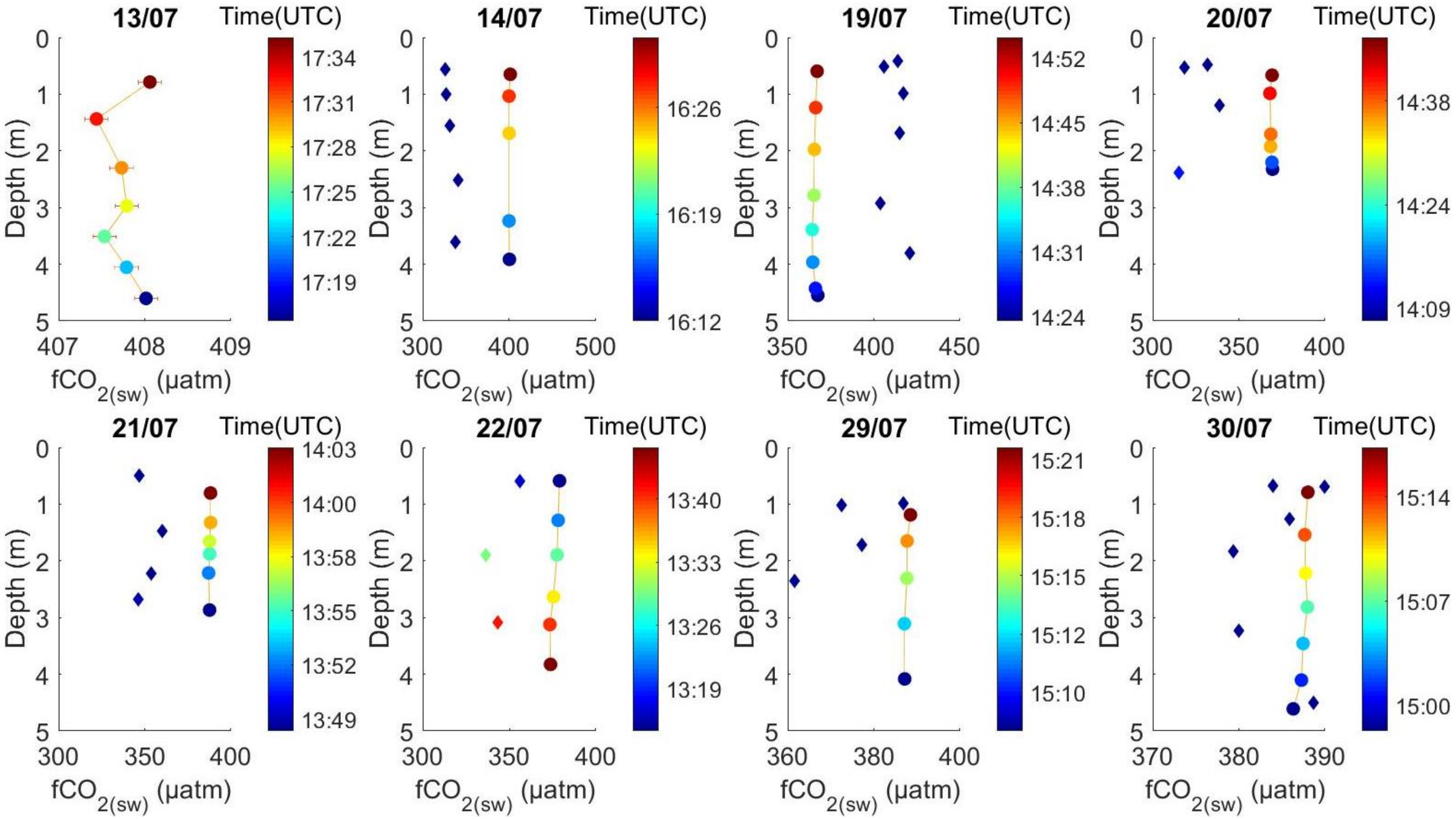

Figure 4.22 JULY 15 Measured and derived (TA/DIC) CO_2

8 profiles collected in the Celtic Sea during JULY 2015. NSOP profiles of CO_2 (circles) were derived using the depth bins determined in chapter 2. Vertical error bars show two standard errors of the mean in each depth bin. The horizontal errors are the propagated errors using the averaged bin variables to calculate fCO_2. The TA and DIC calculated fCO_2 are plotted as diamonds. Data points are coloured by sampling time. The date of each profile is given above each subplot.

4.11.6 JULY15 profile interpretation

A large 5.2 µatm CO_2 gradient was measured between 5m and 0.5m on July 22nd alongside concurrent positive temperature and salinity gradients, high irradiance and low wind speed. The low wind speed and high irradiance conditions would facilitate temperature gradients as mixing is suppressed, this could have allowed the formation of a near surface gradient in CO_2. There was neither a DIC nor TA gradient, this is surprising given the strong gradient in CO_2 and may point to sampling issues related to collecting discrete samples from NSOP. For the magnitude of this CO_2 gradient there should be a DIC gradient of ~4 µmol kg^{-1}.

The positive 1.7µatm gradient between 5m and 0.5m on the 30th was concurrent with a mild temperature gradient in the near surface of 0.14 °C. The establishment of this near surface gradient was possible as there were low wind speeds and high irradiance during the deployment. The bins in the top 4 m of the profile were warmer than the bottom bin at 4.5 m suggesting that the upper 4 m were stratified and cut off from the water below, the same trend is seen in the CO_2. This suggests that the near surface stratification creates two distinct layers with different pCO_2 . This is the only one profile where the calculated CO_2 using the TA and DIC even broadly agrees well with the measured CO_2, this may be because this deployment was at the CCS site aka the open shelf where there are few organic compounds to confound the acid base chemistry.

The profiles (13th, 14th,19th, 20th, 21st and 29th) where the CO_2 gradient was small (<1.5 µatm between 5m and 0.5m) had predominantly no salinity and temperature gradients, the exceptions were the 19th where both the salinity and temperature change concurrently, the 20th where salinity changes by 0.02 and the 30th where the temperature gradient is 0.14°C between 5m and 0.5m. These profiles were with the exception of the 29th all made when the wind was high and the irradiance was weak meaning there was no stratification and thus potential to facilitate the formation of CO_2 gradients. The DIC profiles for the 14th, 21st and 30th all point to changes in DIC of around 5 µ mol kg^{-1}, this would stimulate gradient in CO_2 of around 10µatm between 5m and 0.5m which is much larger than observed. It could be that there perceived large DIC gradients are due to the length of time for which the samples were left before poisoning.

The temperature changes observed on the 19th are large and are unlikely due to surface processes as changes in the direction and magnitude of heating required do not occur on the timescale of the profile. The reduced surface salinity on the 19th and 20th could also be driven by dilution by precipitation but there is no record of rain in the deployment notes. The remaining explanation for these temperature and salinity profiles is that they were caused by the movement of different water masses with similar pCO_2 . This is supported by the salinity and temperature measurements recorded by the ships underway system which show identical trends to those seen in the profiles on the 19th. The profiles on the 19th and 20th were both made off the shelf break, this is known to be a region of significant mixing (Pingree et al., 1981) and may explain the water mass changes observed here.

The 1.35 µatm gradient recorded between 5m and 0.5m on the 29th was recorded when there was a small salinity (-0.0014) and very small temperature gradient (0.02°C) between 0.5 and 5 m. The wind speed was low as was the irradiance, meaning the conditions were conducive for stratification but it appears to have been very mild in this case. If this CO_2 gradient formed when there was so little stratification present then CO_2 gradients could be ubiquitous throughout the ocean. This CO_2 gradient could be caused by changes throughout the water column but as there were no underway CO_2 measurements for the deployment it is impossible to know. The earlier NSOP down cast taken in the 30 minutes before the profile supports the presence of this CO_2 gradient. The DIC samples for this profile do not show any trend but there is a decline in TA towards the surface, a decline in the TA of 5 µmol kg^{-1} as indicates in the profile would increase the CO_2 by ~10 µatm which was about 5 times greater than what was actually observed.

4.12 Explaining TA and DIC noise

As there is a large spread and no structure whatsoever in both the TA and DIC and the changes are much larger than expected from the CO_2 profiles, it is likely that there was a sampling or analysis issue.

All the samples from each profile were analysed at the same time and on the same machine but the profiles were analysed as separate batches at two different times (September 2015 and April 2017). As the spread is seen in samples run for both batches it would have to mean that both instruments were not functioning optimally both of these times, this seems especially unlikely as the instruments were successfully used on two oceanographic cruises in–between when the samples were run. In addition, during sampling replicate CRMs and test seawater samples gave convincing results when samples were run, suggesting the instruments were performing as desired with high precision, accuracy and low drift. Based on this it can be concluded that the analysis was completed properly and points to an issue with the sampling procedure.

The samples were poisoned and stored following the SOP and analysed within the target window of 2 years, therefore it is unlikely that there was an issue with preservation. The remaining likely explanation is that the samples were modified in the time between sampling and poisoning. The water could have been modified along the tubing but there is no indication of this in the CO_2 so it seems very unlikely. Due to the low flowrate of ~500ml min^{-1} for the T'd flow the 250ml samples were collected over 2 minutes allowing for 2 overfills, it is possible that the water reaching the sample was not the same over the two minutes as this is a long integration time. Niskin bottles are given a long time to mix and the water is very homogeneous this would not be the case for samples collected using NSOP over such a long period of time. The peristaltic pump minimises cavitation but it is possible that it introduced bubbles into the flow or the disturbance causing a biological response that altered the chemistry which resulted in the large variability in DIC and TA. The samples for each profile were all collected during a single downcast to 5m which took 30–40 minutes, this sort of time frame is not dissimilar to the time taken to sample a 24 bottle rosette where such issues are not considered problematic. Due to time pressures and the need to monitor the liqui–cel system and alter the sampling depth of NSOP, the collected TA/DIC samples were covered from sunlight and left inside until after the deployment when they could be poisoned, this was often up to an hour later. This long delay before the samples were poisoned may have given time for the biology to change the TA and DIC within the sample. Whilst the wait time for poisoning was known to be a possible source of error it was not thought it would be as impactful as observed here, it was likely worse as these samples were collected on the already productive shelf during periods of high productivity, this likely had a much larger effect then if the samples were taken in the open ocean. With more personnel the late poisoning can be avoided in the future.

4.13 Summary

29 vertical profiles of CO_2, salinity and temperature in the upper 5m were collected during 29 NSOP deployments in UK shelf seas between August 2014 and July 2015. The profiles were measured under a range of wind speeds and irradiances around midday and late afternoon.

Only the profile from the 6th during AUG14 had a large temperature gradient, this coincided with the largest CO_2 gradient (6.3µatm between 5m and 0.5m). There was also a large 2.8µatm gradient between 5m and 0.5m on the 17th in the absence of any temperature or salinity gradients. The other six profiles had small gradients in CO_2 (<±1.5µatm between 5m and 0.5m) and generally coincided with small salinity and temperature gradients. There was a small negative gradient on the 11th which might be attributable to rain and there was a stronger negative gradient on the 7th of 1.4µatm between 5m and 0.5m which coincided with a temperature gradient of 0.08°C between 5m and 0.5m.

There were no large salinity gradients between 5m and 0.5m measured on OCT14 <0.012. The temperature gradients between 5m and 0.5m were also small all less than 0.016°C bar one profile which was 0.04°C. The profile on the 27th was negative and the only large gradient >±1.5 µatm between 5m and 0.5m.

During MAY15, there were a number of large temperature gradients four of the eight profiles had temperature gradients >0.1°C between 5m and 0.5m.There was both a large temperature and CO_2 on the profiles from the 17th May. CO_2 gradients were measured on the 20th and 16th without temperature and salinity gradients. All the other CO_2 gradients were small (<±1.5 µatm between 5m and 0.5m) and generally did not have temperature or salinity gradients.

During JULY15 there were two profiles with large CO_2 gradients between 5m and 0.5m, the 22nd 5.2µatm and the 20th which had a 1.7µatm gradient, these both had temperature gradients between 5m and 0.5m of 0.23° and 0.12°C respectively. The other six profiles had small CO_2 gradients (<±1.5 µatm between 5m and 0.5m) these coincided with small temperature and salinity gradients.

TA/DIC measurements from NSOP were less accurate than desired, doubt that this is due to measurement accuracy and technique and is a result of a delay is preservation which could be avoided in the future. In addition to being less accurate then desired the average values were unable to replicate the measured pCO_2 of both underway systems, this has been observed by others and is not unique to these measurements.

5 A seasonal study of horizontal and vertical near surface variability in surface seawater CO_2 at the Western Channel Observatory

5.1 Introduction

Research cruises allow intense data collection in a short space of time but it is difficult to use them to detect seasonal changes. Whilst one of the aims of the SSB programme was to look at seasonality, there were monthly gaps in the yearly time series between cruises and not all the stations were visited regularly.

To observe seasonality, frequent sampling in the same location was required. A time series of weekly sampling at the Western Channel Observatory station was conducted in an attempt to observe seasonality in surface CO_2.

The seasonal study involved 16 excursions between April and September where horizontal transects were carried out to identify horizontal changes in surface ocean CO_2 (chapter 6) and near surface profiling was conducted to identify near surface ocean CO_2 gradients (chapter 7).

This chapter briefly introduces the hydrodynamics and biogeochemistry of the site and surrounding area to provide context for these measurements.

5.2 The Western Channel Observatory as the seasonal study location

The Western Channel Observatory has been monitored for over 100 years making it one of the longest and most heavily studied regions of ocean in the world (Southward et al., 2004). The Western Channel Observatory encompasses the oceanographic sampling sites at stations L4 (50.25°N and 4.217°W) and E1 (50.035°N, 4.368°W) and the Penlee point atmospheric observatory (50.322°N, 4.193°W). Station L4 is a coastal site 8.19 km from Penlee point. Station E1 is an open ocean site 34.28 km away from the observatory (Figure 5.1).

The extensive historical time series data, the ongoing weekly and bi–weekly sampling at stations L4 and E1 respectively and the continuous measurements made by instruments on the moorings (Smyth et al., 2010a) and at Penlee Point (Yang et al., 2015) make the Western Channel Observatory a logical location for a seasonal study.

The RV Plymouth Quest is operated by the Plymouth Marine Laboratory and conducts the majority of the local oceanographic work including the sampling at stations L4 and E1. Weekly sampling at L4 and bi–weekly sampling at E1 includes one deployment of the CTD rosette to the sea floor and niskin sampling at up to six depths. The core measurements are

- phytoplankton and zooplankton speciation and abundance,
- Concentrations of nitrate, nitrite, phosphate, silicate and ammonium
- pigments, total suspended material, coloured dissolved organic material, particulate absorption
- total and particulate organic carbon and total and particulate organic nitrogen
- chlorophyll
- From the CTD sensor package– temperature, salinity, visible radiance and irradiance, attenuation and absorption, volume scatter, backscatter and fluorescence.

The autonomous buoys at L4 and E1 measure core meteorological variables such as wind speed and direction, pressure, photosynthetically active radiation (PAR) and air pressure. The buoys also measure in water variables at a depth of 1m, including seawater temperature, salinity, oxygen, chlorophyll, turbidity. Significant wave height and wave duration are also measured on the E1 buoy. During the period of the seasonal study, the E1 buoy was undergoing planned maintenance on land and was not recording data.

It takes approximately one hour to reach station L4 and three hours to reach station E1 from Sutton Harbour (where the RV Plymouth Quest is moored). These are considerable transits times, especially to reach station E1. Tidal restrictions in Sutton harbour often meant being kept in the lock at low tide which means a delay in reaching the stations. In the context of air–sea gas exchange and open ocean fluxes it would have made sense for station E1 to be chosen as the primary seasonal study site as it is more likely to be representative of the open ocean than station L4 due to the proximity of L4 to the coast.

Station L4 was chosen over station E1 as the main site for the seasonal study because the autonomous buoy was operational for the entirety of the study, there is more frequent pelagic sampling at the site and considerably less time was taken transiting to station which enabled longer periods of NSOP sampling.

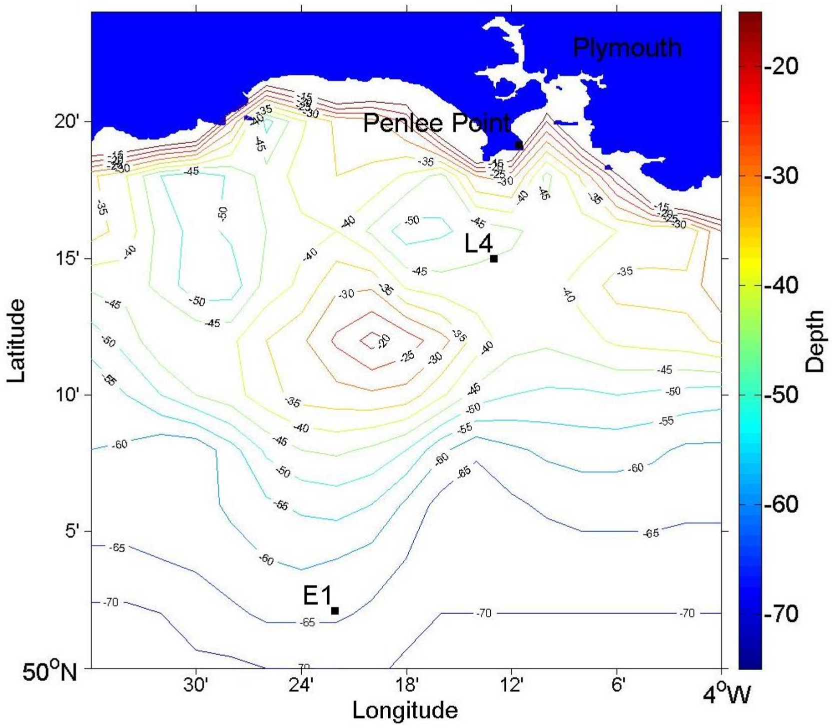

Figure 5.1 Western Channel Observatory Sites

Map of the Western Channel Observatory sites. Land to the north is filled in blue and depth contours in increments of 5m are shown for 15 to 70m. The city of Plymouth as well as the L4, E1 and Penlee Point sites are also indicated on the map by square black markers and labels.

5.3 Local hydrography

One of the main features in the region at all states of the tide is the coastal current which contains buoyant freshwater from the river Tamar outflow. The freshwater travels along the West coast of the Sound past Penlee Point where the coriolis force causes it to veer to the right, past Rame Head Peninsula and towards Whitsand Bay (Uncles et al., 2015).

The surface circulation patterns behind the Plymouth breakwater in the Plymouth Sound and beyond the breakwater towards the Penlee Point observatory and Rame Head Peninsula are determined by the state of the tide (Siddorn et al., 2003). Figure 5.2 shows the changes in the surface circulation are shown every three hours for an average tidal cycle at the Western Channel Observatory.

The tidal currents move the water masses that are close to land leading to surface salinity contours shifting by several km over the tidal cycle (Siddorn et al., 2003). Frontal features are strong enough to be clearly identifiable in photographs and aerial imagery (Uncles and Torres, 2013). Current speeds in the sound are fast (0.2 ms^{-1}) (Uncles et al., 2015). Modelled tidal ellipses and those from admiralty charts indicate that water in the sound, breakwater and at Penlee Point move distances of 5 , 10 and 3 km respectively during a tidal cycle (Siddorn et al., 2003).

LW +3:00 hrs

Three hours before high water (a), the surface currents are South easterly, extremely strong currents are found inside the Plymouth Breakwater. Low salinity freshwater (Figure 5.2) is found up the River Tamar and low salinity waters linger in front of Penlee. (Uncles et al., 2015)

LW +6:00 hrs

At high water (b) surface currents are stronger across the whole region and are predominantly Westerlies, except to the East of Penlee where the current direction is southwards and in the sound where it is south–eastwards. The low salinity waters (Figure 5.3) in front of Penlee are no longer found in front of Penlee with the low salinity waters pooling in the Plymouth sound.

LW +9:00 hrs

Three hours after high water (c), the currents are weaker at L4 with strong south–westward surface currents flowing out either side of the breakwater and around Penlee Point (Figure 5.2). The water in the breakwater and out towards the front of Penlee has a salinity of ~32.8 at this stage of the tidal cycle (Figure 5.3).

LW +0:00 hrs

At low water (d), the current are stronger and the direction of flow is predominantly to the West and Northwest in the open ocean region. At the breakwater the currents are weak and to the north but there is also a strong flow West past Penlee and around the coast. This Westward flow across the breakwater promotes the extrusion of low salinity water (33.6) out in front of Penlee point. There is also an outflow from the Eastern side of the breakwater that crosses in front of Penlee but is separate from the coastal current (Figure 5.2).

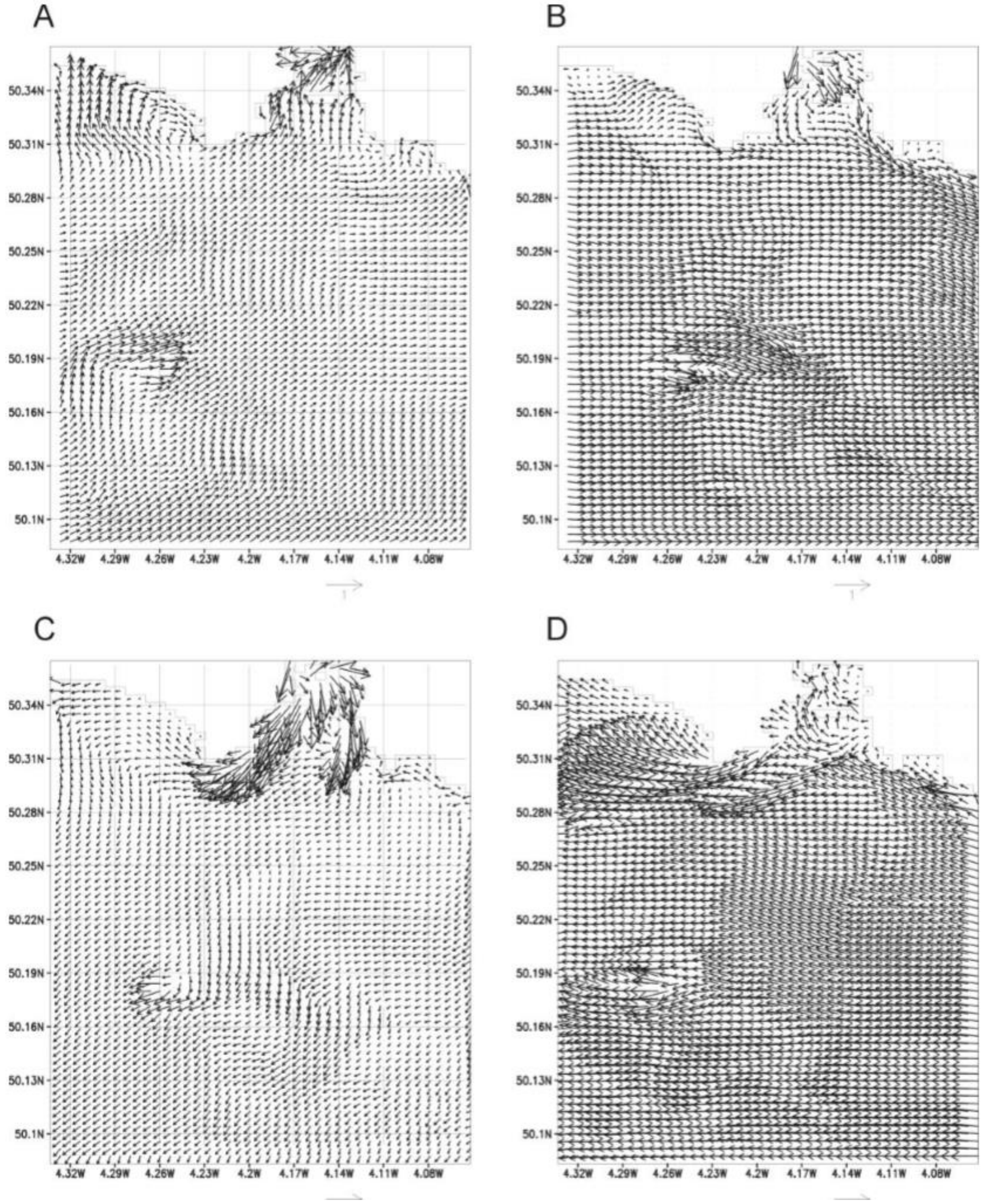

Figure 5.2 Surface currents at the Western Channel Observatory
Tidal currents (ms^{-1}) are shown for different stages of the tidal cycle, LW+3:00 hrs (A), at high water/LW+6:00 hrs (B) , LW+9:00 hrs (C) and low water/LW+0:00 hrs (D) (Siddorn et al., 2003).

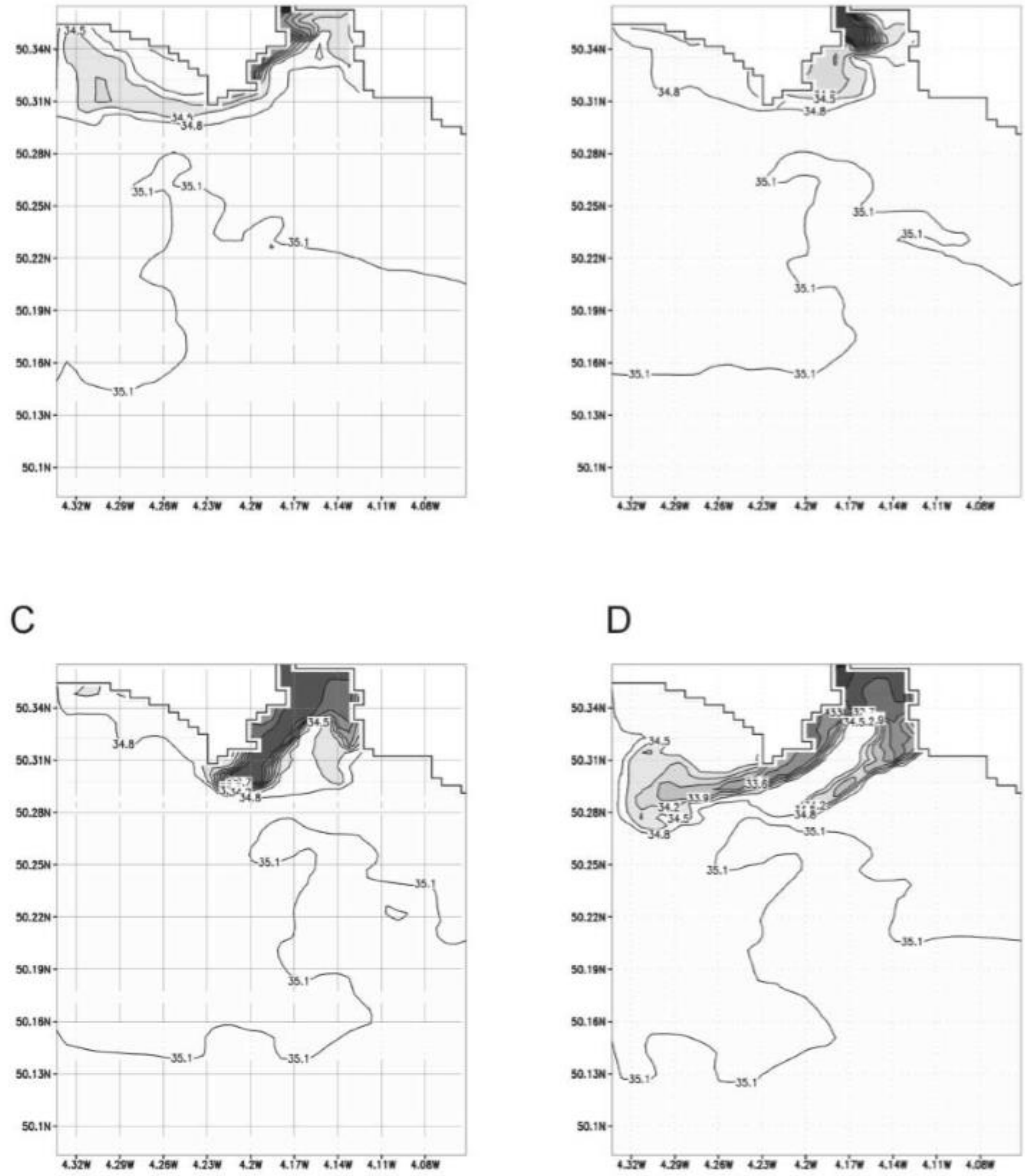

Figure 5.3 Surface salinity fields for the Western Channel Observatory
Modelled surface salinity fields are shown for different stages of the tidal cycle, LW+3:00 hrs (A), at high water/LW+6:00 hrs (B) , LW+9:00 hrs (C) and low water/LW+0:00 hrs (D) (Siddorn et al., 2003).

5.4 Time series measurements at the L4 mooring during the seasonal study

5.4.1 Meteorology

The wind speed recorded from the buoy at station L4 is incomplete (only covering April to early June) and does not cover the majority of the seasonal study (Figure 5.4a). For the period where wind speed data are available from the mooring, the average wind speed was low (5.90 ± 4.23 ms^{-1}) but still typical of the site based on historical data (Smyth et al., 2010b). Wind speed measurements from the Penlee Point Atmospheric observatory provided a substitute record of wind speed for the remainder of the seasonal study. When there was measurement overlap at the start of the seasonal study the wind speed measurements from Penlee broadly agreed (r^2 =0.55) with those from the L4 buoy, differences between the two could be to do with motion of the L4 buoy. The wind speed at Penlee declined during the summer, which typical of mid–latitude winds in summer (Sandwell and Agreen, 1984). The predominant wind direction at station L4 during the course of the seasonal study was from the South West (~225°) (Figure 5.4b). 40 years of historical data (ECMWF ERA–40) indicate that this is the main wind direction at the site (Smyth et al., 2010b). The average PAR recorded at the L4 buoy was 265.67±218.20 Wm^{-2} (Figure 5.4c). The average wind speed and direction during the seasonal study are in broad agreement with the climatological wind speed and direction for the site (Figure 5.5).

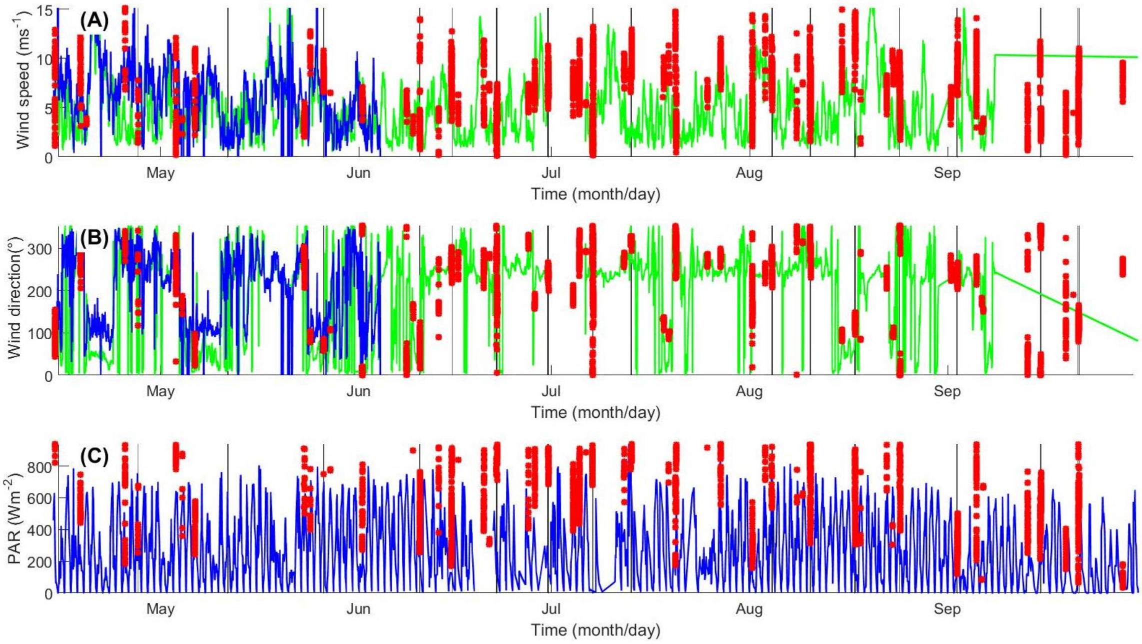

Figure 5.4 Meteorology at the L4 mooring

Wind speed (a), wind direction (b) and PAR (c) are shown for the period between April 15th and November 1st 2016. Measurements made by the L4 mooring are in blue. Those by RV Quest's meteorology system are in red and those from Penlee Point are in green. The time of each of the 16 deployments are indicated by solid vertical lines.

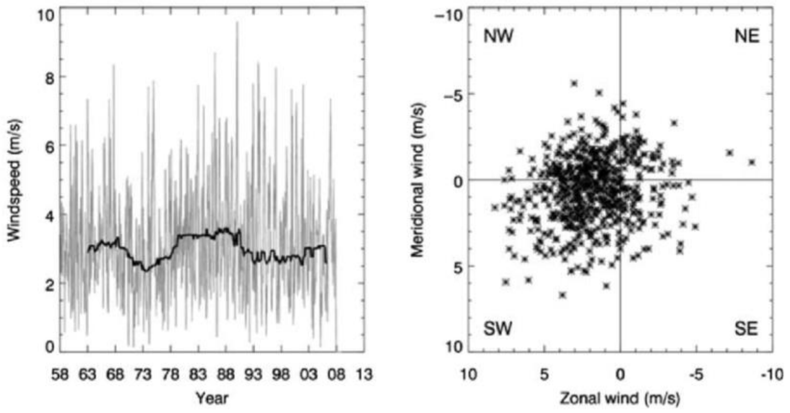

Figure 5.5 Climatological wind speed and direction for station L4

(a) Timeseries of wind speed (b) density plot of wind direction at station L4 based on ECMWF for the period of 1958-2007.

5.4.2 In water variables

An underway seawater system is installed on the Plymouth Quest with an intake depth of 3m. The seawater supply is passed through a debubbler and split between the thermosalinograph (Seabird SBE 45) and the oxygen (Aandera Oxygen optode) and chlorophyll, turbidity and CDOM sensors (Wetlabs C–star transmissometer) and the CO_2

system(Hardman-Mountford et al., 2008, Kitidis et al., 2012). Installed at the top of the ship is an AirMar PB100 Met station with sensors for wind speed, wind direction, air temperature, humidity and pressure. An Atlantic PAR (photosynthetically active radiation) sensor is also installed next to the met station.

Surface seawater temperature is continuously measured on the L4 buoy by a sensor located at ~5m (Figure 5.6a). The mooring temperature agrees well with the temperature measurements made at ~3m from the underway system of the Plymouth Quest whilst the ship was in close proximity (<1km) to the mooring. Six near surface temperature sensors (NSTS) were also installed on the mooring at 0.3, 0.6, 1.5, 2.4, 2.9 and 3.5m for an 18 month period (May 2015 –Oct 2016) (Figure 5.7). All but two of the 16 NSOP deployments were made when the NSTS were operational. All the temperature sensors show a slow warming trend over the course of the seasonal study from April to the end of September. The increase is a gradual trend but superimposed on this trend are several sharp daily increases caused by localised near surface warming. There is clear evidence that there are diurnal near surface temperature gradients at L4 for the large majority of the summer as indicated by differences in temperature between 0.3m and 3.5m (Figure 5.8). In contrast, by the end of September there is a negligible temperature differential between the sensors. The temperature measured at the L4 buoy is representative of the typical seasonal trend Figure 5.9.

The salinity at L4 was very stable during the seasonal study (Figure 5.6). There are numerous events where the salinity drops by as much as 0.5 at the mooring. The salinity drops are most likely due to increased river run off. The salinity sampled from the underway intake at ~3m on the Plymouth Quest in close proximity (<1 km) to the mooring agreed with the measurements from the salinity sensor on the mooring. There were a few times when the Quest was in close proximity but had a >0.1 lower salinity. This suggests that horizontal heterogeneity may be quite strong around L4. The salinity measured at the L4 buoy during the seasonal study appears to be representative of the typical seasonal trend Figure 5.9.

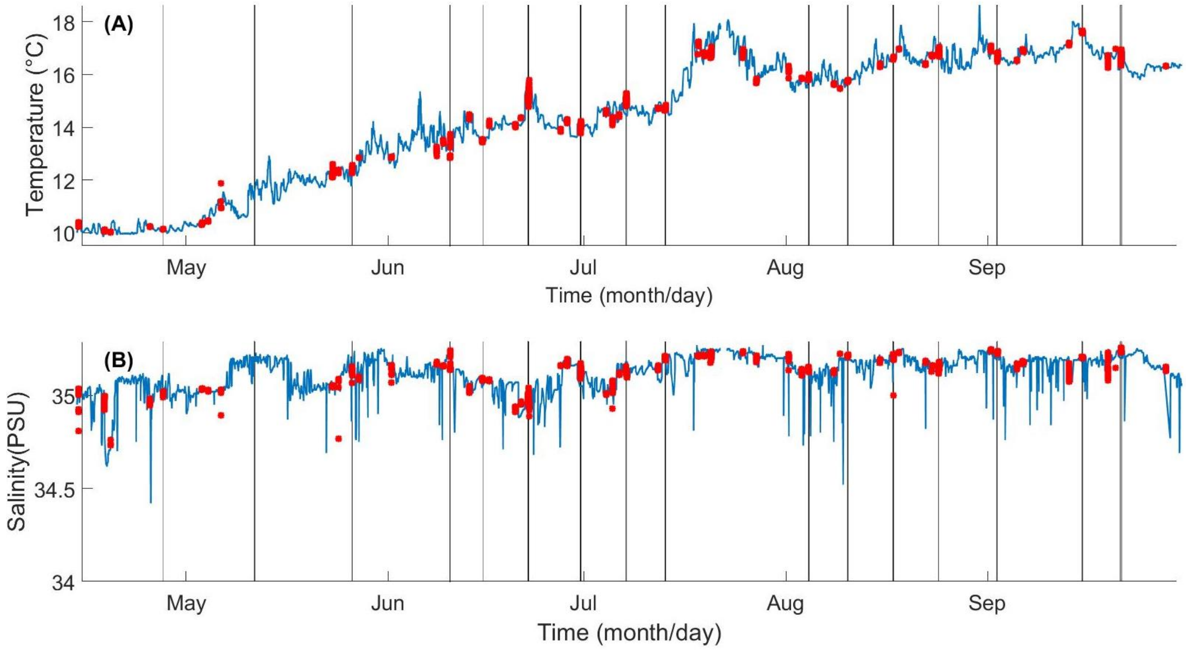

Figure 5.6 Surface temperature and salinity at the L4 mooring

Temperature (a) and salinity (b) are shown for the period between April 15th and September 21st 2016. The time of each of the 16 NSOP deployments are indicated by solid vertical lines. Measurements from the L4 mooring are in blue and those by the Quest's underway system when within 1km of the mooring are in red.

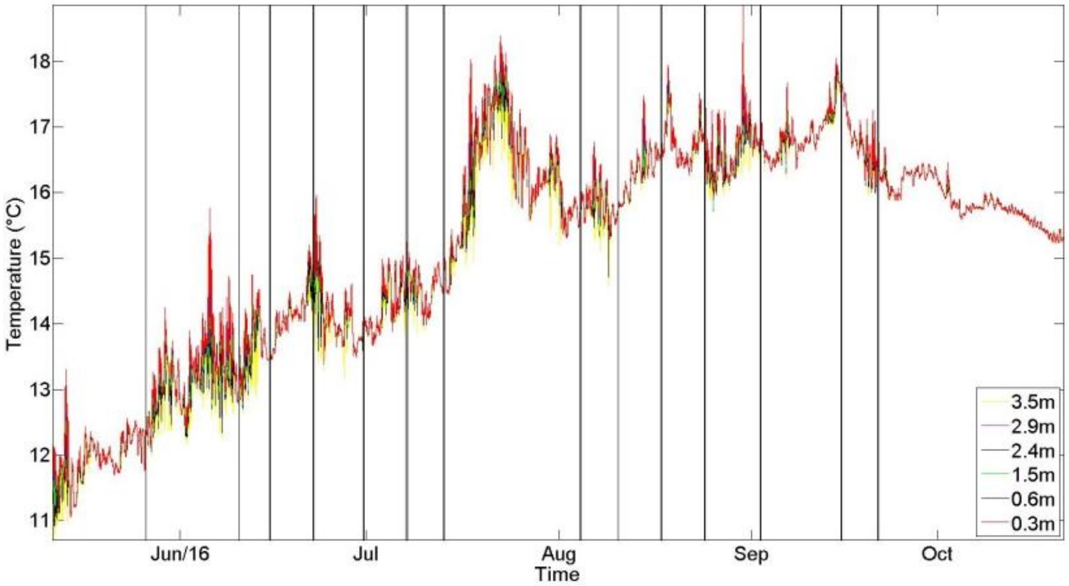

Figure 5.7 Surface temperature measurements at the L4 mooring

Temperature at 0.3, 0.6, 1.5, 2.4, 2.9 and 3.5m for the period 15th May 2016 to the 21st October 2016. The time of each of the 16 NSOP deployments are indicated by solid vertical lines. The colours of the lines correspond to the depths of the temperature sensors as indicated in the legend.

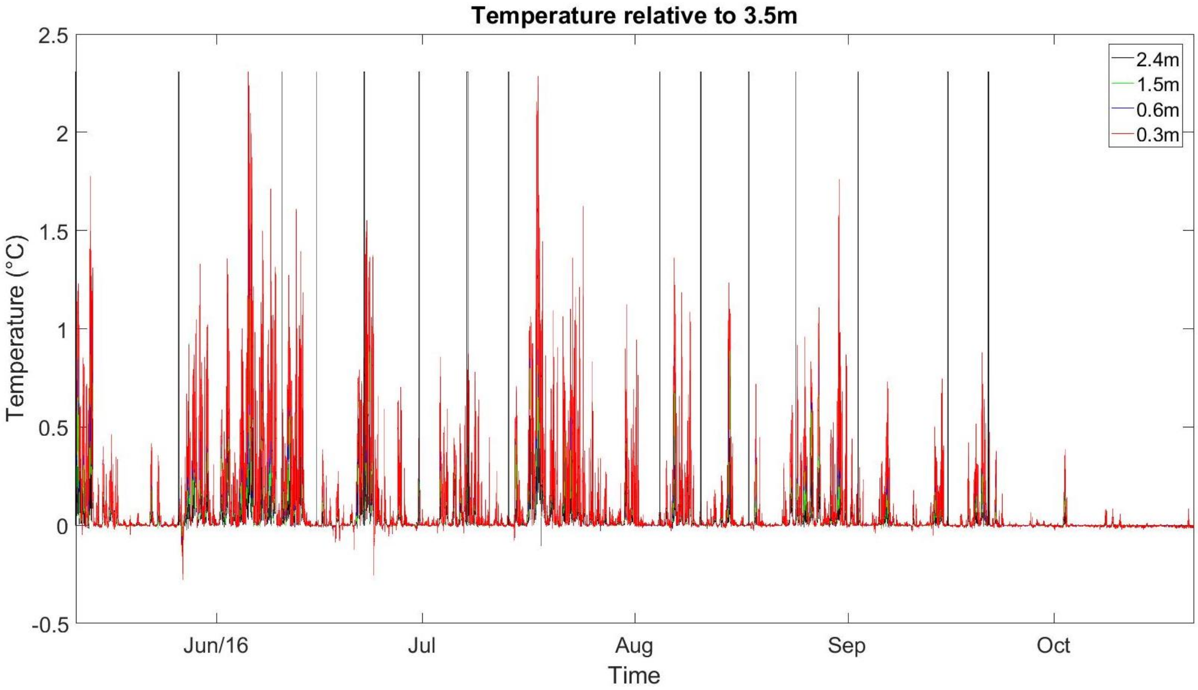

Figure 5.8 Surface temperature differential at the L4 mooring
The temperature differential between 3.5m and 0.3, 0.6, 1.5, 2.4 and 2.9m for the period 15th May 2016 to the 21st October 2016. The time of each of the 16 NSOP deployments are indicated by solid vertical lines. The colours of the lines correspond to the depths of the temperature sensors as indicated in the legend.

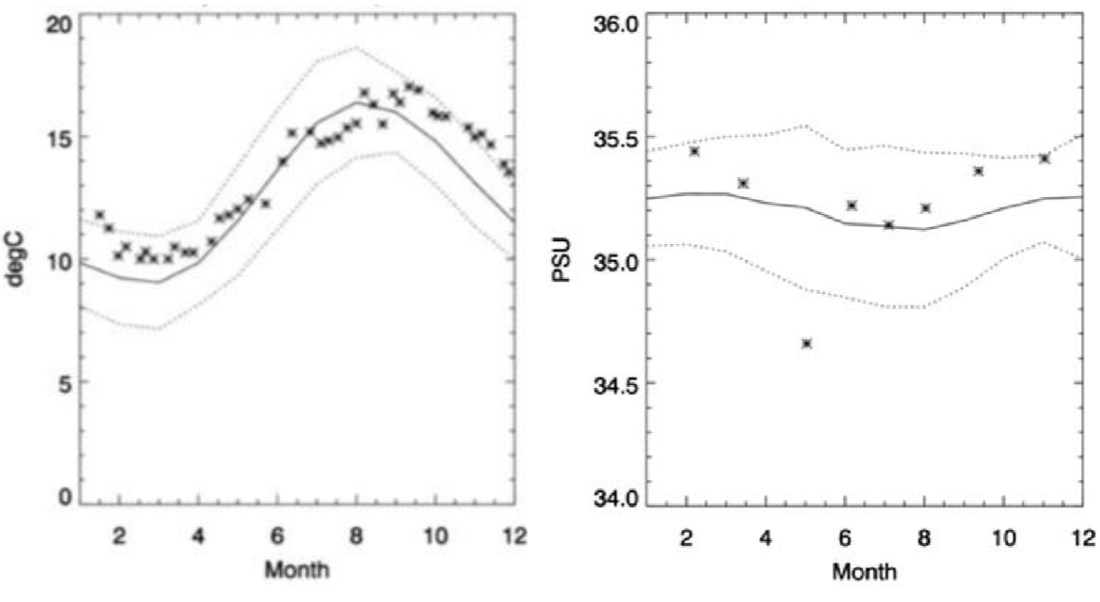

Figure 5.9 Surface L4 temperature and salinity climatology
L4 surface (a)temperature and (b) salinity monthly average climatologies from 1985 to 2010 (Smyth et al., 2010a)

The fluorescence signal recorded at the mooring (Figure 5.10) does not consistently agree with the measurements made by the Plymouth Quest’s underway system. In late spring the fluorescence recorded by the underway system was slightly higher whereas it was much lower during the onset of autumn in September. The fluorescence does not follow the expected trend with an increase after the spring bloom and slow decline throughout the summer; instead the fluorescence remains fairly constant from mid–April through to the start of August where there are two peaks in August and September.

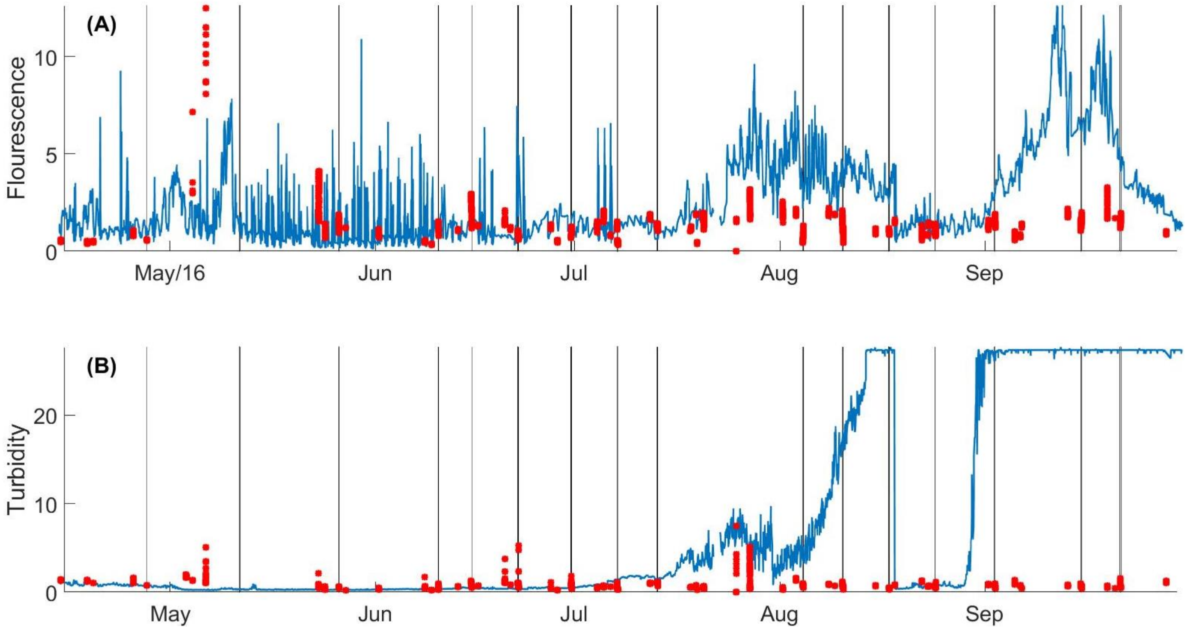

Figure 5.10 Surface fluorescence and turbidity at the L4 mooring
Fluorescence (a) and turbidity (b) are shown for the period between April 15th and November 1st 2016. The time of each of the 16 NSOP deployments are indicated by solid vertical lines. Measurements from the L4 mooring are in blue and those by the Quest's underway system when within 1km of the mooring are in red.

The river Tamar is the largest river flowing into the Plymouth Sound. The daily average flowrate of the river Tamar is measured upstream at Gunnislake; this is shown for the period of the seasonal study Figure 5.11. There were three large spikes in river flowrate $>30 m^3 s^{-1}$ during the deployment on 15/06 and several days before 22/06 and 04/08.

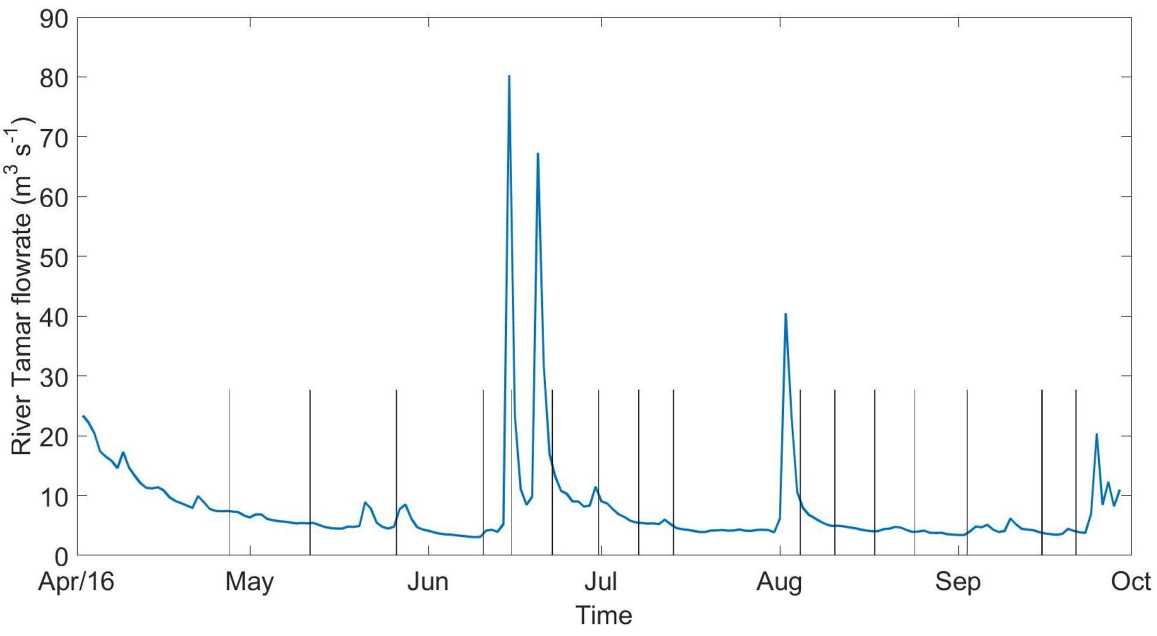

Figure 5.11 River Tamar flowrate recorded daily at Gunnislake

The average daily river Tamar flowrate recorded at Gunnislake (Environment Agency Location 47117, 50° 31'52.6"N 4°13'18.7"W). The time of each of the 16 NSOP deployments are indicated by solid vertical lines.

5.4.3 **Underway fCO_2 at L4**

fCO_2 measured when RV Plymouth Quest was within 1 km of the L4 mooring are shown in Figure 5.12. Seawater CO_2 (Figure 5.12a) declined from near equilibrium with the atmosphere (~400 µatm) at the end of April to ~350 µatm in early June due to the spring bloom. fCO_2 remained fairly stable before increasing back up to around 400µatm in late August and early September. Atmospheric pCO_2 (Figure 5.12b) declined over the summer which is the same trend seen across the northern hemisphere due to terrestrial CO_2 uptake (Pearman and Hyson, 1981). The air–sea CO_2 difference indicates that the seawater was close to equilibrium with the atmosphere at the end of April, was undersaturated over the summer and had reached equilibrium again by late September. These observations agree with past measurements of seasonal variation at the WCO (Kitidis et al., 2012). L4 acts as a sink for CO_2 in the summer similar to the rest of the European continental shelf (Borges, 2005).

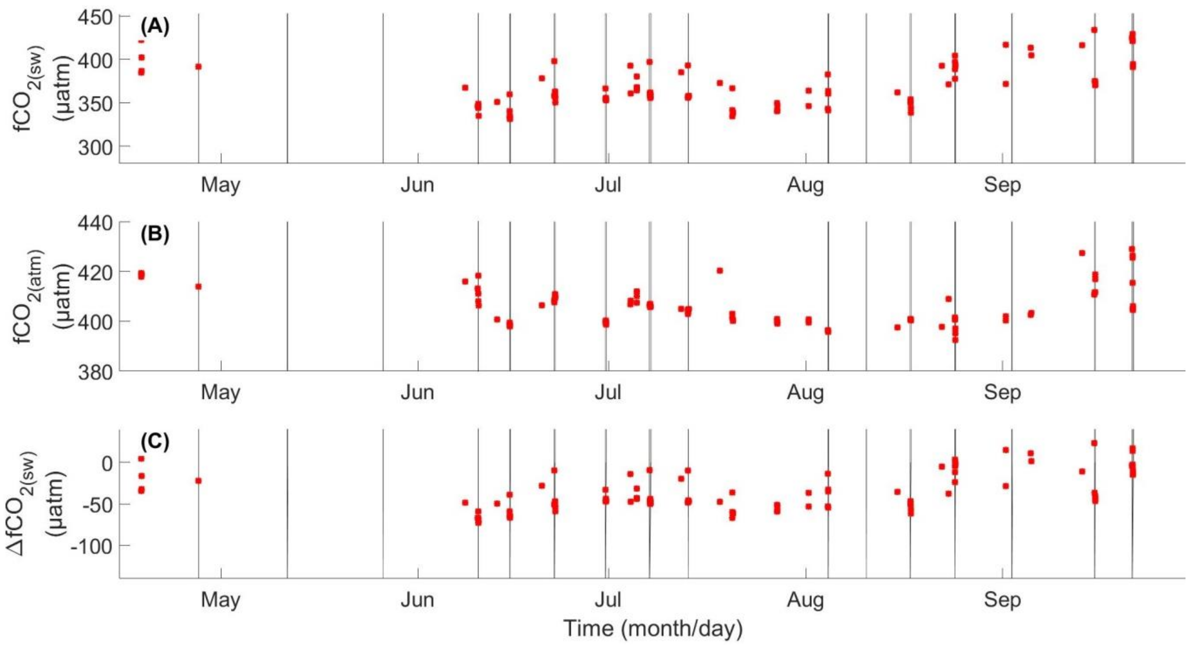

Figure 5.12 Surface fCO$_2$ at the L4 mooring

Seawater fCO$_2$ (a), atmospheric fCO$_2$ (b) and the atmosphere ocean fCO$_2$ differential (c) measured from RV Plymouth Quest within 1 km of station L4 for the period between April 15th and November 1st 2016. The time of each of the 16 NSOP deployments are indicated by solid vertical lines.

5.4.4 Tidal height and stage of the tidal cycle during NSOP deployments

The Sutton harbour lock is closed two hours either side of the lowest point of the tide, completely restricting access into and out of the harbour during this time. Despite the tidal restrictions, the 16 deployments encompassed all stages of the semidiurnal tidal cycle at L4 with deployments spanning the ebb tide; flood tide and periods of high and low water (&).

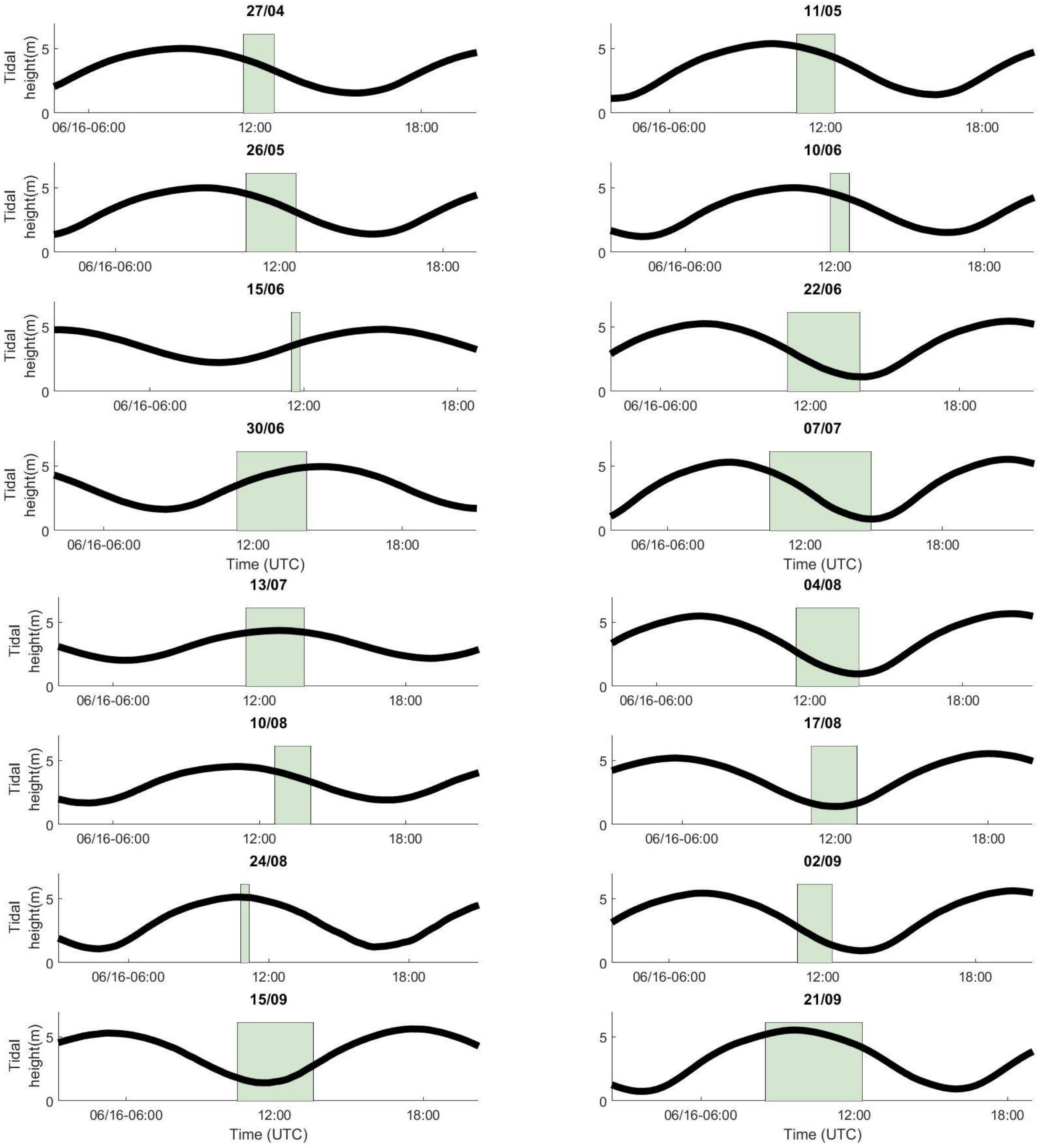

Figure 5.13 Devonport tidal height

Tidal height is shown by a solid black line. The beige area corresponds to the period of the deployment when NSOP was sampling which was used to derive NSOP profiles. The date of each deployment is given above each subplot.

6 Horizontal variability in surface seawater CO_2 close to the Western Channel Observatory

6.1 Introduction

The liqui–cel CO_2 system was connected to the Plymouth Quest’s underway seawater supply during transit to and from station L4 throughout the NSOP seasonal study. The fast measurement frequency and response time of the “liqui–cel” CO_2 system enabled improved spatial resolution (<0.5 km).of surface CO_2 around the Western Channel Observatory. The fast response CO_2 measurements are also compared and evaluated against the slow response measurements made by Plymouth Quest’s “showerhead” CO_2 system.

In this chapter, trends and features in the measured CO_2 transects are explored and explained in the context of the local hydrography. This chapter specifically tests the following hypotheses of this project (section 1.18**),** specifically

Does horizontal variability in CO_2 impact vertical gradients?

6.2 Response times and spatial resolution of the “liqui–cel” and “showerhead” systems

Both CO_2 systems were constantly fed by the underway seawater supply. There is a short < ~30s delay for seawater to go from the seawater inlet to the equilibrators of both systems. As this delay is the same for both systems, at a max speed of $5ms^{-1}$ this would only result in a spatial offset of 300m if it is assumed pumping seawater from the intake to the equilibrators results in a negligible delay. What must be accounted for is the equilibration time of the two systems. The measured fCO_2 do not reflect single points in space but indicate averages across the region through which the ship transited during equilibration. The distance travelled by the ship (in a straight line) can be calculated using the Quest’s cruising speed of nine knots and the equilibration time of the two systems.

For the liqui–cel equilibrator, assuming that the system is almost fully equilibrated by the time it reaches twice the response time (48 s), this distance is 220m. The need to run calibrations and atmospheric measurements and the slow ~5 minute response time of the showerhead style equilibrator (Körtzinger et al., 2000), meant the showerhead CO_2 system on the Plymouth Quest was set to sample every 27 minutes. For the showerhead system the time spent equilibrating is longer than the time required to reach equilibrium, which is twice the response time (10 minutes). In the 27 minutes between measurements the ship travels 7.5 km, so the sampling frequency could be increased. The showerhead pCO_2 are reported at the measurement location, which means they do not accurately reflect the location of the sampled water, just the location of the ship at the time of measurement. This is not considered a problem in the open ocean where the seawater CO_2 is considered to be relatively homogeneous over large areas but is a potential issue in coastal regions.

6.3 Dates and locations of underway measurements made on transit to and from station L4

The long setup time of the liqui–cel CO_2 system on the morning of the deployments meant the system was often not ready to sample until the Quest had reached station L4. The underway sampling by the liqui–cel CO_2 system occurred on some outward journeys (22/06, 30/06, 04/08, 24/08, 02/09, 24/09) but predominantly on the return voyages from L4 (10/06, 15/06, 30/06, 07/07, 13/07, 04/08, 17/08, 24/08, 15/09 and 21/09).

The showerhead CO_2 system on the Quest was functioning properly on all but four of the 16 NSOP deployments (27/04, 11/05, 26/05 and 10/08). Data are missing from these deployments because the showerhead system drier malfunctioned. For the 12 deployments/voyages where the showerhead system was functioning there is measurement overlap with the liqui–cel CO_2 system during the NSOP deployments and return voyages from L4.

The Plymouth Quest travelled along the same route between the Plymouth breakwater and station L4 on all but four journeys where the Quest headed towards the Penlee Observatory (10/06, 30/06, 07/07 and 04/08) (Figure 6.1). Sampling was only conducted when outside Plymouth breakwater as there are concerns about biofouling, high sediment load and coastal debris in the water inside the breakwater.

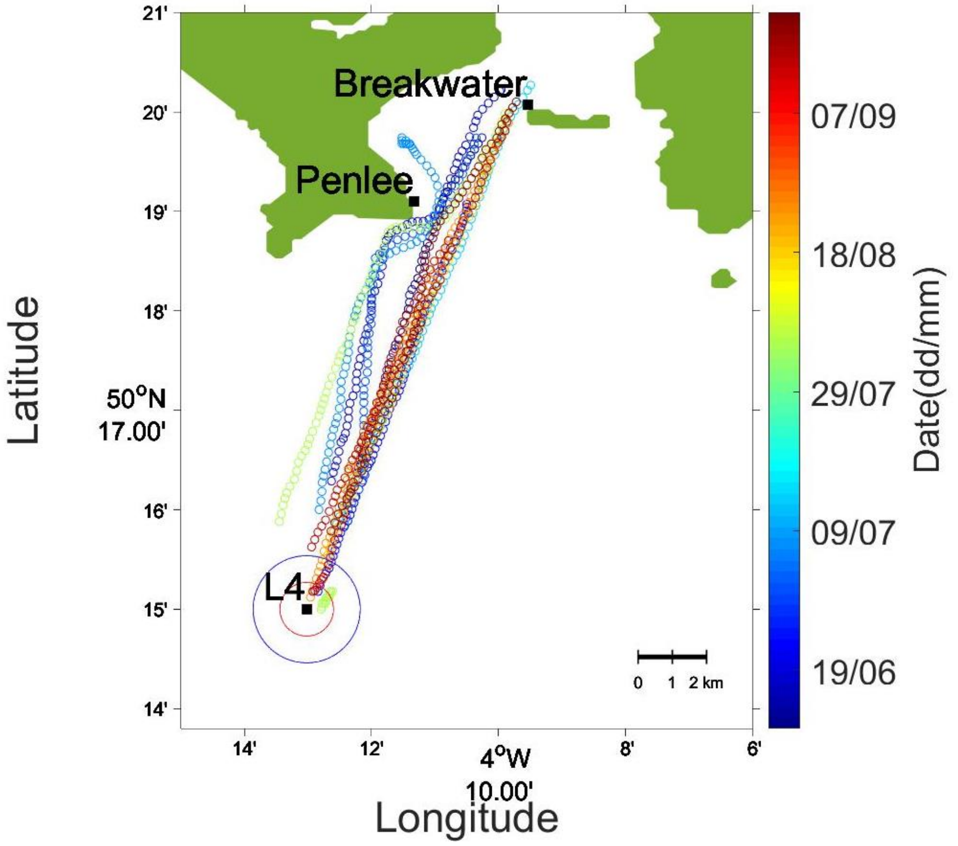

Figure 6.1 Ship tracks during the seasonal study

Ship tracks of the Plymouth Quest during the seasonal study between the breakwater and station L4. Ship tracks are coloured by day of year.

6.4 **“liqui–cel” and “showerhead” underway measurement comparison**

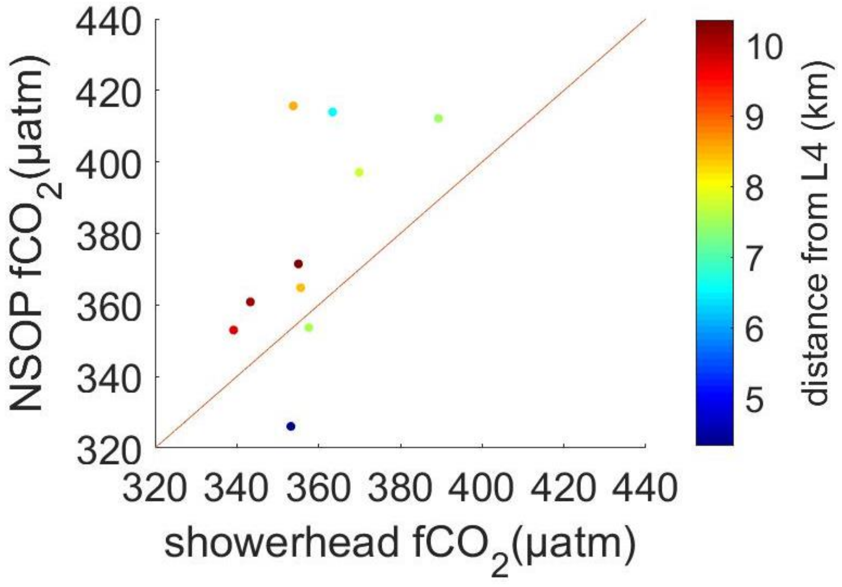

Figure 6.2 Comparison of coincident measurements from liqui–cel and showerhead CO_2 systems

Liqui–cel system measurements at the same time as the measurements from the showerhead system.

The CO_2 underway data intercomparison between the two systems benefits from the shared access to the same underway seawater supply and ancillary temperature and salinity data (Figure 6.2). Based on the expected accuracy of the two systems they should agree within 2 µatm as has been observed in previous intercomparison experiments (Körtzinger et al., 2000, Ribas-Ribas et al., 2014).

The two CO_2 systems agree well whilst on station with the NSOP sampling via NSOP and the showerhead system sampling from the underway supply (Figure 6.3). Most of the agreement can be put down to the fact that whilst at L4, the slower response time of the showerhead system was unimportant as the pCO_2 at L4 do not change over short periods of time allowing the pCO_2 system to fully equilibrate. Some of the disagreement between the two systems whilst on station can partially be explained by sampling depth differences between NSOP and the Quest's underway intake. NSOP data thus also include vertical variability in CO_2.

The two CO_2 systems tended to run in parallel for approximately 30 – 40 minutes between the breakwater and L4 (Figure 6.3). As the period of measurement overlap was so short and the measurements from the showerhead system are so infrequent, there were typically only one or two measurement overlap points between the breakwater and L4. There were ten return voyages with measurement overlap between the two CO_2 systems. Both CO_2 systems indicate that in general the CO_2 is lower at L4 than further inland near the Breakwater. There are a number of voyages where the measurements from the showerhead system agree well (<4 µatm) with the continuous measurements from NSOP such as on 10/06. Good agreement occurred when the pCO_2 measured at the breakwater were similar to the pCO_2 at L4. On all the other voyages, liqui–cel CO_2 is much higher (~40 µatm) than observed by the showerhead system (07/07, 04/08, 17/08, 15/09 and 21/09). On 04/08, 15/09, 21/09 showerhead CO_2 levels at the breakwater increase rapidly to the same value recorded by the liqui–cel system >30 minutes earlier, which suggests the showerhead measurements lag behind the liqui–cel measurements.

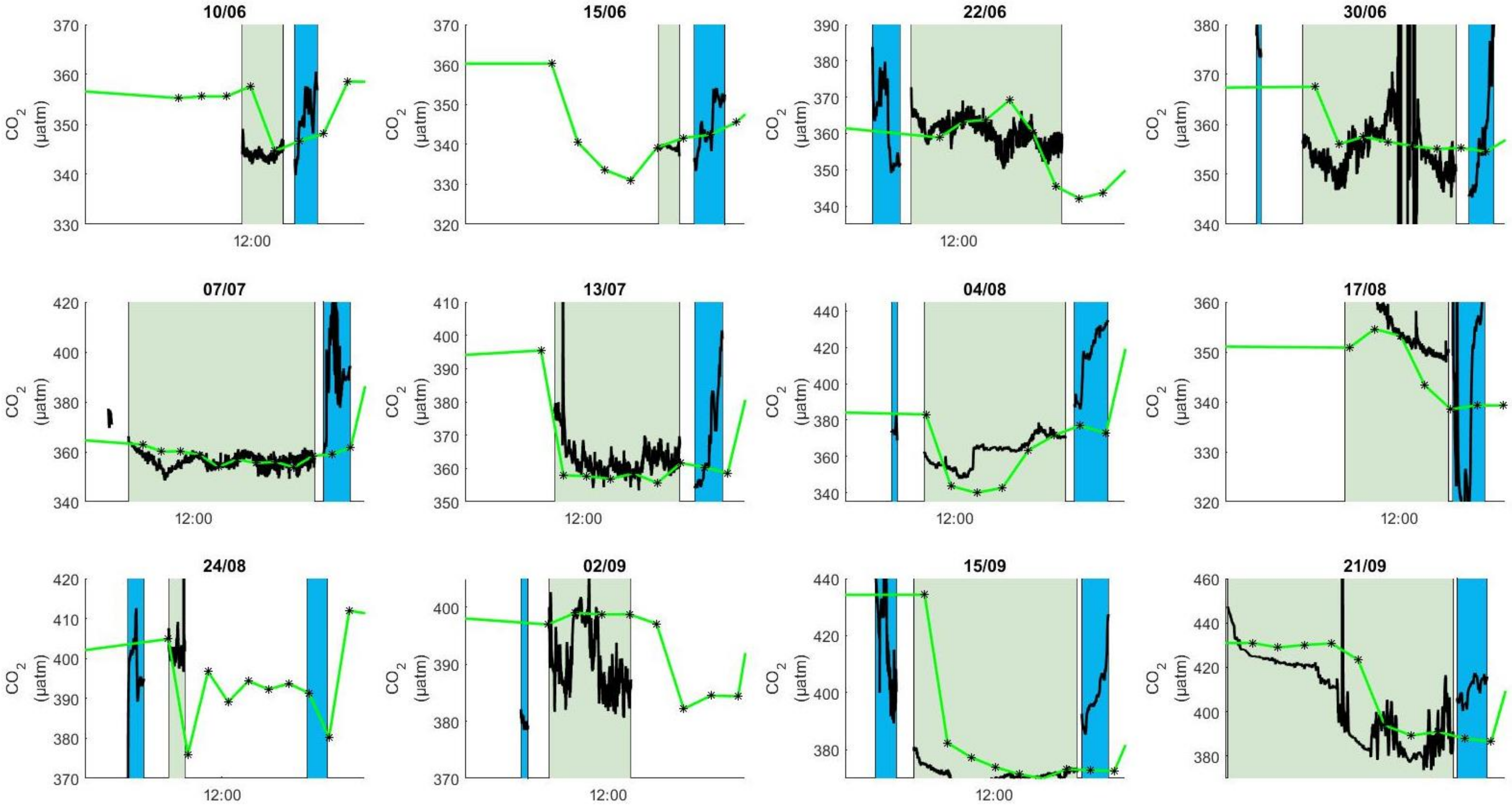

Figure 6.3 Measurement overlap between the showerhead and liqui–cel CO2 systems

fCO$_2$ measured using the liqui–cel CO$_2$ system (sold black line) . fCO$_2$ measurements from the showerhead CO$_2$ system (black stars by solid green lines) In all cases the sequence of activity was (i) transit to L4 (blue background) (ii) NSOP sampling (beige background) (iii) return from L4 to breakwater (blue background).

One explanation for the disagreement between the two systems (Figure 6.2) during the underway sampling is that the showerhead system was not able to fully equilibrate whilst transiting over heterogeneous coastal waters. The inability of the system to equilibrate when transiting over waters with higher CO_2 levels at L4 results in the showerhead system underestimating the CO_2 on the return journey. Incomplete equilibration means that measurements by the showerhead are only able to represent average (spatial and temporal) seawater CO_2. In contrast the liqui–cel system is able to detect smaller scale features in seawater CO_2.

6.5 Surface salinity trends from the Breakwater to L4

During the seasonal study salinity was measured from the underway seawater system on the Quest between the breakwater and L4. Salinity is shown as a function of distance from L4 for all the voyages when CO_2 was measured (Figure 6.4). The general trend is that the salinity declines by >0.5 towards the Breakwater. There are exceptions to this trend (e.g. 17/08 and 21/09) where there is almost no difference in salinity. The salinity measured at the breakwater is highly variable (ranging between 34.2 and 35.2) compared to sites in the Open Ocean and Shelf Seas. The variability in each transect also increased closer to the breakwater with several large spikes (0.4) on 30/06. In contrast, there was much less variability in the salinity recorded in the waters close (<2 km) to L4, with most salinities between 35.1 and 35.2. The salinity in L4 waters is infrequently affected by low salinity riverine waters e.g. (22/06).

The surface salinity for each of the different ship tracks is shown in (Figure 6.4). A key feature from this is that there is much lower salinity on average in front of Penlee Observatory, in Kingsand Bay and inside the breakwater.

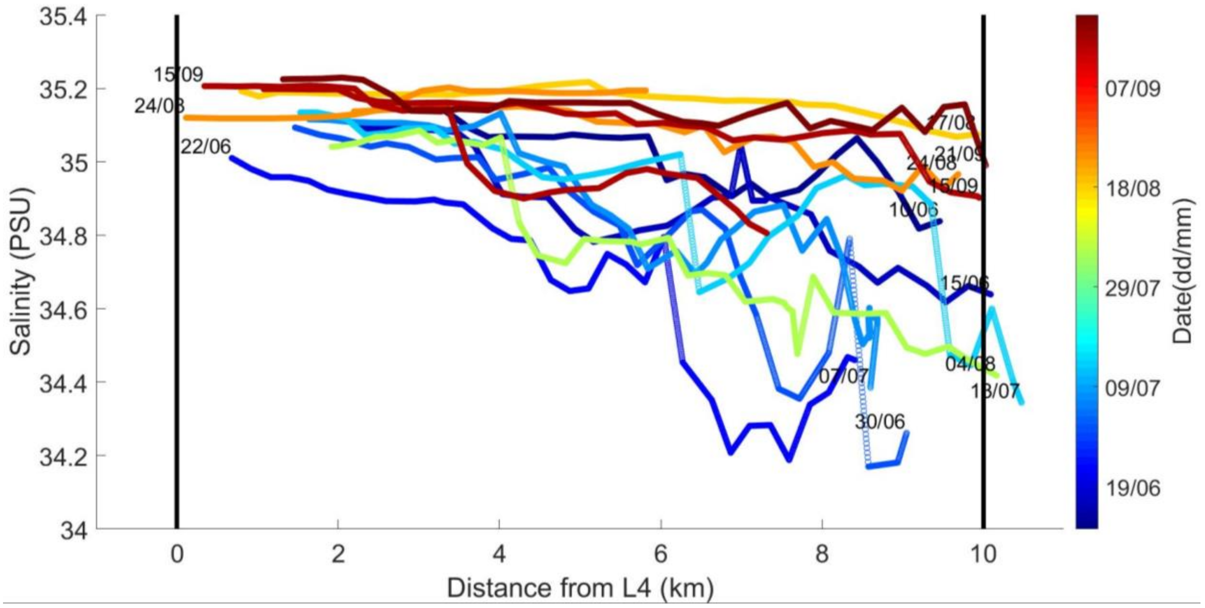

Figure 6.4 Surface salinity versus distance from L4

Surface salinity measurements recorded by the Plymouth Quest during transit to and from station L4 during the seasonal study. Each transect is coloured by time. The date of each deployment is given at the end of each transect. The locations of L4 and the breakwater are indicated by solid black lines.

6.6 Surface temperature trends from the Breakwater to L4

The temperature at L4 slowly increased during the course of the seasonal study. The temperature increase was also fairly uniform across the region between L4 and the breakwater. This can be seen by the fairly consistent increase in temperature between the weekly voyages to and from L4 (Figure 6.5a).

The temperature was constant between the Plymouth Breakwater and station L4 in many of the voyages (e.g. 17/08 and 15/09). During voyages on 10/06, 15/06, 22/06 and 04/08 there were temperature differentials between L4 and the breakwater (Figure 6.5). The temperature differentials predominantly showed that L4 is colder than the waters close to the breakwater (e.g. 10/06 and 04/08) and that there is much less variability in the temperature close (<3km) to L4 (b). The horizontal temperature differentials could be driven by the timing of the local tides, changes in the river flowrate and heating of water caught in the Plymouth Sound or rivers(Siddorn et al., 2003). 3km+ from L4 there appears to be sharp frontal regions where the temperature quickly changes by >0.5°C. On the voyages that approached Penlee Observatory (10/06, 30/06, 07/07 and 04/08)(, the temperature was much more variable than during the voyages when the ship took the more direct route back to the breakwater. On 10/06 and 04/08 the temperature increases rapidly ~4 km away from L4.

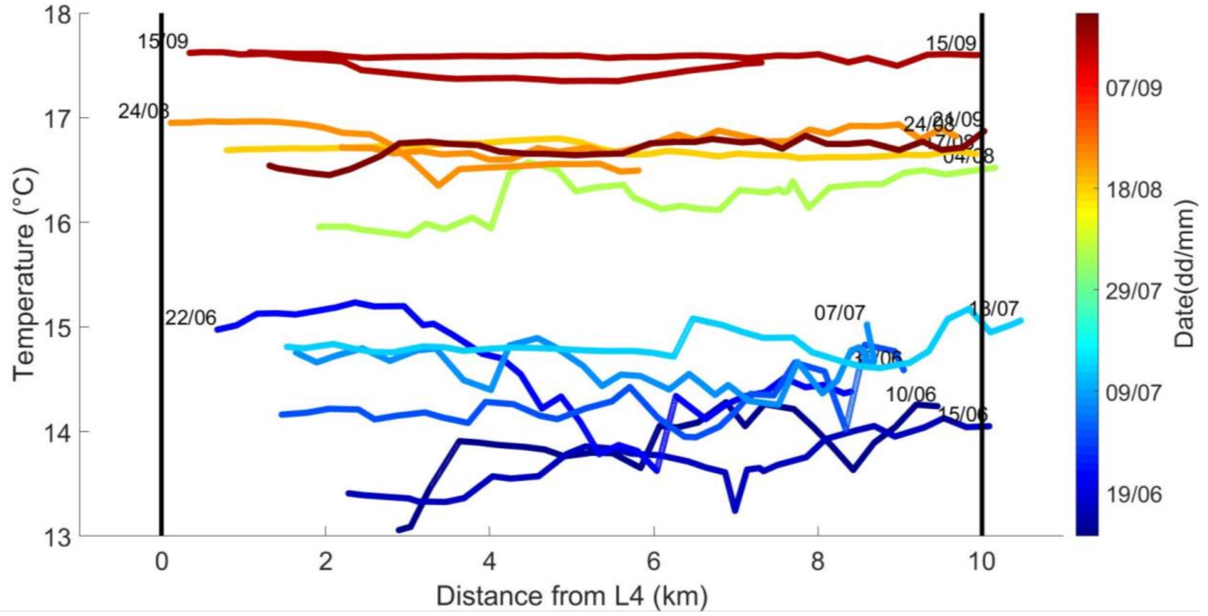

Figure 6.5 Temperature versus distance from L4
Surface temperature measurements recorded by the Plymouth Quest during transit to and from station L4 during the seasonal study. Each transect is coloured by time. The date of each deployment is given at the end of each transect. The distances from L4 and breakwater and indicated by solid black lines.

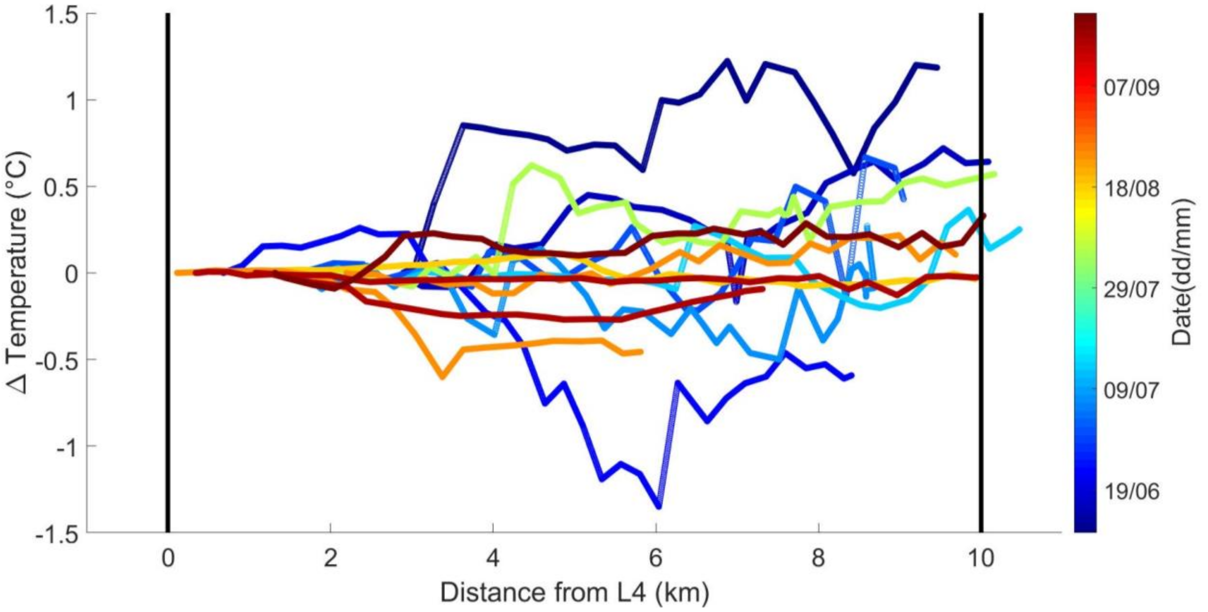

Figure 6.6 Temperature difference relative to L4 versus distance from L4
The temperature relative to that at L4 measured via the underway system during transit to and from station L4 during the seasonal study. Each transect is coloured by time. The distances from L4 and breakwater and indicated by solid black lines.

6.7 Horizontal CO_2 trends from the Breakwater to L4

As the showerhead CO_2 system only usually makes a single measurement during each voyage to and from L4, it is impossible to characterise any near coastal gradients between the breakwater and station L4 on a single day. Using a multiyear dataset of the surface ocean CO_2 at the Western Channel Observatory, (Kitidis et al., 2012) showed that there are horizontal gradients of (~0 – 100 µatm) between the breakwater and station L4. The seasonal study at L4 was conducted between April and September which encompasses the period (June to August) where the largest variability (~100 µatm) in surface CO_2 in the region within 15km from the coast were observed (Kitidis et al., 2012).

The high resolution of the Liqui–cel system allows small scale (<0.5km) features to be identified in the underway signal. Horizontal gradients between the breakwater and L4 measured by the Liqui–cel CO_2 system are shown for all of the outward and return voyages as a function of distance from L4 (Figure 6.7). The slow increase in average CO_2 throughout the summer can be (350 to >400 µatm between 15/06 and 15/09). The data shows many sharp transitions in the CO_2 signal during individual transits out to L4.

The fCO_2 during each voyage is shown as a horizontal differential relative to the fCO_2 at L4 (Figure 6.8). The majority of voyages show a 20 – 40 µatm decrease in CO_2 towards L4. The Quest entered the flux footprint of Penlee on 4 occasions (10/06, 30/06, 07/07 and 04/08). Two profiles (07/07 and 04/08) showed substantially more variability in CO_2 than voyages that took the direct route.

The largest variability and sharpest changes in CO_2 were observed when close to the breakwater or to land. The waters between L4 and the breakwater have distinctly different pCO_2, which might be expected as the area is known to be a dynamic region where different water masses meet (Uncles et al., 2015). The sharp 20 – 40 µatm changes reflect the source histories of the different water masses. Riverine water typically has much higher CO_2 than the open ocean (Zhai et al., 2005). It is worth noting that these changes were not identifiable with the showerhead CO_2 system.

Persistent features such as water masses with different pCO_2 can be identified using the Liqui–cel system, which can resolve features at the ~0.2km length scale, this spatial scale is the same order of magnitude as coastal plankton blooms (Nezlin et al., 2012).

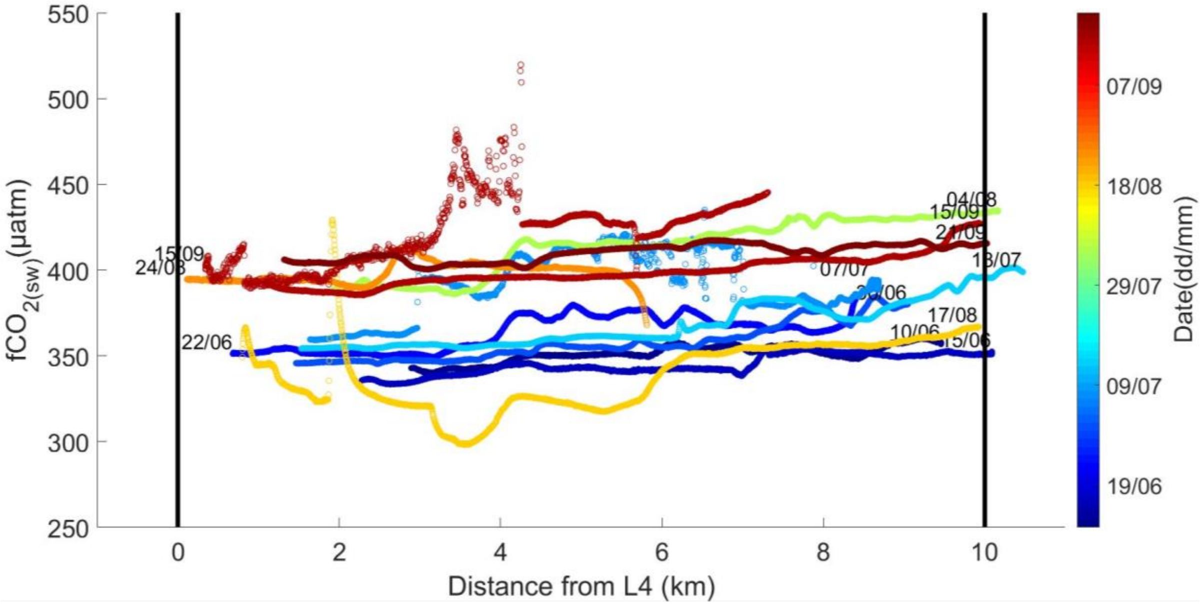

Figure 6.7 fCO_2 versus distance from L4

Measurements of fCO_2 made by the liqui–cel CO_2 system during transit to and from station L4 during the seasonal study. Each transect is coloured by time. The date of each deployment is given at the end of each transect. The distances from L4 and breakwater and indicated by solid black lines.

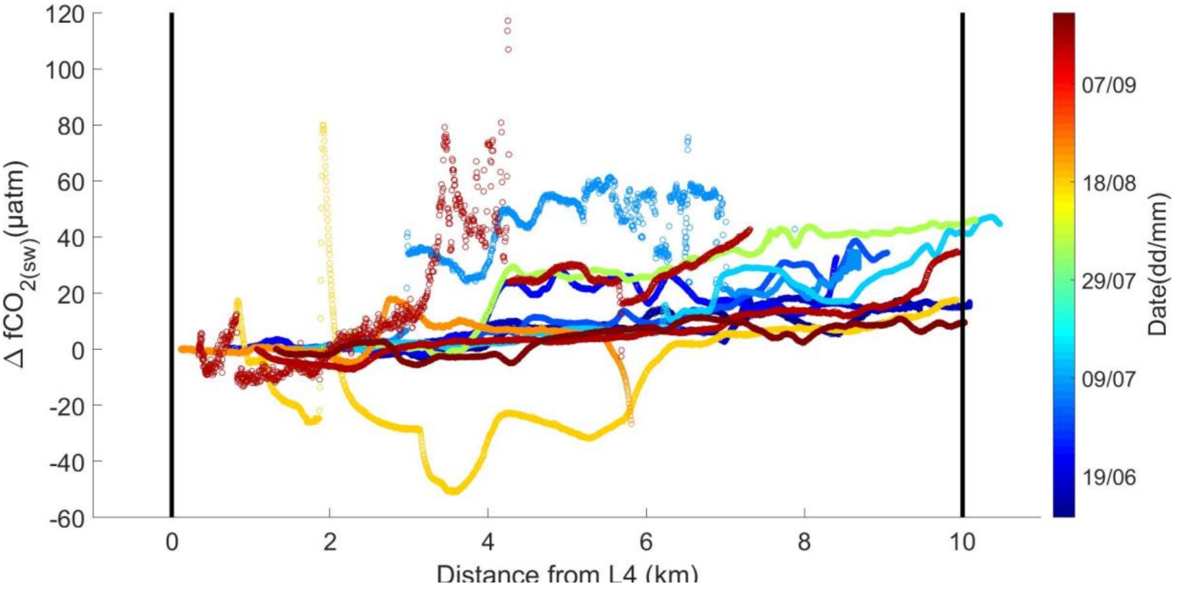

Figure 6.8 fCO_2 relative to L4 versus distance from L4

Measurements of fCO_2 made by the liqui–cel CO_2 system relative to L4 during transit to and from station L4 during the seasonal study. Each transect is coloured by time. The date of each deployment is given at the end of each transect. The distances from L4 and breakwater and indicated by solid black lines.

6.8 Tidal influences on fCO_2 between the Breakwater and Penlee

Changes in trace gas concentrations in the water masses in this region have been identified when measuring air–sea methane fluxes at Penlee point. Fluxes of CH_4 correlate with the state of the tide, with higher fluxes from high methane concentration estuarine waters (Yang et al., 2015). The highest fluxes were observed several hours after low water as the surrounding waters are more influenced by riverine source waters that are enriched in methane. Differences in pCO_2 are less pronounced than in CH_4, making this harder to observe in the CO_2 air–sea flux signal (Yang et al., 2015).

An explanation for the high horizontal variability in salinity (section 6.5) and fCO_2 (section 6.7) was proposed to be the known complex tidal dynamics in the WCO (section 5.3). The time since low water (LW + X:XX hrs) for the average time of the transects was used to separate the transects into four 3 hour tidal periods as in Siddorn et al. (2003) but with mid points of LW + 0, 3, 6 and 9 hrs that lined up better with distinct trends in fCO_2.

LW +0:00 hrs (Low tide)

Two transects were made shortly after low water (LW) at LW+0:24 hrs (07/07) and LW+0:37 hrs (04/08). These transects had salinity minima of 34.4 –34.5 (Figure 6.10) which are similar to modelled salinity (34.5) at low water LW+ 0:00 hrs (Figure 5.3 Panel D). The transect made just after low water on 07/07 had peak CO_2 and minimum salinity in front of Penlee (Figure 6.9). The highest pCO_2 recorded on the transect on 08/04 were found close to the breakwater. In both cases the segments of the transects with higher CO_2 coincided low salinity water. During these profiles the CO_2 difference between L4 and near Penlee was ~ 40 µatm.

At LW+ 1:12 hrs (17/08) and LW+2:09 hrs (15/09) the minimum salinity was much higher (+34.8) (Figure 6.10). The measured salinities are closer to those predicted for LW+3 hrs (34.6) (Figure 5.3 Panel A). The large change in the salinities encountered during these transects vs those measured shortly after low water reflects the large shifts in the direction and strengths of the surface currents just after low water (Figure 5.2). The pCO_2 on these transects were highest near to the breakwater on 08/17 and towards the end of the transect on 15/09. During these transects the CO_2 difference between L4 and Penlee was ~40 µatm.

LW +3:00 hrs (rising tide)

By LW + 3:47 hrs (15/06) there was a much higher pCO_2 near Penlee/ the breakwater (Figure 6.9), coinciding with a distinctly lower salinity 34.7 (Figure 6.10). This salinity agrees well with the predicted salinity (34.6) (Figure 5.3 Panel A). At this point in the tidal cycle the CO_2 difference between L4 and Penlee point was ~5 µatm.

LW +6:00 hrs (high tide)

One transect was conducted at high water (LW + 06:07hrs) on 30/06. The salinity at the breakwater (34.2) corresponds with the modelled salinity at the breakwater at high water (34.2) (Figure 5.3 panel B). During this transect there was essentially no CO_2 difference between Penlee and L4. The CO_2 increased by ~20 µatm from Penlee point towards the breakwater. This is coincident with when the salinity begins to decline.

LW +9:00 hrs (falling tide)

The transects at LW+7:54 hrs (13/07), LW+8:45 hrs (10/06), LW+8:53 hrs (21/09) and LW+9:22 hrs (24/08) were all made during the falling tide at LW + 9:00 hr. A common feature in all these transects is that close to Penlee Point there is a region of high CO_2, followed by a lower CO_2 region and then a second high CO_2 region close to the breakwater (Figure 6.9).

The two high CO_2 regions correspond to coincident salinity changes (high CO_2 – low salinity)/ (low CO_2 – high salinity) (Figure 6.10). These changes correspond with (Figure 5.3 panel C) suggesting that the Quest was moving in and out of the low salinity coastal current. The salinity does not drop to as low as in the model (32.7) in the coastal current. The observed pattern may indicate that the ship transited over a transient freshwater outflow from the eastern side of the Breakwater as in Figure 5.2 panel D.

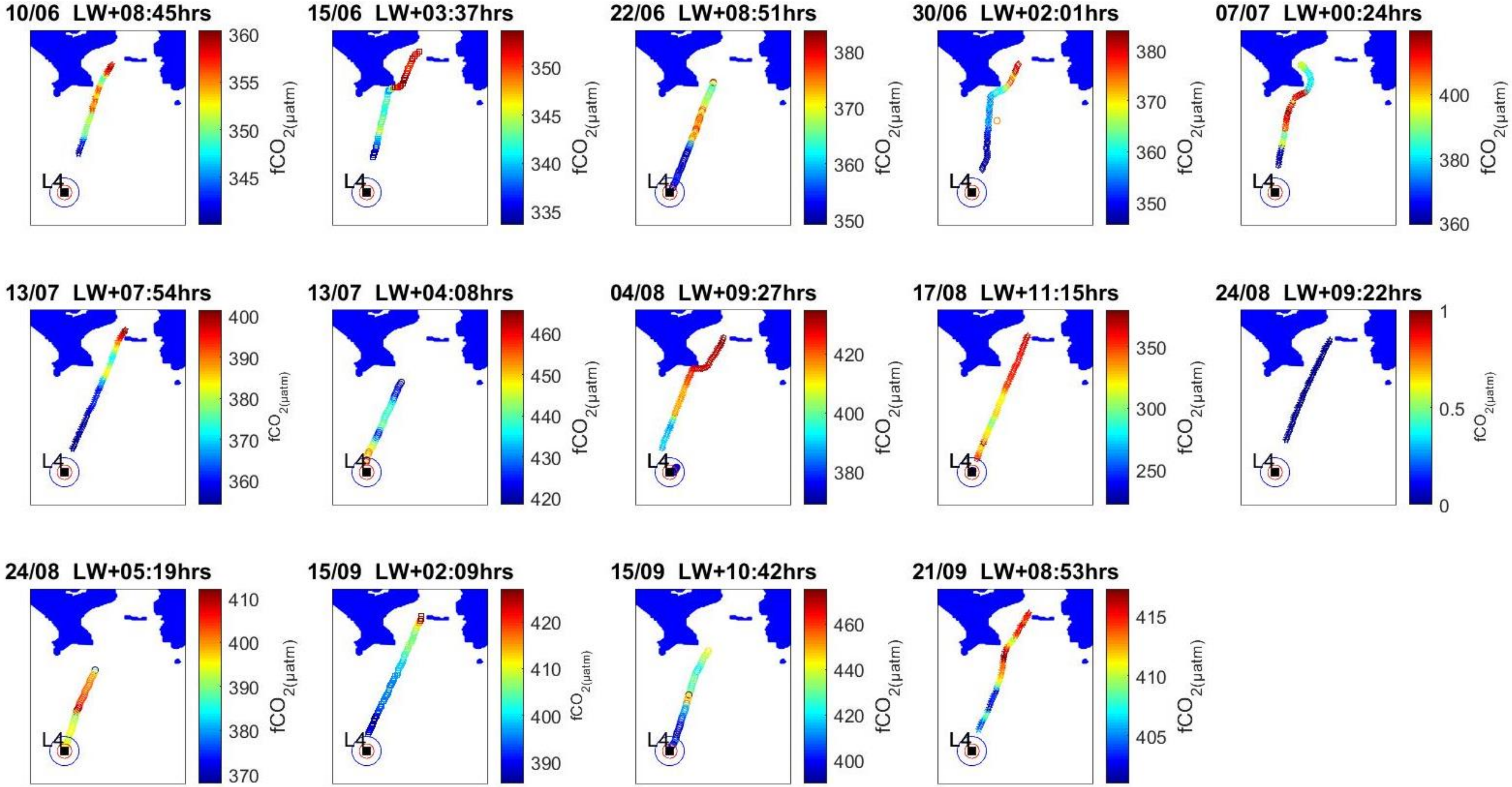

Figure 6.9 Surface CO_2 tracts on voyages between L4 and the breakwater

Surface fCO_2 made using the liqui–cel CO_2 system sampling from the Plymouth Quest's underway seawater supply. The date of the deployment (dd/mm) and the time since low water +HH:MM are given above the plots. The latitude range and longitude range of the maps are 50.23 to 50.35 °N and 4.25 to 4.1 °W.

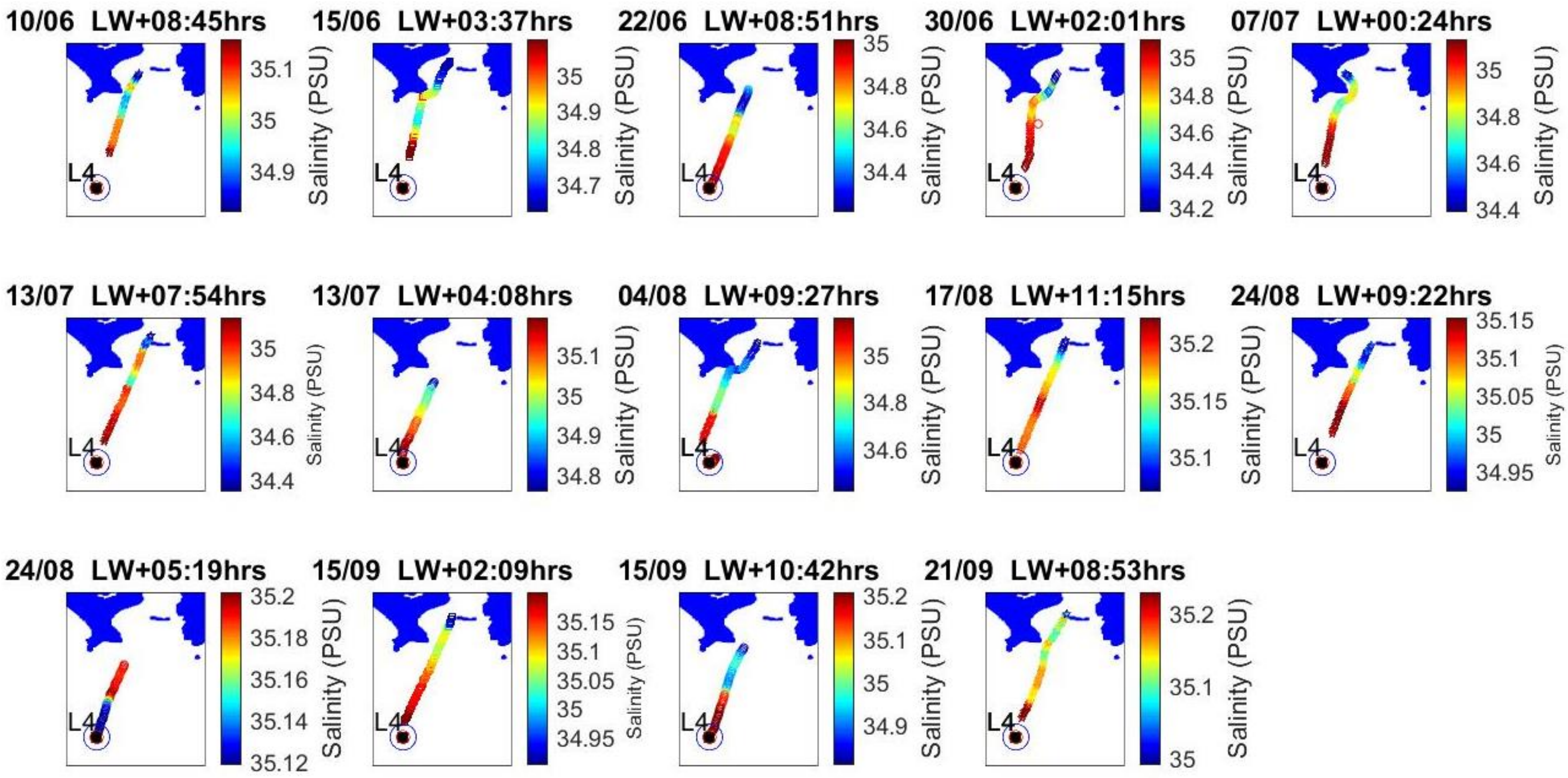

Figure 6.10 Surface salinity tracts on voyages between L4 and the breakwater

Surface salinity measurements made by the Plymouth Quest’s underway seawater system. The date of the deployment (dd/mm) and the time since low water +HH:MM are given above the plots. The latitude range and longitude range of the maps are 50.23 to 50.35 °N and 4.25 to 4.1 °W.

6.9 Implications of horizontal differentials

The association between local surface CO_2 and the stage of the tidal cycle in the region between the breakwater and L4 raises many questions about our understanding of coastal CO_2 variability.

The Plymouth Quest has been measuring surface CO_2 for close to a decade, predominantly during transects from Sutton harbour to stations L4 and E1. The showerhead equilibrator used on the Quest takes 6 –10 minutes to equilibrate and the final measurement is biased towards the most recent water to enter the equilibrator (at the end of the equilibration period|). Over this timeframe and in these waters, fCO_2 can change by >20 µatm. Not only do the reported showerhead measurement locations not evenly represent the water that has influenced them; as the system never fully equilibrates for a single water mass with a fixed fCO_2 the measurements are potentially highly inaccurate. It is possible for the positions of the fCO_2 measurements to be corrected so that they represents the water sampled but the fCO_2 measurements can not be retrospectively adjusted to provide accurate averages of fCO_2 over the sampling region. If the concentration change along the transect is known it would be possible to model the expected showerhead fCO_2 at the time of measurement based on the response time of the equilibrator. The horizontal variability present in this region calls into question the suitability of the showerhead style equilibrator used in the system and therefore the accuracy of the measurements made close (<8km) to the coast.

Over a homogenous region this would have a minimal impact on the flux, but in a dynamic region it complicates the analysis of fluxes and the modelling of sources and sinks of inshore carbon. For localised field observations like those made at Penlee Point Atmospheric Observatory (Yang et al., 2015), having the correct concentration for a localised region such as a flux footprint (typically 1–2 km) is essential. The horizontal variability and slow equilibration time of the showerhead CO_2 system precludes accurate pCO_2 and gas transfer velocity estimates in the footprint when used in conjunction with a method for directly measuring the flux such as eddy covariance or dual tracer analysis.

An important consideration for future measurements is the route taken by the Quest when leaving and returning from L4 and E1. The route has previously been a direct line back to port but this has not provided local high resolution CO_2 measurements. The pCO_2 patterns change substantially depending on the state of the tide and thus the route of the ship crosses different features depending on the state of the tide. For example, at high water the region out from the breakwater is much more homogeneous whereas at other times there are multiple water masses and pCO_2. The timing of the ship leaving and returning to port is influenced by the tide meaning that the pCO_2 are not representative of all stages of the tide. All of this makes it difficult to get representative samples of the regional CO_2.

The large spatial variability in CO_2 is also seen in the temperature over short distances (hundreds of meters). Traversing these distances can take just a few minutes. The thermistors used to measure the underway temperature (e.g. seabird) are incredibly fast (<1s) to respond to temperature shifts and are able to capture the temperature shifts in these regions. In contrast the equilibrator temperature in most CO_2 systems is measured by immersion RTD PT100s which can have a temperature response time of close to a minute (double the response time of CO_2 in the liqui–cel CO_2 system). A temperature response time of a minute is suitable for a showerhead CO_2 system with a long response time and can be used in a homogenous ocean. However the RTD PT100s become limiting in a dynamic region such as near the coast or inshore. These results suggest that the response of the equilibrator temperature sensor should also be considered when sampling in a dynamic coastal region.

6.10 Conclusions

The underway showerhead CO_2 system on the quest is unable to resolve small scale features; these can only be identified using the high resolution liqui–cel CO_2 system. The horizontal transects data using the liqui–cel system demonstrate the large spatial variability between Plymouth Breakwater and L4. The salinity and pCO_2 in the Western Channel Observatory are tidally controlled with the pCO2 fields changing substantially depending on the state of the tide. Changes in CO_2 mirror those in salinity with the highest regions of CO_2 coinciding with the lowest salinity regions and vice versa. Measured salinity agreed well with modelled surface salinity at different states of the tidal cycle and had an inverse relationship with CO_2.

The surface flux from estuaries has been difficult to fully assess without knowledge of the surface area of the estuaries and a lack of data (Borges et al., 2006). The high resolution CO_2 data show that within a tidal cycle coastal waters can quickly transition from a strong source to a strong sink depending on the state of the tide. Inland waters are discounted from regional estimates of CO_2 flux due to lack of data (Chen et al., 2013, Laruelle et al., 2014) but these measurements indicate that they may be sampled using a high response time equilibrator. The liqui–cel high resolution CO_2 data show that coastal regions also needs to be characterised at different states of the tide, complicating the task of data collection even further.

7 A seasonal study of vertical variability in surface seawater CO_2 at the Western Channel Observatory

7.1 Introduction

The chapter follows from chapter 4 and details additional measurements made with the NSOP (chapter 3) as part of a seasonal study at the Western Channel Observatory (chapter 5). This chapter seeks to answer the same hypotheses as those presented in chapter 4 but in the context of the coastal ocean.

How frequent are near surface CO_2 gradients?

How large are near surface gradients in CO_2?

Can near surface CO_2 gradients be predicted with meteorological variables?

Does horizontal variability in CO_2 impact vertical gradients?

7.2 NSOP deployments overview

Rough weather conditions were expected to drastically reduce the number of deployment opportunities in the winter, so the seasonal study was planned for the middle of spring through to the middle of autumn. This also meant that the seasonal study had a sampling bias towards the summer months when stratification was more likely. 16 weekly NSOP deployments were made (April 27th and October 21st 2016) and a total of 71 profiles were collected (Table 5).

Due to the working hours of the crew and the desire to target the time of day with the highest irradiance, all of the deployments were conducted between the late morning and mid–afternoon. The start and end time of day of each of the 71 profiles made during these 16 deployments are shown in (Table 5).

All deployments were made at the Western Channel Observatory 0.5 – 1 km away from the L4 mooring (Figure 7.1). The ship only drifted further than 1 km during the deployments on the 27th April and 26th May.

A one sample Kolmogorov– Smirnov test ($p<0.05$) identified that wind speed for the 71 profiles was normally distributed around an average wind speed of 6.7±3.1 ms^{-1} larger than the median wind speed over of 3 ms^{-1} (Smyth et al., 2010b). The majority of the profiles (64 of 71) were made in ‘calm’ to ‘moderate’ sea states (Beaufort force 1 – 5) when the wind speeds were <11ms^{-1}. 7 of the 71 profiles were made when the sea state was considered ‘rough’ (Beaufort force 6, wind speeds 11 –14 ms^{-1}, wave height 3.0m).

The average PAR during the 71 profiles was 1029.06 ±473Wm^{-2}, as expected for profiles made around midday. The PAR for the 71 profiles had a bimodal distribution as identified by a Hartigan’s dip test ($p<0.05$), with peaks of ~1400 Wm^{-2} and ~600 Wm^{-2}. The strongest irradiances were observed predominantly in mid–summer (June to August) and the lowest irradiances were seen in late summer and early autumn (August and September).

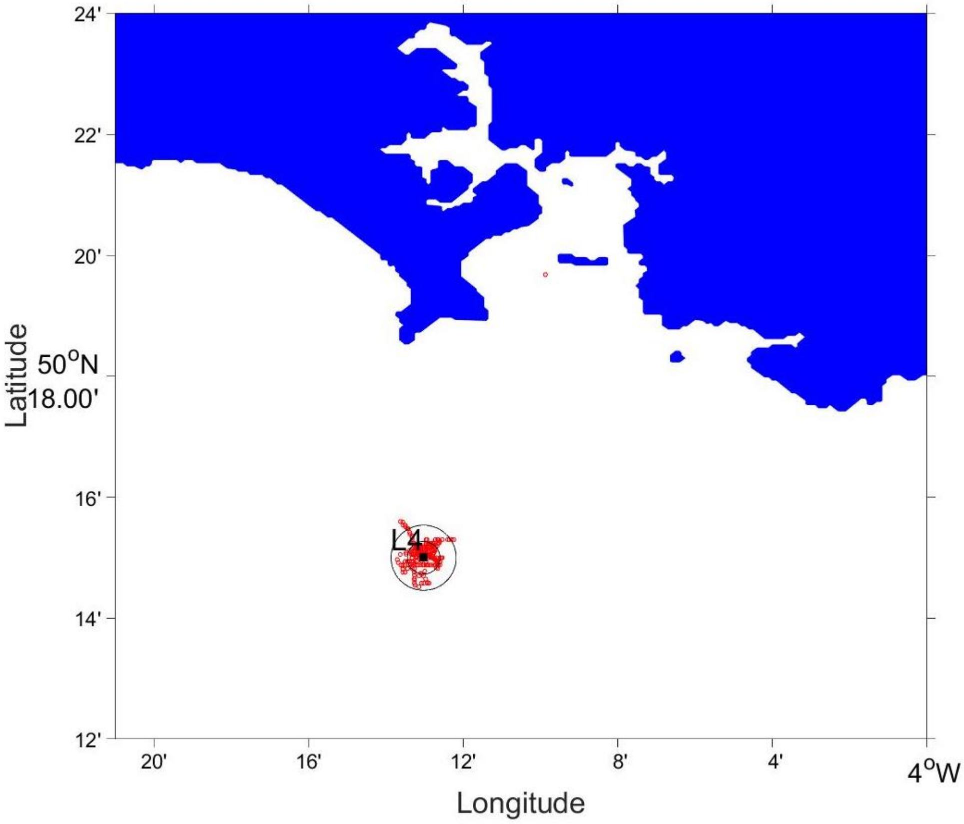

Figure 7.1 Sampling tracks around the L4 mooring

Sampling track of the RV Plymouth Quest (red) around the L4 mooring (black square) during the 16 NSOP deployments of the seasonal study. The two concentric black circles indicate 0.5 and 1 km from the location of the mooring.

Table 5 NSOP seasonal study overview table
NSOP seasonal study deployments overview table.

Deployment date	Profile start and end times (UTC)	Average Wind Speed (ms^{-1})	Beaufort wind speed classification and corresponding sea state description	Average irradiance (Wm^{-2})	Tidal height (m)
2016-04-27	11:33–12:13	2.2025	Smooth	1112.680319	4.7596
	12:13 – 12:38	3.843	Smooth	1602.804501	4.759
2016-05-11	10:53–11:33	4.9419	Slight	726.1784256	5.3617
	11:33 – 11:51	4.9455	Slight	725.8279061	5.3619
	11:56 – 12:11	4.948	Slight	725.5741022	5.3622
	12:11 – 12:18	4.9494	Slight	725.4345895	5.3624
2016-05-26	10:50 – 11:03	8.38	Slight - Moderate	1449.680226	4.9414
	11:48 – 12:05	6.906	Slight - Moderate	1626.964345	4.9409
	12:05 – 12:22	7.7721	Slight - Moderate	1499.379597	4.9407
	12:22 – 12:34	7.8467	Slight - Moderate	1718.180329	4.9405
2016-06-10	11:51 – 12:06	1.8837	Calm (rippled)	592.8960851	4.6583
	12:06 – 12:19	1.587	Calm (rippled)	683.2854364	4.6588
	12:19 – 12:31	1.6791	Calm (rippled)	738.3253433	4.6592
2016-06-15	11:28 – 11:47	9.5959	Moderate	937.9667693	2.2626
2016-06-22	11:06 – 11:38	4.1216	Slight	1378.037896	4.4121
	11:38 – 12:15	1.8677	Calm (rippled)	1404.627855	4.4108
	12:15 – 12:43	5.2695	Slight	1759.389516	4.4097

	12:43 – 13:13	5.9734	Slight	1550.898366	4.4088
	13:13 – 13:34	6.5084	Slight - Moderate	1295.029866	4.4077
	13:34 – 13:54	6.254	Slight - Moderate	890.61485	4.4065
2016-06-30	11:20 – 11:46	6.9918	Slight - Moderate	1428.789126	2.2352
	12:08 – 12:35	6.8993	Slight - Moderate	1617.205382	2.2376
	12:35 – 12:50	6.9845	Slight - Moderate	1783.043276	2.2387
	12:53 – 13:33	8.1834	Slight - Moderate	1234.463324	2.2397
	13:33 – 13:59	8.8484	Moderate	862.8957646	2.2399
	13:59 – 14:06	7.6747	Slight - Moderate	836.5446984	2.2422
2016-07-07	10:26 – 11:01	2.1847	Smooth	809.756373	5.1414
	11:32 – 11:55	1.5435	Calm (rippled)	1652.685604	5.14
	11:55 – 12:23	5.3178	Slight	1409.991497	5.1395
	12:53 – 13:15	1.5527	Calm (rippled)	1442.247356	5.1381
	13:15 – 13:42	9.0273	Moderate	1473.991023	5.1375
	13:55 – 14:12	8.8303	Moderate	1543.443006	5.1365
	14:12 – 14:31	6.7266	Slight - Moderate	1521.026326	5.136
	14:31 – 14:47	10.0309	Moderate	1328.720742	5.1356
2016-07-13	11:26 – 12:04	9.877	Moderate	1015.550035	3.477
	12:04 – 12:28	11.1298	Moderate	1123.008365	3.478
	12:28 – 12:43	11.9417	Moderate	1192.642757	3.4789
	12:49 – 13:01	12.0675	Moderate	1767.786305	3.4799
	13:01 – 13:13	10.7541	Moderate	1197.246275	3.4806
	13:29 – 13:45	10.251	Moderate	2086.568188	3.4823
2016-08-04	11:30 –	8.401	Slight -	1014.02684	4.2303

	12:00		Moderate	3	
	12:09 – 12:40	7.2475	Slight - Moderate	1178.546799	4.2285
	12:40 – 13:25	7.4824	Slight - Moderate	1606.469326	4.2271
	13:25 – 13:47	7.8162	Slight - Moderate	1794.263346	4.2257
2016-08-10	13:02 – 13:18	7.5798	Slight - Moderate	1015.718158	4.2753
	13:18 – 13:29	5.9472	Slight	1264.457109	4.2756
	13:47 – 14:00	4.4288	Slight	794.2961338	4.2764
2016-08-17	11:06 – 11:22	12.0598	Rough	710.6860393	3.4149
	11:33 – 12:01	12.5109	Rough	513.2365762	3.4128
	12:01 – 12:21	12.8163	Rough	502.0763244	3.4116
	12:30 – 12:46	11.5652	Rough	424.6921938	3.4101
2016-08-24	10:47 – 11:07	8.18	Slight - Moderate	1387.500879	4.5651
2016-09-02	11:03 – 11:22	8.8575	Moderate	317.1710916	4.3039
	11:38 – 11:53	9.5042	Moderate	270.0362592	4.302
	11:53 – 12:10	9.1984	Moderate	385.7657767	4.301
2016-09-15	10:29 – 10:51	8.7303	Moderate	384.5946203	2.8855
	11:05 – 11:24	4.188	Slight	411.7287293	2.8835
	11:24 – 11:42	2.8305	Smooth	301.7990713	2.8824
	11:46 – 12:08	2.9515	Smooth	460.0613962	2.881
	12:08 – 12:29	2.8035	Smooth	489.5895672	2.8798
	12:29 – 12:53	3.7037	Smooth	616.1881539	2.8786
	12:53 – 13:11	3.746	Smooth	543.8429727	2.8774
	13:11 – 13:28	2.928	Smooth	633.3702135	2.8764
2016-09-21	08:38 – 9:05	5.8834	Slight	363.8180593	5.158

	09:15 – 9:37	3.935	Smooth	746.167386	5.159
	09:37 – 9:55	3.8256	Smooth	655.0772709	5.1596
	10:14 – 10:39	4.2951	Slight	563.2875196	5.1609
	10:39 – 11:01	7.6377	Slight - Moderate	503.2793009	5.1614
	11:11 – 11:42	9.4115	Moderate	556.1484186	5.1623
	11:42 – 12:06	8.7664	Moderate	825.6362545	5.1629
	12:06 – 12:17	8.8091	Moderate	1358.438424	5.1635

7.3 Data description conventions for salinity, temperature and CO_2

Profiles where a variable increases towards the surface are defined as having positive gradients and vice versa. For simplicity, deployments are referred to by the deployment date (dd/mm) format. Δ Salinity, temperature and CO_2 gradients are always referred to as occurring over ~4.5m between the maximum and minimum NSOP sampling depths of 0.5m and 5m. ΔS, ΔT ΔCO_2 are all gradients measured over a fixed length scale of 4.5m.

7.4 Salinity profiles

Salinity profiles made during each deployment are presented individually (Figure 7.2 &Figure 7.3). Negative ΔS are evident in almost all of the profiles (e.g. deployments on 11/05, 15/06, 13/07, 10/08 and 15/09). The size of the ΔS is variable, with gradients of 0.01 on (08/10 and 09/15) and large gradients of 0.1 between 0.5m and 5m on 22/06 and 30/06. The salinity declines linearly with depth in most of the profiles with a few exceptions where there is evidence of inversions in the ΔS e.g. at 2m on 11/05 and 02/09 and at 1m on 10/06. For many of the deployments where multiple salinity profiles were made, the magnitude and direction of the ΔS is the same between profiles, indicating that the ΔS persist in the short term (>2 hours). There are also some deployments where the salinity declines over time but the magnitude of the gradient remains the same e.g. 07/07 ~0.04–0.05. Deployments on 27/04, 26/05 and 21/09 had salinity profiles that changed considerably over time. Distinct salinity shifts suggest a water mass change. There are very few outliers from among the profiles, with only a few points at deeper depths on 10/06 and 04/08 varying wildly from the rest of the profiles.

7.5 Temperature profiles

Temperature profiles made during each deployment are presented individually (Figure 7.4 & Figure 7.5). The majority of the profiles either had positive gradients (e.g. 22/06, 30/06 and 07/07) or had a negligible (<0.04°C) ΔT (e.g. 10/06, 15/09). There were a number of slightly negative profiles at the start of some deployments (e.g. On 26/05, 13/07 and 17/08), later in these deployments there were positive ΔT. The majority of deployments had at least one profile where there was a strong positive ΔT of >0.1°C, (26/05, 22/06, 30/06, 07/07, 04/08, 10/08, 24/08, 02/09 and 21/09). When there was a ΔT, the general trend in almost all the temperature profiles was for a linear decrease in temperature with depth. There were few exceptions to the linear trend (e.g. on 07/07 when the temperature changed suddenly). Where there were multiple temperature profiles made during the same deployment, many had ΔT of the same direction and magnitude, (e.g. 22/06, 30/06, 07/07, 04/08 and 10/08). During some of the deployments the ΔT changed sharply between profiles (e.g. 27/04, 26/05, 13/07, 17/08, 15/09 and 21/09). Profiles where the temperature drifted suddenly were consistent with when salinity shifted suddenly (e.g. 27/04, 26/05 and 21/09), this could be indicative of water mass change.

7.6 CO_2 profiles

CO_2 profiles made during each deployment are presented individually (Figure 7.6 & Figure 7.7). The CO_2 profiles show multiple examples of both positive and negative gradients. CO_2 profiles from the beginning of the seasonal study in May and early June (11/05, 26/05, 10/06 and 15/06) and those near the end of the study (17/08, 02/09 and 15/09) tended to have smaller (< 3 µatm) gradients. In contrast, profiles at the end of June and the start of

September (22/06, 30/06, 07/07, 13/07 and 10/08) tended to have gradients > 3 μatm. The CO_2 profiles increased or decreased approximately proportionally to depth for the majority of the gradients. A few profiles show distinct changes at 3–4m (27/04, 30/06, 04/08 and 02/09). There are significant differences between profiles on the same deployment for many of the days, (e.g. 04/08 and 17/08) based on a two sampled t-test using data from subsequent profiles. Only 5 deployments (11/05, 04/08, 17/08, 15/09 and 21/09) had similar profiles.

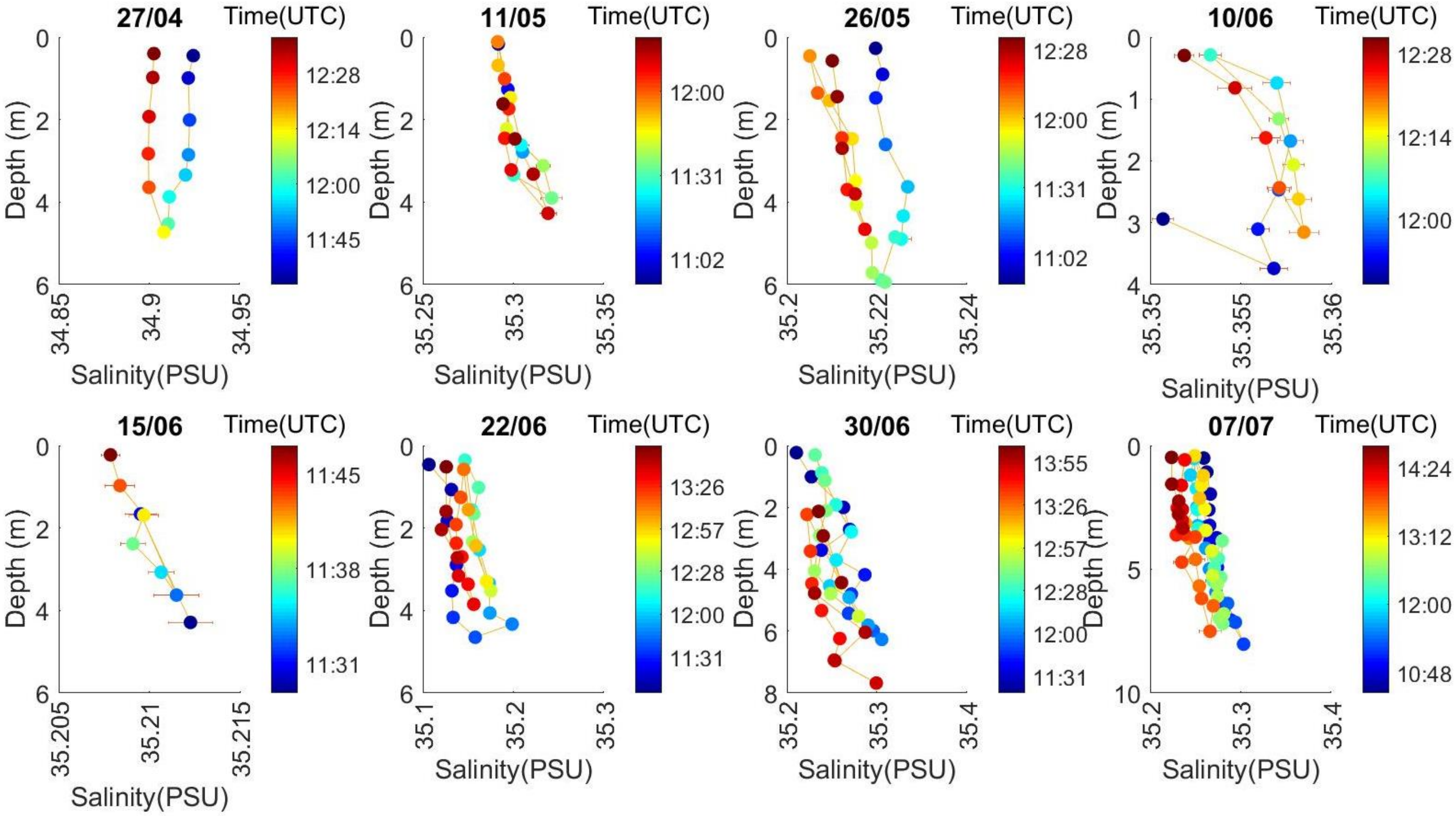

Figure 7.2 Station L4 salinity profiles (1 of 2)

The first 8 of 16 NSOP salinity profiles made at station L4 between April and September 2016. NSOP profiles of salinity were derived using the depth bins determined in chapter 2. Data points are coloured by sampling time. Vertical and horizontal error bars show two standard errors of the mean in each depth bin. The date of each deployment is given above each subplot.

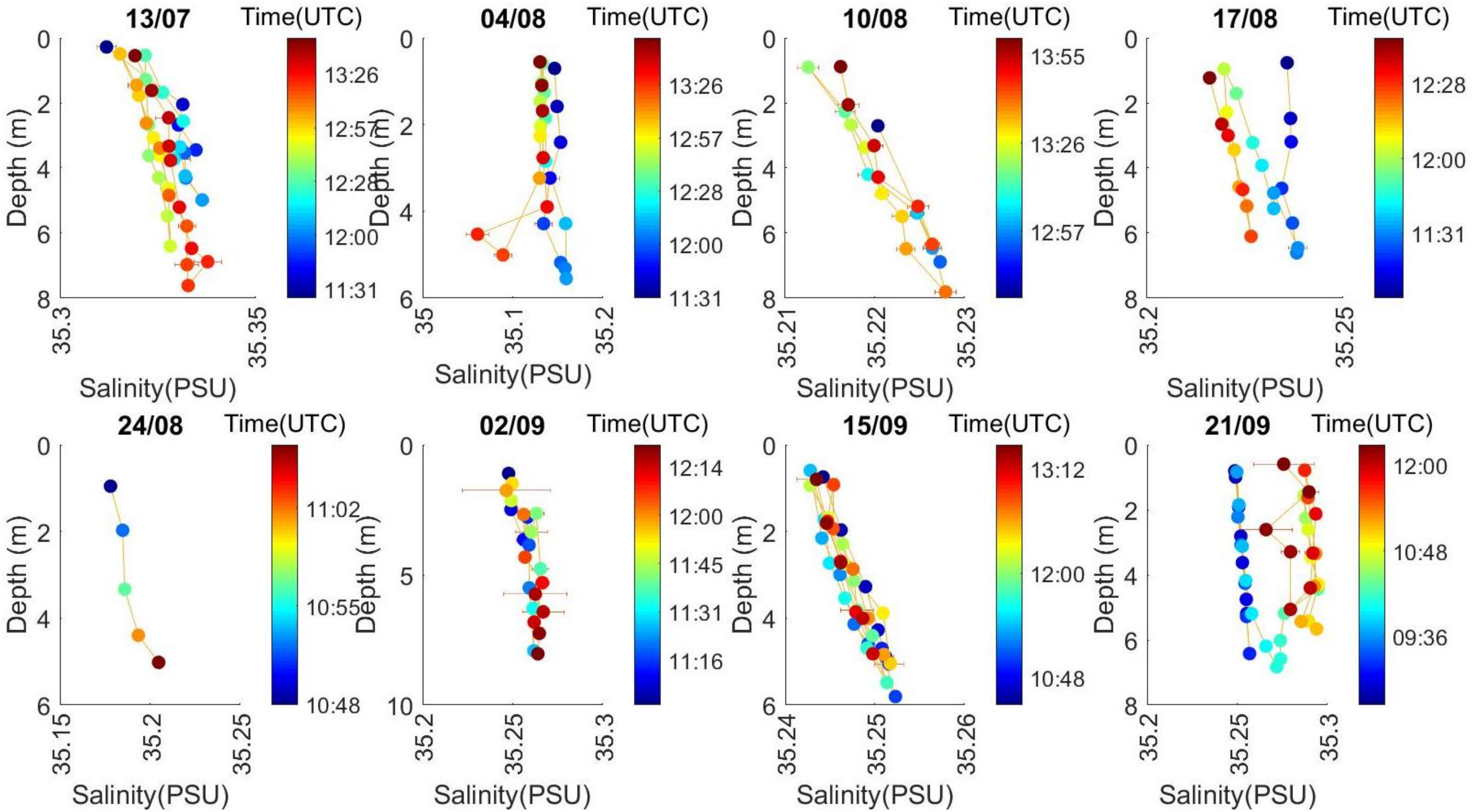

Figure 7.3 Station L4 salinity profiles (2 of 2)

The last 8 of 16 NSOP salinity profiles made at station L4 between April and September 2016. NSOP profiles of salinity were derived using the depth bins determined in chapter 2. Data points are coloured by sampling time. Vertical and horizontal error bars show two standard errors of the mean in each depth bin. The date of each deployment is given above each subplot.

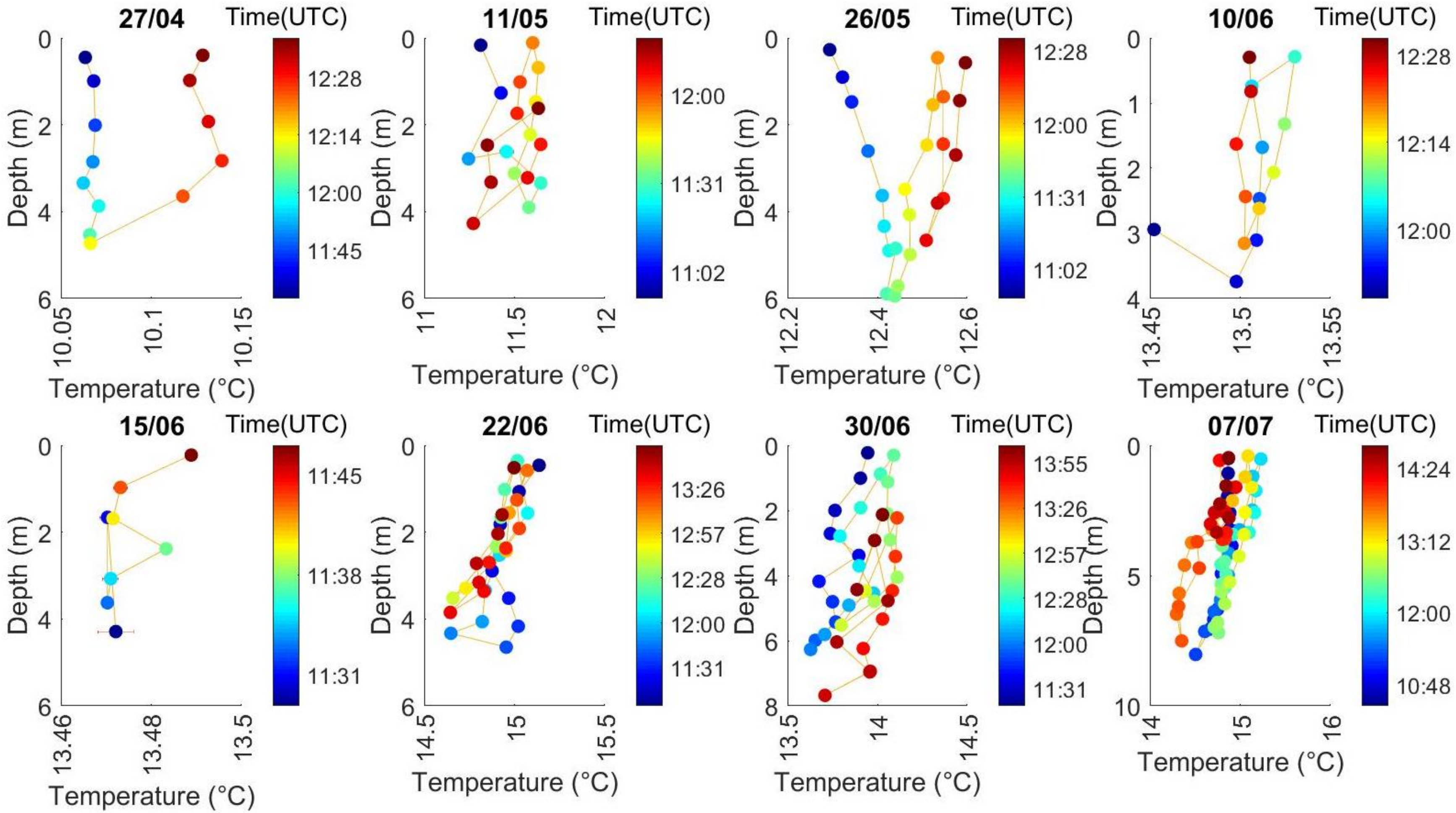

Figure 7.4 Station L4 temperature profiles (1 of 2)

The first 8 of 16 temperature profiles made at station L4 between April and September 2016. NSOP profiles of temperature were derived using the depth bins determined in chapter 2. Data points are coloured by sampling time. Vertical and horizontal error bars show two standard errors of the mean in each depth bin. The date of each deployment is given above each subplot.

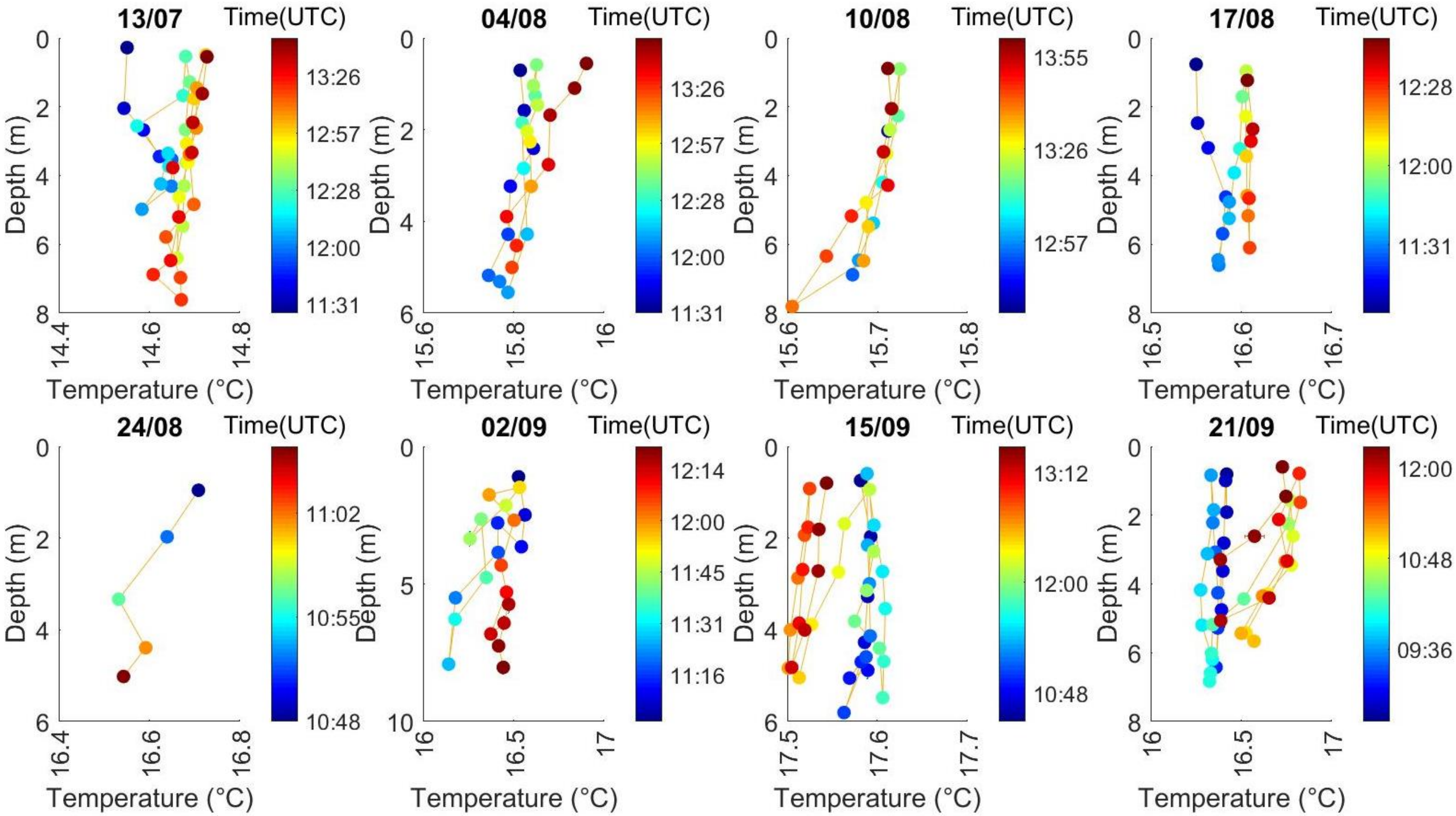

Figure 7.5 Station L4 temperature profiles (2 of 2)
The last 8 of 16 temperature deployments made at station L4 between April and September 2016. NSOP profiles of temperature were derived using the depth bins determined in chapter 2. Data points are coloured by sampling time. Vertical and horizontal error bars show two standard errors of the mean in each depth bin. The date of each deployment is given above each subplot.

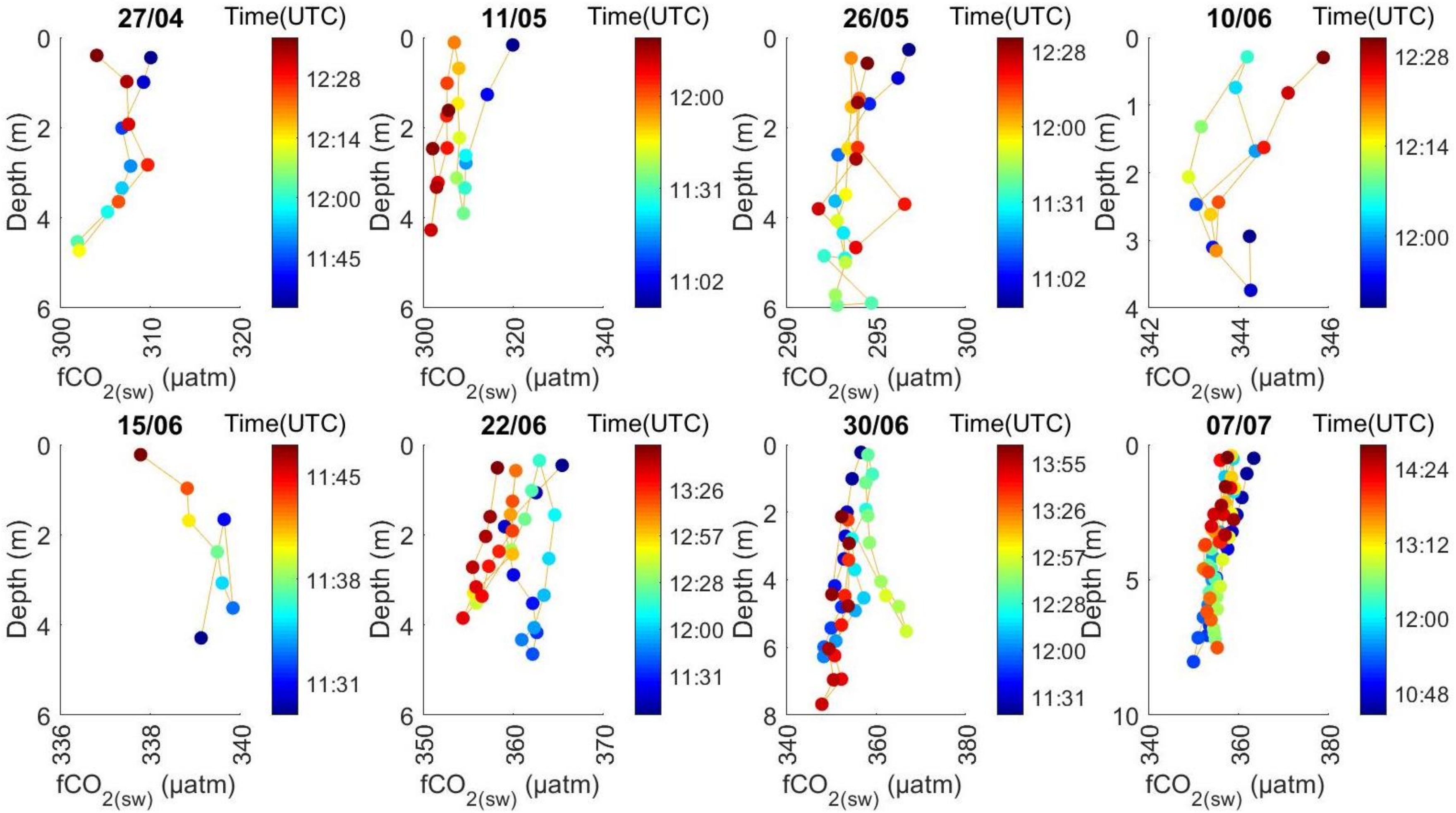

Figure 7.6 Station L4 CO_2 profiles (1 of 2)

The first 8 of 16 CO_2 deployments made at station L4 between April and September 2016. NSOP profiles of CO_2 were derived using the depth bins determined in chapter 2. Data points are coloured by sampling time. Vertical error bars show two standard errors of the mean in each depth bin. The horizontal errors are the propagated errors using the averaged bin variables to calculate fCO_2. The date of each deployment is given above each subplot.

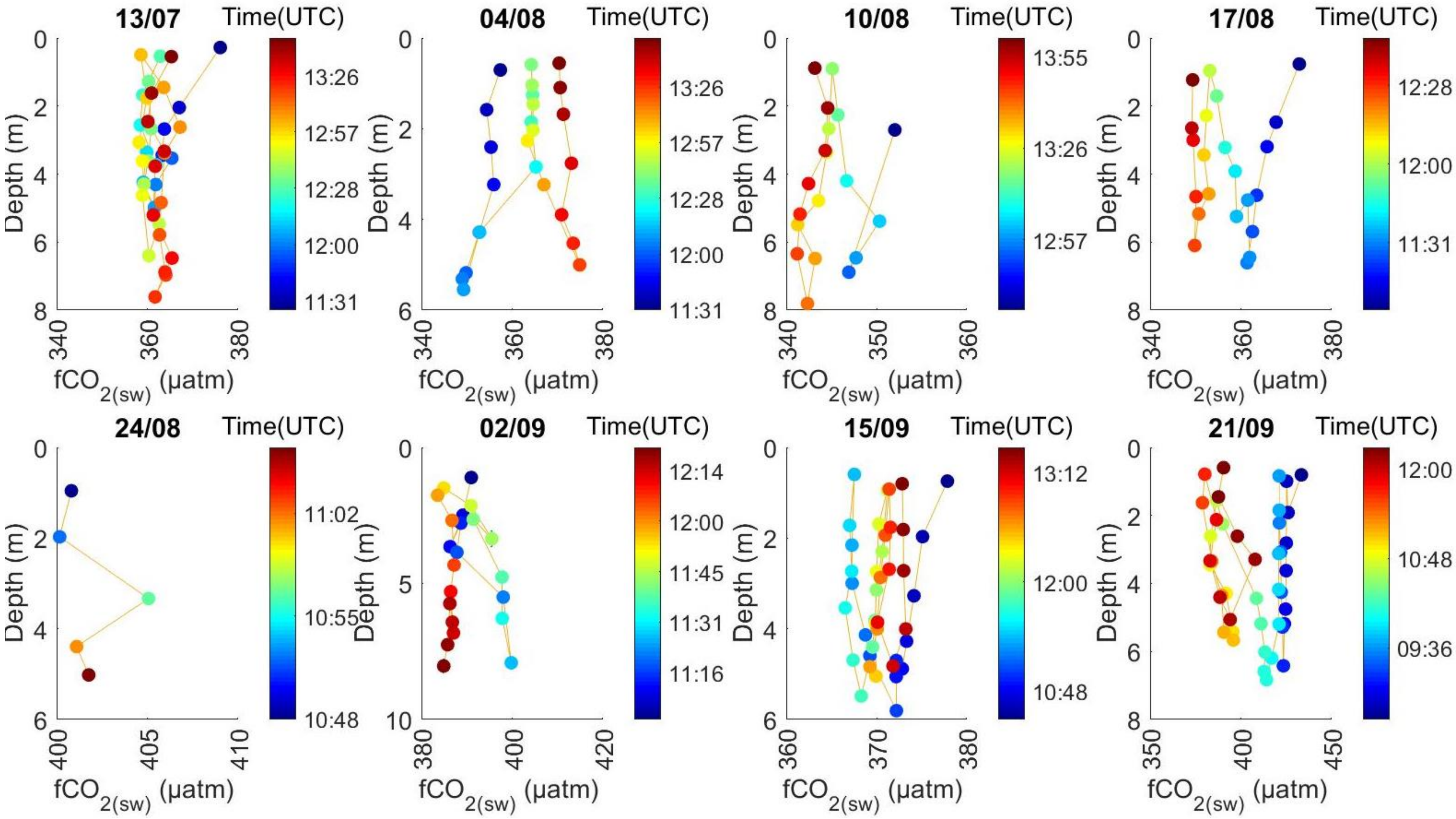

Figure 7.7 Station L4 CO_2 profiles (2 of 2)

The last 8 of 16 CO_2 deployments made at station L4 between April and September 2016. NSOP profiles of CO_2 were derived using the depth bins determined in chapter 2. Data points are coloured by sampling time. Vertical error bars show two standard errors of the mean in each depth bin. The horizontal errors are the propagated errors using the averaged bin variables to calculate fCO_2. The date of each deployment is given above each subplot.

7.7 Profile interpretation

During the deployments on 22/06, 30/06, 07/07 and 02/09 multiple profiles were measured over several hours with strong positive (> 5µatm) ΔCO_2. On these 4 deployments there were also strong persistent ΔT (>0.5°C). On 02/09 there were positive 0.02 gradients whereas on the other three deployments there were negative ΔS of 0.05. Whilst there are clear positive profiles during 30/06 and 02/09 some profiles during the same deployment diverge from the positive trend. The largest ΔCO_2 correspond to the largest ΔS and ΔT and suggests that stratification is an important pre–requisite for the formation of ΔCO_2. There were also strong positive gradients in CO_2 on 27/04 but unlike the deployments described above, the temperature and salinity changed throughout the deployment. Salinity reduced by 0.027 and temperature increased by 0.06°C between profiles. The CO_2 was consistent when these temperature and salinity changes were occurring, these observations are difficult to reconcile as the change in salinity would need to involve mixing which would likely change the CO_2.

On three deployments the CO_2 changed continuously (11/05, 10/08 and 17/08). Constant change was also seen in the temperature profiles on 10/08 and 17/08. Salinity profiles showed consistent negative gradients. During these deployments the largest temperature changes corresponded to the largest CO_2 changes. The profile measured on 04/08 was unique in that the CO_2 was changing throughout the deployment whilst there was a positive ΔT and no ΔS near the surface (< 3m). During individual profiles the CO_2 was constant but changed dramatically below 3m where there were coincident changes in salinity. If the surface 3m was isolated by near surface stratification it is difficult to explain the large 15 µatm decline without assuming these changes were caused by the advection of different water masses.

On 21/09, NSOP profiled continuously for 4 hours from 08:30 to 12:30 and conducted 8 profiles; these profiles show a changing regime. In the morning there were negligible gradients in temperature, CO_2 or salinity. After 10:00 the surface (<4m) quickly became stratified. CO_2 dropped as the temperature increased within the top 4m. The near surface temperature mooring confirms the NSOP observations. Stratification was observed in the surface (<4m) and temperature declined sharply down to 7m. The positional data from the ship indicated that during this deployment, the ship did not drift further than 1 km during the deployment, which excludes drift as a likely explanation for the large drop in CO_2. There is also a large distinct change in salinity concurrent with the temperature and CO_2 change. These data indicate that there must have been a shift in water mass during the deployment. It is possible that the strong negative gradient in the last few CO_2 profiles was caused by CO_2 uptake by phytoplankton once the surface had become stratified but this seems unlikely given earlier calculations (section 2.2.1). The sharp decline in CO_2 was also observed by the underway CO_2 system and is a further indicator of horizontal advection of water across the NSOP station. Temporal and horizontal variability around L4 is a confounding issue when interpreting the vertical profile data. These issues will be discussed further in the following chapter.

Some deployments had negligible ΔCO_2 and little inter profile variability (26/05, 10/06, 15/06, 13/07, 24/08 and 15/09). During some of these deployments such as 10/06, 15/06 and 15/09 the surface ocean was not stratified at the near surface, ΔT (<0.03°C) and salinity (< 0.01) . Mild temperature (~ 0.1–0.2°C) and strong ΔS (~ 0.03°C) correspond with minimal

CO_2 change on 26/05, 13/07 and 24/08. These changes suggest that the water mass did not change during these deployments.

7.8 Advection of water masses at L4

A full diurnal cycle was not conducted as part of the NSOP sampling but the on station sampling often lasted 2–3 hours. For the majority of deployments (15/06, 22/06, 07/07, 13/07, 02/09 and 15/09) the CO_2 recorded by the showerhead system varied by <10 µatm for the duration of the deployment. This gives some confidence that the advection of different water masses did not occur too frequently. However there were two deployments (04/08 and 21/09) where the CO_2 on station changed substantially (Figure 7.7). At the beginning of the deployment (high water) on 04/08 the CO_2 increased rapidly by ~30 µatm whilst on 21/09 the CO_2 decreased rapidly by ~40 µatm half way through the deployment (low water). These large changes were detected by both the showerhead and liqui-cel measurement systems. The salinity dropped 0.05 on 04/08 suggesting a freshwater influence, whereas the salinity increased by 0.05 on 21/09 suggesting mixing with saltier waters.

In a tidally forced coastal system it is expected that the falling tide would bring low salinity/ high CO_2 estuarine waters out to L4 and rising tide would cause the advection of higher salinity/ lower pCO_2 waters from the channel. These changes were observed at low water on 04/08 with higher pCO_2 and lower salinity waters reaching L4 and on 21/09 at high water the pCO_2 falling and the salinity increasing. More evidence for the influence of tides here was that 21/09 was two days after the peak of the spring tide meaning that the tides were strongest at this point and may explain why the transport of riverine waters was observable at L4. The transects from 04/08 and 21/09 show that the high pCO_2 / low salinity riverine water masses extended well past Penlee on these days and it is likely they reached L4 during sampling. Bakker et al. (1996) showed that there is a tidal signal in pCO_2 as did Borges and Frankignoulle (1999) who observed a 20 – 25 µatm tidal signal. At coastal sites riverine input can play a substantial role in regionalised pCO_2 (Else et al., 2008). Waters that are as much as 1 less saline have been observed at station L4 (Smyth et al., 2010b). The influence of freshwater input at L4 has also been seen in nutrient data (Rees et al., 2009).

Diurnal variations in surface CO_2 were observed at L4 as part of a 20 hr eulerian study during September 2008 (Litt et al., 2010). CO_2 increased considerably at dawn from 345 to 385 µatm and remained at that level until morning. The pCO2 change was not part of a semi diurnal cycle so was not attributed to local tides. Litt et al. (2010) postulated that to compensate for this increase at night the pCO_2had to fall by an equivalent amount during the (unsampled) 4 hour window in the morning (08:00 – 12:00 hrs). At dusk a biological regime shift where respiration exceeds photosynthesis was proposed to explain the drop in CO_2. The authors speculated that the regime shift was driven by the onset of photosynthesis in the morning (Litt et al., 2010). The issue with this explanation is that it is not physically possible to explain CO_2 changes of this magnitude with literature production rates (Barnes et al., 2014, Barnes et al., 2015) (see chapter 2).

A ~40 µatm change was observed on 21/09 at low water that was the same magnitude as observed by (Litt et al., 2010). A historical reanalysis of the variability of CO_2 measurements made from the Quest whilst on station at L4 may provide more examples of the large CO_2 changes seen during the seasonal study and by Litt et al. (2010). Combined with historical tidal observations from the Devonport tidal gauge and historical rainfall data it may be possible to explain any large changes in the Quest CO_2 record.

The large shifts like those described above are infrequent and were not observed during the majority (14 of 16) of NSOP deployments but may be frequent enough that at tidal extremes they influence the surface CO_2 making the net flux unrepresentative of L4.

7.9 Summary

71 vertical profiles of CO_2, salinity and temperature profiles in the upper 5m were collected during 16 NSOP deployments at the WCO station L4 between April 27th and October 21st 2016. The profiles were measured under a range of wind speeds, irradiances and tides throughout the morning and afternoon.

The vertical profiling at L4 revealed the prevalence of strong (> 0.1) and persistent (stable >3.5 hours) negative ΔS at L4. Positive ΔT (> 0.1°C) were observed in a number of profiles, predominantly in June but also during July and August. The salinity and temperature were much more variable at L4 than during the SSB cruises.

There were a handful of profiles which can be classified as having no ΔCO_2 but in general the CO_2 profiles from L4 are much more variable than the profiles measured during the SSB cruises. 17 profiles had strong positive $\Delta CO_2 > 5$ µatm mostly during June and were coincident with strong ΔT. These June CO_2 profiles were the only ones to show some repeatable structure during deployments. A synthesis of the size of these gradients, their occurrence, predictability and their impacts on the flux will be discussed in a synthesis chapter (chapter 6) along with SSB results from Chapter 3.

Two L4 CO_2 profiles suggest surface CO_2 changes of to 40 µatm during the time of a deployment. When these large changes in CO_2 occurred, large changes in temperature and salinity were also observed. These large shifts in the CO_2 at L4 are like those seen by (Litt et al., 2010). These changes cannot be explained by the biological production data section 2. The likely explanation for this large variability in salinity, temperature and CO_2 profiles is the horizontal advection of different water masses across L4 as was observed further inland in section 6.

8 A synthesis of near surface gradients

8.1 Introduction

The previous chapters outlined the near surface profiles collected during the shelf sea cruises (chapter 3) and at station L4 (chapter 4). In this chapter these measured gradients are analysed in the context of the physical meteorology thought to force them. Other factors thought to confound the interpretation of gradients such as temporal changes in the water column, horizontal advection of water masses (as seen at L4 in chapter 5) and the correcting to sea surface temperature will be discussed.

8.2 Standardising profiles

To be able to compare profiles between cruises and with the seasonal study it was decided that it would be necessary to synthesis the NSOP profiles. A number of metrics were considered including showing changes in temperature, salinity and CO_2 per meter. Whatever metric was chosen would lose some of the information in the profiles such as the profile shape, these aspects of the profiles were discussed in previous chapters. It was decided that the best metric for the profiles would be one that was directly relevant to the air sea flux, for this reason each profile is simplified to Δ changes between the interface and mixed layer.

For each profile the difference in salinity (ΔS), temperature (ΔT) and CO_2 (ΔCO_2) between the surface and 5 m was calculated. To standardise the profiles and account for the differences in profile depths, the values of the variables in the two bins closest to 0.5m and 5m were used to calculate ΔS, ΔT and ΔCO_2 for all the profiles during the Shelf Sea cruises and the seasonal study at L4. Multiple profiles were collected on the seasonal study deployments. 29 Profiles were collected during the SSB cruises and 71 profiles collected at L4. Each profile was interpreted separately.

The sampling approach was inconsistent on the cruises, such that not all profiles contain measurements at 0.5 and 5m. Six profiles from the SSB cruises (17/8/14, 31/10/2014, 2/11/14, 3/11/14, 3/11/14 and 29/7/2015) had surface bins at >1m. Six profiles had a maximum depth <4m (16/5/2015, 20/5/2015, 21/5/2015, 20/7/2015, 21/7/2015 and 22/7/2015).

8.3 Salinity differences (ΔS)

The ΔS from the SSB cruises were typically small (24/29 ΔS profiles <±0.015), negative (93% of ΔS profiles) and positively skewed (Figure 8.1a). There were no cases of large positive ΔS during the cruises. The ΔS from the L4 profiles were also small -0.011±0.016 and negative (87% of ΔS profiles <0) but were more normally distributed (Figure 8.1b).

These ΔS are much smaller than those observed in the tropics where there is heavy rainfall and ΔS exceed 0.5 (Henocq et al., 2010) but are in line with the average global ΔS of -0.02 (Drucker and Riser, 2014). These observations also agree with Argo data as <3% of Argo observations showed a gradients of >±0.1 (Anderson and Riser, 2014).

These ΔS are unlikely to be rain induced as the salinity only changes in the top 1m during and following rainfall events (Reverdin et al., 2012, Boutin et al., 2016). As diffusion from this surface layer is slow, the bulk salinity below remains unaltered until turbulent forces breakdown the stratified layer (Santos-Garcia et al., 2014). The salinity profiles measured with NSOP showed the salinity increasing with depth down to 3–4m.

There was a large ΔS (-0.1) on July 20th on the July SSB cruise. Whilst this ΔS is the same order of magnitude as for a large rainfall event (Henocq et al., 2010), an identical change in salinity was also observed by Discovery's underway system (at 5m) indicating that salinity changes were seen throughout the water column during this profile. This salinity change is likely the result of water mass movement off the shelf and highlights that advection of water masses can confound profile interpretation (see chapter 1).

Low salinity river water is known to reach station L4 (Smyth et al., 2010b). This occurred during the seasonal study as indicated by the negative salinity anomalies recorded at the mooring. ΔS have been observed in other river plumes such as from the Amazon river (Lentz and Limeburner, 1995) and the same effect may be present at a reduced scale in the Tamar. Freshwater is less dense than seawater and remains at the surface until it is mixed. The depth of this layer and its salinity will be a function of the amount of rainfall and runoff over the land. Stronger ΔS were primarily observed in May and June (Figure 8.1). The large ΔS were seen on 22/06 which was a period when the river flowrate from the river Tamar was strongest, which indicates that high river flowrate corresponds to vertical gradients at L4. It is possible that low salinity water present at the mooring is only observed when the depth of the layer deepens to >1m (below the depth of salinity sensor).

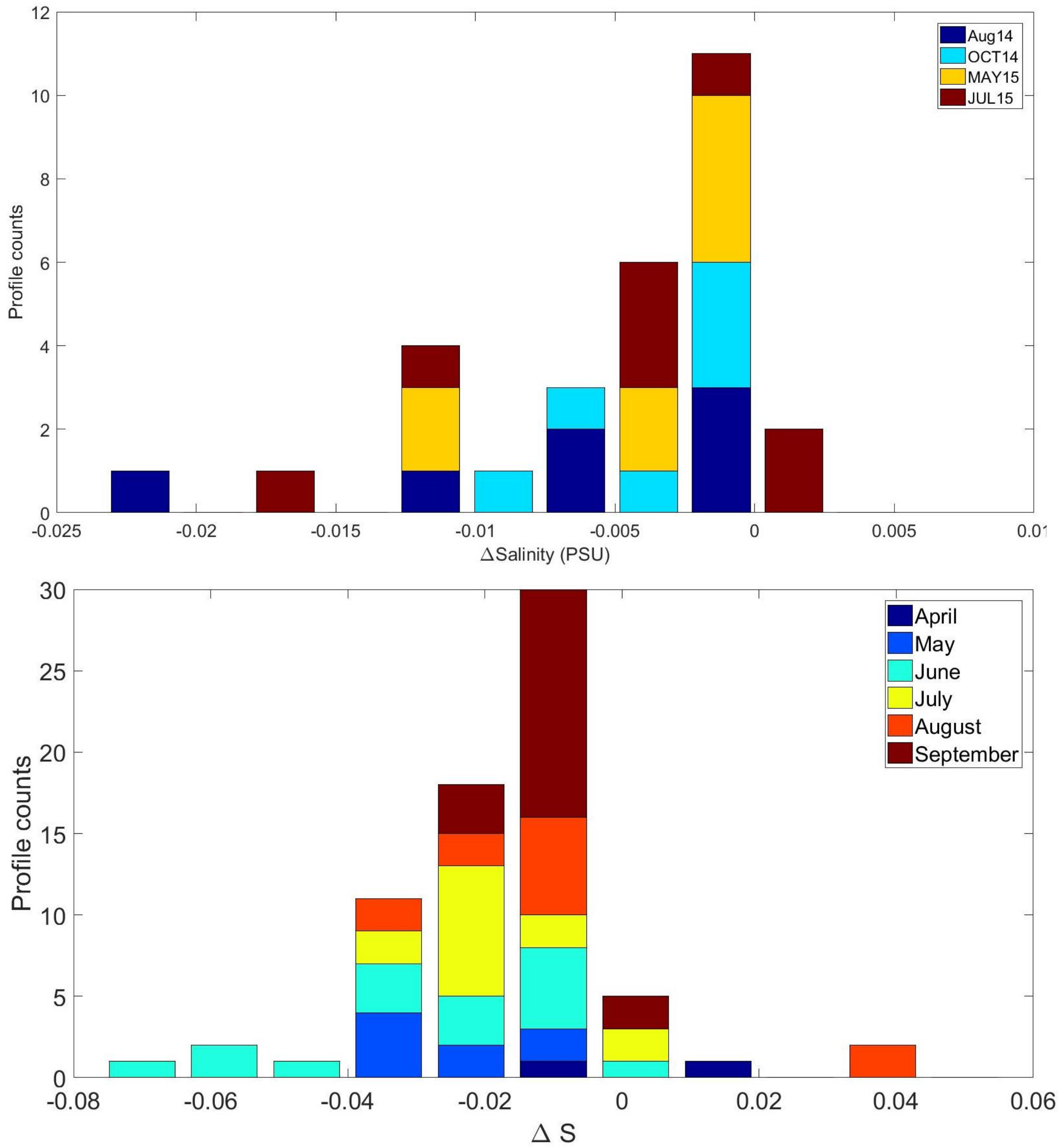

Figure 8.1 Magnitude of ΔS from NSOP profiles
Profile counts for 10 equally spaced bins of the ΔS (as calculated as described in section 8.2) for all 29 profiles from the SSB cruises (a) and 71 profiles made during the 16 NSOP deployments at L4 (b). Note axis limits are not the same.

ΔS from the SSB cruises and L4 are plotted against irradiance (a) and wind speed (b) observed during the deployments in Figure 8.2. There was no correlation between ΔS and the local irradiance during the SSB cruises and at L4. There was no correlation between ΔS and wind speed at L4 whereas during the cruises the larger negative ΔS occur at lower wind speeds. These results suggest that the strength of the physical forcing upon the upper water column does not determine the persistence of ΔS. ΔS are most likely formed due to riverine input and take time to mix into the bulk water.

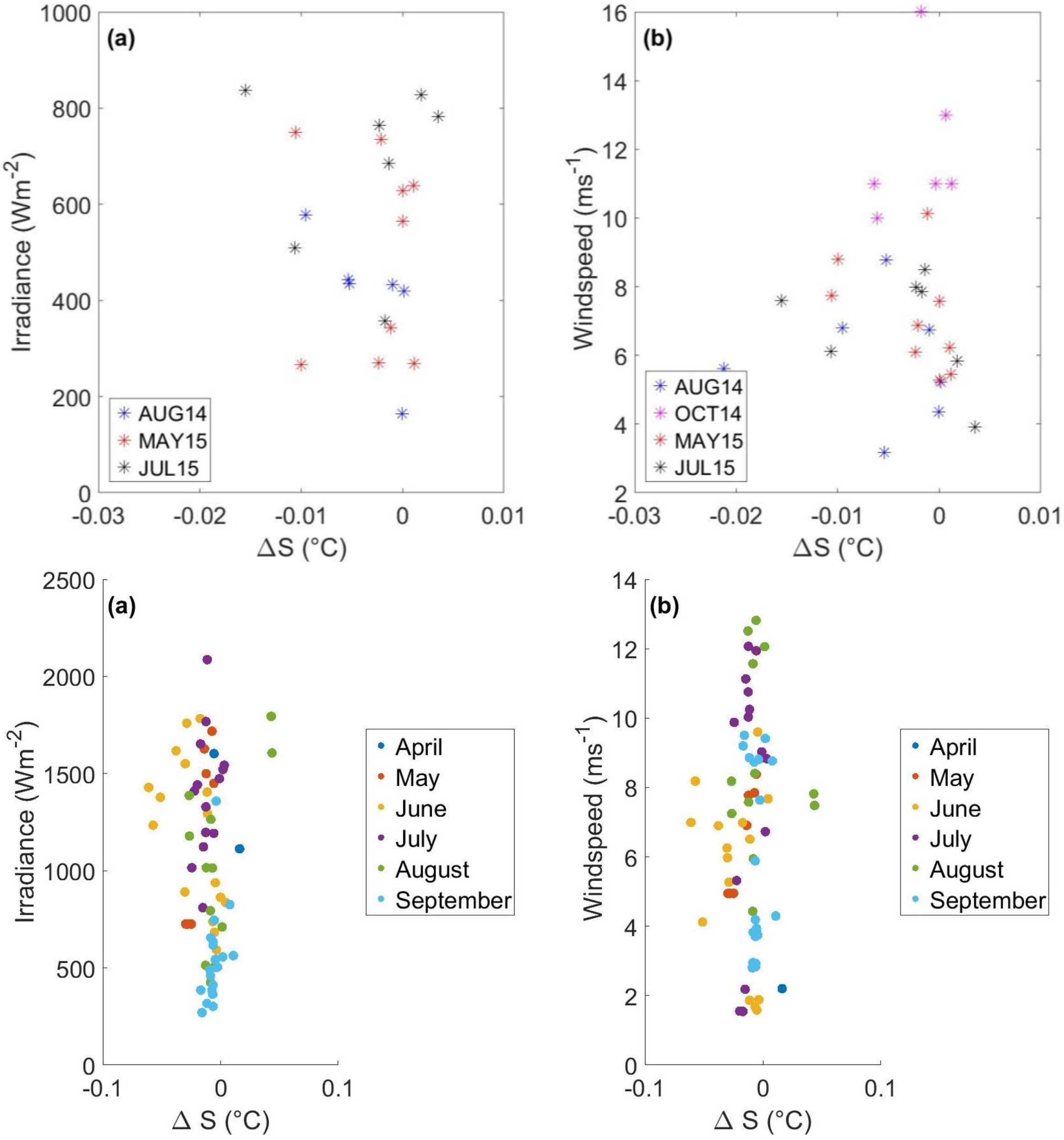

Figure 8.2 ΔS occurrence with irradiance and wind speed

ΔS (as calculated as described in section 8.2) for all 29 profiles from the SSB cruises (top panels) and 71 profiles made during the 16 NSOP deployments at L4 (bottom panels) against the average irradiance (left panels) and wind speed (right panels) of each profile. The marker colours corresponds to different cruises and in different months at L4 as specified in the individual legends. Note axis limits are not the same.

8.4 Temperature gradients

ΔT from the SSB cruises were mostly positive (59% of ΔT profiles >0°C) with an average of 0.17±0.48 °C (Figure 8.3a). The ΔT from L4 were also mostly positive (83% of ΔT profiles>0°C) and had a similar average ΔT of 0.123±0.165°C but a higher maximum ΔT (0.70°C) than the SSB data (Figure 8.3b). The distribution of ΔT is similar for the cruises and L4, with the majority of ΔT being small and positive (44% of L4 profiles 0 to 0.1°C) with fewer observations of higher ΔT. There were few negative ΔT on the SSB cruises. The negative ΔT at L4 were much smaller than the positive ΔT.

The majority of the ΔT measured during AUG14, MAY15 and JULY15 and all ΔT from OCT14 had small ΔT (<±0.05°C). Despite targeting cruises in shelf seas during the spring and summer months and deploying predominantly in the afternoon there were only 5 profiles from AUG14, MAY15 and JULY15 that had a strong positive ΔT (>0.1°C). This is in some ways not surprising given that their formation is weather dependent and the gradients are very transient as indicated by the time series at the near surface temperature mooring (Figure 5.7). These ΔT are much smaller than the near surface profiles measured in equatorial regions where the ΔT are in excess of 0.1°C (Ward et al., 2004a, Prytherch et al., 2013).

Large (>0.1°C) ΔT at L4 did not show a bias to any particular month with days in May, June, July and September experiencing strong ΔT.

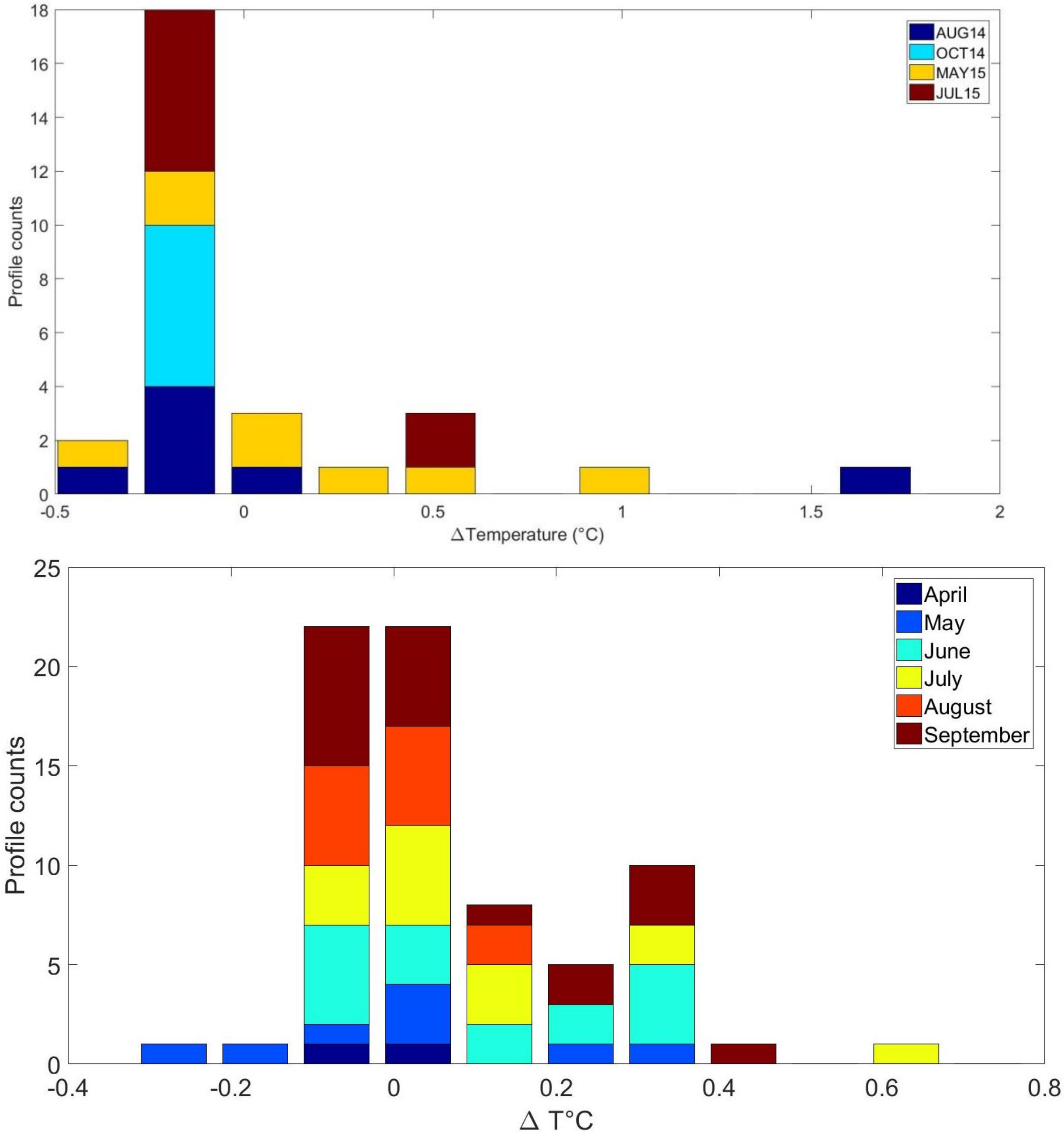

Figure 8.3 Magnitude of ΔT from NSOP profiles

Profile counts for 10 equally spaced bins of the ΔT (as calculated as described in section 8.2) for all 29 profiles from the SSB cruises (a) and 71 profiles made during the 16 NSOP deployments at L4 (b). Note axis limits are not the same.

To determine whether the ΔT recorded with NSOP was seasonally representative of the Celtic Sea and at L4, the measured NSOP ΔT are compared with ΔT determined from the NSTS (near surface temperature sensors) at the CCS (49.403°N, -8.606°E, 2014-08-21 to 2015-08-21) and L4 (2016-05-15 to 2016-11-03) moorings (Figure 8.4). The ΔT at the moorings was calculated every hour as the average difference between the 0.6m (seabird SBE 56 sensors) and 5m (Starmon Centi at the CCS site and Star Odi at L4) temperature sensors. The yearly hourly distribution of ΔT split into100 equally spaced bins is shown for CCS (Figure 8.4a) and L4 (Figure 8.4b).

The distribution of ΔT is very similar at both sites. The majority (88%) of the 8748 ΔT calculated at L4 had a differential between -0.0145 and +0.0106 indicating that a majority of the time there are negligible/no ΔT present in the Celtic Sea. L4 displays a similar pattern. There were a small number of negative ΔT at both sites due to evaporative cooling at the surface during winter when the winds are stronger (Large and Pond, 1982). The frequency of occurrence of larger ΔT were much lower, with ΔT >0.5°C only occurring five times.

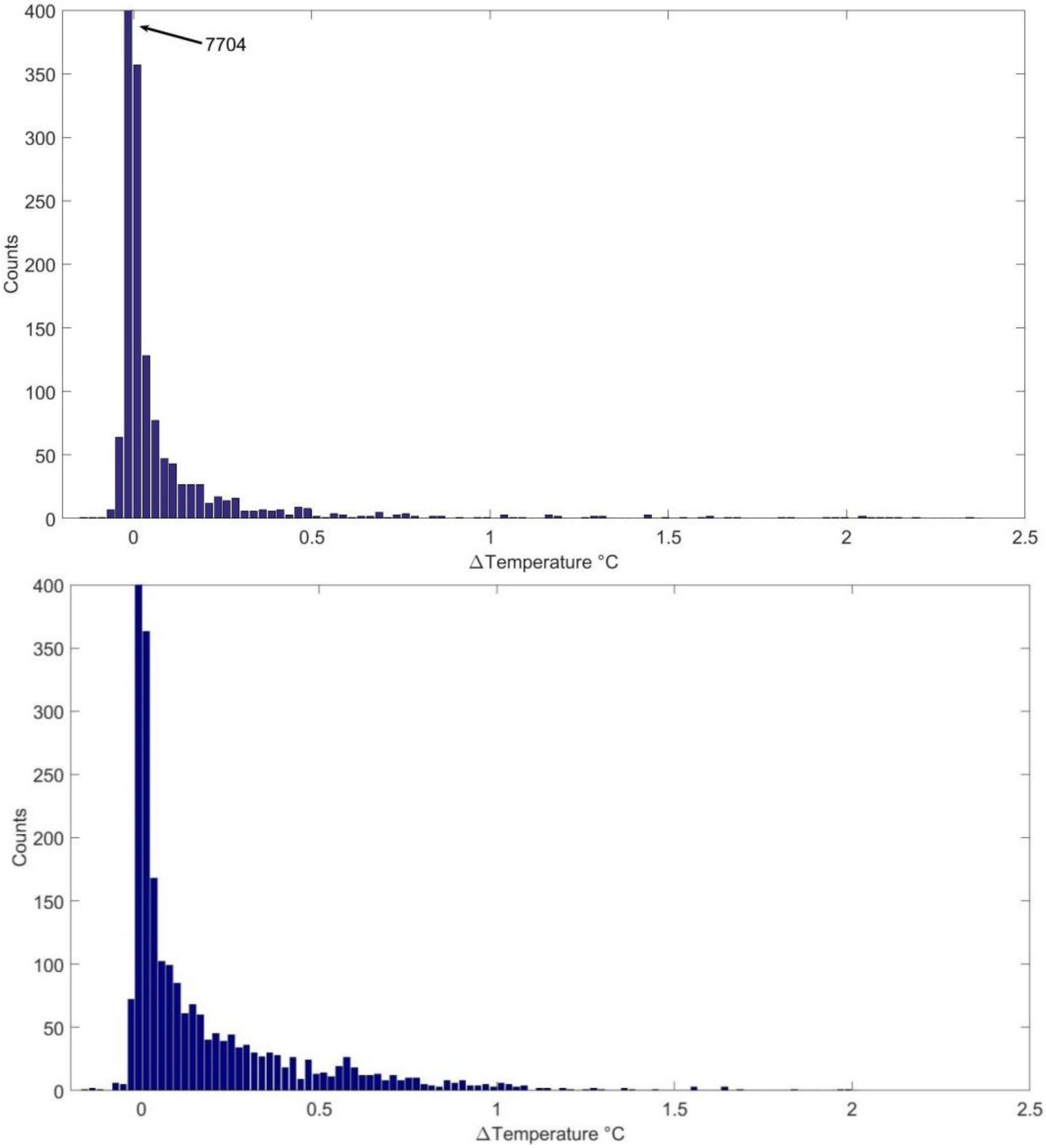

Figure 8.4 Occurrence of ΔT in the Celtic Sea and at L4

The occurrence of ΔT split into 100 bins determined hourly between 0.6 and 5m at the Central Celtic Sea mooring from 2014-08-21 to 2015-08-21 (a) and at the L4 mooring from 2016-05-15 to 2016-11-03 (b). The bins with the largest counts are off scale in both cases and are identified on the figure by their number of counts.

14 of the 16 NSOP deployments at L4 were made whilst the NSTS was deployed and fully functioning. The 71 ΔT determined with NSOP are compared with those determined by the NSTS at the same time (Figure 8.5). The strongest agreement in ΔT occurred when there were small/no ΔT. The large degree of scatter at higher ΔT appear to confirm the heterogeneity of the water at and around the L4 site (as discussed in chapter 1). The black line on Figure 8.5 represents a 1:1 relationship, and indicates that the NSTS derived ΔT is ~20–40% larger than the NSOP derived ΔT. The discrepancy between the ΔT may be explained by the slight differences in sampling depths (0.3 and 3.5m on the NSTS and 0.5 and 5m on NSOP) or the difference in the way time is integrated(the NSOP temperatures were measured over 30 minutes whilst the NSTS represent the difference exactly midway through the deployment). It is also possible that the L4 mooring acts as height island in the summer, if this is true then it is not suitable to use NSTS ΔT to extrapolate relationships over longer time scales.

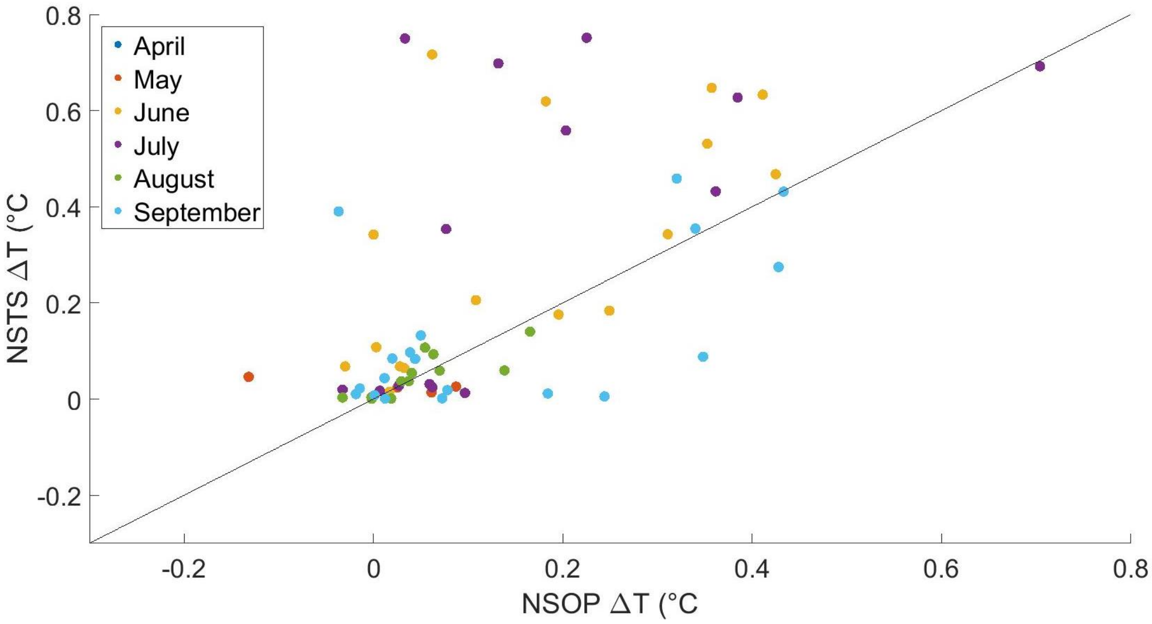

Figure 8.5 Comparison ΔT measured by NSOP and the NSTS at L4
ΔT recorded by NSOP for each of the 71 temperature profiles is shown against the ΔT recorded by the NSTS mounted at 0.3 and 3.5m on the L4 mooring for the same time period as the NSOP profiles. The marker colours corresponds to gradients measured in different months as specified in the legend.

ΔT from the SSB cruises and L4 are plotted against the mean irradiance (a) and wind speed (b) observed during each deployment Figure 8.6.

On the profiles where the ΔT was negligible (<±0.1°C) the irradiance of the deployments was moderately high and very variable (364.85 ± 256.1 Wm^{-2} in the Celtic Sea) and 931.45±472.19 Wm^{-2} at L4. The profiles where there was no ΔT occurred over a wide range of irradiances suggesting no link between the two. The irradiance of profiles with ΔT >0.1°C at L4 were variable (1152.54±463.15 Wm^{-2}) but slightly larger than in the Celtic Sea. For the 6 Celtic Sea profiles with ΔT >0.1°C, the irradiance was much lower and less variable than at L4 (675±138 Wm^{-2}).

For ΔT (<0.1°C) there was a lot of variability in the wind conditions in the Celtic Sea (8.58 ± 4.41 ms^{-1}) and at L4 (6.83± 3.52 ms^{-1}). For ΔT >0.1°C the average wind speed was weaker and less variable (6.01± 2.52 ms^{-1}) during the cruises than the wind speed of profiles with ΔT<0.1°C. At the highest wind speeds >10ms^{-1} there were no ΔT >0.1°C.

The six profiles from the cruises with ΔT > 0.05°C were only present when there was a combination of both high irradiance and low wind speed. These six profiles were also all measured between 11:00 and 15:00 hours when solar irradiance is likely to be greatest. The time of day does not appear to be an indicator of ΔT magnitude during the cruises or at L4 (Figure 8.7).

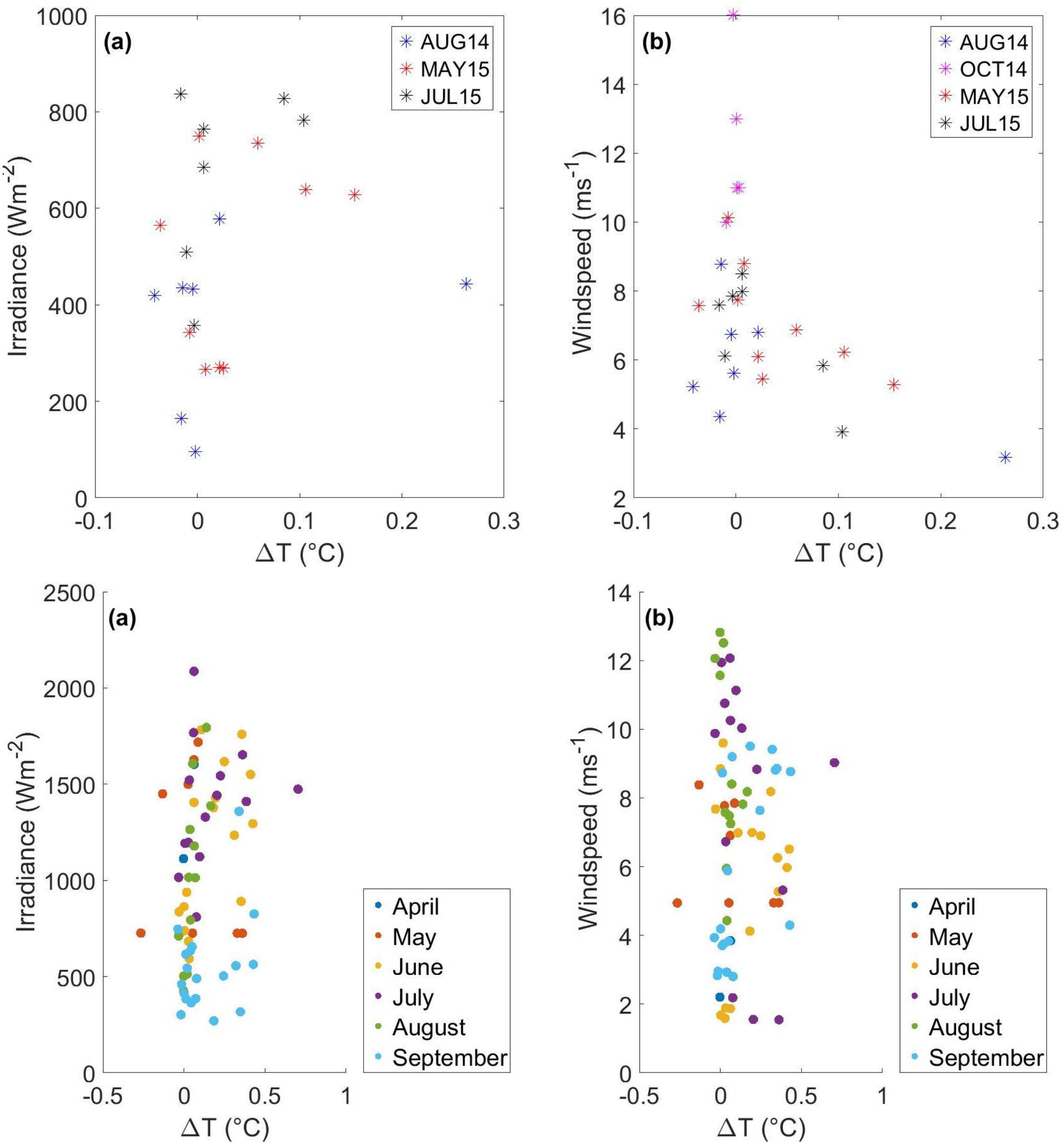

Figure 8.6 ΔT occurrence with irradiance and wind speed

ΔT (as calculated as described in section 8.2) for all 29 profiles from the SSB cruises (top panels) and 71 profiles made during the 16 NSOP deployments at L4 (bottom panels) against the average irradiance (left panels) and wind speed (right panels) of each profile. The marker colours corresponds to different cruises and in different months at L4 as specified in the individual legends. Note axis limits are not the same.

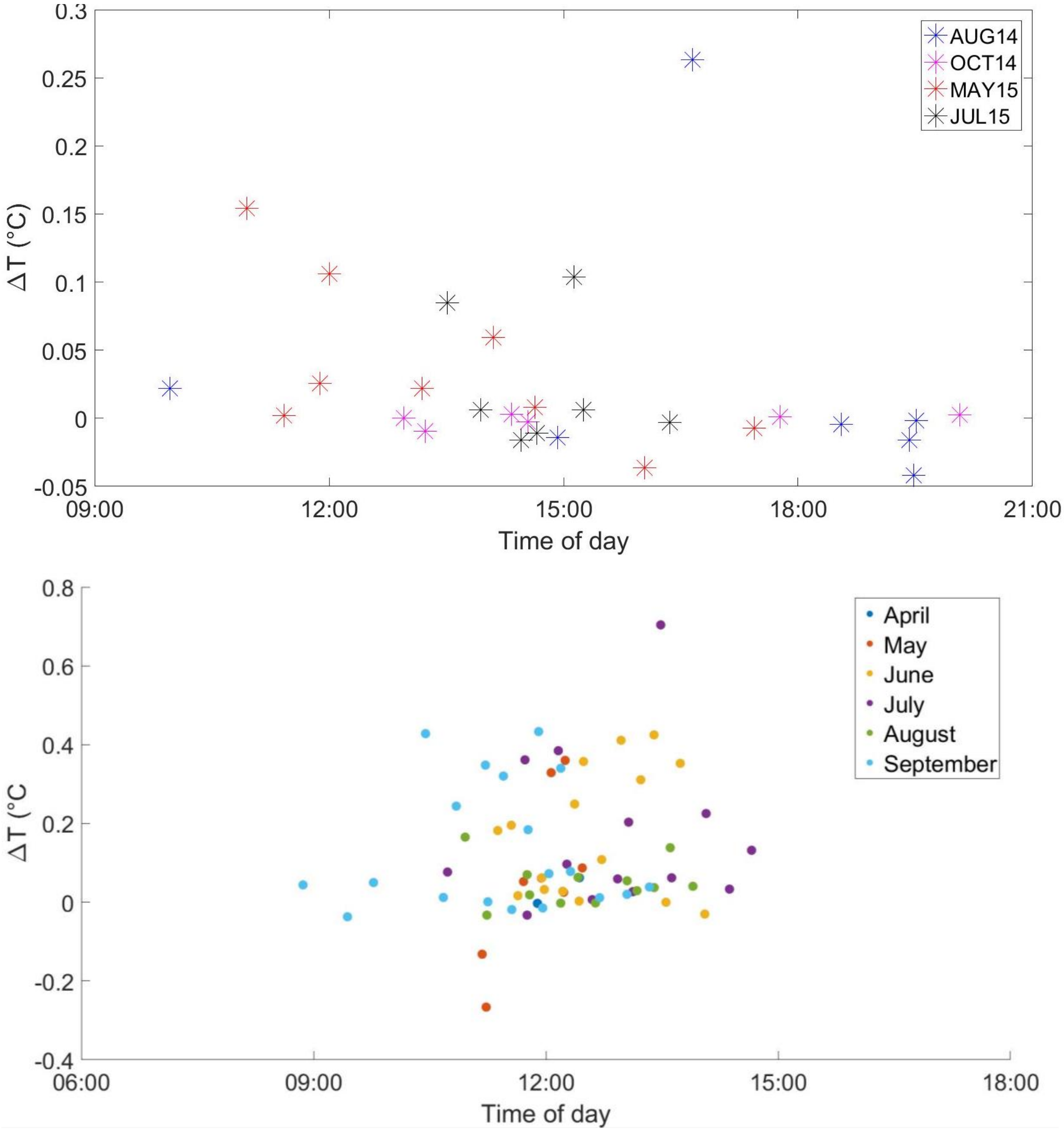

Figure 8.7 ΔT occurrence with time of day

ΔT (calculated as described in section 8.2) for all 29 profiles from the SSB cruises (top panels) and 71 profiles made during the 16 NSOP deployments at L4 (bottom panels) against time of day each profile. The marker colours corresponds to the months of the deployment. Note axis limits are not the same.

The ΔCO_2 from the SSB cruises were mostly positive (76% of ΔCO_2 profiles >0 µatm) with an average ΔCO_2 of 0.9915 ± 1.77 µatm(Figure 8.8a). The ΔCO_2 from L4 were mostly positive (61% of ΔCO_2 >0 µatm) had a similar average ΔCO_2 (0.4150± 8.3 µatm) to that on the cruises and had a larger maximum ΔCO_2 of 14.92 µatm than during the cruises (Figure 8.8b). A one sample Kolmogorov–Smirnov test indicates that ΔCO_2 from the cruises are normally distributed, this is also the case for the L4 ΔCO_2. The majority (97%) and (93%) of ΔCO_2 observed during the cruises and at L4 respectively were statistically significant at the 95% confidence limit as indicated by an unpaired t–test.

The majority of ΔCO_2 from the cruises were small (<±2 µatm), the ΔCO_2 from L4 were larger and the majority (66%) fell within <±5 µatm. There were a lot (24%) of strong (>5 µatm) ΔCO_2 and almost as many (18%) strongly (<-5 µatm) negative ΔCO_2 measured at L4. The majority of the negative ΔCO_2 were made in September and were stronger than the positive gradients. Unlike at L4, Only 2 of the 29 cruises profiles were strong (>±5 µatm).

ΔCO_2 from the cruises and L4 were much smaller than the average ΔCO_2 (13±1µatm) reported by Calleja et al. (2013) who used a similar methodology. They found that temperature could only account for 11% of their pCO_2 variability whereas these results show that accounting for the temperature at each depth accounted for the majority of the pCO_2 variability. Calleja et al. (2013) observed much larger ΔT than in this study as their study sites were off the coast of Mauritania, in the Mediterranean Sea and Antarctica. It is possible that the stronger and more persistent ΔT in these regions facilitated stronger ΔCO_2. They attribute the large ΔCO_2 in their study as being caused by changes in net primary production but they do not substantiate this suggestion quantitatively. Following simple calculations it is shown in section 2 that large changes in the biology are required to force the observed ΔCO_2.

There are no apparent differences in ΔCO_2 depending on the cruise or the month at L4. The largest positive ΔCO_2were observed during the AUG14 and JULY15 summer cruises and in May–August at L4. The largest negative ΔCO_2 were seen during the cruise immediately after the spring bloom(MAY15).

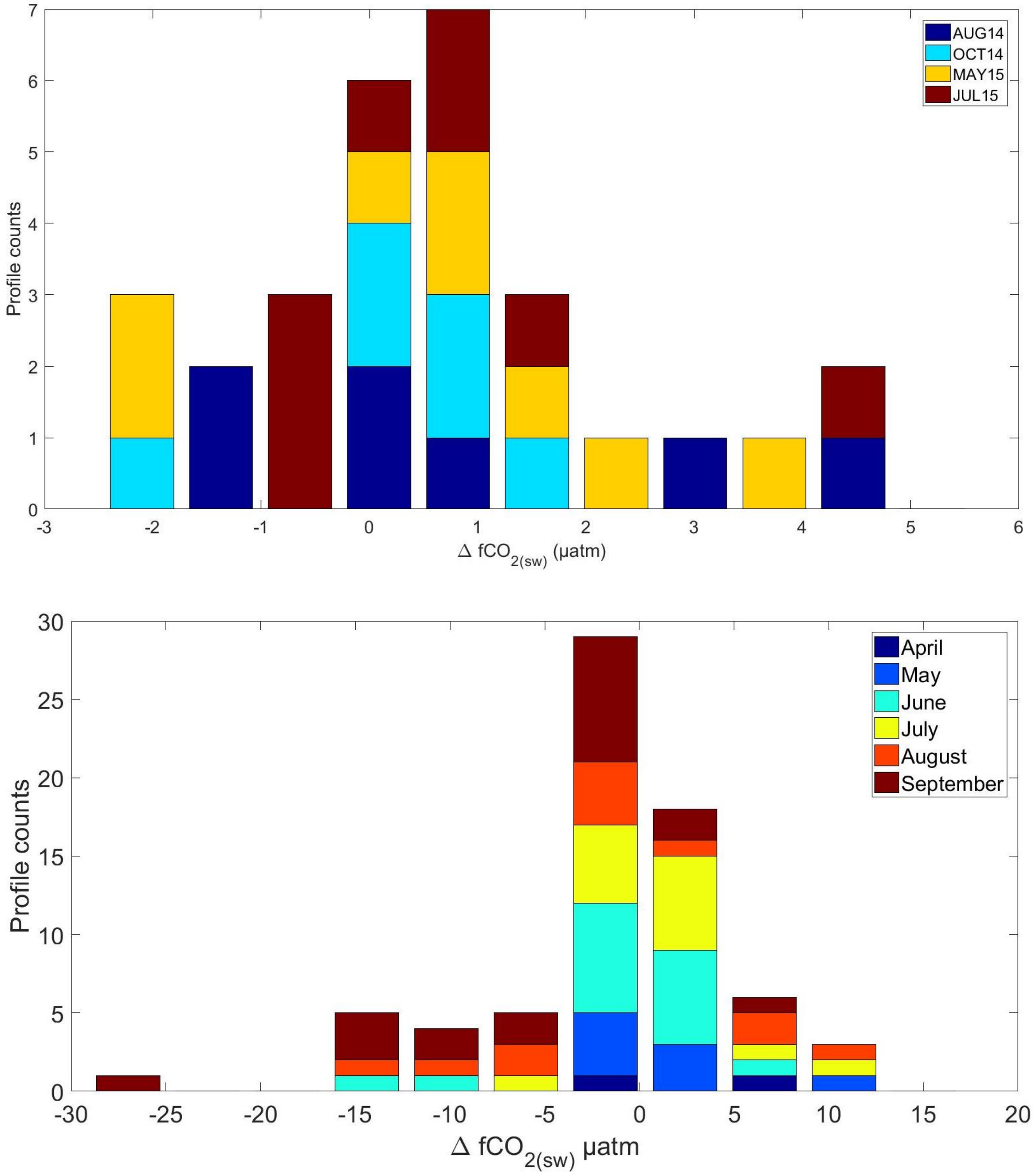

Figure 8.8 Magnitude of ΔCO_2 from NSOP profiles

Profile counts for 10 equally spaced bins of the ΔCO_2 (as calculated as described in section 8.2) for all 29 profiles from the SSB cruises (a) and 71 profiles made during the 16 NSOP deployments at L4 (b). Note axis limits are not the same.

ΔCO_2 are shown alongside the average irradiance and wind speed recorded during that profile as well as in the 4 hours preceding the cruise profiles in Figure 8.9a–d and the L4 profiles (Figure 8.9e–h).

There is no correlation between irradiance and ΔCO_2 from the SSB cruises and at L4. During the SSB cruises the majority of the profiles with gradients of <2.5 µatm were observed at a range of irradiances between 100 and 850 Wm^{-2} and some of the strongest

ΔCO_2 (> 2.5 µatm) were seen at low irradiances around 400 Wm^{-2}.There is also no correlation with irradiance in the 4 hours preceding the SSB and L4 profiles which suggests that the irradiance 'dose' at the site is not a particularly strong influence on the ΔCO_2.

There is a discernible structure in the relationship between ΔCO_2 and wind speed at the time of the profiles and in the 4 hours before the deployments (Figure 6.8b and Figure 6.8d). Strong positive and negative ΔCO_2 were found predominantly at low wind speeds <6 ms^{-1}. There was no correlation between the CO_2 and wind speed at L4, positive ΔCO_2 were observed at a range of wind speed whereas negative ΔCO_2 were almost exclusively found at high wind speeds. When the wind speed over the four hours before the deployment were observed there was also no trend present, the low wind speed profiles (<6ms^{-1}) were equally as variable as the high wind speed profiles. There also does not appear to be any month/ season dependent trends in the wind speed and irradiance suggesting that that neither are explicitly linked to gradient formation at this site.

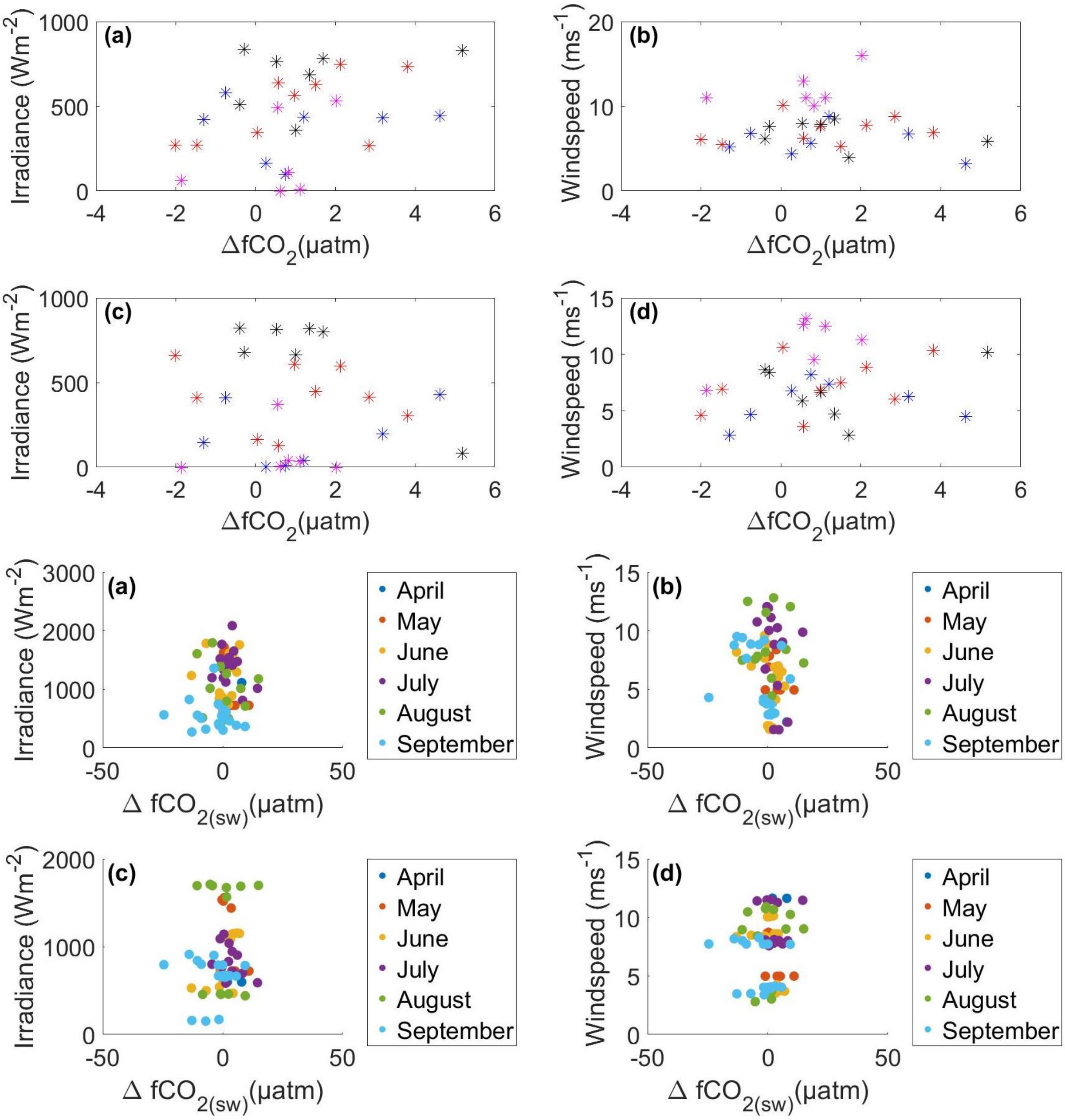

Figure 8.9 ΔCO_2 occurrence with irradiance and wind speed

ΔCO_2 (as calculated as described in section 8.2) for all 29 profiles from the SSB cruises (top panels) and 71 profiles made during the 16 NSOP deployments at L4 (bottom panels) the average irradiance(a) , wind speed (b), irradiance over 6 hours(c) and wind speed over 6 hours of each profile(d). The marker colours corresponds to ΔCO_2 measured during different cruises and months as specified in the legend. Note axis limits are not the same.

8.5 **NSOP derived ΔfCO_2 relative to showerhead CO_2**

The profiles measured with NSOP assume that the surface CO_2 does not change at any depth over the period of sampling, which is an approximation and not realistic of the ocean itself. As all the profiles were measured over the course of ~30 minutes, there is a possibility that ΔCO_2 will also reflect spatial and temporal CO_2 changes. Unidentified temporal changes in the seawater fCO_2 during the NSOP vertical profiling complicates profile interpretation.

Short timescale (~30 minute) changes in CO_2 could be misinterpreted as a vertical gradient in CO_2.

To distinguish a measured gradient from an advective/temporal change throughout the water column, it is necessary to reference against continuous measurements from a constant depth such as the underway system at 5m. The underway showerhead system was only functioning for 10 of the 29 SSB profiles and four of the 16 L4 NSOP deployments. Even when referencing against the showerhead CO_2 system these two effects are difficult to separate as the system lacks the temporal resolution required to monitor the changes (12.5 minutes sampling frequency on the cruises and 27 minute sampling frequency at L4). To demonstrate the differential between the two systems the underway measurements were linearly interpolated for the same time periods as the depth bins (Figure 8.10).

The change in showerhead CO_2 during profiling during SSB was the same magnitude (<±5µatm) as the ΔCO_2 observed with NSOP (Figure 8.10). For a number of profiles the showerhead CO_2 mirrors the same trend in NSOP CO_2 (e.g. 08/08, 19/07, 20/07). The profiles measured on 09/08, 21/08, 30/ 10 and 07/05 show less vertical variability than the underway system shows in the same period of time (~3–4µatm). The profiles on12 /05 and 13/05 show the same magnitude change but the trends do not go in the same direction which is likely a result of the interpolation approach used here.

The showerhead system indicates that there generally are not strong temporal changes in CO_2 at L4 (<10µatm e.g. 30/06, 07/07 and 13/07). There are exceptions (e.g. 04/08 and 21/09) where strong temporal changes did occur during deployments. On 15/09 the showerhead CO_2 changed by 8.6 µatm over the course of the deployment. This change was also observed in the Liqui–cel system, indicating that a large proportion of ΔCO_2 in these profiles is caused by changes throughout the water column or due to advection of different water masses.

Using the underway system as a baseline, ΔCO_2 could recalculated. Due to large variability in and the evident temporal offset in the showerhead system this was not done here. Ideally the temporal change in CO_2 would be subtracted from the ΔCO_2 to only give the vertical component but the temporal resolution of the showerhead system prevents this. To remove this uncertainty from the analysis, the profiles with the largest temporal variability (>10µatm during an NSOP deployment) need to be removed from the meta analyses.

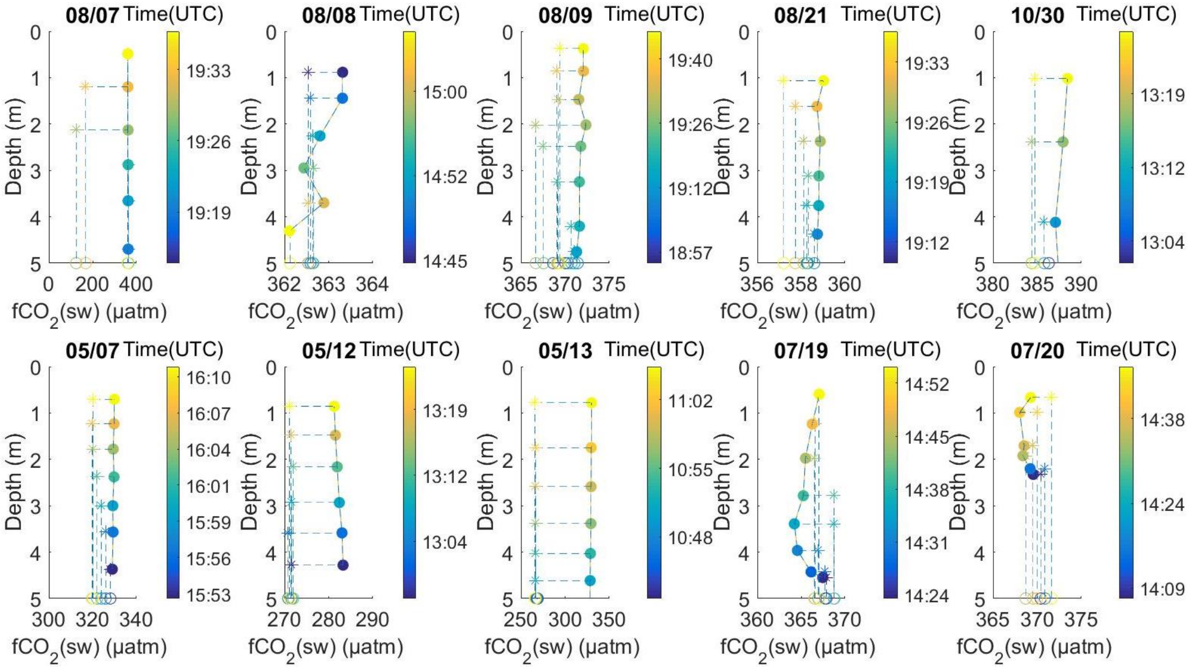

Figure 8.10 CO_2 differential with the underway system

10 profiles collected in UK Shelf Seas between August 2014 and July 2015. NSOP profiles of CO_2 (circles) were derived using the depth bins determined in chapter 2. Vertical error bars show two standard errors of the mean in each depth bin. The horizontal errors are the propagated errors using the averaged bin variables to calculate fCO_2. The fCO_2 measured by the underway system at 5m was interpolated to the same time bins as the NSOP CO_2 and are marked by crosses and coloured by time. The difference between the crosses and filled circles represents the differential at each depth.

8.6 CO_2 and temperature gradients

Assuming that stratification by near surface warming is needed for the establishment of ΔCO_2, then the occurrence of ΔCO_2 should correlate with ΔT. The relationship between ΔT and ΔCO_2 for the 29 cruise profiles and the 71 profiles from L4 are shown in Figure 8.11. ΔT and ΔCO_2 were not correlated (SSB cruises, R–squared=0.037, p=0.11) and (L4 ,R–squared=0.037, p=0.11).

There were 17 profiles from the cruises where there was a small or negligible temperature gradient (<±0.025 °C). The ΔCO_2 for these profiles were mostly small and positive (<2.5 µatm). If temperature stratification is required for a CO_2 gradient, it would be expected that there would have been no ΔCO_2 for all of these profiles. All but one of the slightly negative (-0.25 to 0 °C) ΔT had negative ΔCO_2. However the three slightly positive (>-0.025 & <0.05 °C) ΔT also had negative ΔCO_2. The profiles with the largest ΔT (>0.05°C) all had positive ΔCO_2 >1.25 µatm. Two of these profiles were the largest observed during all the cruises >7.5 µatm. ΔT may not correspond to ΔCO_2 due to the mismatch between time of sampling and the transience of the gradients. For instance, the two largest gradients were measured in the mid afternoon after what was likely a long period of stratification. This is an experimental design limitation and one which would be reconciled by sampling from the onset of stratification through to stratification breakdown.

Once the deployments where there were changes in the underway CO_2 >10µatm were excluded, there was a positive ΔT and ΔCO_2 relationship in the L4 data. There is a large cluster of points where the ΔT and ΔCO_2 were close to 0. There are a number of strong positive ΔCO_2 when ΔT was close to 0.

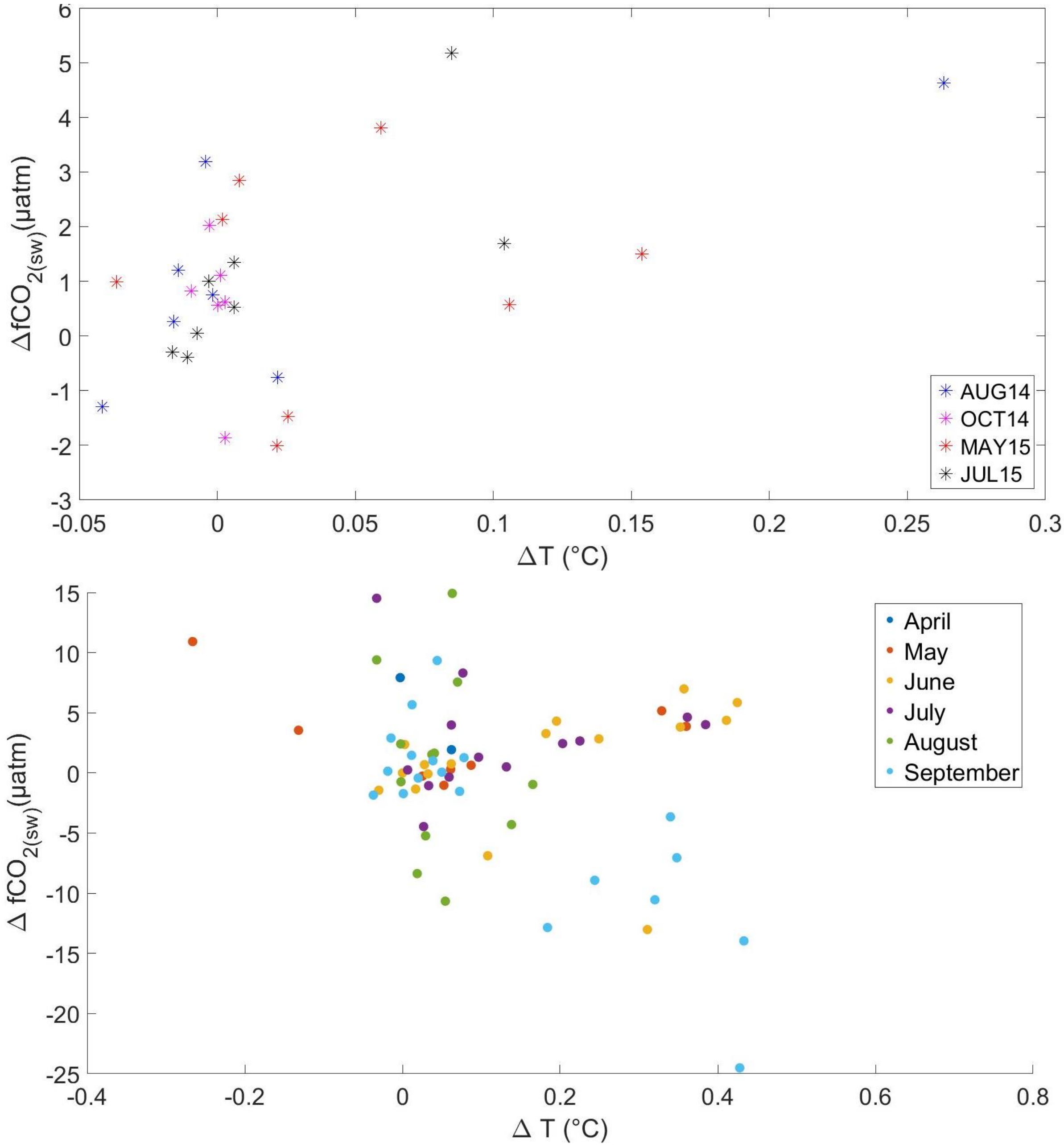

Figure 8.11 ΔT versus ΔCO_2

ΔT vs ΔCO_2, both are calculated as described in section 8.2) for all 29 profiles from the SSB cruises (a) and 71 profiles made during the 16 NSOP deployments at L4 (b). The marker colours corresponds to different cruises and months as specified in the legend. Note axis limits are not the same.

There is minimal structure in the temperature and CO_2 relationship for the full SSB dataset. The data were divided by cruise (Figure 8.12) which revealed a positive relationship between ΔT and ΔCO_2 during AUG14 and JULY15 (the two summer cruises). This may suggest that the magnitude of temperature gradients is linked to CO_2 gradients. A potential reason why the CO_2 in the surface layer is linked to temperature may be that the increased temperature affects the metabolic rate of respiration, photosynthesis or calcification in microorganisms or alters the air sea flux due to changes in the temperature dependence of the Schmidt number and solubility. However, this relationship may also reflect an error in the temperature correction used to adjust the fCO_2 to in situ temperature (Takahashi et al., 1993). The temperature correction applied between the equilibrator and the surface seawater was largest for the two summer cruises (due to additional warming of the water between the CTD and equilibrator). McGillis and Wanninkhof (2006) show that the temperature correction for natural waters lies between 3.7 and 5.3 % $°C^{-1}$ which is a large divergence from the 4.33% $°C^{-1}$ correction used by Takahashi et al. (1993). Errors in the temperature correction (leading to incorrect ΔCO_2) would be largest where the temperature correction is biggest. If the ΔCO_2 observed are purely a result of the error in the temperature correction these slopes could infer the inaccuracy of the correction for these similar shelf sea conditions.

During OCT14, there were negligible ΔT but there were still ΔCO_2. This could indicate that gradients can form in conditions which are unfavourable for near surface stratification. In MAY15, positive and negative ΔCO_2 were observed even when there were no temperature gradients. MAY15 is different in that there were also two cases where there were moderate temperature gradients (>0.02 °C) and no ΔCO_2. There appears to be two distinct groupings which fall on two straight lines in MAY15, it might be expected that the locations of profiles of each group might be linked to different regions of the shelf but this does not appear to be the case. Both OCT14 and MAY15 have instances of strong negative gradients not seen during AUG14 and JULY15, a sustained negative gradient would imply high production and depletion of CO_2 at the surface, such gradients should not be able to be sustained as turbulence at the surface should mix the surface water masses.

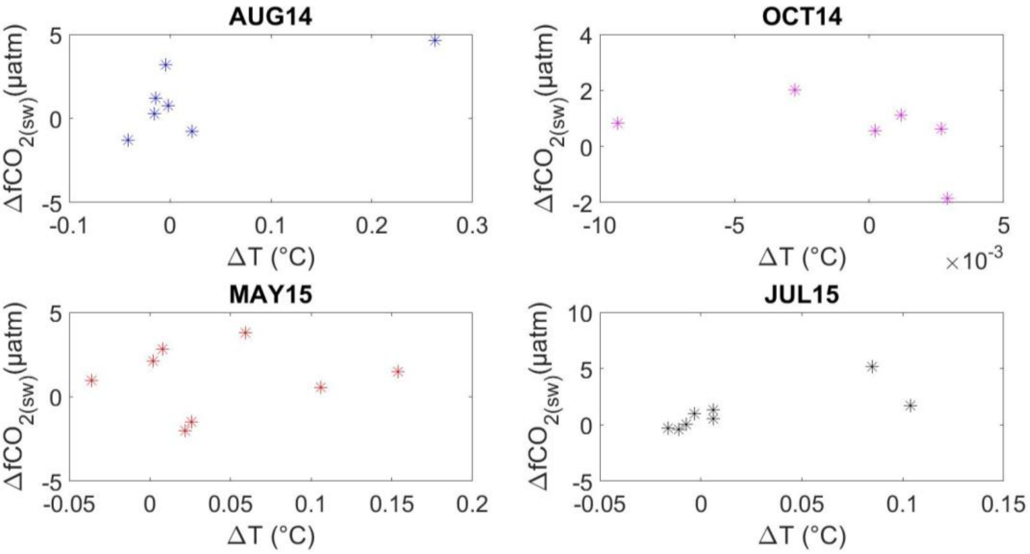

Figure 8.12 Delta temperature and delta CO_2 relationship by cruise
ΔT versus ΔCO_2. Each subplot corresponds to a different cruise indicated by the title and the colour of the data where blue (AUG14), magenta (OCT14), red (MAY15) and black (JULY15).

8.7 Classifying profile shapes

All of the 29 NSOP CO_2 profiles have distinct shapes. As previously mentioned the general trend is that there is a fairly consistent unique proportional relationship between depth and

CO_2 for each profile, this is hence referred to as the linear trend (Figure 8.13a). The linear trend has no units meaning no assumption is made about the size of the CO_2 gradient; this scenario includes extremely small and large gradients. Imposed on these general trends are a number of other features. The first of these features is a discontinuity in the slope of the CO_2 depth relationship which results in the slope of the line changing, this leads to two scenarios, the first where the slope is gentler near the surface(Figure 8.13b) and one where the slope is steeper(Figure 8.13c). The second feature can be thought of a short deviation and return to the linear trend, again this leads to two scenarios one where the deviation is near the bottom of the profile (Figure 8.13d) and another where it is near the surface (Figure 8.13e). The final shape is one where the profile is curved (Figure 8.13f).

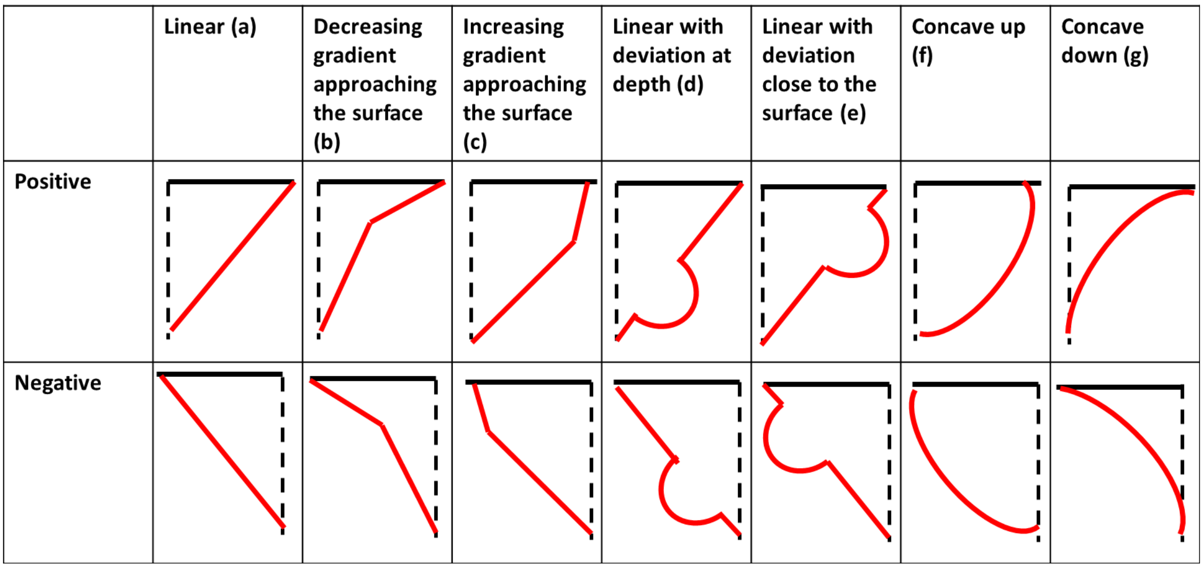

Figure 8.13 Schematic representation of profile shapes

Schematics of profile shapes. The ocean's surface is a solid black line, the CO_2 profile is in solid red and the bottom of the profile is the point where the red line and dashed line meet. These schematics are not to scale in any sense, CO_2 profiles are portrayed this way to exemplify and draw out features seen in the actual profiles. The mirror opposite of each feature is shown for both positive and negative profiles.

8.7.1 Comparing cruise profile shapes

When all the CO_2 profiles are plotted with the surface bin at a reference point of zero it is evident that the CO_2 measured by NSOP is higher at the surface in the majority of the cruise and seasonal study profiles (Figure 8.14). Similarly it appears that a lot of the change in CO_2 occurs near the surface for many profiles. By comparing the profile shapes it is easier to identify common trends amongst profiles. Due to the sheer number of profiles during the seasonal study, only the shapes of the profiles from the SSB cruises will be described in detail here.

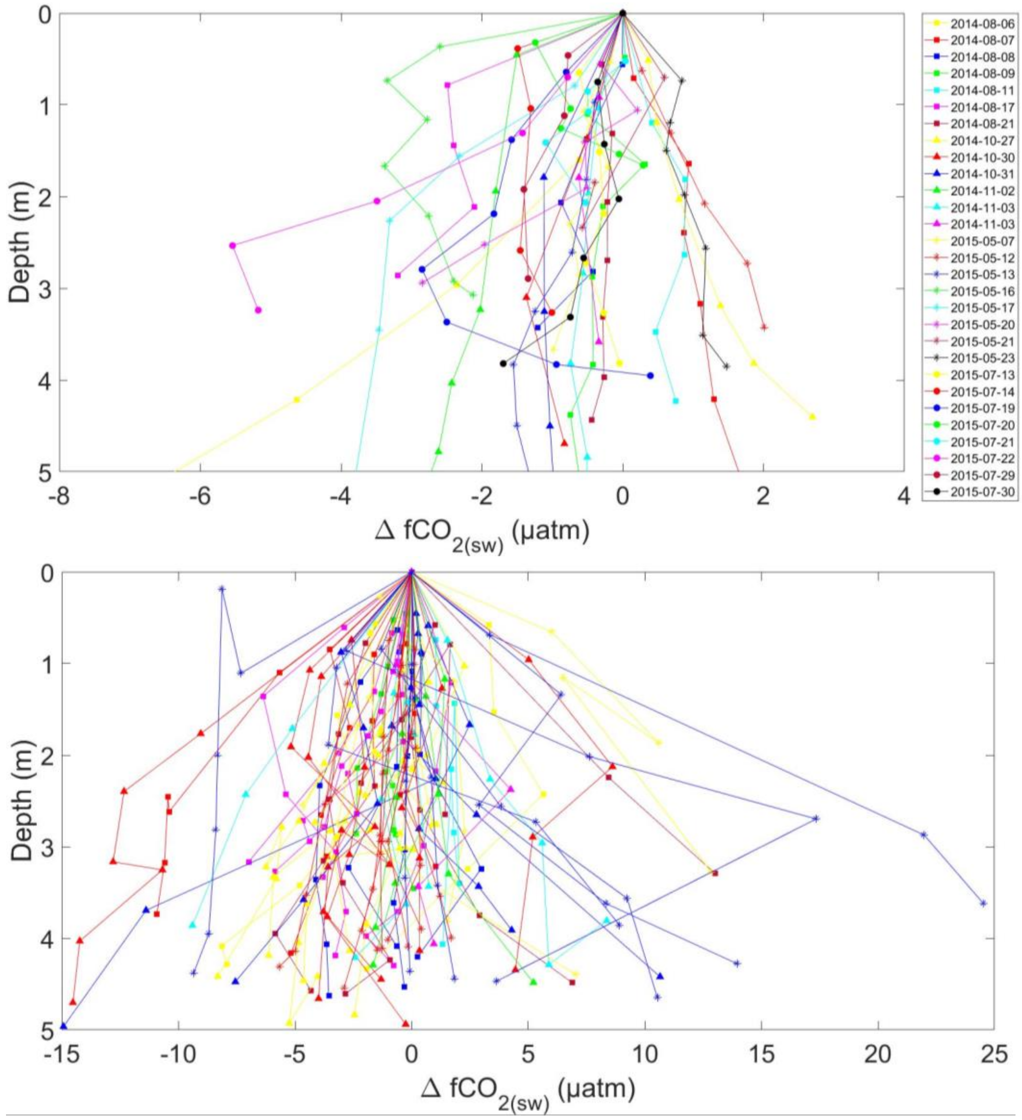

Figure 8.14 CO$_2$ profiles referenced against a surface value of 0
CO$_2$ profiles for the SSB cruises (a) and seasonal study (b) referenced against a surface value of 0. Note axis limits are not the same.

8.7.2 Identifying common profile shapes during the SSB cruises

Almost half of the profiles (12 of 29) show a linear change in the fCO$_2$ (Figure 8.15). In these 12 profiles it would be fair to say a straight line could be drawn through the bottom and top points with all the other points falling on or close to the line. The majority of these profiles (8 of 12) are positive and have gradients of around 1-2 µatm. There were profiles from every cruise that had this linear or straight shape suggesting it was not driven by different levels of production or weather effects or even near surface stratification as 4 of the profiles were from OCT14 where there were no thermal gradients whatsoever.

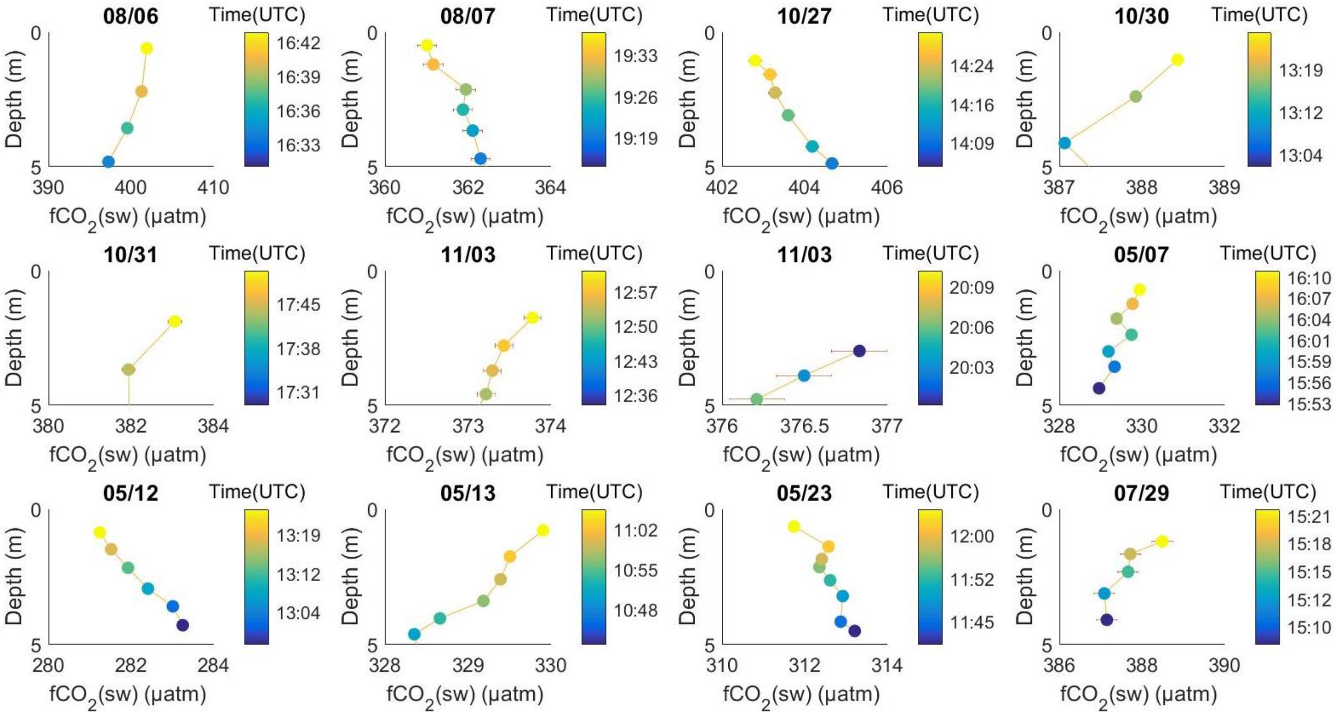

Figure 8.15 Profiles shapes - Linear Profiles

12 profiles collected in the Celtic Sea and the Outer Hebrides between August 2014 and July 2015 that show a linear trend in CO_2 with depth. NSOP profiles of CO_2 were derived using the depth bins determined in chapter 2. Data points are coloured by sampling time. Vertical error bars show two standard errors of the mean in each depth bin. The horizontal errors are the propagated errors using the averaged bin variables to calculate fCO_2. The date of each profile is given above each subplot.

Several of the profiles (6 of 29) follow a generally linear trend where the surface value (always above 2m) is noticeably different Figure 8.16. Excluding the surface bin the profiles are slightly negative but in all 6 profiles the surface bin is always more positive than the point below. These gradients are larger than average with many around 2 µatm. The positive surface bin may be indicative of a process happening exclusively in the top couple of meters that is not seen in the rest of the profiles. As stated previously there was no rain during the profiles so this cannot account for the divergence in the surface bin. In all six cases there are no large (>0.01 and >0.03°C) coincident changes in the accompanying salinity and temperature profiles which does not suggest water mass change. If mixing processes were not important than it could be that a flux from the atmosphere elevated surface CO_2 near the surface.

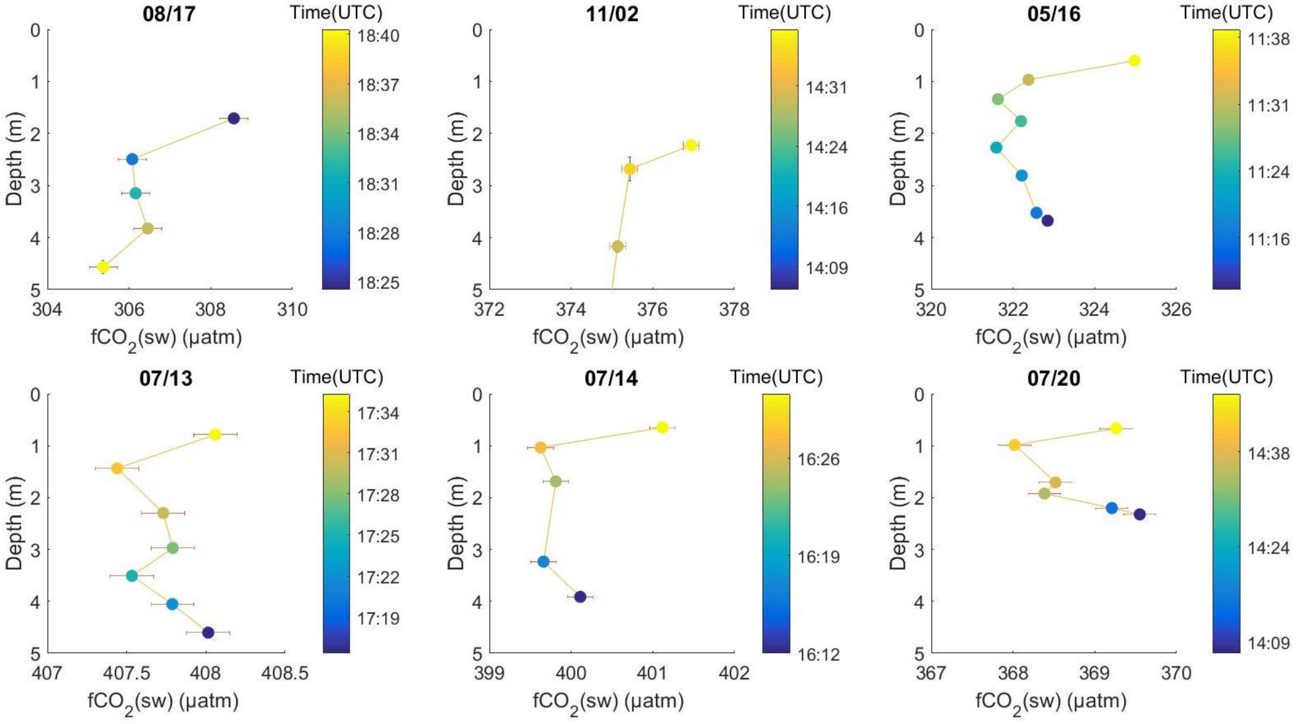

Figure 8.16 Profiles shapes - Change in the gradient near the surface above 2m

Six profiles collected in the Celtic Sea and the Outer Hebrides between August 2014 and July 2015 that show a gradient change in CO_2 with depth at the surface above 2m. NSOP profiles of CO_2 were derived using the depth bins determined in chapter 2. Data points are coloured by sampling time. Vertical error bars show two standard errors of the mean in each depth bin. The horizontal errors are the propagated errors using the averaged bin variables to calculate fCO_2. The date of each profile is given above each subplot.

Another trend seen throughout a number of the profiles (5 of 29) was one where there was a near linear trend in the top 2-3m followed by a change in the gradient below this in the bottom 1-3 points of these profiles (Figure 8.17). These fCO_2 gradients are some of the largest observed during the cruises with the majority >2µatm. In the case of 07/19 and 07/21 the decreasing fCO_2 trend with depth was reversed, whereas for 05/20 and 07/30 the trend was amplified as the fCO_2 decreased more rapidly with depth. For 05/17 the decreasing fCO_2 trend with depth diminishes below 3m indicating no changes below this depth. This shift does point to there being a transition point where the fCO_2 changes. The temperature profiles for these 5 profiles strongly mirror the fCO_2 changes and the depths of the discontinuities in fCO_2 are also the depths of discontinuity in temperature. With the exception of 05/17 these profiles are also the ones where some of the largest temperature gradients were observed.

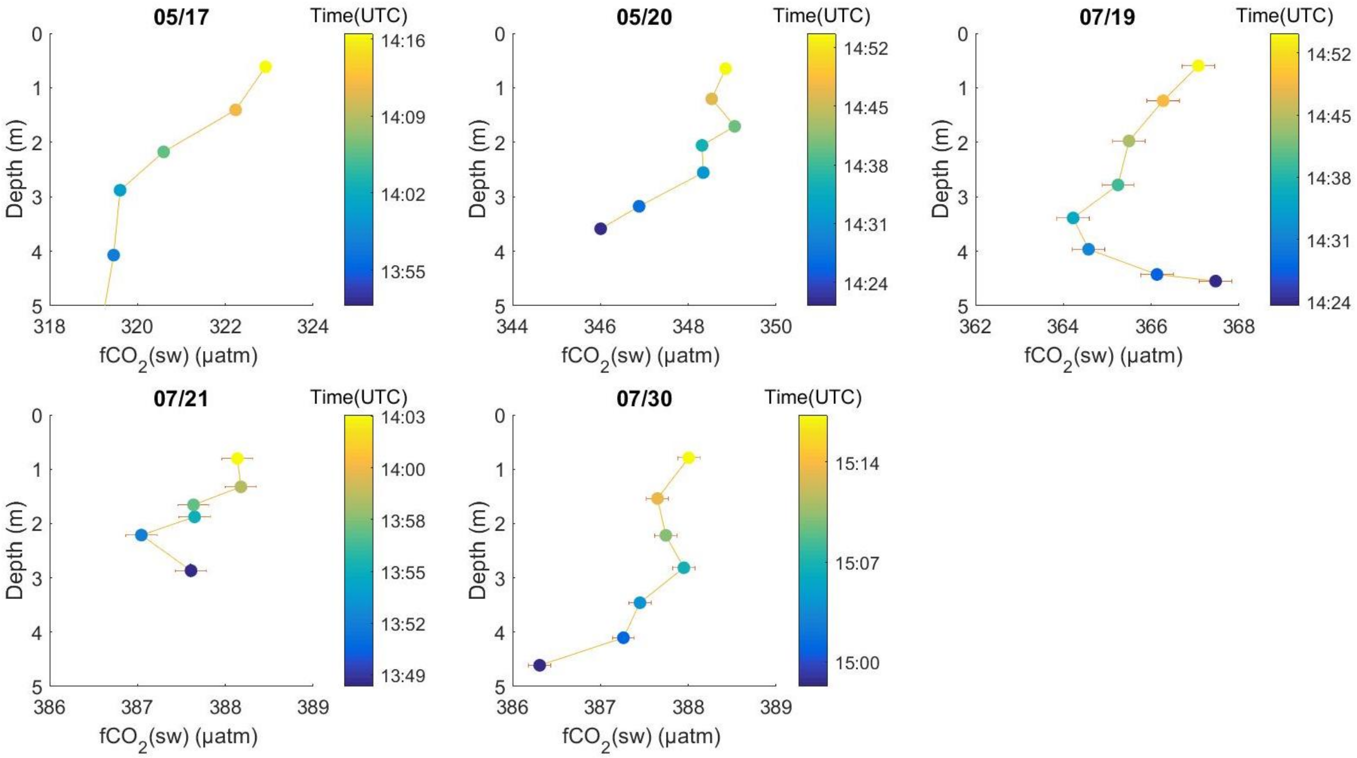

Figure 8.17 Profiles shapes - Change in the gradient below 2m
5 profiles collected in the Celtic Sea and the Outer Hebrides between August 2014 and July 2015 that show a gradient change in CO_2 with depth below 2m. NSOP profiles of CO_2 were derived using the depth bins determined in chapter 2. Data points are coloured by sampling time. Vertical error bars show two standard errors of the mean in each depth bin. The horizontal errors are the propagated errors using the averaged bin variables to calculate fCO_2. The date of each profile is given above each subplot.

Three profiles had a distinct shape where there was a general linear trend but a deviation around 3m before what appears to be a return to the original trend (Figure 8.18). The size of the ΔfCO_2 in these profiles varies with the total ΔfCO_2 in 08/08 <1.5µatm, 08/11 <1µatm and 07/22 >4µatm. The deviation from the linear trend on 07/22 is also seen at the same depths in the temperature and salinity profiles for that deployment, this would suggest that the profiler went through unique water masses during the transition between these depths. There are no similar trends in the temperature and salinity profiles from 08/08 and 08/11, thus water mass changes don’t seem to be the cause. A possibility is that the shapes are then due to temporal changes in biology of ~0.2µatm on the order of 10 minutes which is possible but it is difficult to come up with a reason for why a change in the trend would occur.

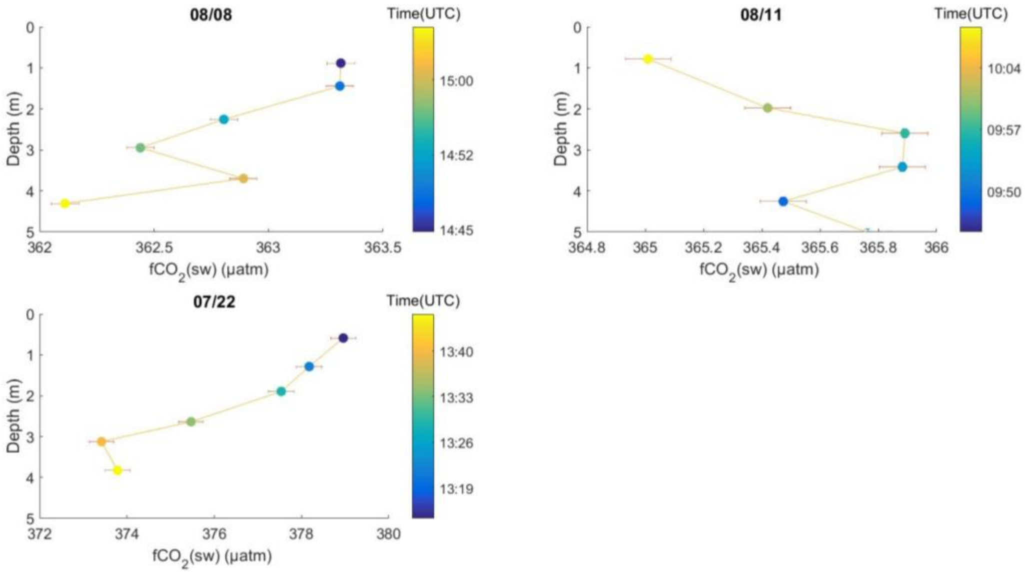

Figure 8.18 Profiles shapes - Linear with deviation around 3m depth

Three profiles collected in the Celtic Sea and the Outer Hebrides between August 2014 and July 2015 that show a deviation around 3m from the linear change in CO_2 with depth. NSOP profiles of CO_2 were derived using the depth bins determined in chapter 2. Data points are coloured by sampling time. Vertical error bars show two standard errors of the mean in each depth bin. The horizontal errors are the propagated errors using the averaged bin variables to calculate fCO_2. The date of each profile is given above each subplot.

Three profiles had a distinct shape where there was a general linear trend but a momentary deviation close to the surface at around 1m (Figure 8.19). The size of the ΔfCO_2 in these profiles is small in all cases <1µatm. The deviation from the linear trend on 05/21 is also seen in the temperature profile from that deployment with the top two points being 0.1°C warmer than the two points below. On 08/21 there is an associated blip in the salinity signal at the same depth as the fCO_2 blip and similarly there is a blip in the temperature at the same depth as the fCO_2 blip on 08/09. The profiles from 08/09 and 08/21 are strong evidence for moving in and then back out of marginally different water masses during the deployment. The profile of 05/21 does point to the existence of a distinctly different water mass below 2m.

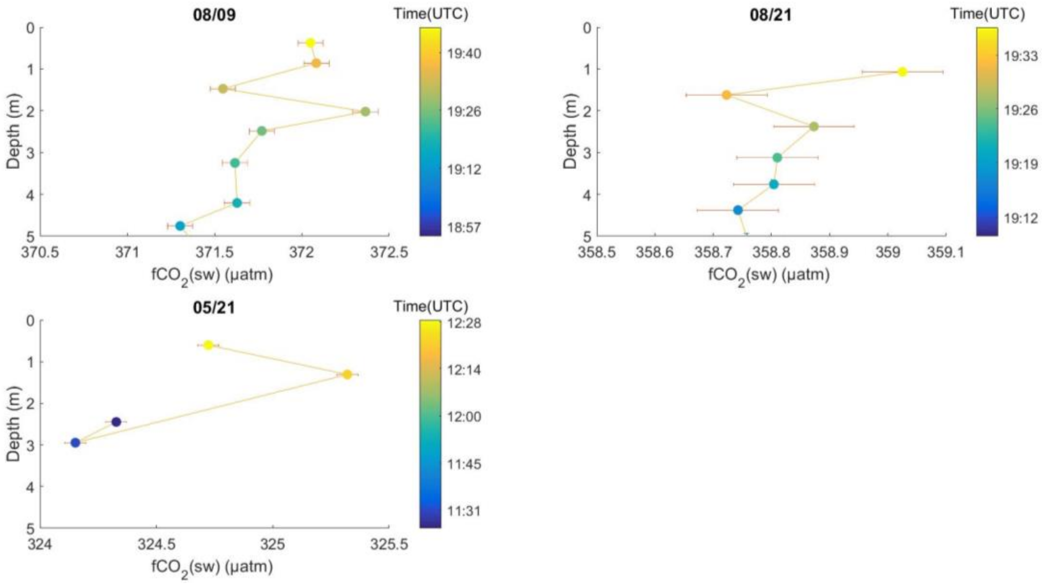

Figure 8.19 Profiles shapes - Linear with deviation at the surface around 1m
3 profiles collected in the Celtic Sea and the Outer Hebrides between August 2014 and July 2015 that show a deviation above 2m from the linear change in CO_2 with depth. NSOP profiles of CO_2 were derived using the depth bins determined in chapter 2. Data points are coloured by sampling time. Vertical error bars show two standard errors of the mean in each depth bin. The horizontal errors are the propagated errors using the averaged bin variables to calculate fCO_2. The date of each profile is given above each subplot.

8.7.3 Insights from profile shapes

There are evidently a number of distinct profile shapes from the profiles collected during the cruises, these shapes reappear in different cruises and are unlikely to be coincidental.

The most common shape for the profiles was linear; many of the smallest gradients observed followed this trend and were also the profiles where there was not stratification. This may suggest that these linear trends reflect steady changes in the water mass CO_2 over time. A small number of the linear profiles still show large coincident changes in CO_2 and temperature. The majority of these profiles were measured around midday.

There were six profiles that followed a generally linear trend with a divergence in the surface bin, none of these profiles were where there was stratification and again all the CO_2 are small. It is not clear why the surface bins are different but it may reflect issues with profiling close to the surface, this is supported by the fact that all 6 of these profiles were made on deployments when the wind speed was $>7ms^{-1}$ where it might be concluded that the sea state was rough.

Where there appears to be deviations and returns to linear trends whether in the surface 2m or deeper the CO2 gradients tended to be small and were not linked to coincident temperature gradients. It may be possible to attribute some of these ‘blips’ to noise whilst profiling.

Five profiles have a distinctive structure where there is a noticeable shift below 2m. These profiles had the largest CO_2 changes and were all found to have thermal stratification. The temperature profiles for all five of these profiles strongly mirror those for CO_2 which is strong evidence that the discontinuity in the profile is between the diurnal warm layer and the mixed layer below. Coincidentally all of these profiles were measured in the mid-afternoon round 15 hrs. It is these profiles that are the most convincing at showing the link between CO_2 and diurnal warm layers. As the selection of profiles by shape was not done using any criteria and based on judgement it is possible that some of the other large CO_2 gradients that mirror temperature but do not have a marked discontinuity or might have a deeper discontinuity like 08/06 could also be grouped in this category.

8.8 Gradients by region

As detailed in Chapter 1, a number of physical forcings act on water masses in Shelf Seas. As different physical processes dominate the movement of water in different regions(Sharples et al., 2007), it is necessary to consider their location and effect on gradients. To do this, the profiles were sorted into 4 different dynamic regimes which are broadly characterised by the local depth. These 4 regimes were off shelf (deeper water > 200 m), shelf break (close to the shelf break at ~200 m), central shelf (away from both the shelf break and inland areas ~150 depth) and those made in the nearshore region (~100 m depth). The regime allocation for each of the 29 profiles is shown on the topographic maps of the Central Celtic Sea (Figure 8.20) and the Hebridean shelf (Figure 8.21).

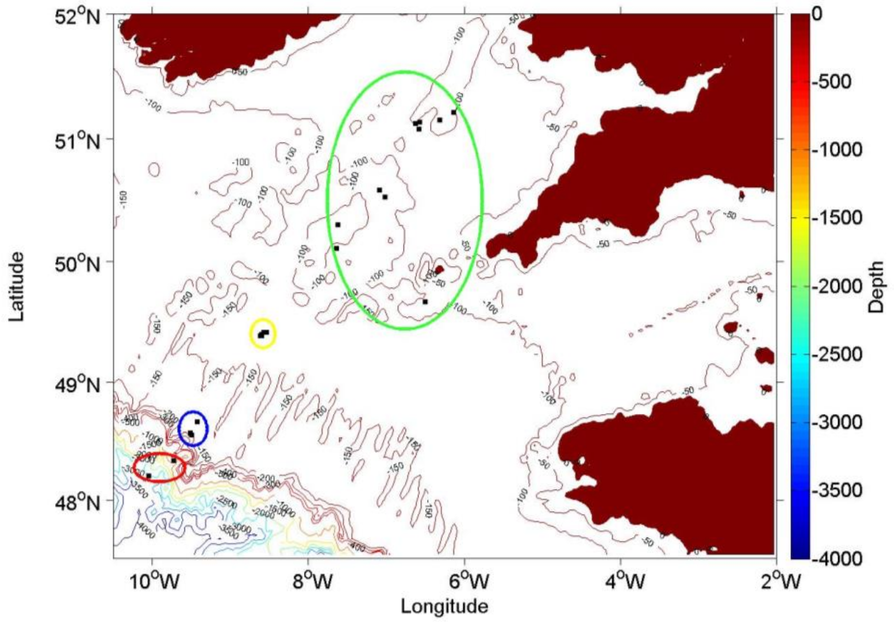

Figure 8.20 Topographic map of the Celtic Sea region

Topographic map of the Celtic Sea. Land is burgundy coloured. Depth contours are shown for 50, 100,150,200m and every 500m then on to 4000m. NSOP deployment locations are marked by black squares and are grouped into 4 depth regimes (where off shelf (red), shelf break (blue), central shelf (yellow) and nearshore region (green)) identified by coloured ellipses.

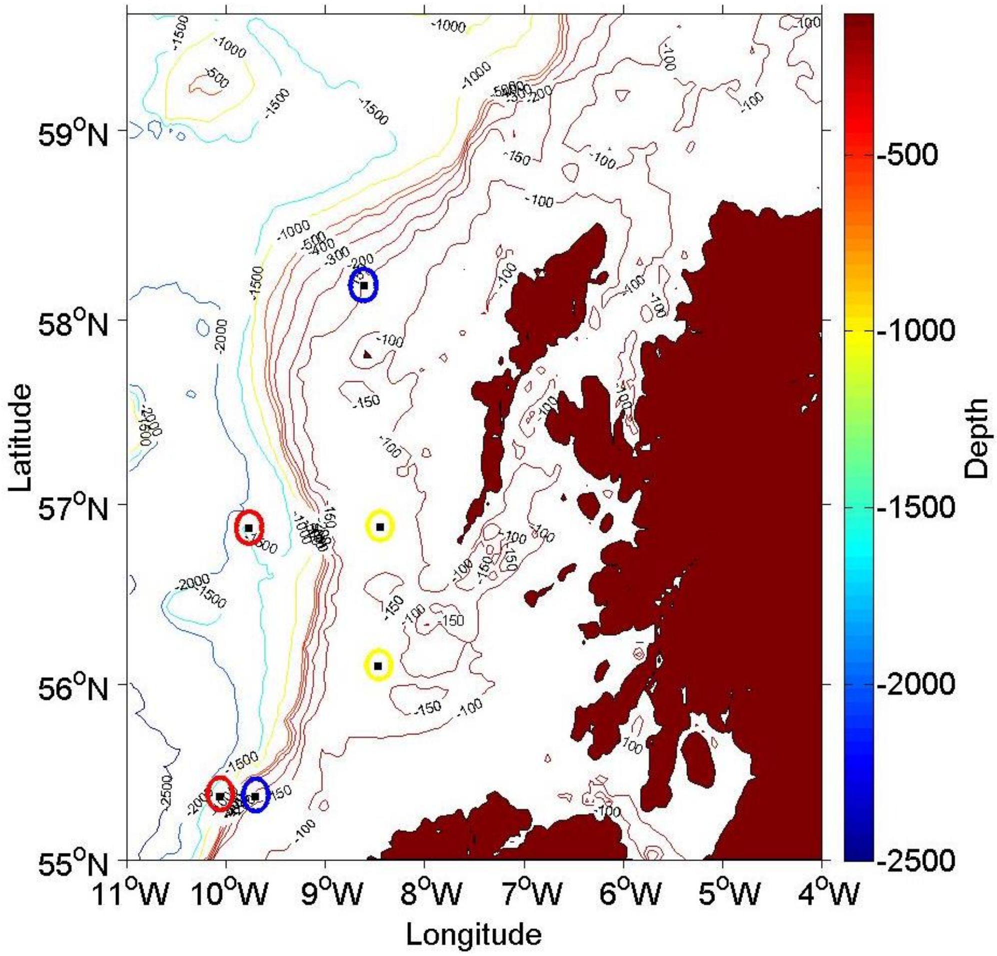

Figure 8.21 Topographic map of the Hebridean Shelf region

Topographic map of the Hebridean Shelf. Land is burgundy coloured. Depth contours are shown for 100,150,200m and every 500m then on to 2500m. NSOP deployment locations are marked by black squares and are grouped into 4 depth regimes (where off shelf (red), shelf break (blue) and central shelf (yellow)) identified by coloured ellipses.

ΔT and ΔCO_2 for each of the four individual regions does not vary much from the overall trends (Figure 8.22). The main exception to this appears to be the shelf edge CO_2 profiles which appear to be more negative. This largely indicates that the processes that distinguish these regions such as the strength of the tides, regional productivity and fresh water input do not play a major role on the formation of gradients. Some of these processes are less impactful at the near surface but it is surprising to see no clear relationships as the influence of the tides are impactful on the near surface.

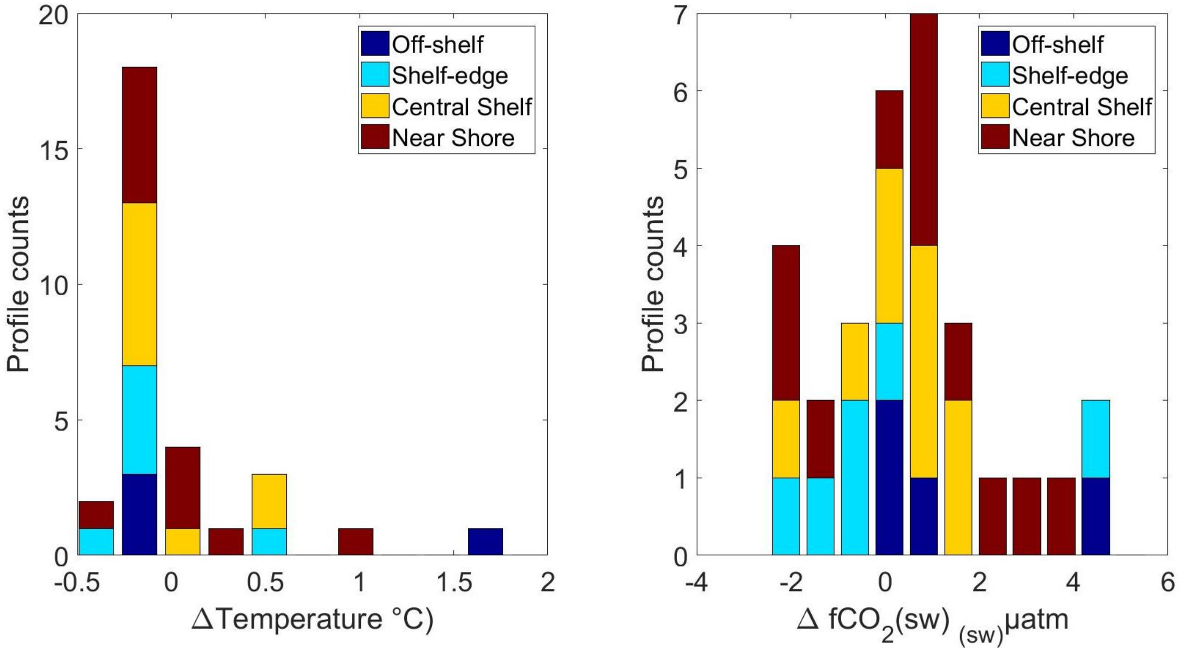

Figure 8.22 ΔT and ΔCO_2 by region

Profiles counts of the average ΔT(a) and ΔCO_2 (b) for all SSB profiles as calculated as described in section 8.2 split into 10 equally spaced bins. The columns are coloured by region as indicated in (section 8.8).

8.9 Correction to in situ temperature

The correction to account for the effect upon fCO_2 due to the difference between the equilibrator and the in situ surface seawater temperature is typically large. The accepted correction uses a constant of 4.23%°C^{-1} (Takahashi et al., 1993). This constant was calculated from a single cruise in the North Atlantic and has since been used to account for the temperature effect in all subsequent studies of global oceanic CO_2 (Takahashi et al., 2009). This correction involves two key assumptions (1) that the carbon system is linear with temperature and (2) that the carbonate chemistry in the North Atlantic is representative of the rest of the ocean, in reality it has been shown that constants of between 3.7 and 5.3%°C^{-1} are appropriate for seawater (McGillis and Wanninkhof, 2006). To reduce the errors arising from applying the correction, changes to the temperature of the system are minimised by locating the CO_2 systems close to the seawater intake and excluding data with a temperature differential >3°C (Bakker et al., 2016).

Any error arising from this correction is not apparent during data inter–comparisons as all systems utilise the same correction and back to a single temperature (Ribas-Ribas et al., 2014). The NSOP CO_2 data are calculated for multiple depths with different temperatures. Errors in the temperature correction have the potential to generate a spurious CO_2 profile. Based on calculations of the carbonate system and using the dissociation constants from Mehrbach et al. (1973). McGillis and Wanninkhof (2006) showed that the error associated with the temperature correction diminished around 15°C. For seawater at 10°C the difference between the error associated with using the difference from the 4.23 % °C^{-1} is about 0.125% °C^{-1}. For a seawater CO_2 of 380μatm this equates to 0.475μatm for a temperature correction of 1°C.

Part of the NSOP methodology involved running tubing along the deck which meant that the seawater temperature increased before reaching the equilibrator. The average temperature correction applied to the data on the SSB cruises and -1.04°C at L4 is shown in Figure 8.23. The water always warmed on deck except when it cooled during OCT14. The seawater warmed substantially in the tubing during the summer months with over half of the L4 profiles (51%) and 24% of the cruise profiles warming by >1°C.

There does seem to be a trend between the magnitude of the temperature correction and the ΔCO_2 (Figure 8.23). Many of the largest ΔCO_2 were from deployments where the temperature differential was big. This link may be coincidental or may reflect the issue with using the 4.33% $°C^{-1}$ constant. Another explanation is that the days with high solar irradiance where there were ΔT and thus ΔCO_2 may have also been the same days that the tubing was heated, this seems a likely explanation.

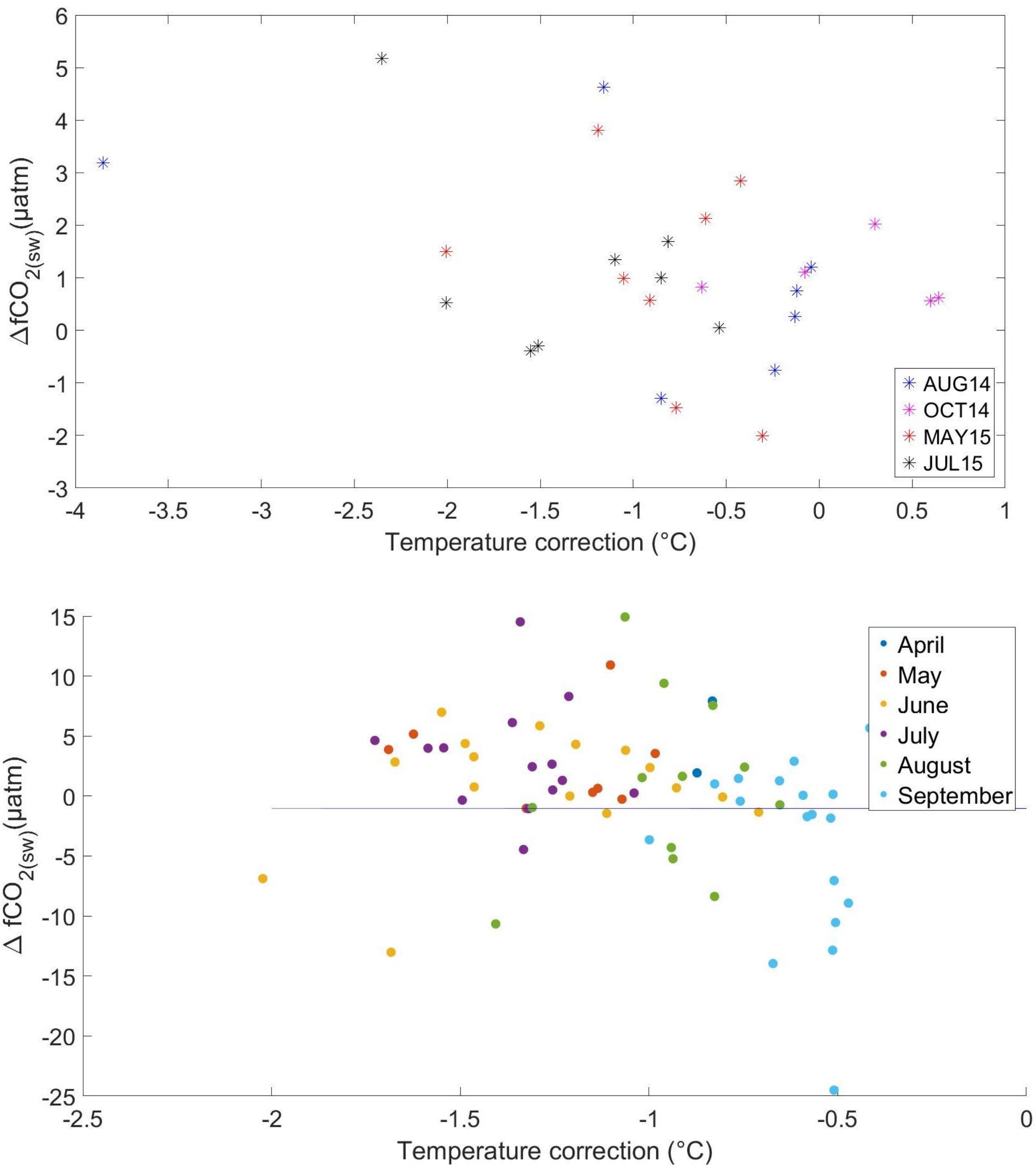

Figure 8.23 Temperature correction and ΔCO_2 relationship

The temperature different between the CTD and equilibrator temperature (CTD-equilibrator) and ΔCO_2.The marker colours corresponds to gradients measured in different cruises and months as specified in the legend. Note axis limits are not the same.

Whilst no measurement methodology was provided, an example of a measured CO_2 surface gradient was provided in Garbe et al. (2014). Using the temperature and measured CO_2 with no temperature correction, an alternative temperature dependence was inferred. The profile data suggested a fractional change of 6.2%°C^{-1}, much greater than 4.33%°C^{-1}. Up until this point in the thesis only the 4.33%°C^{-1} has been used, here we apply the same correlation analysis as Garbe et al. (2014) to derive a new fractional constant for each profile (Figure

8.24). If the ΔCO_2 are driven solely by temperature, it is expected that the fractional constant would be between 3.7%°C^{-1} and 5.3%°C^{-1} (McGillis and Wanninkhof, 2006). Many of the derived fractional constants are out of this range which means that biases in the temperature correction alone can not explain the CO_2 profiles.

The fractional change in CO_2 per °C is extremely variable at L4. A large number of profiles suggest a fractional change >10%°C^{-1} and <2%°C^{-1}. Negative constants are highly unlikely as this requires fCO_2 to reduce as water warms. The large divergence from the known relationship for these profiles at L4 indicates that there is another factor at play. There were salinity gradients in the majority of the L4 profiles which may have caused this discrepancy as salinity is assumed to be constant when calculating fractional constants with CO2SYS. The influence of marine/coastal TA/DIC or organics may alter the alkalinity and change the fCO_2 –temperature correction factor.

For several profiles from AUG14 and JULY15, the fractional constant is in the expected range and fCO_2 correlates strongly with temperature. However there are also a number of profiles where fractional constants are outside the expected range fCO_2 does not correlate strongly with temperature.

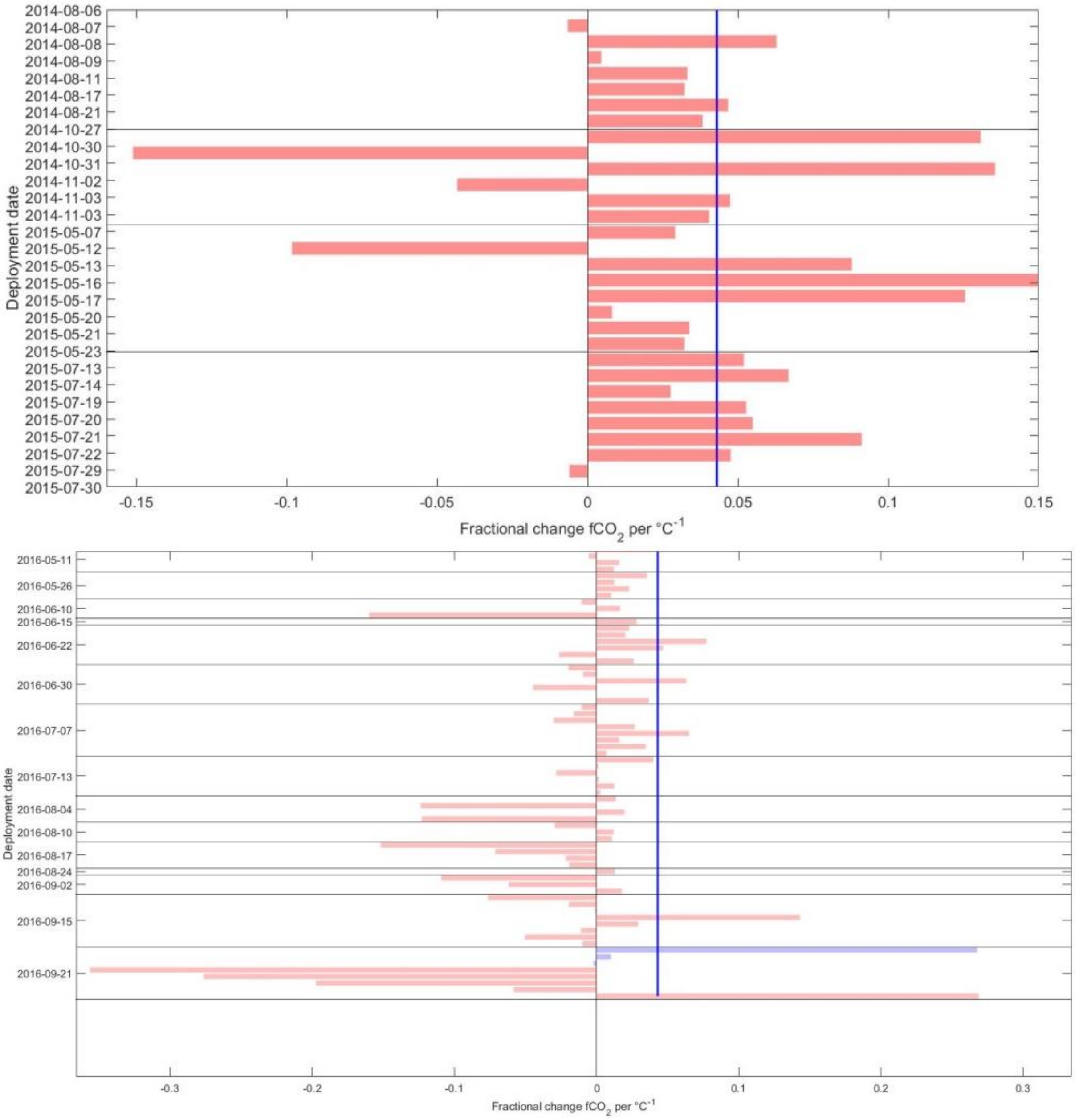

Figure 8.24 Temperature and fCO_2 derived fractional CO_2 constants

The fractional change in fCO_2 for all 29 profiles from the cruises (a) and 71 profiles made during the 16 NSOP deployments at L4 (b) are indicated by the red bars. The profiles from each cruise and different deployments are separated by black horizontal lines. The fractional change constant of (Takahashi et al., 1993) is indicated by a vertical blue line. Note axis limits are not the same.

TA and DIC were measured for most of the profiles during MAY15 and JULY15, CO2SYS (Lewis et al., 1998) Matlab V1.1 (Van Heuven et al., 2011) was used to calculate a fractional change in CO_2 that is more representative of shelf seawater than the 4.23 % $°C^{-1}$ constant. The calculation used the dissociation constants of Mehrbach et al. (1973), the dissociation constants for potassium sulphate from Dickson (1990) the borate to salinity relationship of Uppström (1974), silicate and phosphate concentrations of 2 and 0.5 µmol kg^{-1}(Poulton et al., 2017),the average TA and DIC of the profiles and the relevant salinity and temperature data from the profile. Despite issues with the TA and DIC samples they are still representative of the stations they were collected. The calculated fCO_2 with the new constants is shown alongside the calculated fCO_2 using the 4.23 % °C-1 constant for cruise MAY15 and JULY15 (Figure 8.25).

The reason that the fCO_2 agree so well for MAY15 is that the fractional change constants were extremely close to the 4.23 % $°C^{-1}$ constant whereas during JULY15 the fractional changes were around 4.10% $°C^{-1}$. The change in fCO_2 calculated with the TA/DIC derived constants in MAY15 did not vary much from those derived using the 4.33% $°C^{-1}$. May 13th was an exception where fCO_2 was roughly 1µatm greater. For the profiles from JULY15 the fCO_2 calculated with the fractional change constant was ~1-2µatm greater than the fCO_2 calculated with the 4.33 % $°C^{-1}$ constant. Nearly all the profiles for JULY15 mirror the structure of the profiles calculated with the 4.33 % $°C^{-1}$ constant. The profile on the 29th July was an exception, this profile had a ΔT that was smaller for the surface values.

This comparison shows that after accounting for the possibility of an inaccurate temperature correction vertical CO_2 gradients are still present. The gradients measured here are not just an artefact of an error in the temperature correction.

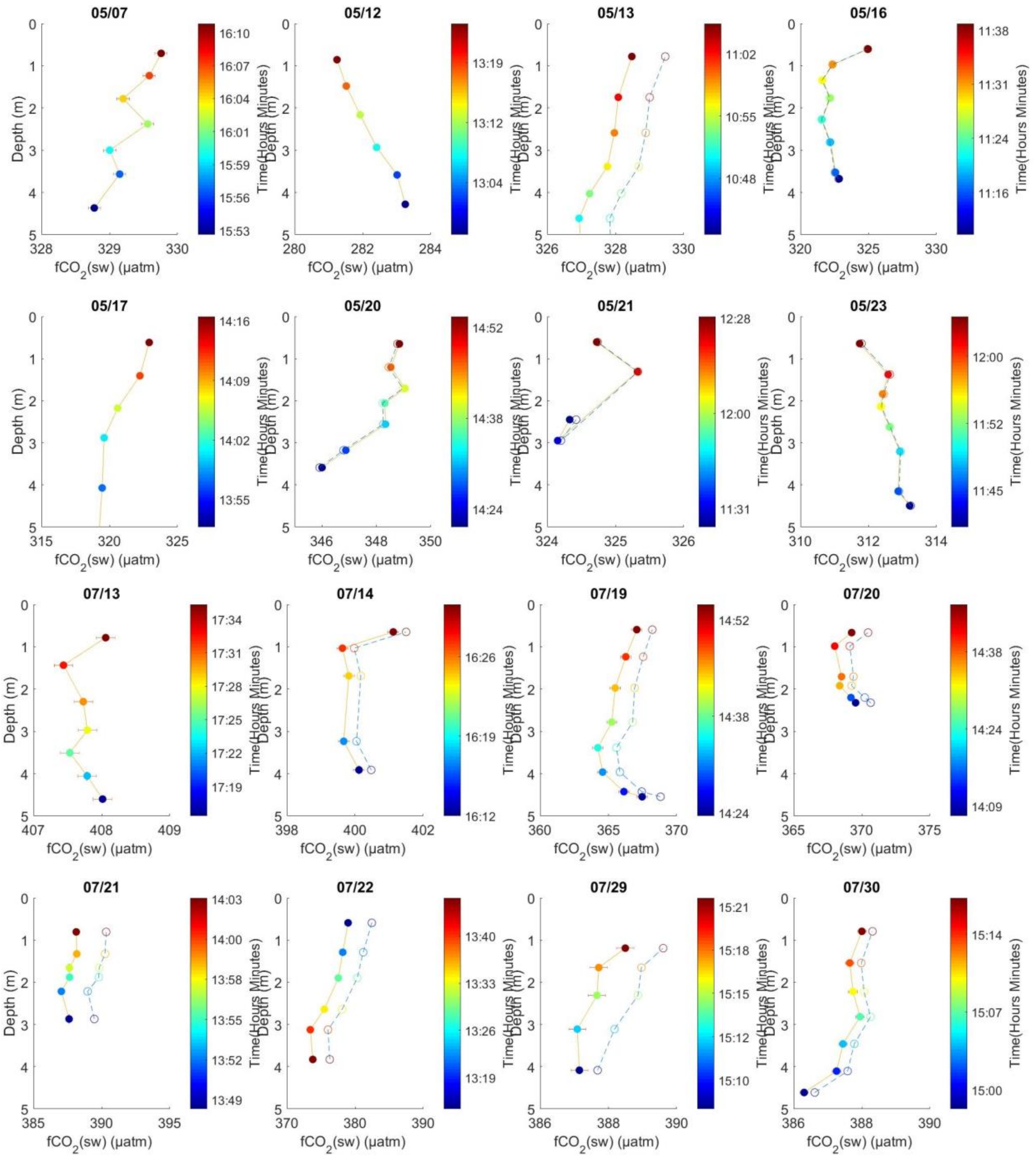

Figure 8.25 MAY15 and JULY15 CO$_2$ profiles using calculated fractional constant

Eight profiles collected in the Celtic Sea during MAY15(a) and JULY15(b). NSOP profiles of CO$_2$ were derived using the depth bins determined in chapter 2 and calculated with the constant of 4.33%°C (filled circles) or a fractional constant calculated using the TA/DIC values (unfilled circles). Vertical error bars show two standard errors of the mean in each depth bin. The horizontal errors are the propagated errors using the averaged bin variables to calculate fCO$_2$.

8.10 Which scenarios can feasibility explain observed gradients in a shelf sea environment?

The degree to which each processes alters the DIC pool and affect surface fCO_2 are summarised in Table 2. The feasibility for gradients to form for each of the four scenarios is demonstrated using the rates at which each process alters CO_2. The four scenarios are then compared to the gradients observed during the 4 cruises in AUG14, OCT14, May 15 and JULY15,

The effect of calcification on CO_2 is small, such that the rate would need to be two orders of magnitude higher in the surface to produce the gradients observed on the cruises. For this reason it can be assumed that its impact is negligible and is unable to create near surface gradients in all scenarios.

It is important to note that photosynthesis and respiration can produce positive and negative gradients without the need for NPP to be negative. For respiration/photosynthesis induced gradients to form in a confined surface layer, it is only necessary for the NPP to be different between the two layers.

Scenario 1 requires the CO_2 to drop in the sublayer; this would require enhanced photosynthesis or reduced respiration (>5m). Surface values of primary production vary substantially at the CCS site in April with sharp transitions at depth. On a daily basis, primary production rates remain very stable in the surface 20m (García-Martín et al., 2017). With the high production rates in April, only small differences in NPP between the two layers would be required to create gradients. Unfortunately no NPP data were collected with NSOP.

Scenario 2 requires the CO_2 to increase in the sublayer, which would require enhanced respiration or reduced photosynthesis (>5m). Scenario 2 is similar to scenario 1 in that it requires a mechanism to enhance respiration at depth compared to the surface. On April 15th at the CCS site, when the pycnocline was 15m, the community respiration was twice as large at 10m than at 5m. The increased respiration was attributed to the >0.8µm size fraction. The primary production in the upper surface 10m was fairly constant at this time (García-Martín et al., 2017). The NSTS indicate the water between 0.3–3.5m was 0.4°C warmer than at 7m at this time.

Another mechanism for increased surface layer respiration could be migration of zooplankton. The abundance of plankton in the surface ocean may be altered due to the grazing of migrating zooplankton into to the surface layer in the evening and out during the day(Lampert, 1989, Hays, 2003). Vertical movement of zooplankton is hard to determine as mean population movements do not correspond to migration (Pearre Jr, 1979). Zooplankton leaving the surface ocean during the day to avoid harmful radiation (Rhode et al., 2001) would reduce the respiration rate in the surface and increase the respiration rate below, decreasing surface CO_2. In the Irish sea ~60% of all phytoplankton species migrate between 0–10m each day (Irigoien et al., 2004). Increased respiration below the surface layer by migrating zooplankton could contribute to a NPP gradient by reducing the CO_2 uptake in the surface and increasing uptake at depth.

Scenario 3 requires CO_2 to decrease in the surface layer. This would require an outward flux of CO_2 to the atmosphere, a rainfall event or increased NPP. The atmosphere/ocean ΔCO_2 favoured CO_2 outgassing on three of the NSOP profiles (04/08/14, 27/10/14 and 13/07/15). Only one profile (27/10) had a negative seawater ΔCO_2 of 2µatm. Whilst the wind speed before the deployment (~7ms^{-1}) was low enough for a gradient to form, the low ΔCO_2 of 5.6µatm would have meant a surface layer would have changed at ~0.05 µatm hr $^{-1}$ which would be too slow to explain the gradient observed. It is unlikely that outgassing of CO_2 can explain any of the negative gradients observed with NSOP. Rainfall is a strong candidate to explain the observed negative gradients. Unfortunately, the deployment notes do not mention any deployments occurring in the rain, similarly there was little evidence of dilution of the surface salinity in the profiles which would also indicate a rain event. Whilst the dilution effect on CO_2 can not be shown with these data it remains a viable way for negative surface gradients to form. Some of the largest negative gradients measured with NSOP were in MAY15 and could feasibly be explained by enhanced phytoplankton production in the surface. There is no production data from the cruises in the upper 5m to support this (García-Martín et al., 2017).

Scenario 4 requires the CO_2 to increase in the surface layer. This scenario requires an inward flux of CO_2, increased respiration or reduced photosynthesis at the surface. Photo inhibition of phytoplankton has been observed diurnally (Behrenfeld et al., 1998). The maximum electron transport rate in photosystem 2 was also shown to significantly correlate with optical depth (Moore et al., 2006). Photo inhibition is possible in the surface ocean but there appear to be no comprehensive studies in the surface 10m, most likely due to sampling difficulties. Community respiration in the surface microlayer has been recorded as being 1.4 to 28 times greater than in the underlying water(Obernosterer et al., 2005). These respiration rates could also drive net heterotrophy and feasibly explain scenario 4.

Without complete profiles of the rates of primary production and respiration in the surface 10m it is difficult to attribute gradients to each process or to say whether rates measured from bulk surface CTD samples are representative of the surface few meters. The predominantly positive gradients measured during the 4 cruises are most likely explainable by an air sea flux into a confined surface layer. Over the course of an afternoon 1.9 µatm gradients are explainable which is around the size of ΔCO_2 observed in AUG14 and JULY15.

8.11 Conclusions

ΔT had a slight positive correlation with irradiance and a strong negative correlation with wind speed on both the cruises and at L4. ΔT >0.1°C were very infrequent in the shelf seas around the UK, which meant that only a few profiles were measured in these conditions despite targeted sampling.

ΔS on the cruises were small and negative. ΔS at L4 were also predominantly negative and substantially larger than on the cruises with some as large as 0.1. The majority of ΔS were <0.001 and >0.001. These gradients are substantially larger than those observed during the SSB cruises. ΔS was not correlated with either wind speed or irradiance.

The measured ΔCO_2 were predominantly small at L4 (69% <1.5µatm) and (93% <2.5µatm), much smaller than observed by Calleja et al. (2013). There was no link between the strength of ΔCO_2 and different regions of the shelf. The strength of ΔCO_2 did not correlate strongly with the strength of the solar irradiance but was found to negatively correlate with wind speed. The occurrence of the largest ΔCO_2 were observed at wind speeds < $6 ms^{-1}$ during the cruises. Small ΔCO_2 were observed even when there were no gradients in temperature or salinity. Large temperature and ΔCO_2 were concurrently observed at low wind speeds. The formation of large ΔCO_2 >2.5 µatm appears to be dependent on low wind speed conditions and large ΔT. The relationship between ΔT and ΔCO_2 was not statistically significant for all the cruises but was evident for AUG14 and JULY15.

As all the profiles were measured over the course of ~30 minutes, there is a possibility that the gradients measured here reflect spatial and temporal changes in the CO_2. This could account for many of the smaller ΔCO_2 (<1.5µatm – the same size of temporal changes). It was difficult to account for advection and temporal changes that may have confounded the interpretation of the results here.

The correction to in situ temperature is a source of error in the ΔCO_2 due to the large temperature correction applied. The fractional constants derived from the temperature relationship varied considerably with those from AUG14 and JULY15 falling close to the 0.433 constant whereas those from OCT14 and MAY15 and those from L4 vary considerably. The TA/DIC calculated fractional constants from MAY15 and JULY15 were very close to the 0.433 constant. However the ΔCO_2 can not be explained by an imperfect temperature correction.

Simple budget calculations show that fluxes into the ocean can explain the magnitude of the positive gradients observed on the timescales of the deployments. Rainfall may also play a role. Calcification is too small an influence on CO_2 to force the observed gradients. Changes in the ratio of NPP between a confined surface layer and at depth are capable of forcing the observed gradients but no data exists from the upper 5m to prove that this is the case. Calculations using biological production make the ΔCO_2reported by (Calleja et al., 2013) difficult to explain.

9 Gradient modification on the air–sea flux

9.1 Introduction

It is not apparent whether the times where ΔCO_2 are observed also correspond to periods of high flux. The effect of the observed ΔCO_2 on the absolute and relative changes in the flux is dependent on a number of other variables including the wind speed, temperature and the atmosphere ocean concentration gradient. The change in the flux can be represented as a proportional change relative to the flux measured at 5 m or an absolute increase or decrease in the flux. CO_2 fluxes are computed using in situ variables from the intake depth due to the lack of available surface temperature and salinity measurements(Takahashi et al., 2009). Current approaches seek to utilise satellite-derived observations of temperature and salinity in the surface skin of the ocean(Shutler et al., 2016).

For comparison, fluxes are computed in three ways:

1. Using the 5m, temperature, salinity and CO_2 measured with NSOP–(the traditional approach – approximately comparable to a ships underway system)

2. Using CO_2 from 5m and utilising near surface ~0.5m temperature and salinity measured with NSOP (similar to the approach in (Shutler et al., 2016))

3. Using CO_2, temperature and salinity measured at the near surface ~0.5m –(the NSOP approach)

9.2 Fluxes calculated using measurements from 5m

Fluxes (Figure 9.1) are almost all negative indicating a flux into the ocean, supporting previous conclusions that the shelves are a sink for carbon (Frankignoulle and Borges, 2001).

The largest fluxes were seen in May just after the spring bloom. The flux is fairly constant except during the deployment on the 12th. The wind was not particularly strong but the surface ocean was very undersaturated at all the sites measured during the cruise. This site was closer to land compared to the cruise deployments.

The AUG14 and JULY15 fluxes were smaller because of a small air–sea ΔCO_2 and low wind speeds. Across the shelf there was large variability between sites. For example on July 13that the CCS site there is an ocean to atmosphere flux but by the following day and upon the repeat profiles on the 29th and 30th the flux was reversed.

Despite the surface seawater CO_2 being near equilibrium and a low atmosphere ocean ΔpCO_2, the fluxes measured during OCT14 are still large due to the strong winds encountered on the cruise. The magnitude and direction of the fluxes measured here agree with previous flux calculations (Painter et al., 2016).

Three profiles indicate a flux out of the ocean, one of these on the 13th July was measured in the central shelf (CCS) in summer. The shelf is close to coming into equilibrium with the atmosphere by late summer so this seems plausible but it is not clear why the direction of the flux would change within one day. The profile made on the 6th August at the shelf edge was oversaturated, again this is difficult to reconcile as the shelf was never shown to be heterotrophic. Repeat transects have shown that the North Atlantic oligotrophic gyre is a carbon source between 10 and ~45°N for a short period (~50 days) in the summer due to the increased temperature (Watson et al., 2009). It is possible that oversaturated water was encountered at the shelf edge. The other time the flux was positive was on 27th October inland near Stornoway.

At L4 the largest fluxes were seen in May (following the spring bloom), mid–July and mid–August, the fluxes are large as the oceanic CO_2 is depleted and the gradient enhanced. Between deployments there is huge variability in the size of the flux, driven mainly by changes in the wind speed. For example the flux is ten times larger between the 10/06 and 15/06 mostly driven by the increase in the wind speed from $1.71 ms^{-1}$ to $9.60 ms^{-1}$. Within deployments, the flux from the profiles is fairly constant. For example on 05/11 all the profiles have a flux of ~ -200 $\mu mol\ m^{-2}\ hr^{-1}$, this is mostly driven by the short term stability of the wind speed over the course of an NSOP deployment. Despite slight to moderate wind speeds (5 – 10 ms^{-1}) near the end of the seasonal study such as during deployments on 09/21 the fluxes were not that large as the delta concentration between the atmosphere and ocean had become much smaller. The fact that the atmosphere and ocean were so close to equilibrium explains how it was possible for the ocean to transition from a source to a sink over the length of the deployment.

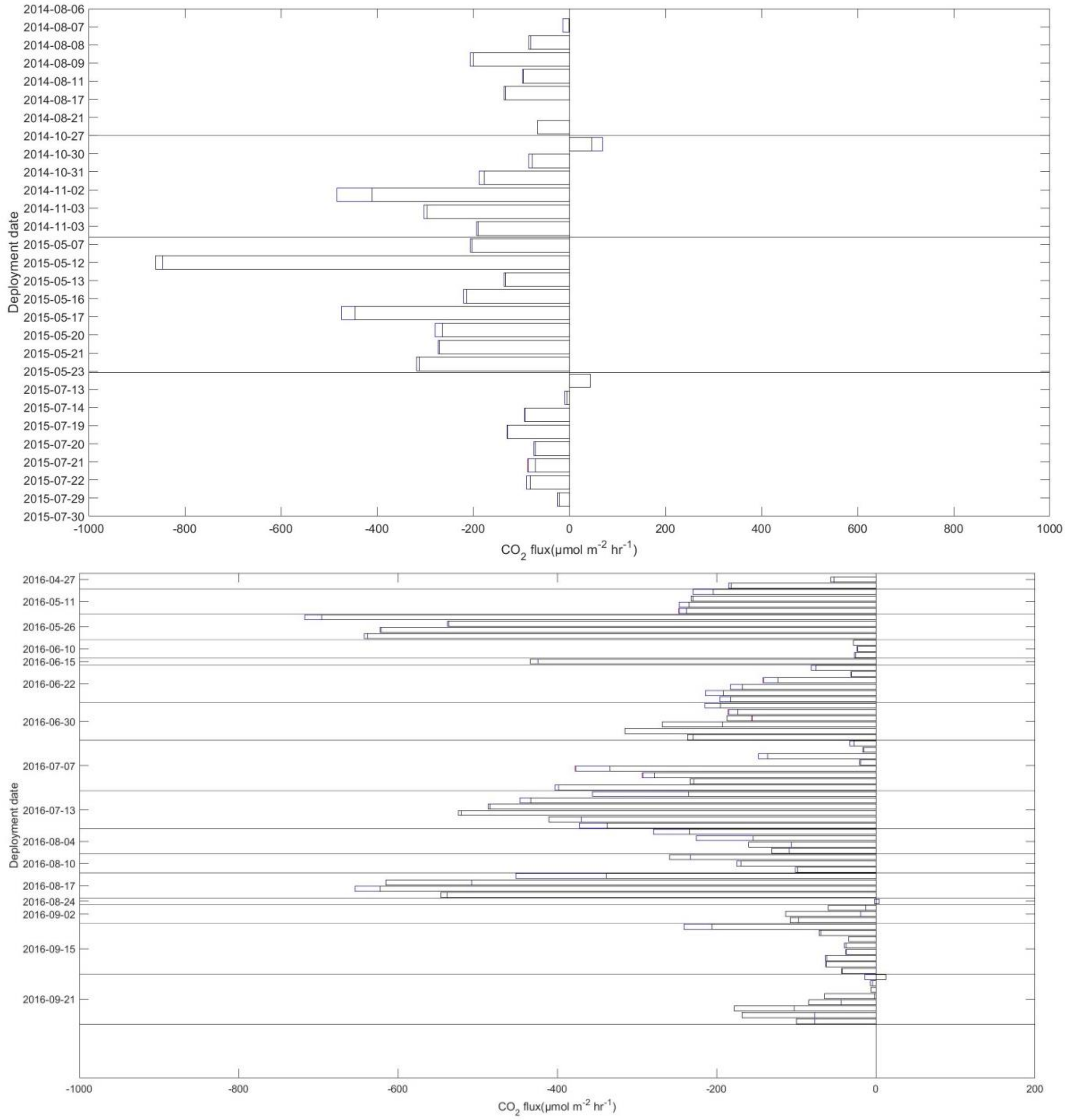

Figure 9.1 CO_2 fluxes calculated using NSOP parameters from different depths

The CO_2 flux for all 29 NSOP cruise profiles (top panel) and all 71 seasonal study profiles (bottom panel) calculated using variables from 5m (red), the surface temperature and salinity and CO_2 from 5m (blue) and all variables from the surface (black). The date of each profile is given on the axis. The horizontal lines identify which profiles were measured on each of the 4 cruises and each of the 16 seasonal study deployments.

9.3 Percentage change in flux using surface temperature and salinity

If the flux is calculated using the CO_2 from 5m and the surface temperature and salinity values, the effect is small. Almost all the L4 profiles have considerable negative ΔS and many had ΔT of 0.5 °C. The flux changes by a negligible amount <0.2% for all profiles (Figure 9.2). The salinity was constant in almost all the SB cruise profiles, the change between the fluxes calculated between methods 1 and 2 demonstrates the effect of temperature on the flux. The maximum ΔT was <0.5°C so it is not surprising that this effect was small. The temperature is used 4 times to calculate the flux. The largest effects on the solubility and Schmidt number almost cancel out and make the effect smaller than it otherwise would be (Woolf et al., 2016).

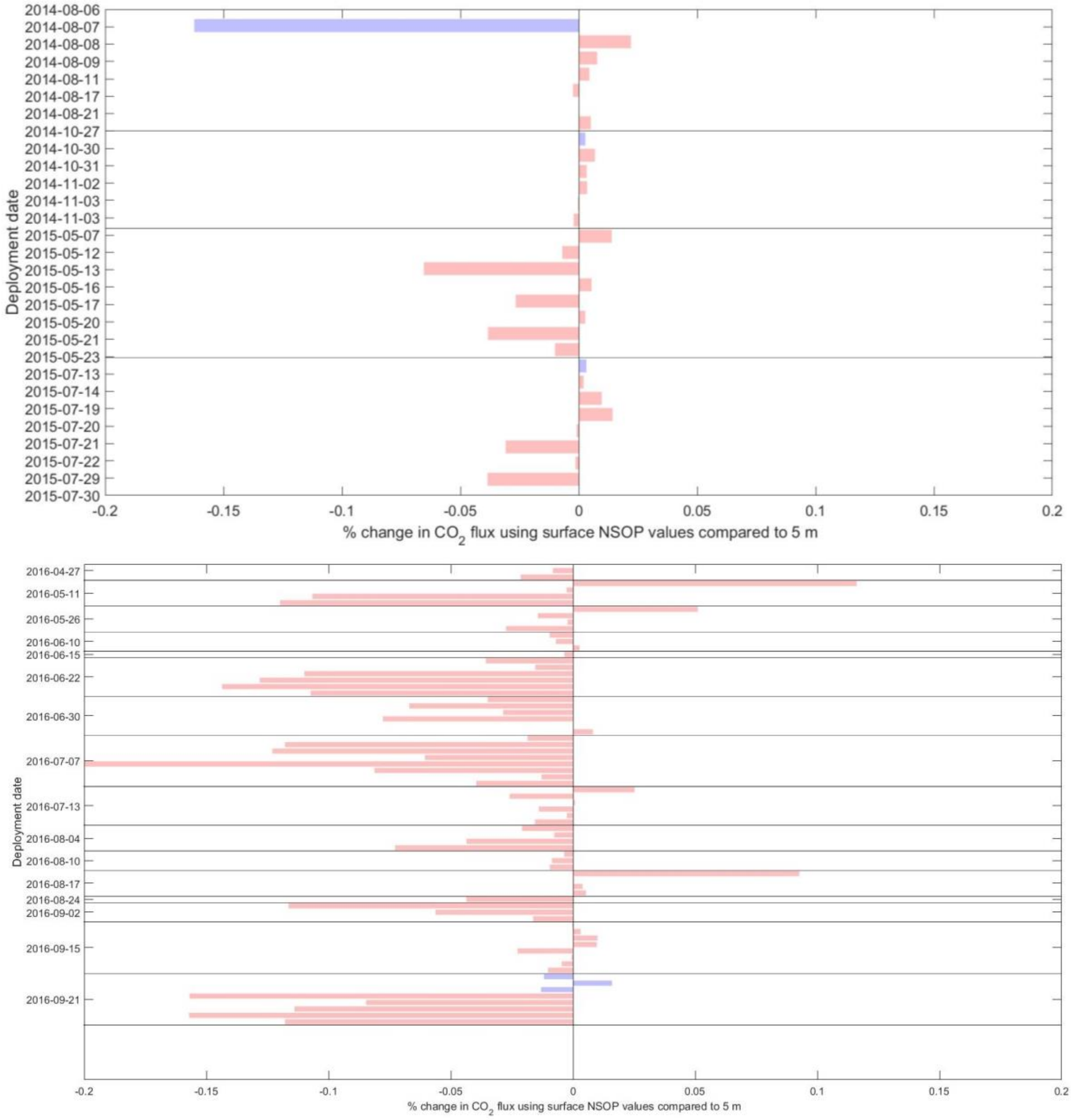

Figure 9.2 Percentage change in flux using surface salinity and temperature

The percentage change in the CO_2 flux calculated using temperature, salinity and CO_2 from 5m and using CO_2 from 5m and temperature and salinity from the surface for all 29 NSOP cruise profiles (top panel) and all 71 seasonal study profiles (bottom panel). The date of each profile is given on the axis. The horizontal lines identify which profiles were measured on each of the 4 cruises and each of the 16 seasonal study deployments. The red bars indicate profiles where the flux was into the ocean whereas the blue bars indicate a flux out of the ocean.

9.4 Percentage change in the flux using surface salinity, temperature and CO_2

When the measured surface CO_2 as well as surface salinity and temperature were used to calculate the flux, the flux was on average 3.1% smaller during the cruises (Figure 9.3). This indicates that the majority of the observed change was due to the CO_2 gradient but the temperature effect on the water vapour and the fugacity is also implicit in this as well. In some instances such as the 6 & 7th Aug, 27th October and 14th July the percentage change in the flux was very large (>20%). These were also some of the smallest absolute fluxes from all the deployments. The largest CO_2 gradients were observed when the wind speed was low, which also reduces the magnitude of the flux. The largest absolute fluxes seen in OCT14 and MAY15 (Figure 9.3) by and large had the smallest modulation in their fluxes using the surface measured CO_2 to calculate the flux.

At L4, the largest decreases in the absolute fluxes were seen on the largest fluxes in mid–July and mid–August, with many of the fluxes declining by >50 µmol m^{-2} hr^{-1}. The largest increases in the absolute fluxes were observed in September (02/ 09 , 21/09 and 04/08). 39% of the profile fluxes change by more than 10% and 18% of the profiles change by greater than 20%, the profiles undergoing the most extreme changes make up a small proportion of the total number of profiles. For the profiles near equilibrium in September, the changes in CO_2 drastically alter the flux (>>100%).

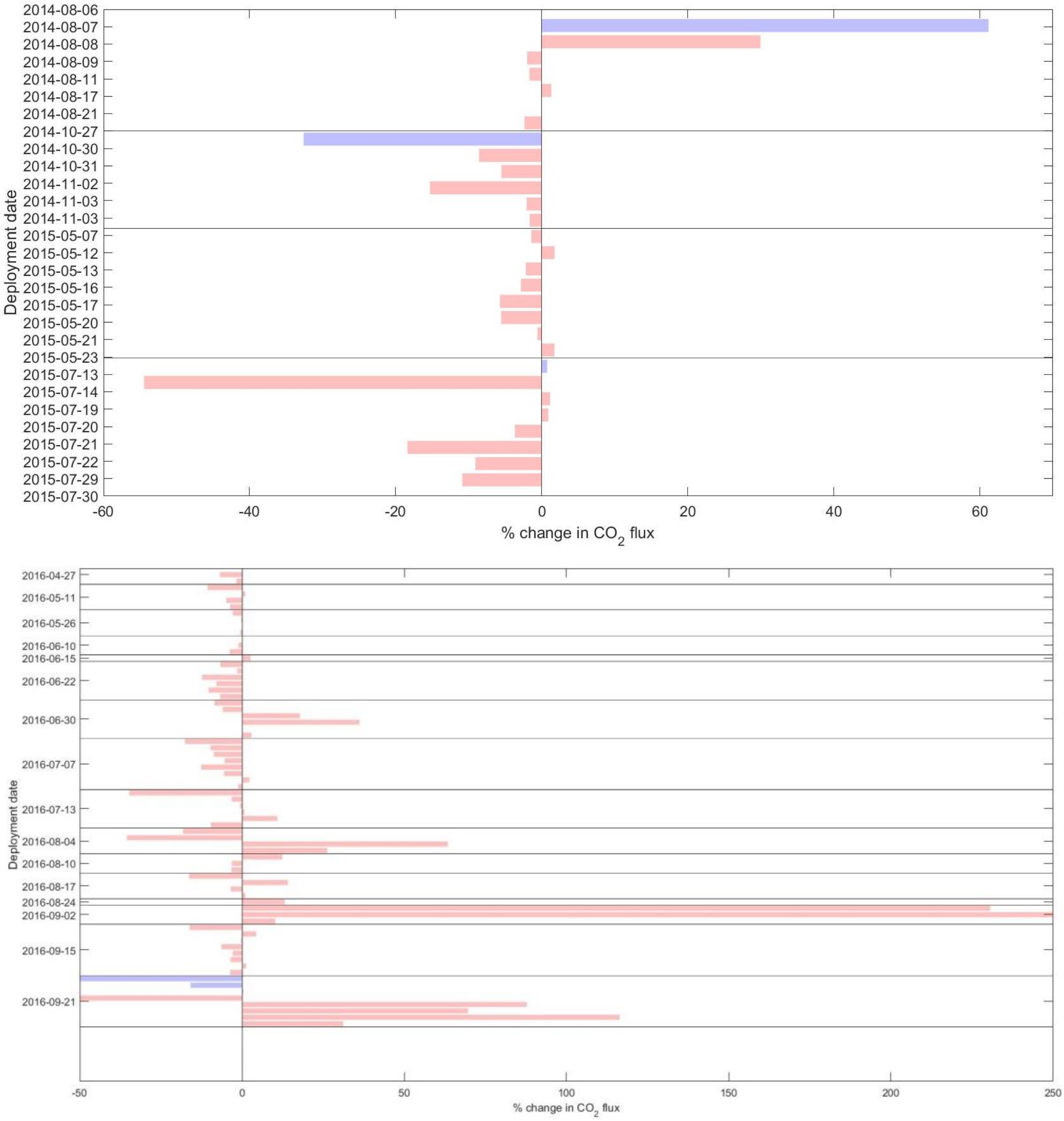

Figure 9.3 Percentage change in flux using surface NSOP values

The percentage change in the CO_2 flux calculated using temperature, salinity and CO_2 from 5m and surface CO_2 ,temperature and salinity for all 29 NSOP cruise profiles (top panel) and all 71 seasonal study profiles (bottom panel). The date of each profile is given on the axis. The horizontal lines identify which profiles were measured on each of the 4 cruises and each of the 16 seasonal study deployments. The red bars indicate profiles where the flux was into the ocean whereas the blue bars indicate a flux out of the ocean.

9.5 Conclusions

Almost all of the calculated CO_2 fluxes from both the cruises (26 of 29) and the seasonal study (67 of 71) were negative. Fluxes varied between each of the weekly deployments at L4 but were fairly consistent between profiles. The fluxes were largest after the spring bloom and in the high wind speed conditions during OCT14. The lowest fluxes were calculated during the two summer cruises AUG14 and JULY15.

Using the NSOP temperature and salinity has a very small effect on the flux (<0.2%). When NSOP surface CO_2 was used the flux for the majority of the profiles changes by 10–20% and for some of the smaller profiles by >200%.

The largest fluxes are those where high wind speeds are observed. The profiles with the large CO_2 gradients tend to occur at low wind speeds as this facilitates near surface stratification. This means that the relative flux changes substantially but the changes in the absolute fluxes are relatively small.

10 Implications for Shelf Seas globally

10.1 Implications of this work on the air sea flux of CO_2 in other Shelf Seas

In previous chapters, the irradiance, wind speed, the atmosphere ocean ΔCO_2, biological productivity rate and rainfall rate were identified as being explanatory variables that control the occurrence, and magnitude of near surface CO_2 gradients. These variables vary by location and time of year meaning their relative importance on the formation of near surface gradients will differ between individual shelf seas substantially. Ideally a full global biogeochemical model with a high resolution in the surface ocean and a short enough time step to characterise the physics in the near surface would be run for several years to assess the impact of gradients globally. Unfortunately, this would be extremely computationally expensive and is beyond the scope of this thesis. Instead, this section seeks to critically assess the relative importance of the different variables driving near surface gradients in shelf seas globally using large global datasets, back of the envelope calculations and insights from previous chapters. The major limitation of this approach is that the following calculations and conclusions are based on a number of assumptions but a degree of speculation is necessary to reveal the same insights as a biogeochemical model.

10.2 Global coverage of shelf seas

A global seafloor geomorphic features map (GSFM) created using Shuttle Radar Topography Mapping, provides a comprehensive overview of seabed physiography. This GSFM states that continental shelves cover 8.91% of the surface ocean (Harris et al., 2014). This value of continental shelf coverage varies slightly from those stated previously as it is based on the International Hydrographic Organisation (IHO) definition of continental shelves that encompasses, low relief (<10 m), medium relief (10-50 m), high relief (>50 m), shelf valleys, glacial troughs, coral reefs, shelf perched basins and sills (IHO, 2008). Whilst this methodology is original and diverges slightly from previous estimates, it is self-consistent and gives an excellent breakdown of global continental shelf coverage by ocean basin (Figure 10.1). It is worth noting that the global projection used for this figure distorts the actual surface areas by over exemplifying the Polar Regions.

The global surface area of the continental shelves on each of the ocean basins is shown in (Table 6). The largest area of continental shelf is found in the North Atlantic Ocean, the majority of this shelf area is part of the European shelf (where the NSOP profiles were made) as well as in the Caribbean Sea and the Scotian Shelf. The second largest region of shelf is located in the Arctic Ocean, the largest shelf regions are the Laplev Shelf, East

Siberian Shelf and the Chukchi Shelf with smaller regions in the Beaufort shelf and Barents shelf. The third largest region of continental shelf is the North Pacific; this is broken into three similarly sized shelf seas, the East China Shelf, the Sundra Shelf and the Bering Sea. A small amount of continental shelf is found in the Mediterranean on the Tunisian-Libya continental shelf and the Adriatic Sea. The ocean basins in the Southern hemisphere all have comparatively lower regions of continental shelf compared to the Northern hemisphere. The continental shelf in the Indian Ocean is generally narrow, except on the Northwest Australian coast but still constitutes a large surface area of 4,047,570 km^2. In the South Pacific there is relatively little continental shelf off the West coast of South America with the majority found on the Eastern coast of Australia in the gulf of Carpentaria, the Great Barrier Reef Shelf and the Shelf Seas around Tasmania. The vast majority of the continental shelf in the South Atlantic is found on the Patagonian Shelf with only very narrow regions of shelf off the West coast of Africa. The continental shelf in the Southern Ocean is found predominantly in the Weddell and Ross seas.

As the continental shelf in each basin is predominantly concentrated in individual shelf seas, the largest from each basin will be taken to be representative of the entire basin for the purposes of this analysis. The analysis below is not as comprehensive as that (Laruelle et al., 2014) who split the global shelf seas into the 45 MARgins and CATchment Segmentation zones(MARCAT), here the shelf seas are split into eight ocean basins with 17 large shelf regions identified. The 17 shelf regions identified for this analysis for all intents and purposes overlap with the largest catchment identified in (Laruelle et al., 2014).

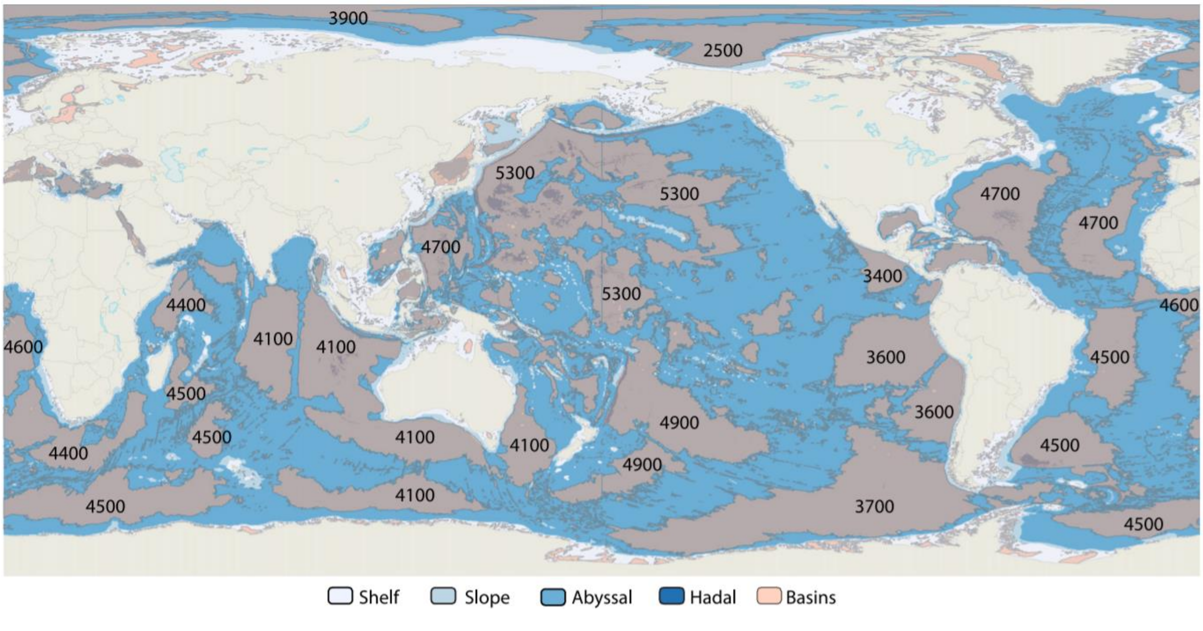

Figure 10.1 Global map showing the spatial extent of shelf seas
Global surface projection of the world’s oceans coloured according to underlying bathymetry depth. Areas of continental shelf are shown in white(Harris et al., 2014).

10.3 Shelf sea surface irradiance

Several components of the surface ocean heat budget: sensible heat, latent and net longwave radiation are readily calculable using the following known constants and variables:

the specific heat capacities of air, sensible and latent heat transfer coefficient, latent heat of evaporation, the wind speed (U_{10}), atmospheric temperature, oceanic temperature, the 10m specific humidity, the Stefan Boltzmann constant, absorptivity of the atmosphere and surface albedo. As the variables and constants are known, calculating global fields of these three heat fluxes in models is relatively straightforward, global projections of these variables are reproduced and collected in Large and Yeager (2004).

The global meridional heat budget of the ocean is given in (Figure 10.2). The incoming surface irradiance is the only net positive component of the surface heat flux meaning that it is the surface irradiance that drives diurnal warming making it a necessary variable in order to model the formation of diurnal warm layers.

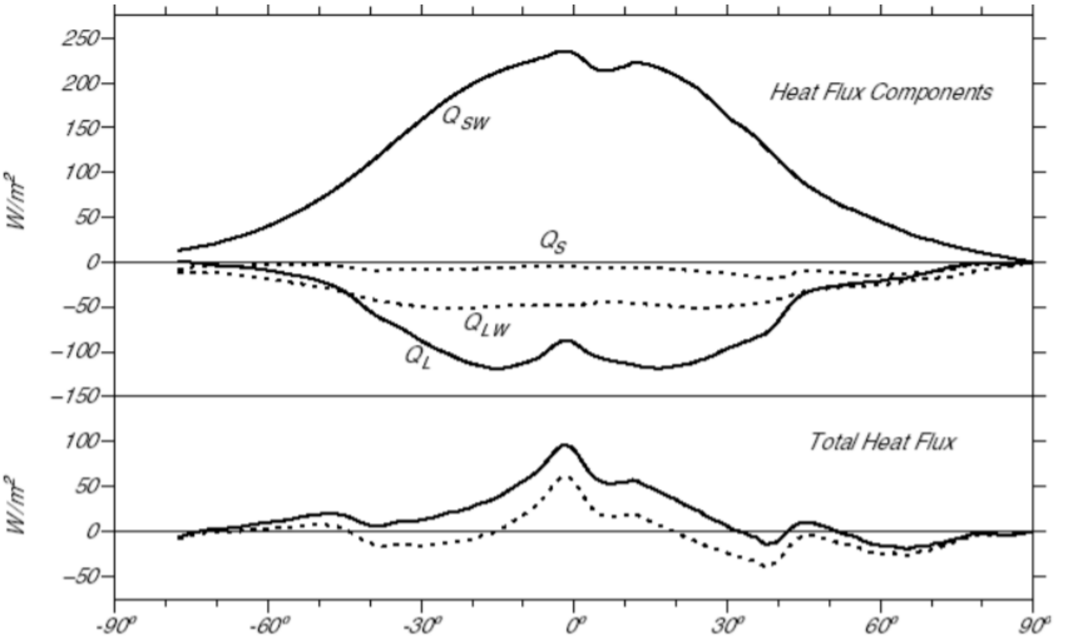

Figure 10.2 Meridional averages of the ocean heat flux
Zonal averages of the components of the ocean heat flux (Wm^{-2}), where Q_{sw} is shortwave insolation, Q_S is the sensible heat flux, Q_{LW} is the outgoing longwave radiation flux and Q_L is latent heat flux (da Silva et al., 1994)

Global top of the atmosphere irradiance is calculable relatively easily using the suns solar output, distance from the sun and the spherical law of cosines. Surface irradiance differs from the top of the atmosphere irradiance depending on the composition of the atmosphere as aerosols and water vapour (mostly in the form of clouds) absorb and reflect a fraction of the incoming solar irradiance. Variables such as the number of clear sky/cloudless days are often used as proxies to indicate the importance of clouds, as can be seen in Figure 10.3, this is geographically and seasonally variable. The interactions between incoming shortwave radiation and the atmosphere are complex and result in large uncertainties in the global surface irradiance values. Another important point regarding surface irradiance is that it varies substantially on different temporal scales: on a daily scale it is close to 0 wm^2 at night and usually peaking in daylight hours at 800-1200 wm^2, on a day to day scale irradiance is heavily impacted by local weather and on monthly scales the irradiance is dominated by the tilt of the earth.

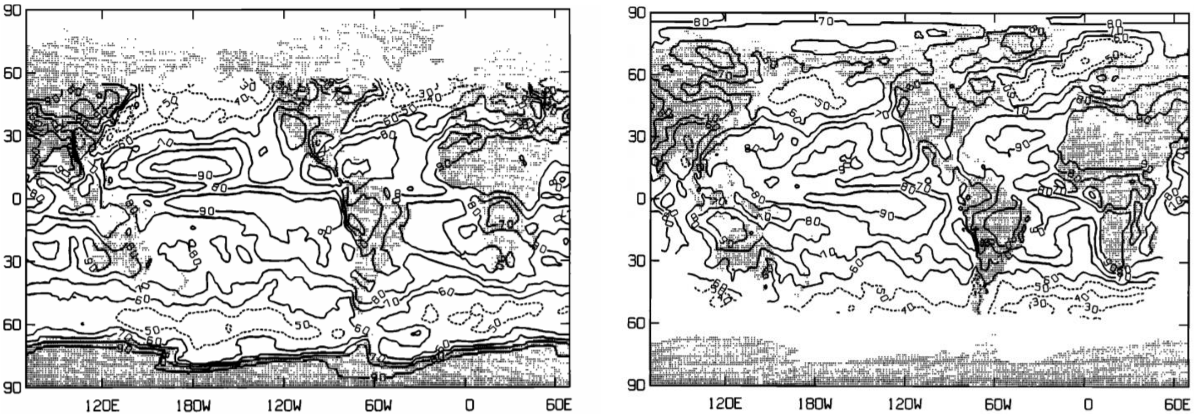

Figure 10.3 Clear sky days
Percentage clear sky irradiance in January 1984 (left) and July 1983 (right) (Bishop and Rossow, 1991).

Due to insufficient sampling at the ocean’s surface, surface irradiance climatologies have been constructed using surface measurements from predominantly from land based sites. Due to the limitations of creating a global measurement based climatology, considerable effort has gone into modelling surface irradiance (Badescu, 2014). There are a number of unique methodological approaches to modelling the surface irradiance including calculations utilising time series analyses, satellite photography, satellite retrieved data, sunshine and cloud cover, Boltzmann statistics, air temperature, neural networks, machine learning and radiative transfer equations (Badescu, 2014).

Model output of global surface irradiance is typically expressed as monthly or yearly averages, for example global surface irradiance data for January and July (Bishop and Rossow, 1991) (top 2 panels Figure 10.4) and global surface solar irradiance (Ohlmann et al., 1996). These synthesised products are useful for climatological studies but without additional finer detail information such as daylight hours, clear sky days (Figure 10.3), and daily diurnal distribution of irradiance it is exceedingly difficult to use them alone to infer whether and at what frequencies these irradiances would result in thermal stratification.

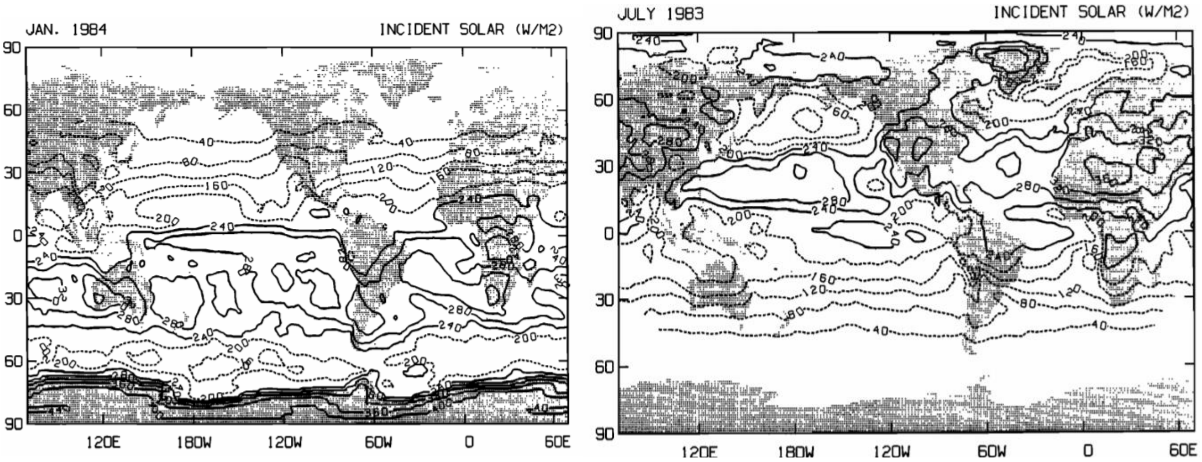

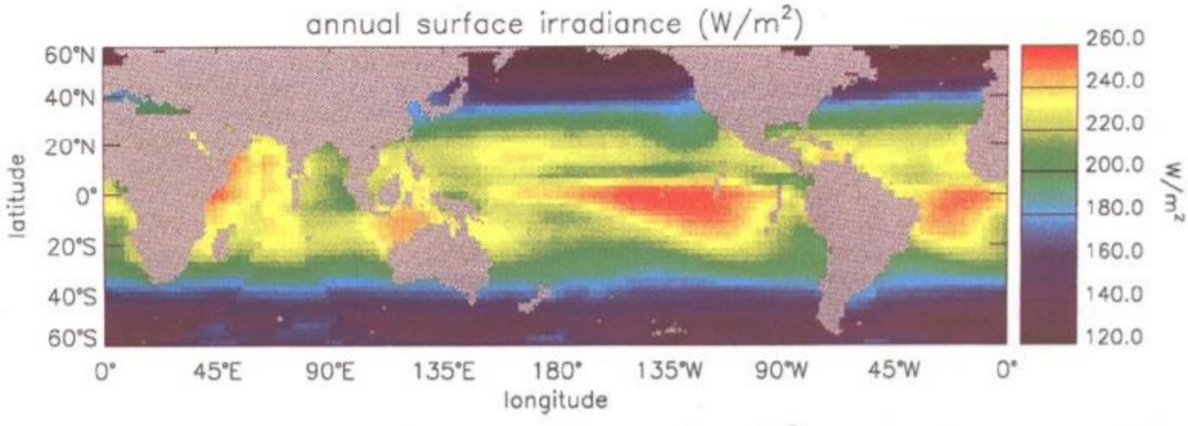

Figure 10.4 Global average solar irradiance

Average monthly surface solar irradiance in January 1984 (top left) and July 1983 (top right) (Bishop and Rossow, 1991). Average surface solar irradiance (Bottom panel) (Ohlmann et al., 1996).

One alternative to average climatological maps for the purpose of diagnosing the occurrence of near surface gradients is to use another indicator such as peak surface irradiance. An example of this is shown for the equatorial region for a single day by (Webster et al., 1996).

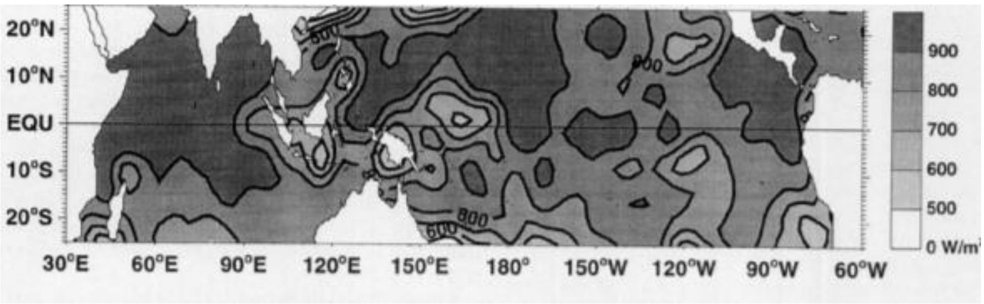

Figure 10.5 Maximum surface insolation values

Maximum surface insolation values for the tropics on 1st April 1998 calculated using surface radiation budget analysis (Webster et al., 1996).

To obtain global coverage for surface irradiance the common approach has been to use radiative transfer models and satellite observational data of the distribution of clouds and their brightness from METEOSAT (Bishop and Rossow, 1991). This approach has many advantages as it provides the spatial and temporal scales needed as an input dataset to force near surface gradient models e.g. global coverage <1° and temporal scales of ~1hr. 3 decades of hourly 0.05° processed METEOSAT data is now readily available as input data for diurnal warming models (Müller et al., 2015).

Diurnal warming models forced with similar high resolution solar irradiance data are required to infer the likelihood of diurnal warming for specific locations; this has been done in other studies and is discussed in section 10.6.

10.4 Shelf sea wind speed

The influence of the wind on the surface of the ocean is often given by the wind stress in both its northward and eastward components but as the conversion is simple, this discussion will focus only on wind speed. A common source of wind speed data is the NCEP 40 year wind speed climatology which is often used for climatological purposes (Kalnay et al., 1996). Satellite retrievals of wind speed by QuikScat are completed at much higher temporal resolution of every 12 hours at a very high spatial resolution of 0.25° grids (Risien and Chelton, 2008). The climatological wind speed from QuikScat is shown in (Figure 10.6a). There are differences in the NCEP and QuikScat data that lead to differences in the average global wind speed and depending on the gas transfer parameterisation the air sea flux estimate of 43% (Wanninkhof et al., 2009). The wind speed distributions from scatterometer data and from modelled data were reconciled by (Monahan, 2006).

The wind speed distribution is an important factor for influencing near surface gradients as gradients are only likely to form when the wind speed is <6ms^{-1}. The amount of time the wind speed is <6ms^{-1} is not apparent from the average wind speed alone. The wind speed distribution is partially encompassed by the standard deviation in the average wind speed (Figure 10.6b). There are some issues with using the bulk formulation for wind speed as the wind speed follows a Raleigh distribution (Wentz et al., 1984). Therefore it is necessary to account for the variability in the wind speed, the improved temporal resolution of QuickScat is better as it catches this variability (Wanninkhof et al., 2002). The wind speed distributions do not follow a perfect Raleigh distribution across the whole globe, the regions where this is the case have now been identified (Marcos et al., 2018). The skew and the kurtosis are both useful indicators of the distribution (Figure 10.6c and Figure 10.6d).

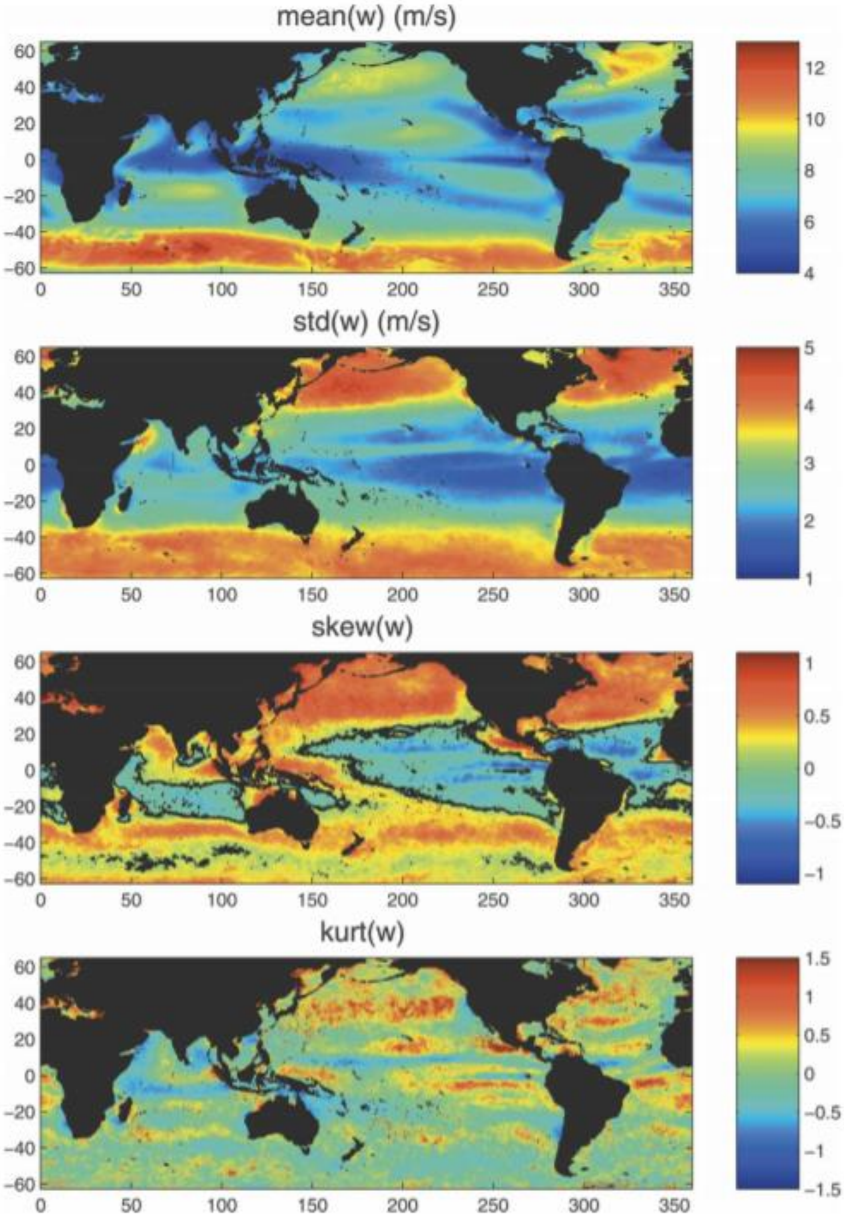

mean(w) (m/s)

std(w) (m/s)

skew(w)

kurt(w)

Figure 10.6 Global wind speed distribution

Global distributions of the mean, the standard deviation, the skew and kurt of the wind speed (Monahan, 2006).

The regions with the highest average wind speeds are found in the mid latitudes, the European Shelf, Scotian Shelf, Bering Sea, Patagonian Shelf and Tasmanian Shelf, all of these shelves have large standard deviations in their wind speeds (> 4ms^{-1}) which suggests that there is a wide range of wind speeds and the wind speeds are often quite high.

In contrast, the shelves found in the lower mid latitudes and tropics which includes the Sundra Shelf, Adriatic Sea, Caribbean Sea, West Australian Shelf, Gulf of Carpentaria and the Great Barrier Reef Shelf have lower wind speeds of 4-7 ms^{-1} and standard deviations in their wind speeds of 2-3 ms^{-1}. As the wind speed is lower and less variable on all of these shelves it would be expected that there would be a higher chance of near surface stratification here. There is no wind speed for the Polar shelves in (Monahan, 2006) but from other sources the wind speed is also lower at ~6 ms^{-1}.

The map showing the curt is informative about the wind speed distribution. The high curt in the Caribbean Sea, Scotian Sea and Adriatic Sea mean there is less variability in the wind speed there. The negative curt in the East China Sea and the Gulf of Carpentaria indicate there is a lot more variability at the wind extremes, in both these shelves this would indicate more periods of low wind speed and more chance of thermal stratification. The skew of the wind speed is largely positive across the whole ocean which is what is expected due to the Raleigh distribution, the only negatively skewed areas are in the tropical Atlantic and Pacific where there are no major shelf seas.

It is important to note that the wind speed has an increasingly important effect on the latent and sensible heat fluxes when the air temperature is warmer at higher wind speeds (Figure 10.7).

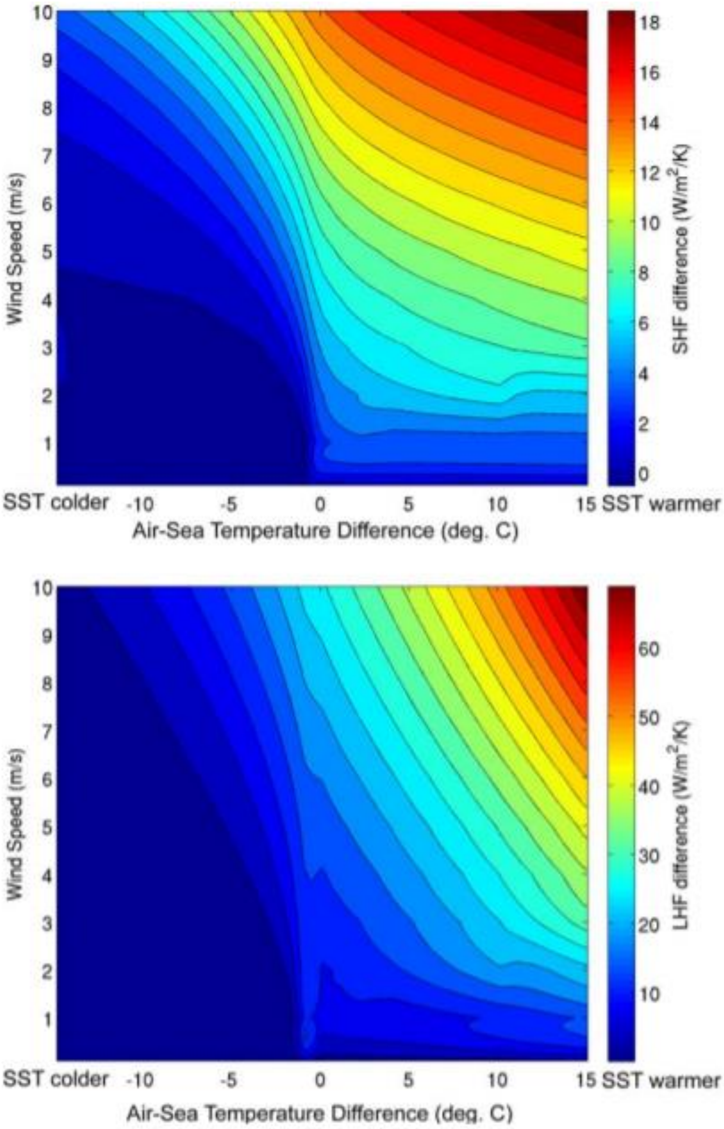

Figure 10.7 Latent and Sensible heat flux controls

Modelled Sensible (A) and latent (B) heat fluxes as functions of the wind speed and the atmosphere ocean temperature difference (Weihs and Bourassa, 2014).

10.5 Modelled wind and irradiance scenarios for diurnal warming events

Numerical models such as those introduced in the introduction are capable of predicting the near surface warming given the wind speed and the solar irradiance as inputs. Multiple model runs under different forcings can be used to inform the strength of diurnal warming in each scenario, this is called a sensitivity study. An example of this (Figure 10.8) shows the diurnal warm layer expected under five different wind speed scenarios and a range of daily peak solar radiation (Webster et al., 1996). These model results indicate that diurnal warming only occurs at <10ms^{-1} but predominantly at <5ms^{-1} unless irradiance is also strong. If the wind speed is <3ms^{-1} the solar radiation is not the determinant of the diurnal warming but only the magnitude of the gradient between 0.5°C and 2.5°C. A different sensitivity study performed with the POSH model of Gentemann et al. (2009) but with max diurnal radiation as the dependent variable show the exact response, warming of 1 – 2.5°C at wind speeds <3ms^{-1} and general no diurnal warm layer above 7 – 8 ms^{-1} except in strong irradiance conditions (Figure 10.9).

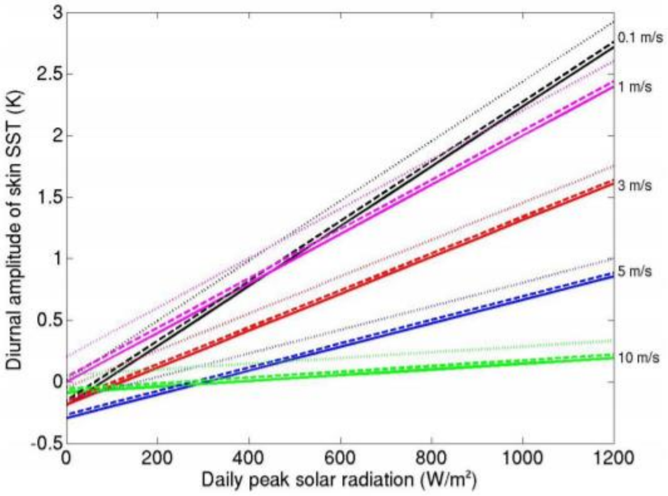

Figure 10.8 Diurnal warming as a function of peak radiation and wind speed

Size of daily diurnal warming as a function of wind speed and peak solar irradiation and precipitation Solid, broken and dotted lines represent precipitation rates of 0,1 and 5mm hr^{-1} respectively. The different colours correspond to different wind speed thresholds. (Kawai and Wada, 2007) reproduction of (Webster et al., 1996).

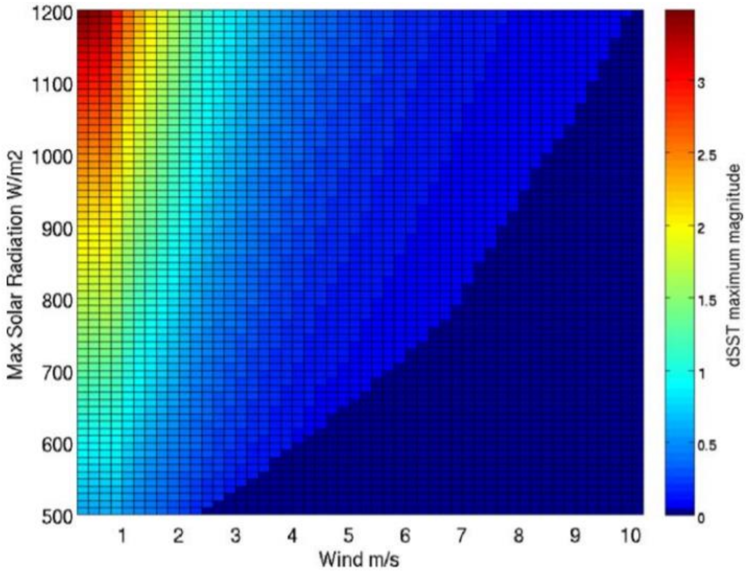

Figure 10.9 Peak solar radiation and wind speed control on diurnal warming
Sensitivity study of the amplitude of diurnal warming as a function of the maximum solar radiation and wind speed using the POSH model. Wind speed is held constant and peak solar radiation follows a bell shaped curve of solar radiation. SST is 20°C and air temperature 19°C (Weihs and Bourassa, 2014).

Shown as probability difference curves for a number of wind speeds <5ms^{-1} (Figure 10.10), it is evident that larger diurnal warm layers are much more likely at lower wind speeds and that for wind speeds between 4.5 and 5 ms^{-1} the diurnal warm layer is most likely to be 0.1-0.2°C.

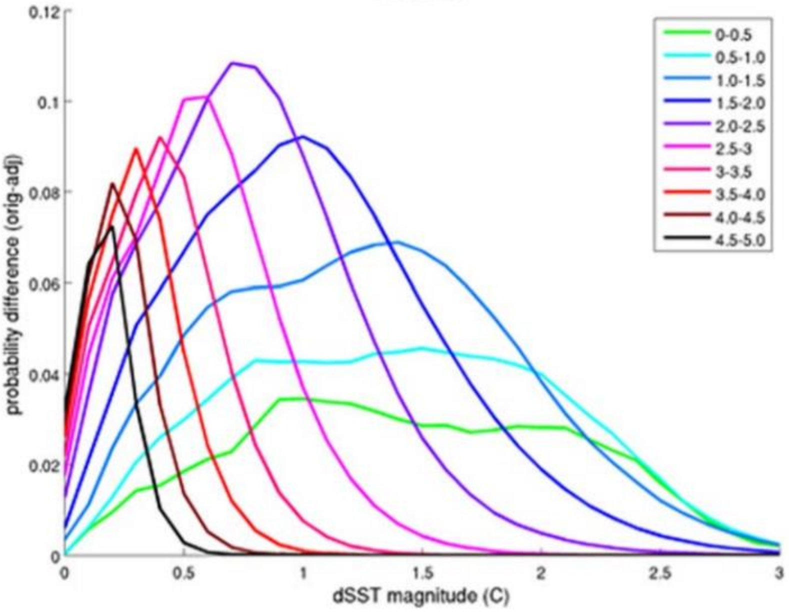

Figure 10.10 Probability difference for diurnal SST formation
Exceedance probabilities for the size of diurnal warming depending on the wind speed between 0 and 5 ms^{-1} (Weihs and Bourassa, 2014).

10.6 Climatological diurnal warming

Using numerical modelling it is possible to predict diurnal warming for a given wind speed and irradiance. For an informative view of whether 'on average' there are likely to be gradients at a given location, the average wind speed (Figure 10.6) and irradiances (Figure 10.4/Figure 10.5) could be used to infer the degree of warming (Figure 10.9). There is a big problem with doing this as it is not help to determine the occurrence of gradients nor the distribution of their magnitude. The occurrence and magnitude of diurnal warming in different parts of the ocean can be computed using the detailed wind speed and irradiance climatologies mentioned above (QuikScat and METEOSAT).

Diurnal warming was modelled globally (Weihs and Bourassa, 2014) for 5 years between 2000 and 2004 and split into six two month periods (Figure 10.11). The key feature of this is the large seasonal variability across the ocean. With the exception of May to August in the Northern hemisphere and November to February in the Southern hemisphere there is on average essentially no diurnal warming at all outside the tropics 30°S to 30°N.

In the Polar Shelf Seas and the Bering Sea there are no gradients at any time of the year, even during the hemispheric summers. Whilst the wind speeds are not particularly high around the Arctic or Antarctica the incoming irradiance is very low here and would only have a chance of forming when there was no wind. There are similarly limited gradients in both the Bering Sea and the Tasmanian Shelf but this is most likely due to high winds in both cases. An additional obstacle is that at these high latitudes the Ekman mixing makes the formation of diurnal warm layers more difficult (Soloviev and Lukas, 2006).

The Shelf region which has consistent yearlong warming of 0.15 – 0.2 °C and >0.25°C between May and June is the Sundra Shelf and the region around Malaysia. Tunisian-Libyan and Adriatic shelves in the Mediterranean have no diurnal warming between November and February but are between 0.2 and 0.3°C between May and August and 0.1°C for the rest of the year. Another shelf with near year round thermal stratification is the West Australian Shelf which is between 0.1 and 0.25°C except between May to June where there are no gradients. There is on average 0.1°C of diurnal warming for the entire year in the Caribbean Sea except for between November and February. All of these shelves are close to the tropics where the irradiance is higher and the mean wind speeds are lower.

In the mid latitude shelves there are diurnal warming events but these are predominantly in the hemispheric summer months with there being no gradients found for the remainder of the year. On the European Shelf there is on average 0.1°C of warming between May and August, on the Scotian Shelf the diurnal warming is on average 0.15°C again between May and August and on the East China Sea there is an average of 0.15°C of warming between March and August. The Southern hemisphere shelves, the Patagonian Shelf, the Gulf of Carpentaria and the Great Barrier Reef Shelf have an average of 0.1°C of diurnal warming between September and February and November to February in the case of the Patagonian Shelf.

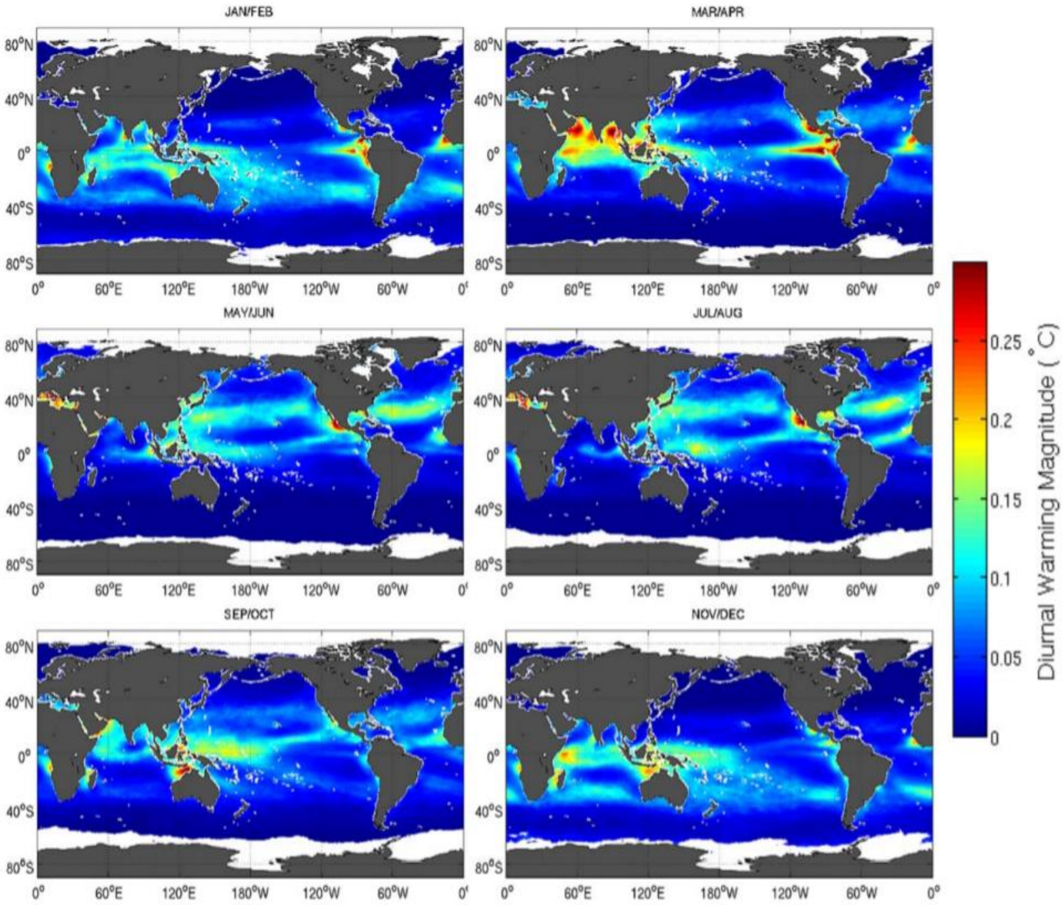

Figure 10.11 Modelled average diurnal warming

Global average ocean diurnal warming for 6 bimonthly periods computed between 2000 and 2004 (Weihs and Bourassa, 2014).

The degree of warming can also be determined by calculating the difference in the day and night sea surface temperatures recorded by satellites Figure 10.12. Day vs night , first shown by (Stuart-Menteth et al., 2003) and again by (Dong et al., 2006). Whilst the same latitudinal trends are present in both datasets the magnitude of the warming on the Sundra shelf is much higher in the satellite derived diurnal warming as is the diurnal warming predicted for the North Atlantic and North Pacific between June and August.

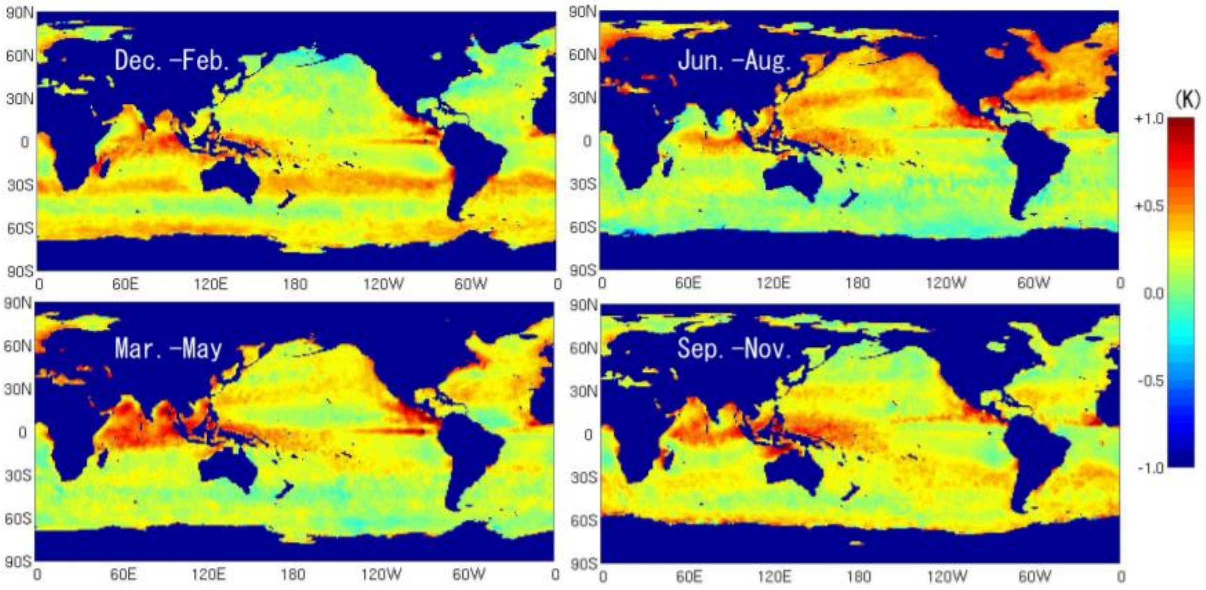

Figure 10.12 Satellite derived diurnal warming

Seasonal day(13:30 hrs) vs night (01:30hrs) seas surface temperature differences from AMSR-E for the period June 2002 to May 2006(Kawai and Wada, 2007).

The climatological occurrence of diurnal warming can be represented by the percentage of days when diurnal warming exceeds 0.1°C, this was done for the 20 year period between 1998 and 2008 (Figure 10.13). This analysis indicated that the occurrence of diurnal warming is largely dependent on the latitude. Diurnal warming of >0.1°C occurring on >70% of days between 20°S and 20°N, warming of >0.1°C occurring on 40-70% of days between 20°S and 40°S and 20°N and 40°N, above 40° the occurrence is <20% approaching 0% towards the two poles. The exceptions to this global trend will be caused primarily by regional wind and cloud dynamics. If the importance of the size of the gradients is ignored in the context of changes occurring in a confined layer, it is evident from this that there will be isolated warm layers throughout the tropics which will be effected by biology, the air sea flux and precipitation.

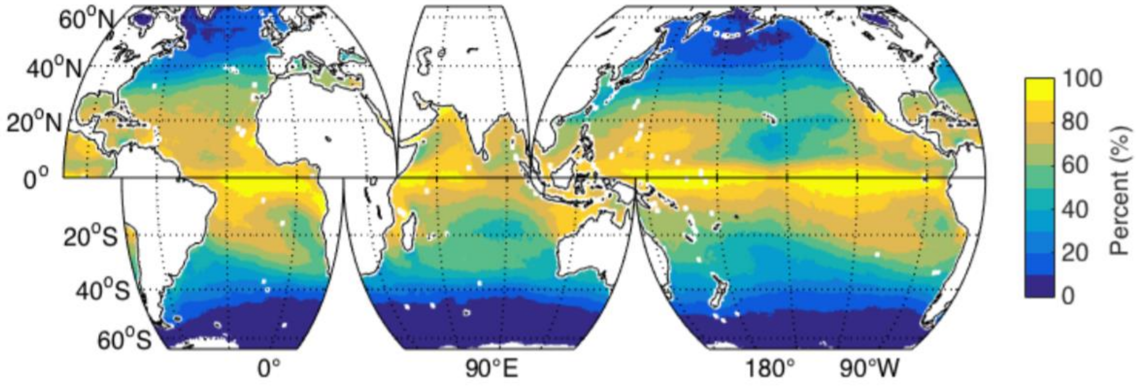

Figure 10.13 Global map of the percentage of days where diurnal warming exceeds 0.1°C

The percentage of days in a year where diurnal warming exceeds 0.1°C, using the Clayson diurnal warming parameterisation averaged over the period of 1998-2008

(Bogdanoff, 2017).

10.7 Shelf sea rainfall rate

The global daily mean rainfall rate is not uniform with many regions showing an order of magnitude difference in rainfall rate. The highest rainfall rates are found along the equator in the inter tropical convergence zone (ITCZ) due air rising and cooling as part of the Hadley cell. The easterly trade winds transport water to the East coast of subtropical landmasses before releasing it resulting in high rainfall on the East Coasts. The median rainfall rate across the midlatitudes is 2-3 mm d^{-1}. Low rainfall is found at both poles due to the low air temperature and the incapacity of cold air to transport significant amounts of water.

The low rainfall at both poles means precipitation is unlikely to drive near surface gradients in Arctic (Laplev Shelf, East Siberian Shelf and the Chukchi Shelf) or Antarctic (Weddell and Ross Seas) shelf regions. In the North Atlantic the rainfall on the European Shelf, Mediterranean Sea and the Caribbean Sea are close to the global average rainfall rate, whereas the Scotian Shelf is a region of high rainfall so is more likely to be effected by rainfall. A similar pattern is present in the North Pacific with average rainfall in the mid latitudes around the Bering Sea but much higher rainfall on the East China and Sundra Shelves. In the South Atlantic and South Pacific there is limited shelf, the main regions of shelf in the South Atlantic (Patagonian Shelf) and the South Pacific (Gulf of Carpentaria, the Great Barrier Reef Shelf and the Shelf Seas around Tasmania) have average rainfall. Whilst there is high rainfall > 6 mm d^{-1} over most of the Indian Ocean most of these regions are not covered by Shelf Seas for example the North West Australian Shelf, the Shelf around Malaysia that links to the Sundra Shelf is a region of high rainfall however.

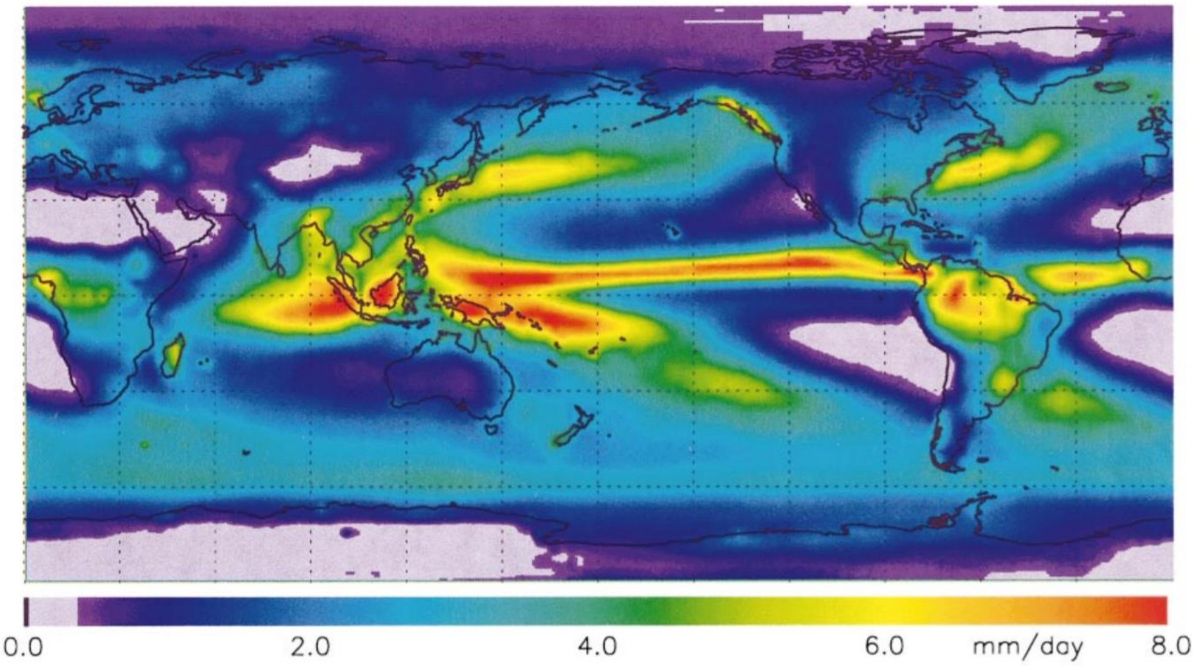

Figure 10.14 Global map of daily rainfall

Global map of annual mean daily rainfall in mm d^{-1} for the period between 1979 and 2001 from V2 of the global precipitation climatology project (GPCP) (Adler et al., 2003).

Total rainfall does not translate to occurrence of near surface gradients as the rainfall effect will depend on the frequency and intensity of rainfall events. The rainfall frequency is the number of days per year when it rains; this is given as a decimal fraction Figure 10.15. The rainfall frequency distribution is starkly different to the average daily rainfall rate. The main feature is that north of 30°N and south of 40°S (the mid latitudes), the rainfall frequency is above 0.1 and up to 0.3. The only other main region where the rainfall frequency exceeds 0.1 is over the inter tropical convergence zone in the Pacific Ocean. The rainfall rate over most of the tropics between 30°N and 40°S has very infrequent rainfall 0.0-0.1. What this indicates is that the annual rainfall in the mid latitudes can be thought of as being split over more rainfall events whereas the rainfall at the tropics occurs over fewer more intense events.

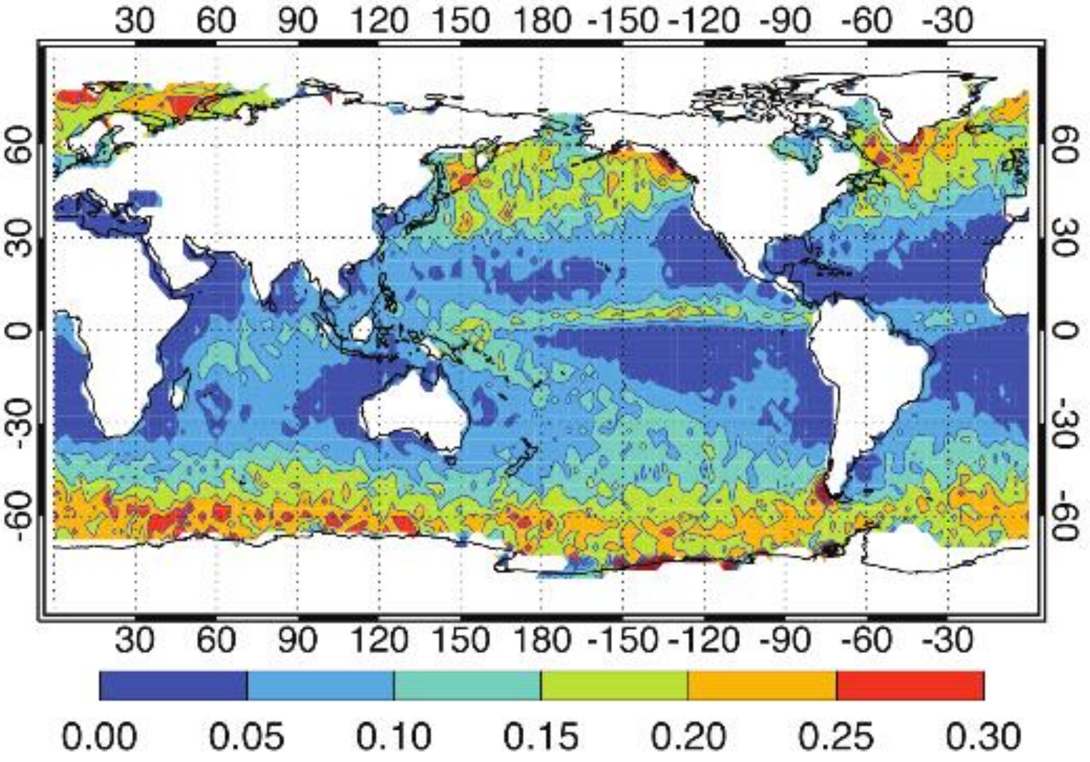

Figure 10.15 Global map of precipitation incidence

Precipitation incidence as a fractional percentage for the global oceans (Ellis et al., 2009).

The rainfall frequency does not indicate how the rainfall varies by season; this is shown by latitude for three month periods (Figure 10.16). Southern hemisphere rain generally does not vary significantly between months with the except of more rain in the summer and slightly less rain in the winter between 30°S and 50°S. In contrast to the Southern hemisphere the rainfall rate varies considerably more in the Northern hemisphere annually. Between 0°N and 20°N rainfall is substantially higher between June and November. Between 20°N and 50°N, there is more rain in the winter and less in the summer which is the opposite of the Southern hemisphere. North of 50°N the rainfall is higher in autumn.

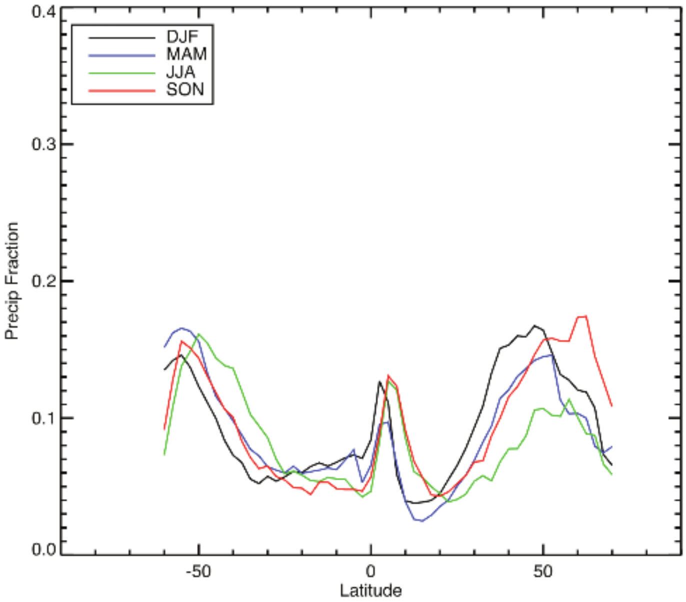

Figure 10.16 Global zonal mean seasonal cycle of precipitation
Zonal mean seasonal precipitation fraction (Ellis et al., 2009).

Overall what this means for each shelf is as follows, making a number of assumptions we can work out the rainfall intensity when it rains by multiplying the average annual daily rainfall by the average annual rainfall incidence. Moderate rainfall was previously stated as 10 mm hr^{-1} was shown to cause near surface gradients. It is necessary to make several assumptions here that are based on results from (Drushka et al., 2016), firstly, that rainfall rates >2mm hr^{-1} always results in stratification in the top meter or deeper, secondly that rainfall rates of 10-20 mm hr^{-1} and greater result in stratification that persists for ~2 hours at wind speeds as high as 10 ms^{-1} but in the region of 3-5 and potentially up to 8 hours at wind speeds below $6ms^{-1}$ which would be a long enough time frame for the rainfall to be impactful on the flux.

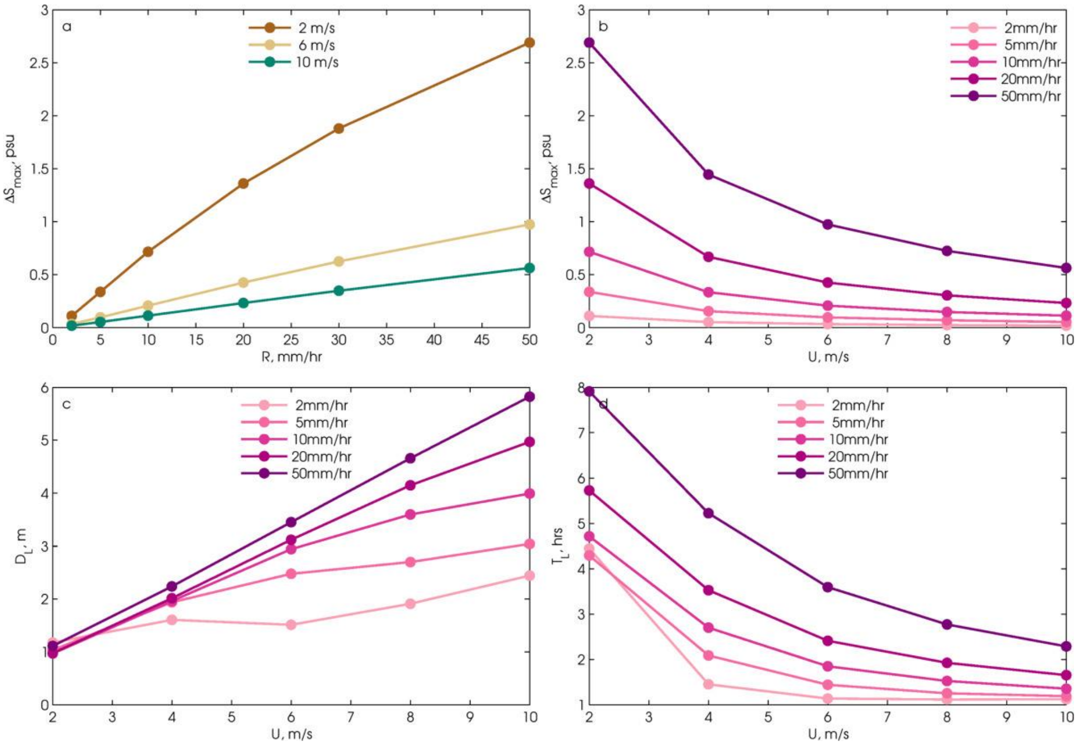

Figure 10.17 Figure legend

GOTM experiments of varying wind speed and precipitation rates, (a) peak ΔS for different wind speeds (b) peak ΔS for different rainfall rates , (c) fresh lens thickness in meters for different rainfall rates and (d)lifetime of fresh lens at different rainfall rates (Drushka et al., 2016).

On the East China Sea and the Sundra shelf around Malaysia there is very high rainfall on 5-10% of days meaning that there is intense rainfall on these days likely to cause stratification but not most of the time, likely during the monsoon season. By taking daily averages of 4-6 and 6-8 mm d^{-1} and assuming a 10% rainfall incidence rate equates to 40-60 mm d^{-1} 60-80 mm d^{-1} rainfall rates on days when it does rain. Assuming that this rain all falls over a 1-3 hour time frame, this is likely to have a large impact on the flux at this time.

On the Scotian, Bering and European Shelves there is high 6-7 mm d^{-1} and moderate rainfalls 3 and 2-3 mm d^{-1} respectively, all in the mid latitudes have moderate incidence of 10-20% meaning it rains frequently and the rainfall rate is fairly consistent except in summer. On these shelves it would be expected that the average rainfall on a day when it rains would be 1/0.15 *2-3 mm d^{-1} and 1/0.15 *6-7 mm d^{-1} equal to 13.3-20 mm d^{-1} and 40 -46.6 mm d^{-1}, these rates would be more than sufficient to drive near surface gradients. Relevant to the European and Bering shelves is whether the rain all falls within a several hour period or if it is spread out over the course of a day it is unlikely to persist and will not have a large impact based on the results of (Drushka et al., 2016).

On the West coast of Australia, the Tasmanian shelf, the reef shelf, the Gulf of Carpentaria shelf, Patagonian Shelf and the Caribbean Sea there is a moderate rainfall rate of 1.5-3 mm d^{-1} and low incidence <5% meaning that this rain occurs over only a few days, at 5% this is equivalent to 30-60 mm d^{-1} on the days it actually rains, however if the incidence was as low as 2% this would be 75-150 mm d^{-1} again this would be more than enough to drive near surface gradients. Low rainfall is also seen across the Mediterranean on the Tunisian and Adriatic shelves with low rainfall but low incidence, this would similarly drive near surface gradients but as this is a mid-latitude location the rain most likely falls during storms when there also tends to be higher wind speeds which would quickly destroy stratification.

Over both poles there is low precipitation <1mm d^{-1} but high rates of incidence 15-20% suggesting it rains often but the rain events are low intensity, these low intensity events are unlikely to have a significant impact on driving stratification and gradients here.

The dilution effect on DIC and salinity are both functions of the rainfall intensity. The rain also introduces turbulence and sensible heat. Both of these have an impact on the formation of near surface gradients. The sensible heat flux due to precipitation was shown to have a negligible effect over the tropical ocean (Gosnell et al., 1995) but this does not necessarily mean this is the case elsewhere, where the atmospheric and ocean temperatures are much larger. The sensible heat flux associated with precipitation is included implicitly in the POSH model simulations of (Weihs and Bourassa, 2014) which are shown above.

10.8 Sea ice melt rate

A number of studies have shown that sea ice melt can have an effect on the underlying salinity, temperature and CO_2 (Fransson et al., 2017, Lovely et al., 2015). A recent study by Miller et al. (2018) suggests large differences (-180 to 160 µatm) in CO_2 measured at different depths in the Arctic. Sea ice melting could result in the formation of near surface gradients on the shelf seas of the Arctic and Antarctica.

To make a quick comparison between the freshwater input from sea ice melt and rainfall, a simple approximation will be made about summer melt rates. The thermal expansion of water is only 9% so is ignored. Sea ice thickness is typically ~1.5m with the largest melting (~40%) occurring in July (Steele et al., 2010). Melting is known to be nonlinear due to the positive feedback of melt ponds but for simplification it is assume that this July melt of 600mm is spread evenly over the 30 days in July, this is equivalent to 20 mm d^{-1}. As around 2/3 of the sea ice melting is forced by interactions with the ocean it will be assumed that the melting is evenly distributed evenly over a 24 hour period meaning that the freshwater input is equivalent to <1mm hr^{-1}. This is unlikely to have a large effect on the stratification unless the influence of the sea ice suppresses wind driven turbulence allowing the fresh water pool to persist. Modelling whether a fresh layer would persist beneath sea ice would require complex modelling which is beyond the scope of this work to explore. There is evidence of salinity induced gradients in the top 0.5m below sea ice in a number of sea ice studies (Else et al., 2015) so there is precedence for assuming sea ice induced stratification.

10.9 Shelf sea atmosphere ocean ΔpCO_2

The concentration gradient ΔpCO_2 is another metric that must be considered in calculating gradients as it has a critical impact on the air-sea flux into near surface layers which from the box modelling was shown to be the most likely driver of gradients. The difference between the partial pressure of the atmosphere and ocean is wildly variable depending on location (Figure 10.18).

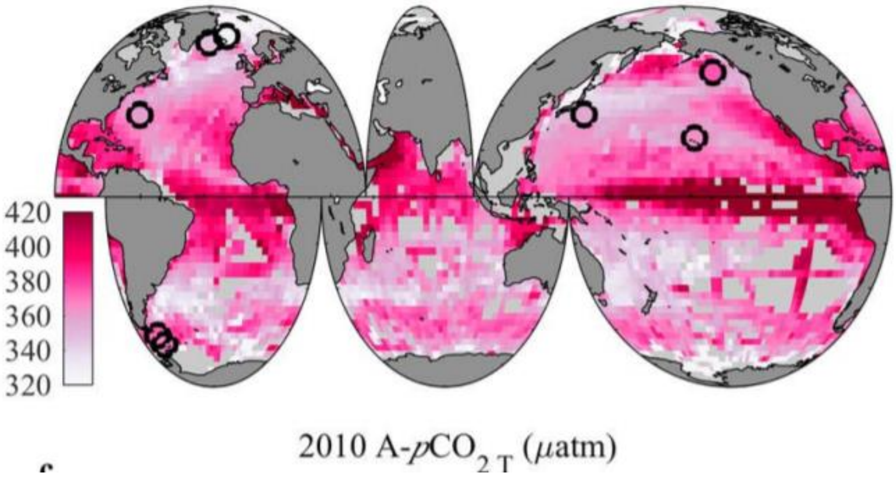

Figure 10.18 Global annual average ΔpCO_2 (seawater – air) climatology
The global average seawater CO_2 partial pressure normalised to 2010, data from SOCATv4 CO_2 partial pressures(Fassbender et al., 2018).

The average partial pressure difference doesn't account for the large inter-seasonal changes that occur in the oceanic partial pressure of CO_2. The maximum partial pressure differences in the monthly climatology reveal the regions that undergo the most seasonal change (Figure 10.19). The general pattern over the open ocean is that there are smaller amplitude changes (<20) whereas near the coasts there is considerably more variability (>20). Regions where there seems to be particularly strong changes are the Ross Sea (80 to 195), Scotian Shelf (80 to 140), Bering Sea (80 to 195), East China Sea (80 to 140), Patagonian Shelf (60-80), and European shelf (60). There is comparatively less variability on the more tropical Shelves, the Caribbean Sea (40), Sundra Shelf (<20), the Gulf of Carpentaria (40), the Great Barrier Reef Shelf (40), Tasmanian Shelf (40) and the Weddell Sea (<20).

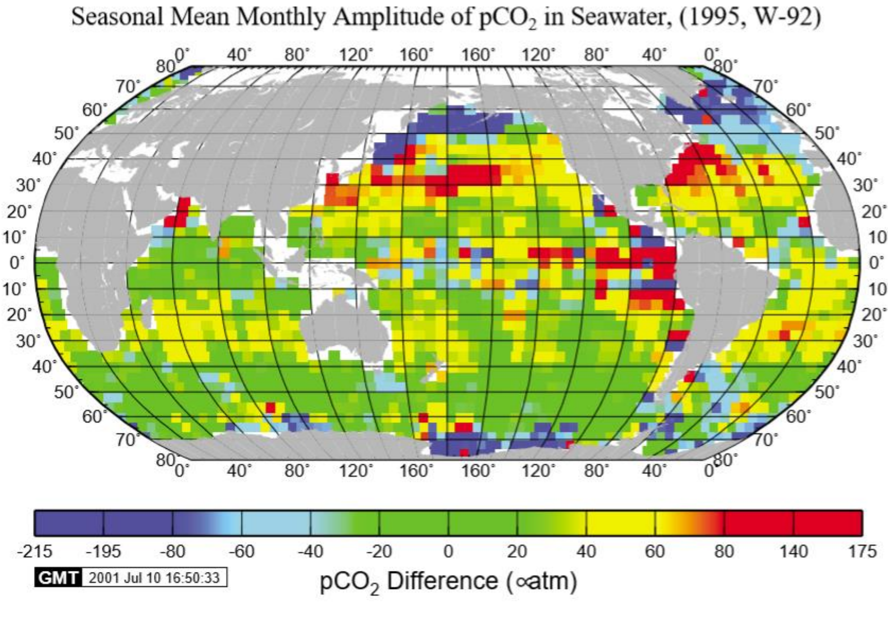

Figure 10.19 Peak differences in seasonal amplitude
Maximum partial pressure differences in the monthly sweater pCO_2 climatology

(Takahashi et al., 2002). Positive values are when maximum values occur in warm seasons whereas negative values occur when maximum values are found in cold seasons.

The monthly oceanic pCO_2 climatology (Takahashi et al., 2009) is presented in (Figure 10.20). As might be expected many of the features identified in the peak differences in the seasonal amplitude are also apparent in the monthly climatology.

The majority of the shelves show a seasonally cycle where the drawdown is timed with the spring/ summer of the hemisphere each shelf is in. The Weddell and Ross seas both show a similar trend with large positive values in July to December (25 to 90) and negative (-60) to slightly positive (15) values between January and June. The Scotian and East China Seas are two of the most seasonal shelves with negative values down to -90 up to positive values of 30 to 45, in both cases lowest values are seen in April to June and positive values in the latter half of the year July to December. The European shelf is slightly undersaturated the majority of the year -60 to 0 with the period encompassing the spring bloom heavily undersaturated at -105. The change in CO_2 is sharp on the Patagonia Shelf with values of 0 to 45 in October to December rapidly changing to -60 to 0 during January to March, in the Southern hemisphere winter the Patagonian Shelf is near equilibrium. In great contrast to the maximum peak figure, the monthly climatology indicates more variability in the Caribbean Sea with regions dropping to -60 between January and March in some regions and reaching 45 in the summer between July and September. The west coast Australian shelf is near equilibrium between January and June but diverges to -45 between July and September and slowly reaching equilibrium through to December. The Great Barrier Reef shelf, the Tasmanian Shelf and the Gulf of Carpentaria all show seasonality, more positive values are seen in the Gulf of Carpentaria and the great barrier reef shelf in January to March and more negative between July and September whereas on the Tasmanian shelf the largest negative values are seen between January and March and equilibrium is observed between July and September.

The Laptev Shelf and the Sundra Shelf show the least variation which was the same as above, in both cases there was only a single 3 month period that diverged from the yearly average, JFM on the Sundra shelf and AMJ on the Laptev shelf. The Chukchi Sea shows small variation at the extreme of under saturation with values found between -75 and -120. Close to the Chukchi Sea, the Bering Sea has some variability but remains roughly in the range of -90 to 0 throughout the year. The East Siberian Shelf similarly shows little seasonality with values between -45 and -15 the majority of the year with slightly less negative (-30) and some values close to 0 between July and September.

Overall the general conclusion from observing these maps is that the global shelf seas are not in equilibrium and there are large and temporally varying ΔpCO_2 present year round. The simple explanation for the changing seasonal ΔpCO_2 is the changing primary production rate (section 10.10). The fact that there are large ΔpCO_2 in almost all shelf seas means that under stratifying conditions

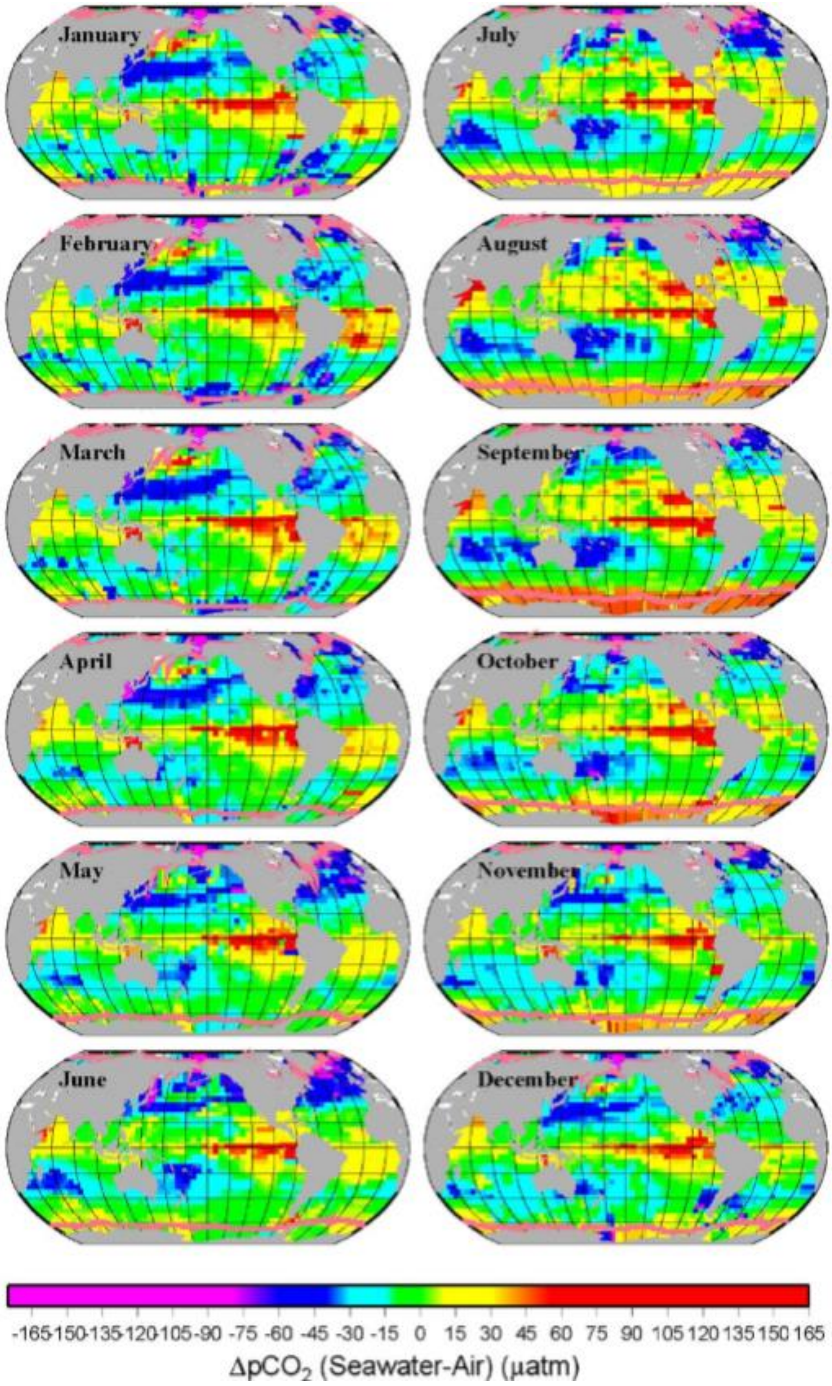

Figure 10.20 Global ΔpCO_2 (seawater – air) monthly climatology
Global ΔpCO2 (seawater – air) monthly LDEO climatology standardised to the reference year 2000 (Takahashi et al., 2009).

10.10 Shelf sea productivity rate

The seasonal drawdown of CO_2 by biology (Figure 10.21) strongly mirrors the pattern for peak differences in pCO_2 seasonality (Figure 10.19). However these changes are not purely biological and it is important to look at other production rate indicators. For several decades ocean primary production has been inferred from satellites using chlorophyll-fluorescence as a proxy indicator. Satellite retrievals observe chlorophyll in the top few meters of the ocean which is the chlorophyll and thus productivity rate relevant to the formation of near surface gradients. It should be noted however that chlorophyll whilst a good proxy is not a direct measurement of primary production.

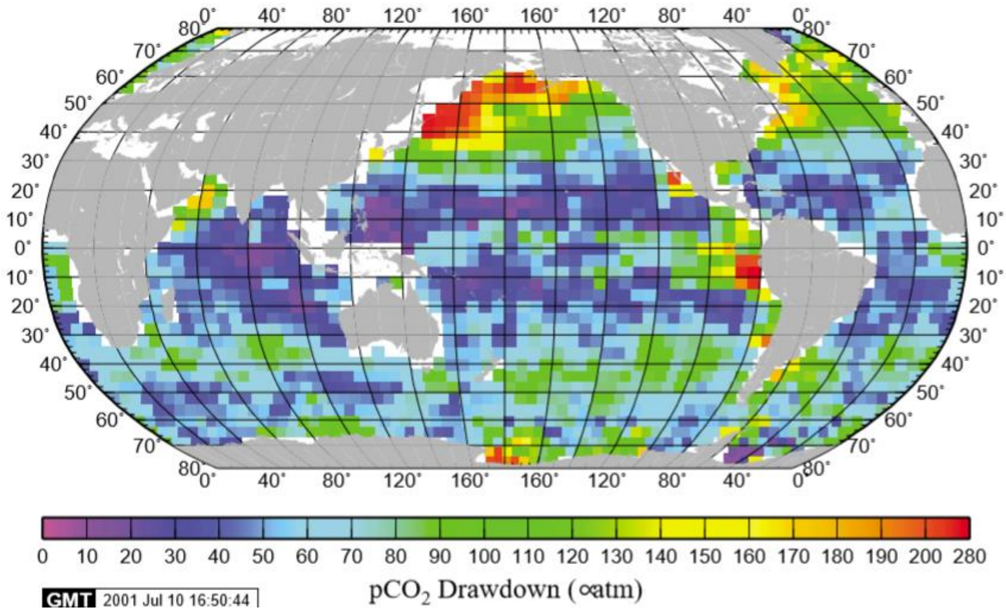

Figure 10.21 Biological drawdown of CO_2
Biological drawdown of CO_2 represented as the seasonal amplitude in pCO_2 after accounting for temperature variations (Takahashi et al., 2002).

Average daily production rates are inferred globally using satellite retrieved global chlorophyll concentrations (Figure 10.22). There is well over an order of magnitude difference between the highly productive and unproductive regions. The least productive regions are the nutrient depleted oligotrophic gyres and the most productive regions are the shelf seas and the equatorial and coastal upwelling regions (Behrenfeld et al., 2006). A common misconception is that shelf seas bound all major land masses; this is not the case (Figure 10.1). For this reason it is important to identify the many highly productive regions near the coast which aren’t Shelf Sea, these include the West Coast of North and South America, the West Coast of Africa, the Western and Northern regions of the Indian Ocean and the region around New Zealand.

Whilst production is much higher in the shelf seas there are still large variations between them, this paragraph will breakdown the average productivity rate across the main shelf regions of the ocean. In the North Atlantic both the Scotian and European Shelves are highly productive (750-1000 mg C m^{-2} d^{-1}) whereas the Caribbean, Adriatic and Tunisian Shelves are about half as productive (400 mg C m^{-2} d^{-1}). In the South Atlantic the entire Patagonian shelf is extremely productive (1000 mg C m^{-2} d^{-1}). In the North Pacific the East China Sea is highly productive (1000 mg C m^{-2} d^{-1}) whereas the Bering Sea has variable production rates (400-1000 mg C m^{-2} d^{-1}) depending on the location. The Sundra shelf has comparatively low production rates (250-350 mg C m^{-2} d^{-1}). The Tasmanian Shelf has high production rates (750-1000 mg C m^{-2} d^{-1}) and the Barrier Reef Shelf and Gulf of Carpentaria have slightly lower production rates (600 mg C m^{-2} d^{-1}). A large portion of the Polar Shelves are covered in sea ice for around half the year, regions that are partially ice free such as the Laptev Shelf have high production rates (750-1000 mg C m^{-2} d^{-1}).

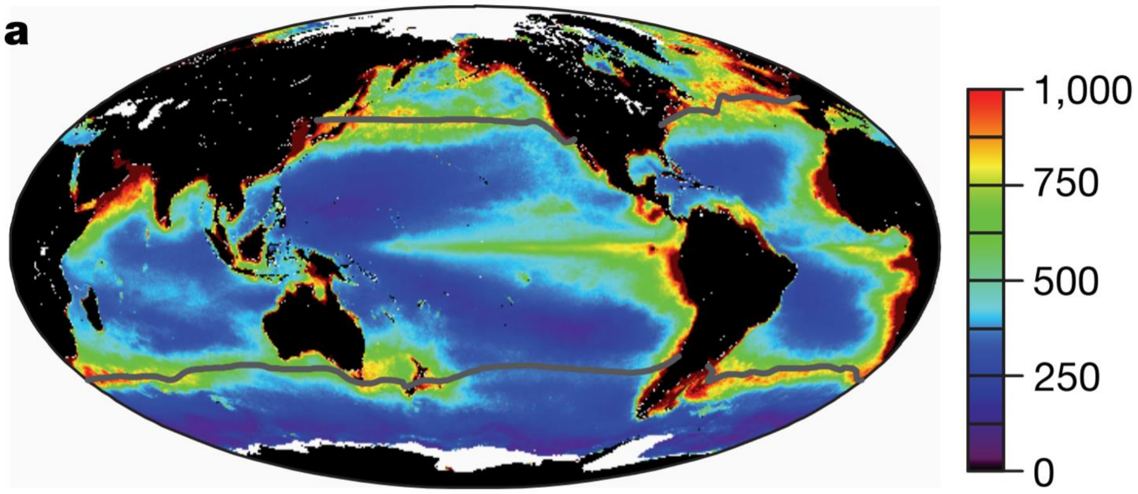

Figure 10.22 Satellite derived global annual column NPP inferred from surface chlorophyll concentrations
Column NPP in the Euphotic zone (mg C m^{-2} d^{-1}) (Behrenfeld et al., 2006).

Primary production in shelf seas is extremely seasonal, this is demonstrated by the production rate split into seasonal 3 month periods (Figure 10.23). The main trend is that there is greater production in the northern hemisphere and austral summer than the northern hemisphere winter and austral winter respectively. It should be noted that the annual average values from (Behrenfeld et al., 2006) and the seasonal values from (Antoine et al., 1996) do disagree slightly, this is likely due to differences in the ocean colour algorithms, the averaging periods for the data and the resolution of the different satellites used. Notable differences between both outputs is that the European and Patagonian shelves are have much greater production rates in (Behrenfeld et al., 2006).

There is extreme seasonality in lots of locations; the most obvious region for this is across the European shelf, here the production rate is 100-200 mg C m^{-2} d^{-1} from October to March but increases rapidly in spring and summer to 550-800 mg C m^{-2} d^{-1}, this a 4-5 fold increase in production. The Scotian Sea whilst having higher production in autumn and winter 300-400 mg C m^{-2} d^{-1} from October to March still has twice the production rate between April and September. The Sundra shelf also shows considerable seasonal variability in production with a minimum between April and June 200-350 mg C m^{-2} d^{-1}a peak between October and December 300-1000 mg C m^{-2} d^{-}1 and slightly lower peak values in the intermediary months 300-850 mg C m^{-2} d^{-1}.

There are irregular seasonal patterns in production in the Shelf regions of Australia, in the Gulf of Carpentaria production rates peak between April and June with the lowest between October and December whereas on the barrier reef shelf production is low between January and June and greater between July and September and slightly greater between October and December, the third Australian shelf has the pattern that might be expected with much greater production rates between October and March 300-450mg C m^{-2} d^{-1} than April to September 100-300 mg C m^{-2} d^{-1}.

The production rate on the Patagonian shelf also shows seasonality with the maximum and minimum rates much higher between October and March 300-1000 mg C m^{-2} d^{-1} than April to September 100-800 mg C m^{-2} d^{-1}. There is a slight enhancement in production in the East China Sea 350-1000 mg C m^{-2} d^{-1} between April and September and slightly lower (350-800 mg C m^{-2} d^{-1}) for the remainder of the year. The production rates in the Caribbean Sea are wide ranging year round 350-1000 mg C m^{-2} d^{-1} but it is only between April and June where the maximum rate extends to 2000 mg C m^{-2} d^{-1}.

The Western Australian shelf is the shelf region and the Tunisian and Adriatic shelves in the Mediterranean have the least seasonality. The Arctic and Southern Ocean production rates are very low in 50 mg C m^{-2} d^{-1} in each hemispheres winter and whilst comparatively higher in each respective summer 200-300 mg C m^{-2} d^{-1}, these production rates remain low. As satellites can't penetrate ice to retrieve chlorophyll estimates, it is difficult to determine seasonality at either pole so this poorly validated. The production rates in the Bering Sea mirror the trend seen on the polar shelf seas with high production in the summer but overall low production.

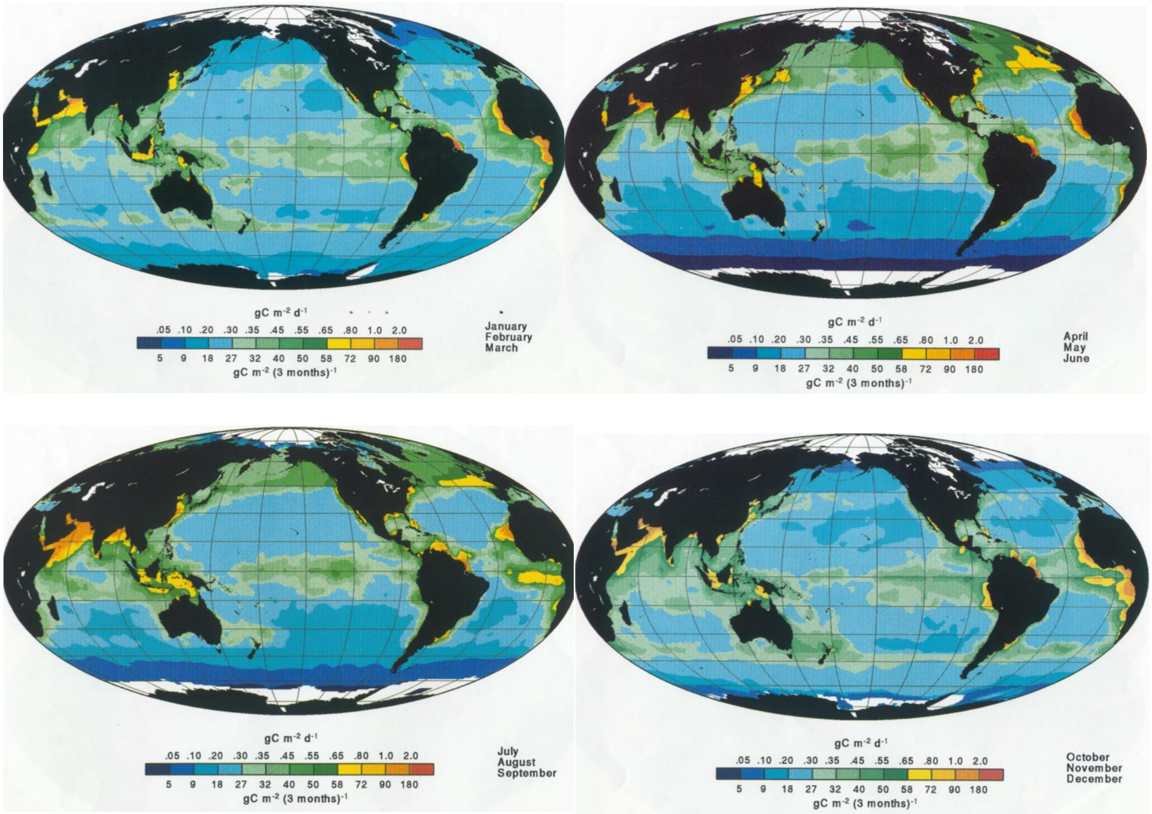

Figure 10.23 Satellite derived global seasonal column NPP inferred from surface chlorophyll concentrations

Seasonal patterns of satellite derived primary production globally (mg C m^{-2} d^{-1}) (Antoine et al., 1996).

Table 6 Summary of near surface gradients indicator variables in different shelf seas

Name of Shelf Region	Surface Area (km^2)(Harris et al., 2014)	Main shelf seas/regions	Average Wind Speed (ms^{-1}) (Monahan, 2006)	Average size of warm layers (Weihs and Bourassa, 2014)	Formation of diurnal warm layers (% DOY) (Bogdanoff, 2017)	ΔpCO_2 (Seawater – Atmosphere) (Takahashi et al., 2009)	Primary production rate (mg C m^{-2} d^{-1})(Antoine et al., 1996)	Precipitation rate mm d^{-1}(Adler et al., 2003)	Precipitation incidence (Ellis et al., 2009)
Arctic Ocean	6,727,440	Laptev Shelf	6?	0	<10	JFM 0, AMJ -30 to -15, JAS 0, OND 0	JFM 50-200, AMJ 200-450, JAS 50-350, OND NAN	<1	0.15-0.2
		East Siberian Shelf	6?	0	<10	JFM– -45 to -15, AMJ -30 to -15, JAS -30 to 0, OND -45 to -15	JFM- NAN, AMJ NAN, JAS 100-300, OND NAN	<1	-
		Chukchi Shelf	6?	0	<10	JFM ~ -120, AMJ ~ -120, JAS -105 to -75, OND -105 to -75	JFM NAN, AMJ NAN, JAS 50-300, OND NAN	<1	0.10-0.15
Indian	4,047,5	continental shelf	5±3	0.1	80-90	JFM 0 to 15,	300	2-3	0-0.05

Ocean	70	off the West coast of Australia		degrees all seasons except May to June		AMJ 0, JAS -45 to 0, OND -30 to 0			
		Shelf region Malaysia	6±2	Present year round 0.15 to 0.2 highest March to April >0.25	70-80	JFM 0 to 15, AMJ 0 to 15, JAS 0, OND 0	JFM 300-400, AMJ 300-450, JAS 550-800, OND 550-800	6-8	0-0.1
Mediterranean and Black Sea	709,990	Tunisian-Libya continental shelf	7±3	Nothing Nov to Feb, 0.2 to 0.3 May to Aug and 0.1 rest year	60-70	JFM NAN, AMJ NAN, JAS NAN, OND NAN	350	<1	0-0.05
		Adriatic Sea	5±3	Nothing Nov to Feb, 0.2 to 0.3 May to	60-70	JFM NAN, AMJ NAN, JAS NAN, OND NAN	350	<1	0-0.05

				Aug and 0.1 rest year					
North Atlantic Ocean	7,313,790	European shelf	8±4	0.1 May to Aug	10-20	JFM -60 to 0, AMJ -105 to -15, JAS -60 to 0, OND -60 to 15	JFM 100-200, AMJ 550-800, JAS 550-800, OND 100-200	2-3	0.1-0.2
		Caribbean Sea	6±3	Nothing Nov to Feb, 0.1 rest of the time	60-80	JFM -60 to -30, AMJ -30 to 30, JAS 15 to 45, OND -30 to 30	JFM 350-800, AMJ 350-2000, JAS 350-1000, OND 350-1000	2-3	0-0.05
		Scotian Shelf	9±4	May to Aug only 0.15	30-40	JFM -45 to 0, AMJ -60 to -90, JAS -30 to 45, OND -45 to 0	JFM 300-400, AMJ 550-800, JAS 550-800, OND 300-350	6-7	0.1-0.2
North Pacific Ocean	6,144,810	East China Shelf	7±4	Mar to Aug 0.15 nothing rest year	40-70	JFM -75 to -60, AMJ -90 to -15, JAS -30 to +30,	JFM- 350-800, AMJ 350-1000, JAS 350-1000, OND 350-800	4-6	0.05-0.1

						OND -45 to 30			
		Sundra Shelf	6±2	Present year round 0.15 to 0.2 highest Mar to Apr >0.25	70-100	JFM -15 to 30, AMJ 0 to 15, JAS 0 to 15, OND 0 to 15	JFM- 300-850, AMJ 200-350, JAS 350-800, OND 300-1000	6-8	0.05-0.1
		Bering Sea	10±5	0	<20	JFM - 90 to 0, AMJ -90 to -15, JAS -90 to -15, OND -90 to -15	JFM- 200-300, AMJ 300-350, JAS 300-350, OND 50-100	3	0.1-0.15
South Atlantic Ocean	2,036,140	Patagonian Shelf	7±4	Nov to Feb 0.1, nothing rest time	40-60	JFM -60 to 0, AMJ – 0, JAS 0, OND 0 to +45	JFM 300-1000, AMJ 100-650, JAS 100-800, OND 350-1000	2	0.05
South Pacific Ocean	2,547,450	Gulf of Carpentaria	4±3	Dec to May 0.1 , 0.5 Jan to Mar	80-90	JFM 45 to 90, AMJ -15 to 90, JAS -30 to 45, OND 0 to 45	JFM 450-550, AMJ 650-800, JAS 450-550, OND	3	0-0.05

							350-450		
		the Great Barrier Reef Shelf	7±3	Dec May 0.1 , 0.5 Jan to Mar	40-70	JFM 0 to 15, AMJ -30 to 0, JAS -60 to -30, OND -30 to -15	JFM 200-350, AMJ 200-300, JAS 450-550, OND 350-450	2	0-0.05
		Shelf Seas around Tasmania	8±5	0	30	JFM -60 to -15, AMJ -30 to -15, JAS 0, OND -30 to 0	JFM 300-450, AMJ 100-300, JAS 100-300, OND 300-450	1.5	0-0.05
Antarctica	2,715,360	Weddell Sea	6?	0	<10	JFM -45 to 0, AMJ – 0 to +15, JAS 25 to 60, OND 0 to 60	JFM 200-300, AMJ NAN, JAS NAN, OND 50-100	<1	0.15-0.2
		Ross Sea	6?	0	<10	JFM -60 to 0, AMJ -30 to 30, JAS- 30 to 90, OND- 30 to 90	JFM 200-300, AMJ NAN, JAS NAN, OND 50-100	<1	0.15-0.2

10.11 Synthesising disparate data – a theoretical approach

Near surface stratification is the process by which a distinct near surface layer may form. A near surface gradient is usually referred to as forming from a diurnal warm layer but a near surface gradient may form due to changes in salinity due to rain or ice melt. In both cases physics constrains the formation of diurnal surface layers. Global rainfall rates, wind speed and irradiances have been collected above to identify their impact on the formation of near surface gradients. A key observation by (Soloviev and Lukas, 2006) for the purpose of this analysis is that entrainment in a diurnal warm layer is minimal, this is important as it means that regardless of the degree of stratification the near surface layer is for all intents and purposes isolated from the water below.

The variables which were shown via box modelling to be capable of changing the amount of CO_2 in a near surface layer, precipitation, biological production and the air sea flux (a function of the wind speed and ΔCO_2) are also collected.

Following this reasoning, shelf seas where there is no near surface stratification can be ignored as there will be no near surface layers. The shelf seas where there should be near surface layers may not necessarily have a large impact on the air sea flux of CO_2 as this depends on the role of precipitation, biological production and the air sea exchange in each shelf sea.

10.12 Shelf by shelf analysis

10.12.1 European Shelf

Low mid latitude irradiances and high wind speeds across the European Shelf are seen throughout most of the year preventing stratification. When the wind speed decreases and irradiance increases between May and August, thermal gradients with an average size of 0.1°C are typically seen. Gradients are on average observable on 10-20% of days of the year. The high biological productivity between March and September could cause biologically induced gradients. There is a very large (>100ppm) ΔpCO_2 so a flux into a surface layer from the atmosphere will change increase the surface CO_2 and reduce the flux in the course of several hours it won't greatly affect the magnitude of fluxes. It rains frequently (every 5-10 days) on the European shelf, when it does rain on these days the average rainfall amount is 10mm a day, depending on the timeframe over which this rain falls e.g. 1-2 hours it could be impactful on the flux but not if the rainfall is spread equally across a 24 hour period.

10.12.2 Scotian Shelf

Despite very high wind speeds (9±4 ms^{-1}) on the Scotian Shelf there are thermal gradients of on average 0.15°C on 30-40% of days of year predominantly between May and August. High productivity between March and September coincides with the thermal stratification and has the potential to drive biologically induced CO_2 gradients in these thermal layers. The rainfall here is exceptionally high, 6-7mmd^{-1} on average with rainfall occurring on 10-20% of days of the year. From these numbers it can be inferred that on days it rains the daily rainfall amount would be 30 to 70 mm which is impactful whether occurring in short rainfall events of if the rainfall is spread across the whole day. There is a large (>60ppm) ΔpCO_2 so a flux into a surface layer from the atmosphere whilst reducing the flux won't greatly affect the magnitude of fluxes.

10.12.3 Polar Shelf Seas

The Arctic (Laptev Shelf, East Siberian Shelf and Chukchi Shelf) Antarctic shelves (Weddell Sea and Ross Seas) and Bering Sea will be grouped together as they have similar conditions. The solar irradiance is too low in these regions for thermal stratification in the water column even under very low wind conditions. The formation of gradients is very unlikely in an exceptionally windy region like the Bering Sea 10±5 ms^{-1}. As mentioned above, salinity induced stratification from sea ice melt will create near surface stratified layers due to the inhibition of wind induced turbulence. This period of sea ice melt lasts for 90 days so will only have an impact for around ¼ of the year and not the rest of the time during ice free and ice covered conditions. The production data for the Laptev shelf indicate that during this period of melting are some of the highest biological production rates in these seas which would could lead to different CO_2 concentrations in these layers, the persistence of the fresh lens during the entire period of melting may promote different phytoplankton communities in this layer which could have different production rates. There is reduced air sea gas exchange due to the ice so whilst there may be a near surface gradient with different CO_2 below it may not actually exchange with the atmosphere. The flux through sea ice is not fully understood but for the flux that does occur is not extreme as the ΔCO_2 is not extremely large in these seas no more than 30μatm. As the saline layer is thin it is possible that through exchange with the atmosphere it could quickly become close to equilibrium with the atmosphere and limit further gas exchange, the rate of exchange would then be constrained by the mixing of high CO_2 waters out of the fresh lens into the waters below. As the Polar shelf seas particularly the Arctic are very large areas, this has the potential to be impactful on the air sea gas exchange.

10.12.4 Caribbean Sea

In the Caribbean Sea the irradiance is high and the wind speed is low year round, this results in average stratification of 0.1°C on between 60-80% of days of the year, stratification is only really absent between November and February. The ΔpCO_2 goes from negative to positive through the year, when undersaturated there would be positive gradients and the flux into the surface ocean layer will be reduced whereas when oversaturated the gradient would be negative and the flux leaving the ocean would be reduced. As the Caribbean is undersaturated for more of the year than oversaturated the net effect on the flux would be to reduce the net annual flux into the ocean. As the ΔpCO_2 is not close to equilibrium throughout most of the flux would be reduced slightly but this would not be likely to have a large effect on the magnitude of the flux. The productivity in the Caribbean Sea isn't very seasonal but does show large variations over short geographic distances, in certain areas the 2000 mg C m^{-2} d^{-1} production rates would likely be the largest process changing CO_2 in a diurnal warm layer. Rainfall is low and infrequent here and not likely to be impactful on the formation of gradients or the flux.

10.12.5 Tunisian-Libya continental shelf and Adriatic Sea

Low wind speeds in the Adriatic and moderate wind speeds across the Tunisian-Libya continental shelf and high irradiances across both lead to significant thermal stratification. Stratification is present on 60–70% of days of the year, between May and August stratification is on average 0.2–0.3°C and 0.1° the rest of the year besides November to February. There is very little variability in seasonal production with limited production in the Mediterranean shelf seas. Rainfall is low and infrequent here and not likely to be impactful on the formation of gradients or the flux.

10.12.6 Continental shelf off the West coast of Australia

There are low wind speeds and moderate irradiances over the continental shelf off the West coast of Australia for almost the entirety of the year. The low wind speed and moderate irradiance drive moderate 0.1°C gradients throughout most of the year 80–90%, the period when there are no gradients occurs between austral winter May to June. The period when there are no warm layers is the period when the ocean and atmosphere are close to equilibrium. Warm layers exist when the ocean is slightly and quite oversaturated between January and March and July and September but also when it is undersaturated between October and December. As the shelf is oversaturated for longer and taking into account the magnitude of the ΔpCO_2 seasonal differences it is likely that the diurnal warm layers reduce the flux to the atmosphere here. Biological production is low as are rainfall rate and incidence so they are unlikely to have a large effect on CO_2 based on previous calculations.

10.12.7 East China Shelf

Despite the high wind speeds there is still diurnal warming on the East China Shelf 40-70% of the time depending on the location. The diurnal warming is around 0.15°C between March and August and absent the rest of the year. There is huge seasonal and spatial variability in the East China shelf, it is slightly over and under saturated between July and September and general very undersaturated for the remainder of the year. This would drive positive gradients towards the surface via the atmosphere to ocean flux and due to the magnitude of the ΔpCO_2 would reduce uptake by the ocean. High year round production has the potential to drive NPP produced gradients at almost any time of the year. Reasonably high rainfall 4–6 mm d^{-1} with a low occurrence of 5–10% could make rainfall important here in periods when it does rain as the expected rainfall on those days would be 40–120 mmd^{-1} which has the potential to force large gradients.

10.12.8 Shelf region Malaysia and the Sundra Shelf

There is a moderate wind speed and high irradiance across both shelves in this region which drives diurnal warm layers of 70-100% of days, the average of these diurnal warm layers is 0.15-0.2°C for the majority of the year and between March and April they exceed 0.25°C. Whilst both regions are closer to equilibrium than most of the other shelf seas the Sundra Shelf is still slightly oversaturated whereas the shelf closer to Malaysia is slightly undersaturated. As the ΔpCO_2 is small the flux into or out of the layer is small so the pCO_2 in the layer will only change slightly but this will have a large effect on the relative flux for a large portion of the day in this region. High year round production in the Sundra Shelf could drive NPP gradients in this region and due to the reliable formation of warm layers they could be significant here, lower production close to Malaysia could stimulate small NPP gradients that are also important not to dismiss. High daily rainfall with low incidence on both shelves is driven by the short passage of the monsoon over the shelves, at this time the rainfall rates will be extremely high and will certainly drive gradients.

10.12.9 Patagonian Shelf

Despite the above global average wind speeds, diurnal warm layers of 0.1°C are able to form in austral summer between November and February, this works out as around 40% of the days of the year. In austral winter the region is very close to equilibrium but in the austral summer the waters are quite undersaturated with CO_2. The flux into the warm layer will increase the pCO_2 in the layer and reduce theΔpCO_2 and thus the flux, this will have a small effect on the flux. High production year round may also drive NPP gradients. The rainfall rate and incidence are low so rain is unlikely to have a large effect on CO_2 based on previous calculations.

10.12.10 Gulf of Carpentaria

Low wind speeds 4±3 ms^{-1} in the Gulf of Carpentaria lead to mild diurnal warming for around 80% of the days of the year, this is around 0.4°C in September to November and around 0.1°C for the remainder of the year. The Gulf of Carpentaria transitions from very oversaturated at the start of the year to being partially undersaturated in the middle of the year; overall it appears to be a strong source region. There is high year round production particularly between April and July, this could drive gradients here. Rain is infrequent which means the rain is concentrated on a handful of days, meaning when it does rain it is heavy, and this could drive gradients here.

10.12.11 The Great Barrier Reef

The Great Barrier Reef shelf has moderately high wind speeds 7±3 ms^{-1} there is an average gradient of 0.1°C for 40-70% of the year mostly between the months of September and February. The shelf is undersaturated the majority of the year besides January to March, this would drive a moderate air sea flux into the ocean creating a layer with higher CO_2. There is much lower production on the great barrier reef shelf compared to the other shelf seas this could drive small gradients here as there is thermal stratification around half the year. Rain is infrequent which means the rain is concentrated on a handful of days, meaning when it does rain it is heavy, and this could drive gradients here.

10.12.12 Tasmanian shelves

The Tasmanian shelf has very high wind speeds 8±5 ms^{-1} which explains why there does not appear to be any gradients forming here regularly, possibly on <30% of days when there is higher irradiance. The shelf is undersaturated for most of the year could drive a downward flux into the surface ocean on the few days when there is thermal stratification. There are comparatively low production rates here compared to the other shelves, the highest rates do coincide with the higher end of the production here between October and March. There is very little and infrequent rain here which is unlikely to drive gradients outside of intense rainfall events.

10.13 Summary - In which shelf seas are near surface gradients important

Generally the diurnal warm layers are not close to lasting all day, typically 0–10 hours depending on location conditions and time of year so are not important at all times. The effect of the flux into or out of a confined layer also changes the longer the layer is present. When it starts undersaturated compared to the atmosphere the pCO_2 will slowly increase and the flux depreciates over time as the ΔpCO_2 decreases. If the layer is oversaturated it will also lower the flux over time as the pCO_2 and ΔpCO_2 decrease. Therefore another important thing to consider is the timescale over which diurnal warm layers are expected to last. With this in mind it would be expected that the regions that have the conditions best suited for diurnal warm layers are also the regions where the warming would be expected to last longest.

Surface diurnal warming magnitudes and occurrences do indicate that outside of the Poles (where there are some of the largest shelf seas) and the upper mid latitudes there is frequent diurnal warming in shelf seas. Stratification due to salinity is difficult to assess due to lack of measurements but this could be as important as thermal stratification in the tropics for forming confined surface layers.

The European shelf the site of the vertical NSOP sampling has low occurrences of diurnal warming (~10-20%) and by this metric was a poor location for detecting near surface gradients. The high production occurs before the diurnal warm layers form in the summer meaning they are not important, similarly by the summer the shelf is becoming less undersaturated. The shelf seas around Tasmania have similar conditions to the European Shelf and are unlikely to be impactful for near surface gradients.

In contrast to the European shelf which has low occurrences of diurnal warming, other mid latitude shelves such as the East China Sea, Scotian Shelf, Patagonian shelf and the great barrier reef shelf have diurnal warming ~30–70% of the time which is very frequent. As diurnal warming is frequent the high production rates on these shelves could drive changes in NPP in the surface ocean leading to gradients. Heavily undersaturated shelves like the East China Sea would drive large fluxes into the confined layers here which would reduce the flux. The Patagonian shelf goes from a source to sink but regardless of where it is undersaturated or oversaturated diurnal warming would reduce the flux. The effect on the flux is greatest where the wind speed is highest without destroying the near surface stratification as in the East China Sea and Patagonian shelf 7±4 ms^{-1}. These shelf seas are all large making gradients potentially very important here.

The regions with the highest occurrence of diurnal warming (~60 –100%) are found in and around the tropics, the Caribbean Sea, the Mediterranean, the Sundra Shelf, the West Coast of Australia and the Gulf of Carpentaria. Most of these regions go from slightly over to slightly undersaturated depending on the season, the winds are low enough that they do not disrupt thermal stratification but would drive a flux into a confined surface layer. Changes in the air sea flux due to gradients in these tropical regions likely has the largest effect on total flux. Of these shelves the only large one is the Sundra/Malaysian shelf region.

Rainfall is modest on most shelf seas except over the East China Sea, the Scotian shelf and the Sundra shelf where it is large and likely to come down heavily when it does rain. These high rainfall rates could drive stratification and gradients on the 10% of days during which they occur in these shelf seas. Heavy rainfall falling onto an established diurnal warm layer could create two distinct layers in the near surface ocean.

11 Conclusions and future recommendations

The Near Surface Ocean Profiler (NSOP) was developed as a novel measurement system to make near surface profiles of trace gases in the surface 5m of the ocean. NSOP was successfully deployed on 4 cruises and as part of a seasonal study, measuring 100 CO_2, salinity and temperature profiles.

The majority (24/29) of ΔCO_2 from the cruises were <2.5µatm. ΔCO_2 during the L4 seasonal study was much more variable that during the cruises. The largest ΔCO_2 (>4µatm) from the cruises were exclusively observed when there were $\Delta T > 0.05°C$ and low intermediate wind speeds (<6ms^{-1}). There was no relationship between ΔCO_2 and wind speed during the seasonal study. There was no correlation between ΔCO_2 with irradiance during the cruises or the seasonal study.

NSOP ΔCO_2 are much smaller than the only other measurements of CO_2 gradients (Calleja et al., 2013). A simple model suggests that for phytoplankton production to drive the observed positive CO_2 gradients, the NPP rates would need to be ~2.5x lower in an isolated surface layer than in the subsurface water.

The most likely explanation for the positive CO_2 gradients in the vast majority of cruise profiles and in >50% of the L4 profiles is a sustained 3+hr downward flux into a confined undersaturated surface layer.

The interpretation of CO_2 gradients at L4 was complicated by the advection of water masses with distinctly different CO_2. Large tidally controlled ~40µatm variations in fCO_2 were observed between the Plymouth Breakwater and L4. The observation that surface distributions of CO_2 changed during the tidal cycle further complicates coastal flux estimates.

Small CO_2 gradients (<1.5µatm) may not be authentic vertical gradients as temporal changes in the water column CO_2 during the period of sampling (~30minutes) are the same extent as the CO_2 gradients. This explanation could account for the profiles that have CO_2 gradients when there was no near surface stratification.

Fluxes calculated with the surface temperature and salinity measurements from NSOP were only slightly affected (<0.2%) because temperature and salinity gradients were small. Fluxes calculated with NSOP surface CO_2 measurements changed by close to 10% for most of the cruise profiles and at L4. There are four profiles from the SSB cruises where fluxes were more influenced (20–65%). Fluxes from L4 profiles were often changed by >50%. In these cases the wind speeds were low and fluxes small. The absolute flux change was small but the relative flux change was large. This suggests that regions with low wind speed and high atmosphere–ocean concentration gradients have the potential to be most influenced by near surface gradients.

Shelf seas in spring and summer are heavily undersaturated with the atmosphere–ocean pCO_2 difference~100 µatm. The error in seawater surface fCO_2 has a small effect on the flux. In the open ocean, in regions where the atmosphere ocean CO_2 difference is smaller, a 1.5µatm change in surface water fCO_2 will drastically change the flux.

Future work

Faster measurements would help to minimise the effect of temporal changes in water column CO_2. This could be achieved by measuring fewer depths, perhaps only the surface and at 5m or by sampling in the continuous sampling mode. Having a faster response reference CO_2 system would be a great asset for future near surface gradient work.

CO_2 sensors on gliders would offer an alternative way of collecting extensive ΔCO_2 measurements which could then be used as part of a more comprehensive meta-analysis of near surface CO_2 gradients.

The liqui–cel equilibrator was prone to fouling making it difficult to quantify the equilibration. Another fast response equilibrator that is easier to clean would make the measurements more reliable.

The near surface temperature sensors revealed that temperature gradients >0.5°C are very infrequent in the Shelf Seas of the UK. To test the relationship between CO_2 gradients and strong temperature gradients it would be necessary to make more profiles in regions where diurnal warming is strong and frequent (e.g. the tropics). This would quantify some of the speculation made about larger and more frequent gradients in tropical and the lower mid latitudes shelf seas.

The processes that are proposed to cause near surface gradients in CO_2 are equally applicable to a number of other trace gases. Near surface gradients of other trace gases that have a biological component such as DMS may be important. Other trace gases are not buffered by the repartitioning of the carbon system so may reveal large gradients. Many trace gases such as DMS and a range of organic volatile organic compounds (OVOCs) have a much lower solubility than CO_2 and a much stronger atmosphere ocean concentration gradient which could make the air sea flux even more important for these trace gases.

12 Appendix

12.1 RRS Discovery

The Shelf Seas Biogeochemistry programme cruises were the first on RRS Discovery. The ship is 99.7m long and has a beam of 18m. The maximum displacement tonnage of the ship is 6260.8T. The ship has two azimuth thrusters (5 bladed, fixed pitch, 3.6m diameter) located at the bow of the ship, these are complimented by an additional forward retractable azimuth thruster and a Tees Gill water– jet thruster (Figure 3.2). These thrusters enable a maximum speed of 12 Knots. Azimuth thrusters can be rotated 360°, this modern feature called dynamic positioning, is automatic and requires no user input, yet allows the ship to be positioned on station with minimum manoeuvring and to be kept on station with high precision. The system used on RRS Discovery was a Kongsberg K–POS DP–22 system and allows the deployment of equipment from both the stern and starboard side of the ship.

The ship has a full suite of winches and handling systems for scientific deployments (Figure 3.2). On the starboard side of the ship is the starboard P–Frame (from which the CTD is deployed using the steel CTD winches. Sediment cores are deployed using the coring winch and other equipment using the general purpose winch). Immediately aft of the P–Frame is the starboard beam from which the trace metal CTD is deployed using the clean CTD winch. The trawl and deep tow winches are located at the bow of the ship and can be fed through the ships aft A– frame. Two additional deck based winches and two aft cranes are also located on the aft deck which can be used to deploy small scientific equipment.

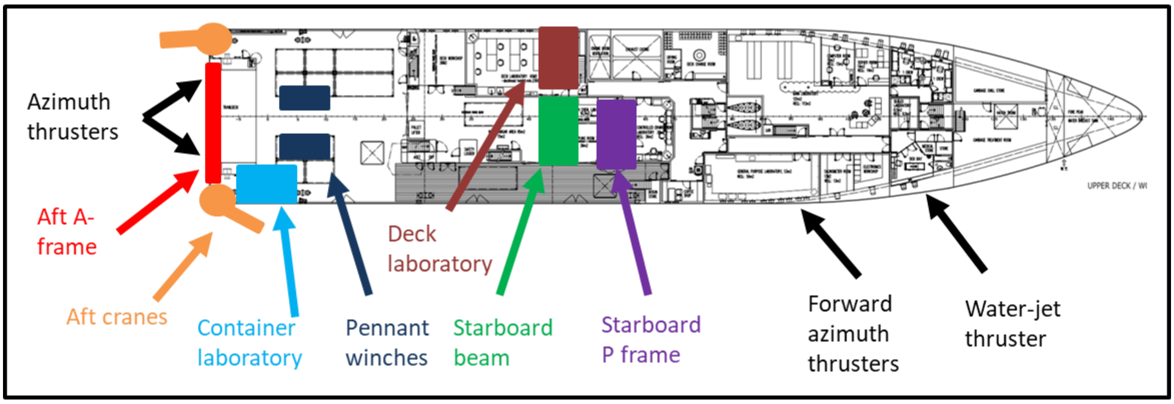

Figure 12.1 RRS Discovery propulsion and handling systems
Schematic of the main deck level of RRS Discovery. The locations of the propulsion systems on RRS Discovery are indicated by black arrows but are beneath mean deck level. The handling systems used are labelled and individually coloured on the schematic as are the laboratory spaces.

12.2 Deployment location from RRS Discovery

Largely due to the size and sophisticated manoeuvrability of RRS Discovery, a number of considerations were taken into account when determining the optimal location for NSOP deployments. These were (1) where the ship generated the least turbulence, (2)where NSOP could be lifted over the bulwark and lowered 5m to the sea surface and recovered in the same way, (3) where would NSOP drift the most from the ship, (4) where was the best access to the laboratory, (5) where was visibility best for the bridge and (6) what was a safe distance away from the ships propellers to have ropes and tubing in the water.

As mentioned in section 3.4 there were a number of handling systems capable of deploying NSOP, these were the general purpose winch on either the starboard P–frame or the starboard beam, one of the 2 aft cranes or one of the winches with the aft A–frame. The A–frame location was unsuitable because of the proximity to the aft propellers, which had the potential to cause line entanglement and create localised turbulence. The starboard P–frame and starboard beam also proved unsuitable as it was desirable to disconnect NSOP from the crane in order for it to free float, and if this was done here it would have been very difficult to recover the NSOP again.

Hence the chosen location for the deployment was starboard aft as the aft cranes could lift NSOP over the bulwark, release it and then reconnect to it once the deployment was over. There was continuous line of sight for the bridge on the starboard aft side of the ship which assisted the captain in positioning the ship. This site was also further away from the influence of the ship’s propellers which reduced concerns about line entanglement and turbulence. The deck was long enough that the two slack lines could be spread out more than 10 m apart on the deck, which helped maintain position. The crane arm could also be extended to help keep NSOP away from the ship. The closest laboratory to the starboard deck is the deck lab located on the port side of the ship through the CTD hanger; this was unfortunately a considerable distance away and demanded the use of long inlet tubing (50 m).

12.3 Changes to methodology between cruises

The methodology described in Chapter 2 represents the best standard methodology. There was a concerted effort to keep the methodology consistent between cruises. However, this was not always possible as it was necessary to change instruments and methodologies between cruises.

12.3.1 Instrument Changes

It was necessary to make changes to the instruments used in response to technical faults or instrument availability.

A fast response microCTD was desired for the cruises; unfortunately the only cruise where there was access to a fast profiling instrument was MAY15 during which a Valeport miniCTD capable of logging at 1Hz was used. For cruises AUG14, OCT14 and JULY15 a Seabird 37 microCTD was used instead, the maximum logging frequency of this microCTD was 1/6 Hz. Due to the discrete profiling regime chosen for the cruises, the slower logging frequency of the CTD did not impact the results significantly as changes at each discrete depth could still be assessed with less data.

Due to difficulties overcoming the 5m hydraulic head on the first cruise (AUG14) using a Watson Marlow 620s pump, a more powerful Watson Marlow 701IB/R pump was used on the 3 subsequent cruises. The Watson Marlow 701IB/R was capable of supplying 2–3.5 LPM whereas the Watson Marlow 620s could only supply a reliable flowrate of 1–2 LPM. In addition to changing the pump, user positioning of the peristaltic tubing on the rollers improved over time. There were two benefits to this, firstly it reduced the chance of tubing rupture from abrasion and secondly it meant the tubing did not slip and the flowrate remained more constant during the deployment.

An error by the National Marine Facilities technicians in labelling lines to the ship container on the aft deck meant that during JULY15 the air conditioning coolant waste was pumped through the liqui–cel instead of seawater. Whilst the liqui–cel was later repeatedly rinsed with freshwater it was decided to forego using it for the remainder of the cruise due to possible damage to the membrane, instead a new unit was used for the entirety of the cruise.

On the first three cruises the NSOP CO_2 system was located in the deck lab of the ship, for JULY15 space conflicts meant that the CO_2 system was located in a container at the aft of the ship which was closer to the deployment location. The increased proximity to NSOP meant the 50m of tubing could have been shortened or replaced; this would have reduced the lag time, mixing along the pipe, dampened temperature changes and reduced the time for the chemistry of the water to change in the tubing. In spite of these potential advantages it was decided to not alter the tubing and maintain consistency between deployments.

During cruise OCT14 the winch controls receiver on NSOP was damaged during NSOP recovery, the damage allowed the slow ingress of water into the receiver unit resulting in an electronics failure. Unfortunately the damage to the circuit board was impossible to repair on the cruise deployments, so NSOP was could not be used for profiling. After the fault was detected the remaining three deployments on the 2nd and 3rd October 2014 were instead made using the NSOP frame, a small aft deck winch and a block connected to the aft crane arm (Figure 12.2). Incremental markings of 0.5m were made on the winch cable so that pay–out by the crew member manually controlling the deck winch was consistent. Whilst deployments using the crane were undesirable due to the poorer depth resolution it still provided additional data and provided the opportunity to assess the depth resolution using this method. The receiver was replaced for the remaining cruises.

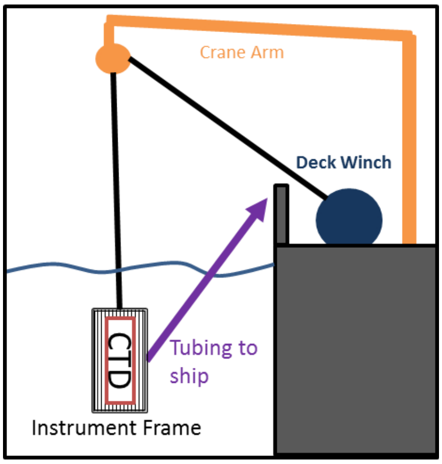

Figure 12.2 Crane deployment schematic
Cross section schematic of the NSOP sampling frame being deployed independently using a block connected to the ships crane arm and a deck mounted winch.

12.3.2 Methodological Improvements

The methodology was altered when there were perceived improvements in understanding and alternative approaches were proposed that were thought to improve upon the original methodology.

In response to strong tides observed during MAY15 when NSOP was deployed in the heavily tidal region around the benthic sites, it was deemed necessary to include a 10kg lead weight to prevent horizontal movement by the frame. On subsequent deployments and cruises outside of this region it was not deemed necessary to attach the weight. This prevented the tide pushing the CTD cage horizontally and making it possible to only sample the top 2m.

On AUG14 and OCT14 NSOP had tended to drift towards Discovery, the two slack lines were able to maintain its position along the ship but not away from it. On MAY15 and JULY15 the crane was used as a third point to position NSOP and the rear slack line was looped through an outstretched arm. These two changes were small changes that considerably increased (+5 m) the distance NSOP was away from the ship.

On AUG14 the water flowrate was measured intermittently every 30 minutes using a 1 L measurement beaker and a stopwatch. During the cruise it became apparent that the flowrate from the pump tended to decline over time. The flowrate for the AUG14 cruises was estimated by interpolation using the measured seawater flowrate measured throughout the deployment. A flowrate sensor was installed for all subsequent cruises.

During AUG14 the gas side flow rate was reduced mid–deployment from 100 ml min^{-1} to 50 ml min^{-1} to account for the drop in efficiency caused by the declining waterside flowrate. It was believed that this would keep the equilibration efficiency high however this change decreased the response time and was not repeated during future cruises.

On AUG14 the carrier gas entering the liqui–cel was compressed air, this was chosen as its nominal partial pressure is closer to that in the seawater. After AUG14 the carrier gas was changed to nitrogen for the remaining cruises. As there was incomplete equilibration, the efficiency correction and thus error in the calculated fCO_2 was higher with nitrogen so it would have been better to continue using compressed gas which is closer to the seawater fCO_2 value.

12.3.3 RV Plymouth Quest

RV Plymouth Quest (Figure 12.3) is operated by the Plymouth Marine Laboratory and conducts the majority of the local oceanographic work including the sampling at stations L4 and E1. The vessel is 21.5 m long with a draught of 3.02 m and is manned full time by four members of crew. The rear stern gate is located on the main deck (~ 0.5 m above the water line) and is retractable so that instruments can be lowered into the water by the 10 ton hydraulic crane. The propellers of the ship are located below the stern of the ship and can be stopped completely when on station. Due to its small size the Quest is very manoeuvrable, which was an asset during deployments. In contrast to RRS Discovery the Captain always had line of sight with the NSOP during deployments.

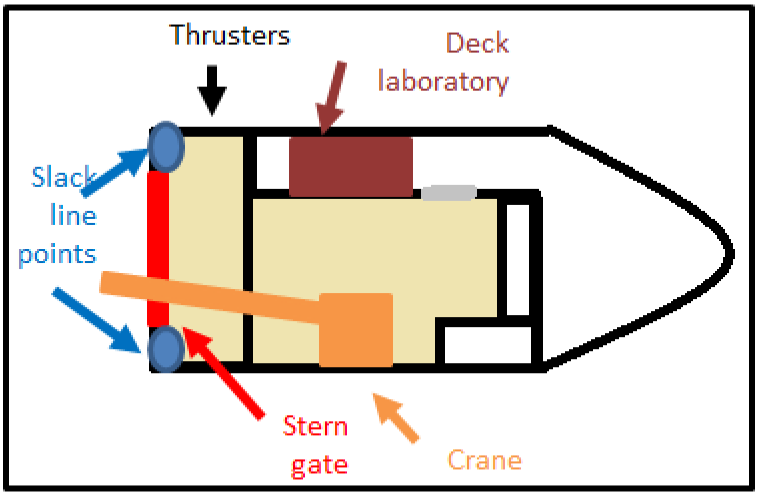

Figure 12.3 Plymouth Quest schematic
Top down schematic of RV Plymouth Quest (not to scale). Identified on the figure are the crane, stern gate, slack lines, deck laboratory and the location of the thrusters under the ship.

12.3.4 Sampling considerations and methodological changes specific to RV Quest

During NSOP sampling the Quest remained on station (Eulerian approach) by manoeuvring into the wind. The thrusters were only used sparingly to adjust the position of the ship. This was different to the methodology used on the SSB cruises where the ship was left to drift (Lagrangian approach). NSOP deployments at L4 were unlikely to have sampled the same water mass for the entire duration of the deployment, meaning that the L4 profiles may also contain CO_2 changes associated with the transition of different water masses across station L4. The vertical profiles measured with NSOP assume a static water mass for the duration of the deployment.

Unlike on RRS Discovery which had a dynamic positioning system, the propellers of the Quest could be stopped to reduce turbulence at the rear of the ship. Turning off the propellers meant that NSOP could be deployed from the stern of the ship without concerns about the near surface being disrupted. The size of the Plymouth Quest means that it is often not safe to deploy any instruments in rough weather conditions above Beaufort force 5 (wind speed 10 ms^{-1} and wave height 2.0m). This restriction and the requirement to prioritise weekly western channel observatory sampling ultimately limited the number of deployments. Due to the size and weight of NSOP, it was deployed with the main crane. During deployments the stern gate was lowered and NSOP was lowered into the water. The NSOP was then tethered to two points at the rear of the ship at the left and right of the vessel so that it could drift ~10–15 m behind the ship. The ship was then left to drift for the length of the deployment unless the distance from the L4 buoy exceeded more than 1 km. In this case the ship slowly steamed back to the buoy for no more than 20 minutes whilst sampling.

During the seasonal study some of the NSOP equipment was different to that used during the SSB work. The CTD was an RBR model XR-620 set to sample substantially faster (6Hz) than the Seabird 37 used on the SSB cruises. The pump was a Watson Marlow 620S peristaltic pump which delivered a steady seawater supply of ~4 $Lmin^{-1}$ when the hydraulic head was ~0.5m. Damage to the winch receiver during a deployment near the end of the seasonal study meant that as for OCT14 the instrument cage had to be deployed from the crane arm of the ship on the last four deployments (Figure 12.2).

13 References

ADLER, R. F., HUFFMAN, G. J., CHANG, A., FERRARO, R., XIE, P.-P., JANOWIAK, J., RUDOLF, B., SCHNEIDER, U., CURTIS, S. & BOLVIN, D. 2003. The version-2 global precipitation climatology project (GPCP) monthly precipitation analysis (1979–present). *Journal of hydrometeorology,* 4, 1147-1167.

ANDERSON, J. E. & RISER, S. C. 2014. Near-surface variability of temperature and salinity in the near-tropical ocean: Observations from profiling floats. *Journal of Geophysical Research: Oceans,* 119, 7433-7448.

ANGUELOVA, M. D. & WEBSTER, F. 2006. Whitecap coverage from satellite measurements: A first step toward modeling the variability of oceanic whitecaps. *Journal of Geophysical Research: Oceans (1978–2012),* 111.

ANTOINE, D., ANDRÉ, J. M. & MOREL, A. 1996. Oceanic primary production: 2. Estimation at global scale from satellite (coastal zone color scanner) chlorophyll. *Global Biogeochemical Cycles,* 10, 57-69.

ASHER, W. E., JESSUP, A. T., BRANCH, R. & CLARK, D. 2014. Observations of rain-induced near-surface salinity anomalies. *Journal of Geophysical Research: Oceans,* 119, 5483-5500.

ASHER, W. E., KARLE, L. M., HIGGINS, B. J., FARLEY, P. J., MONAHAN, E. C. & LEIFER, I. S. 1996. The influence of bubble plumes on air-seawater gas transfer velocities. *Journal of Geophysical Research: Oceans,* 101, 12027-12041.

ATKINSON, A., HARMER, R. A., WIDDICOMBE, C. E., MCEVOY, A. J., SMYTH, T. J., CUMMINGS, D. G., SOMERFIELD, P. J., MAUD, J. L. & MCCONVILLE, K. 2015. Questioning the role of phenology shifts and trophic mismatching in a planktonic food web. *Progress in Oceanography,* 137, 498-512.

BADESCU, V. 2014. *Modeling solar radiation at the earth's surface*, Springer.

BAKKER, D., HANKIN, S., OLSEN, A., PFEIL, B., SMITH, K., ALIN, S., COSCA, C., HALES, B., HARASAWA, S. & KOZYR, A. 2014. An update to the Surface Ocean CO2 Atlas (SOCAT version 2). *Earth*.

BAKKER, D. C., DE BAAR, H. J. & DE WILDE, H. P. 1996. Dissolved carbon dioxide in Dutch coastal waters. *Marine Chemistry,* 55, 247-263.

BAKKER, D. C., PFEIL, B., LANDA, C. S., METZL, N., O'BRIEN, K. M., OLSEN, A., SMITH, K., COSCA, C., HARASAWA, S. & JONES, S. D. 2016. A multi-decade record of high-quality fCO 2 data in version 3 of the Surface Ocean CO 2 Atlas (SOCAT). *Earth System Science Data,* 8, 383.

BANGE, H. W., BELL, T. G., CORNEJO, M., FREING, A., UHER, G., UPSTILL-GODDARD, R. C. & ZHANG, G. 2009. MEMENTO: a proposal to develop a database of marine nitrous oxide and methane measurements. *Environmental Chemistry,* 6, 195-197.

BARNES, M. K., TILSTONE, G. H., SMYTH, T. J., SUGGETT, D. J., ASTORECA, R., LANCELOT, C. & KROMKAMP, J. C. 2014. Absorption-based algorithm of primary production for total and size-fractionated phytoplankton in coastal waters. *Marine Ecology Progress Series,* 504, 73-89.

BARNES, M. K., TILSTONE, G. H., SUGGETT, D. J., WIDDICOMBE, C. E., BRUUN, J., MARTINEZ-VICENTE, V. & SMYTH, T. J. 2015. Temporal variability in total, micro-and nano-phytoplankton primary production at a coastal site in the western English Channel. *Progress in Oceanography,* 137, 470-483.

BEHRENFELD, M. J., O'MALLEY, R. T., SIEGEL, D. A., MCCLAIN, C. R., SARMIENTO, J. L., FELDMAN, G. C., MILLIGAN, A. J., FALKOWSKI, P. G., LETELIER, R. M. & BOSS, E. S. 2006. Climate-driven trends in contemporary ocean productivity. *Nature,* 444, 752.

BEHRENFELD, M. J., PRASIL, O., KOLBER, Z. S., BABIN, M. & FALKOWSKI, P. G. 1998. Compensatory changes in photosystem II electron turnover rates protect photosynthesis from photoinhibition. *Photosynthesis Research,* 58, 259-268.

BELL, T., DE BRUYN, W., MARANDINO, C. A., MILLER, S., LAW, C., SMITH, M. & SALTZMAN, E. 2015. Dimethylsulfide gas transfer coefficients from algal blooms in the Southern Ocean. *Atmospheric Chemistry and Physics,* 15, 1783-1794.

BELL, T., DE BRUYN, W., MILLER, S., WARD, B., CHRISTENSEN, K. & SALTZMAN, E. 2013. Air–sea dimethylsulfide (DMS) gas transfer in the North Atlantic: evidence for limited interfacial gas exchange at high wind speed. *Atmospheric Chemistry and Physics,* 13, 11073-11087.

BIRCHILL, A. J., MILNE, A., WOODWARD, E. M. S., HARRIS, C., ANNETT, A., RUSIECKA, D., ACHTERBERG, E. P., GLEDHILL, M., USSHER, S. J. & WORSFOLD, P. J. 2017. Seasonal iron depletion in temperate shelf seas. *Geophysical research letters,* 44, 8987-8996.

BISHOP, J. K. & ROSSOW, W. B. 1991. Spatial and temporal variability of global surface solar irradiance. *Journal of Geophysical Research: Oceans,* 96, 16839-16858.

BOGDANOFF, A. S. 2017. *Physics of diurnal warm layers: turbulence, internal waves, and lateral mixing.* Massachusetts Institute of Technology.

BORGES, A. & FRANKIGNOULLE, M. 1999. Daily and seasonal variations of the partial pressure of CO 2 in surface seawater along Belgian and southern Dutch coastal areas. *Journal of marine systems,* 19, 251-266.

BORGES, A., SCHIETTECATTE, L.-S., ABRIL, G., DELILLE, B. & GAZEAU, F. 2006. Carbon dioxide in European coastal waters. *Estuarine, Coastal and Shelf Science,* 70, 375-387.

BORGES, A. V. 2005. Do we have enough pieces of the jigsaw to integrate CO2 fluxes in the coastal ocean? *Estuaries,* 28, 3-27.

BORGES, A. V. & FRANKIGNOULLE, M. 2003. Distribution of surface carbon dioxide and air-sea exchange in the English Channel and adjacent areas. *Journal of Geophysical Research: Oceans,* 108.

BOUTIN, J., CHAO, Y., ASHER, W. E., DELCROIX, T., DRUCKER, R., DRUSHKA, K., KOLODZIEJCZYK, N., LEE, T., REUL, N. & REVERDIN, G. 2016. Satellite and in situ salinity: understanding near-surface stratification and subfootprint variability. *Bulletin of the American Meteorological Society,* 97, 1391-1407.

BOYD, P. & TRULL, T. 2007. Understanding the export of biogenic particles in oceanic waters: is there consensus? *Progress in Oceanography,* 72, 276-312.

BOZEC, Y., THOMAS, H., ELKALAY, K. & DE BAAR, H. J. 2005. The continental shelf pump for CO2 in the North Sea—evidence from summer observation. *Marine Chemistry,* 93, 131-147.

BREWER, P. G. & GOLDMAN, J. C. 1976. Alkalinity changes generated by phytoplankton growth. *Limnology and Oceanography,* 21, 108-117.

BRION, N., BAEYENS, W., DE GALAN, S., ELSKENS, M. & LAANE, R. W. 2004. The North Sea: source or sink for nitrogen and phosphorus to the Atlantic Ocean? *Biogeochemistry,* 68, 277-296.

CALLEJA, M. L., DUARTE, C., PRAIRIE, Y., AGUSTÍ, S. & HERNDL, G. 2009. Evidence for surface organic matter modulation of air-sea CO 2 gas exchange. *Biogeosciences,* 6, 1105-1114.

CALLEJA, M. L., DUARTE, C. M., ÁLVAREZ, M., VAQUER-SUNYER, R., AGUSTÍ, S. & HERNDL, G. J. 2013. Prevalence of strong vertical CO2 and O2 variability in the top meters of the ocean. *Global Biogeochemical Cycles,* 27, 941-949.

CALLEJA, M. L., DUARTE, C. M., NAVARRO, N. & AGUSTÍ, S. 2005. Control of air-sea CO2 disequilibria in the subtropical NE Atlantic by planktonic metabolism under the ocean skin. *Geophysical Research Letters,* 32, L08606.

CARR, N., DAVIS, C. E., BLACKBIRD, S., DANIELS, L. R., PREECE, C., WOODWARD, M. & MAHAFFEY, C. 2018. Seasonal and spatial variability in the optical characteristics of DOM in a temperate shelf sea. *Progress in Oceanography*.

CHEN, C.-T., HUANG, T.-H., CHEN, Y.-C., BAI, Y., HE, X. & KANG, Y. 2013. Air-sea exchanges of CO2 in the world's coastal seas. *Biogeosciences,* 10, 6509.

CHIERICI, M. & FRANSSON, A. 2009. Calcium carbonate saturation in the surface water of the Arctic Ocean: undersaturation in freshwater influenced shelves. *Biogeosciences,* 6, 2421-2431.

CIAIS, P., SABINE, C., BALA, G., BOPP, L., BROVKIN, V., CANADELL, J., CHHABRA, A., DEFRIES, R., GALLOWAY, J. & HEIMANN, M. 2014. Carbon and other biogeochemical cycles. *Climate Change 2013: The Physical Science Basis. Contribution of Working Group I to the Fifth Assessment Report of the Intergovernmental Panel on Climate Change.* Cambridge University Press.

COOPER, D. J., WATSON, A. J. & LING, R. D. 1998. Variation of< i> p</i>< sub> CO2</sub> along a North Atlantic shipping route (UK to the Caribbean): A year of automated observations. *Marine chemistry,* 60, 147-164.

COPIN-MONTEGUT, C. 1988. A new formula for the effect of temperature on the partial pressure of CO< sub> 2</sub> in seawater. *Marine Chemistry,* 25, 29-37.

D'ASARO, E. & MCNEIL, C. 2007. Air–sea gas exchange at extreme wind speeds measured by autonomous oceanographic floats. *Journal of marine systems,* 66, 92-109.

DA SILVA, A. M., YOUNG, C. C. & LEVITUS, S. 1994. Atlas of surface marine data 1994 Vol. 4: Anomalies of fresh water fluxes.

DAVIS, C. E., BLACKBIRD, S., WOLFF, G., WOODWARD, M. & MAHAFFEY, C. 2018. Seasonal organic matter dynamics in a temperate shelf sea. *Progress in Oceanography*.

DE HAAS, H., VAN WEERING, T. C. & DE STIGTER, H. 2002. Organic carbon in shelf seas: sinks or sources, processes and products. *Continental Shelf Research,* 22, 691-717.

DEACON, E. 1977. Gas transfer to and across an air-water interface. *Tellus,* 29, 363-374.

DICKSON, A. 1981. An exact definition of total alkalinity and a procedure for the estimation of alkalinity and total inorganic carbon from titration data. *Deep Sea Research Part A. Oceanographic Research Papers,* 28, 609-623.

DICKSON, A. G. 1990. Standard potential of the reaction: AgCl (s)+ 12H2 (g)= Ag (s)+ HCl (aq), and and the standard acidity constant of the ion HSO4− in synthetic sea water from 273.15 to 318.15 K. *The Journal of Chemical Thermodynamics,* 22, 113-127.

DICKSON, A. G. & MILLERO, F. J. 1987. A comparison of the equilibrium constants for the dissociation of carbonic acid in seawater media. *Deep Sea Research Part A. Oceanographic Research Papers,* 34, 1733-1743.

DICKSON, A. G., SABINE, C. L. & CHRISTIAN, J. R. 2007. Guide to best practices for ocean CO_2 measurements.

DONG, S., GILLE, S. T., SPRINTALL, J. & GENTEMANN, C. 2006. Validation of the Advanced Microwave Scanning Radiometer for the Earth Observing System (AMSR-E) sea surface temperature in the Southern Ocean. *Journal of Geophysical Research: Oceans,* 111.

DONLON, C., MINNETT, P., GENTEMANN, C., NIGHTINGALE, T., BARTON, I., WARD, B. & MURRAY, M. 2002. Toward improved validation of satellite sea surface skin temperature measurements for climate research. *Journal of Climate,* 15, 353-369.

DONLON, C., NIGHTINGALE, T., SHEASBY, T., TURNER, J., ROBINSON, I. & EMERGY, W. 1999. Implications of the oceanic thermal skin temperature deviation at high wind speed. *Geophysical research letters,* 26, 2505-2508.

DONLON, C., ROBINSON, I., WIMMER, W., FISHER, G., REYNOLDS, M., EDWARDS, R. & NIGHTINGALE, T. 2008. An infrared sea surface temperature autonomous radiometer (ISAR) for deployment aboard volunteer observing ships (VOS). *Journal of Atmospheric and Oceanic Technology,* 25, 93-113.

DRUCKER, R. & RISER, S. C. 2014. Validation of Aquarius sea surface salinity with Argo: Analysis of error due to depth of measurement and vertical salinity stratification. *Journal of Geophysical Research: Oceans,* 119, 4626-4637.

DRUSHKA, K., ASHER, W. E., WARD, B. & WALESBY, K. 2016. Understanding the formation and evolution of rain-formed fresh lenses at the ocean surface. *Journal of Geophysical Research: Oceans,* 121, 2673-2689.

DUARTE, C. M. & AGUSTí, S. 1998. The CO2 balance of unproductive aquatic ecosystems. *Science,* 281, 234-236.

DURHAM, W. M., KESSLER, J. O. & STOCKER, R. 2009. Disruption of vertical motility by shear triggers formation of thin phytoplankton layers. *Science,* 323, 1067-1070.

ELLIS, T. D., L'ECUYER, T., HAYNES, J. M. & STEPHENS, G. L. 2009. How often does it rain over the global oceans? The perspective from CloudSat. *Geophysical research letters,* 36.

ELSE, B., RYSGAARD, S., ATTARD, K., CAMPBELL, K., CRABECK, O., GALLEY, R., GEILFUS, N.-X., LEMES, M., LUECK, R. & PAPAKYRIAKOU, T. 2015. Under-ice eddy covariance flux measurements of heat, salt, momentum, and dissolved oxygen in an artificial sea ice pool. *Cold Regions Science and Technology,* 119, 158-169.

ELSE, B. G., PAPAKYRIAKOU, T. N., GRANSKOG, M. A. & YACKEL, J. J. 2008. Observations of sea surface fCO2 distributions and estimated air-sea CO2 fluxes in the Hudson Bay region (Canada) during the open water season. *Journal of Geophysical Research: Oceans (1978–2012),* 113.

EMERSON, S. & HEDGES, J. 2008. *Chemical oceanography and the marine carbon cycle*, Cambridge University Press.

FAIRALL, C., BRADLEY, E. F., GODFREY, J., WICK, G., EDSON, J. B. & YOUNG, G. 1996. Cool-skin and warm-layer effects on sea surface temperature. *Journal of Geophysical Research,* 101, 1295-1308.

FAIRALL, C., BRADLEY, E. F., HARE, J., GRACHEV, A. & EDSON, J. 2003. Bulk parameterization of air-sea fluxes: Updates and verification for the COARE algorithm. *Journal of Climate,* 16, 571-591.

FALKOWSKI, P. G., BARBER, R. T. & SMETACEK, V. 1998. Biogeochemical controls and feedbacks on ocean primary production. *Science,* 281, 200-206.

FARMER, D., MCNEIL, C. & JOHNSON, B. 1993. Evidence for the importance of bubbles in increasing air–sea gas flux.

FASSBENDER, A. J., RODGERS, K. B., PALEVSKY, H. I. & SABINE, C. L. 2018. Seasonal asymmetry in the evolution of surface ocean pCO2 and pH thermodynamic drivers and the influence on sea-air CO2 flux. *Global Biogeochemical Cycles*.

FASSBENDER, A. J., SABINE, C. L. & PALEVSKY, H. I. 2017. Nonuniform ocean acidification and attenuation of the ocean carbon sink. *Geophysical research letters,* 44, 8404-8413.

FEELY, R. A., DONEY, S. C. & COOLEY, S. R. 2009. Ocean acidification: Present conditions and future changes in a high-CO_2 world. *Oceanography,* 22, 36-47.

FIEDLER, B., FIETZEK, P., VIEIRA, N., SILVA, P., BITTIG, H. C. & KÖRTZINGER, A. 2013. In situ CO2 and O2 measurements on a profiling float. *Journal of Atmospheric and Oceanic Technology,* 30, 112-126.

FIELD, C. B., BEHRENFELD, M. J., RANDERSON, J. T. & FALKOWSKI, P. 1998. Primary production of the biosphere: integrating terrestrial and oceanic components. *Science,* 281, 237-240.

FISCHER, T., KOCK, A., AREVALO-MARTINEZ, D. L., DENGLER, M., BRANDT, P. & BANGE, H. W. 2018. Gas exchange estimates in the Peruvian upwelling regime biased by multi-day near-surface stratification. *Biogeosciences Discussions*, 1-34.

FRANKIGNOULLE, M. & BORGES, A. V. 2001. European continental shelf as a significant sink for atmospheric carbon dioxide. *Global Biogeochemical Cycles,* 15, 569-576.

FRANKIGNOULLE, M., BOURGE, I., CANON, C. & DAUBY, P. 1996. Distribution of surface seawater partial C0< sub> 2</sub> pressure in the English Channel and in the Southern Bight of the North Sea. *Continental Shelf Research,* 16, 381-395.

FRANSSON, A., CHIERICI, M., SKJELVAN, I., OLSEN, A., ASSMY, P., PETERSON, A. K., SPREEN, G. & WARD, B. 2017. Effects of sea-ice and biogeochemical processes and storms on under-ice water fCO2 during the winter-spring transition in the high Arctic Ocean: Implications for sea-air CO2 fluxes. *Journal of Geophysical Research: Oceans,* 122, 5566-5587.

FREW, N. M., GOLDMAN, J. C., DENNETT, M. R. & JOHNSON, A. S. 1990. Impact of phytoplankton-generated surfactants on air-sea gas exchange. *Journal of Geophysical Research: Oceans (1978–2012),* 95, 3337-3352.

GALÍ, M., SIMÓ, R., VILA-COSTA, M., RUIZ-GONZÁLEZ, C., GASOL, J. M. & MATRAI, P. 2013. Diel patterns of oceanic dimethylsulfide (DMS) cycling: Microbial and physical drivers. *Global Biogeochemical Cycles,* 27, 620-636.

GARBE, C., RUTGERSSON, A., BOUTIN, J., DE LEEUW, G., DELILLE, B., FAIRALL, C., GRUBER, N., HARE, J., HO, D., JOHNSON, M., NIGHTINGALE, P., PETTERSSON, H., PISKOZUB, J., SAHLÉE, E., TSAI, W.-T., WARD, B., WOOLF, D. & ZAPPA, C. 2014. Transfer Across the Air-Sea Interface. *In:* LISS, P. S. & JOHNSON, M. T. (eds.) *Ocean-Atmosphere Interactions of Gases and Particles.* Springer Berlin Heidelberg.

GARCÍA-MARTÍN, E. E., DANIELS, C. J., DAVIDSON, K., LOZANO, J., MAYERS, K. M., MCNEILL, S., MITCHELL, E., POULTON, A. J., PURDIE, D. A. & TARRAN, G. A. 2017. Plankton community respiration and bacterial metabolism in a North Atlantic Shelf Sea during spring bloom development (April 2015). *Progress in Oceanography*.

GARCIA-MARTIN, E. E., MCNEILL, S., SERRET, P. & LEAKEY, R. 2014. Plankton metabolism and bacterial growth efficiency in offshore waters along a latitudinal transect between the UK and Svalbard. *Deep Sea Research Part I: Oceanographic Research Papers,* 92, 141-151.

GARCIA-SOTO, C. & PINGREE, R. D. 1998. Late autumn distribution and seasonality of chlorophyll-a at the shelf-break/slope region of the Armorican and Celtic Shelf. *Journal of the Marine Biological Association of the United Kingdom,* 78, 17-33.

GEMMRICH, J. R., BANNER, M. L. & GARRETT, C. 2008. Spectrally resolved energy dissipation rate and momentum flux of breaking waves. *Journal of Physical Oceanography,* 38, 1296-1312.

GENTEMANN, C. L., DONLON, C. J., STUART-MENTETH, A. & WENTZ, F. J. 2003. Diurnal signals in satellite sea surface temperature measurements. *Geophysical research letters,* 30, 1140.

GENTEMANN, C. L., MINNETT, P. J. & WARD, B. 2009. Profiles of ocean surface heating (POSH): A new model of upper ocean diurnal warming. *Journal of Geophysical Research: Oceans,* 114, C07017.

GIERING, S. L., WELLS, S. R., MAYERS, K. M., SCHUSTER, H., CORNWELL, L., FILEMAN, E., ATKINSON, A., COOK, K. B., PREECE, C. & MAYOR, D. J. 2018. Seasonal variation of zooplankton community structure and trophic position in the Celtic Sea: a stable isotope and biovolume spectrum approach. *Progress in Oceanography*.

GODDIJN-MURPHY, L., WOOLF, D. K. & CALLAGHAN, A. H. 2011. Parameterizations and algorithms for oceanic whitecap coverage. *Journal of Physical Oceanography,* 41, 742-756.

GOSNELL, R., FAIRALL, C. & WEBSTER, P. 1995. The sensible heat of rainfall in the tropical ocean. *Journal of Geophysical Research: Oceans,* 100, 18437-18442.

GOYET, C., MILLERO, F. J., POISSON, A. & SHAFER, D. K. 1993. Temperature dependence of CO2 fugacity in seawater. *Marine Chemistry,* 44, 205-219.

GOYET, C. & POISSON, A. 1989. New determination of carbonic acid dissociation constants in seawater as a function of temperature and salinity. *Deep Sea Research Part A. Oceanographic Research Papers,* 36, 1635-1654.

HALES, B., CHIPMAN, D. & TAKAHASHI, T. 2004. High-frequency measurement of partial pressure and total concentration of carbon dioxide in seawater using microporous hydrophobic membrane contractors. *Limnol. Oceanogr.: Methods* 2, 356-364.

HANSSON, I. 1973a. The determination of the dissociation constants of carbonic acid in synthetic sea water in the salinity range of 20–40‰ and temperature range of 5–3 C. *Acta Chem. Scandinavica,* 27, 931-944.

HANSSON, I. 1973b. A new set of acidity constants for carbonic acid and boric acid in sea water. *Deep Sea Research and Oceanographic Abstracts,* 20, 461-478.

HARDMAN-MOUNTFORD, N. J., MOORE, G., BAKKER, D. C., WATSON, A. J., SCHUSTER, U., BARCIELA, R., HINES, A., MONCOIFFÉ, G., BROWN, J. & DYE, S. 2008. An operational monitoring system to provide indicators of CO_2-related variables in the ocean. *ICES Journal of Marine Science: Journal du Conseil,* 65, 1498-1503.

HARE, J. E., FAIRALL, C. W., MCGILLIS, W. R., EDSON, J. B., WARD, B. & WANNINKHOF, R. 2004. Evaluation of the National Oceanic and Atmospheric Administration/Coupled-Ocean

Atmospheric Response Experiment (NOAA/COARE) air-sea gas transfer parameterization using GasEx data. *Journal of Geophysical Research: Oceans,* 109, C08S11.

HARRIS, P., MACMILLAN-LAWLER, M., RUPP, J. & BAKER, E. 2014. Geomorphology of the oceans. *Marine Geology,* 352, 4-24.

HARTMAN, S., HUMPHREYS, M., KIVIMÄE, C., WOODWARD, E., KITIDIS, V., MCGRATH, T., HYDES, D., GREENWOOD, N., HULL, T. & OSTLE, C. 2018. Seasonality and spatial heterogeneity of the surface ocean carbonate system in the northwest European continental shelf. *Progress in Oceanography*.

HAYS, G. C. 2003. A review of the adaptive significance and ecosystem consequences of zooplankton diel vertical migrations. *Migrations and Dispersal of Marine Organisms.* Springer.

HENOCQ, C., BOUTIN, J., REVERDIN, G., ARNAULT, S. & LATTES, P. Vertical variability of Near-Surface Salinity in the Tropics: Consequences for SMOS Calibration and Validation. EGU General Assembly Conference Abstracts, 2009. 2761.

HENOCQ, C., BOUTIN, J., REVERDIN, G., PETITCOLIN, F., ARNAULT, S. & LATTES, P. 2010. Vertical Variability of Near-Surface Salinity in the Tropics: Consequences for L-Band Radiometer Calibration and Validation. *Journal of Atmospheric and Oceanic Technology,* 27, 192-209.

HO, D. T., BLIVEN, L. F., WANNINKHOF, R. & SCHLOSSER, P. 1997. The effect of rain on air-water gas exchange. *Tellus B,* 49, 149-158.

HO, D. T., LAW, C. S., SMITH, M. J., SCHLOSSER, P., HARVEY, M. & HILL, P. 2006. Measurements of air-sea gas exchange at high wind speeds in the Southern Ocean: Implications for global parameterizations. *Geophysical research letters,* 33.

HOLT, J., BUTENSCHON, M., WAKELIN, S., ARTIOLI, Y. & ALLEN, J. 2012. Oceanic controls on the primary production of the northwest European continental shelf: model experiments under recent past conditions and a potential future scenario. *Biogeosciences,* 9, 97-117.

HORROCKS, L. A., CANDY, B., NIGHTINGALE, T. J., SAUNDERS, R. W., O'CARROLL, A. & HARRIS, A. R. 2003. Parameterizations of the ocean skin effect and implications for satellite-based measurement of sea-surface temperature. *Journal of Geophysical Research: Oceans (1978–2012),* 108.

HUMPHREYS, M. P., ACHTERBERG, E. P., HOPKINS, J. E., CHOWDHURY, M. Z., GRIFFITHS, A. M., HARTMAN, S. E., HULL, T., SMILENOVA, A., WIHSGOTT, J. U. & WOODWARD, E. M. S. 2018. Mechanisms for a nutrient-conserving carbon pump in a seasonally stratified, temperate continental shelf sea. *Progress in Oceanography*.

HUTHNANCE, J. M. 1995. Circulation, exchange and water masses at the ocean margin: the role of physical processes at the shelf edge. *Progress in Oceanography,* 35, 353-431.

HUTHNANCE, J. M., HOLT, J. T. & WAKELIN, S. L. 2009. Deep ocean exchange with west-European shelf seas. *Ocean Sci.,* 5, 621-634.

IHO 2008. *Standardization of undersea feature names: guidelines, proposal form, terminology*, International Hydrographic Bureau.

IRIGOIEN, X., CONWAY, D. V. & HARRIS, R. P. 2004. Flexible diel vertical migration behaviour of zooplankton in the Irish Sea. *Marine Ecology Progress Series,* 267, 85-97.

IVANOV, V. V., SHAPIRO, G. I., HUTHNANCE, J. M., ALEYNIK, D. L. & GOLOVIN, P. N. 2004. Cascades of dense water around the world ocean. *Progress in Oceanography,* 60, 47-98.

JACOBS, C., FRIIS KJELD, J., NIGHTINGALE, P., UPSTILL-GODDARD, R., LARSEN, S. & OOST, W. 2002. Possible errors in CO2 air-sea transfer velocity from deliberate tracer releases and eddy covariance measurements due to near-surface concentration gradients. *Journal of Geophysical Research: Oceans,* 107, 3128.

JAMES, I. 1977. A model of the annual cycle of temperature in a frontal region of the Celtic Sea. *Estuarine and Coastal Marine Science,* 5, 339-353.

JEFFERY, C., ROBINSON, I., WOOLF, D. & DONLON, C. 2008. The response to phase-dependent wind stress and cloud fraction of the diurnal cycle of SST and air–sea CO< sub> 2</sub> exchange. *Ocean Modelling,* 23, 33-48.

JICKELLS, T. D. 1998. Nutrient Biogeochemistry of the Coastal Zone. *Science,* 281, 217-222.

JOHNSON, M. T. 2010. A numerical scheme to calculate temperature and salinity dependent air-water transfer velocities for any gas. *Ocean Sci.,* 6, 913-932.

KALNAY, E., KANAMITSU, M., KISTLER, R., COLLINS, W., DEAVEN, D., GANDIN, L., IREDELL, M., SAHA, S., WHITE, G. & WOOLLEN, J. 1996. The NCEP/NCAR 40-year reanalysis project. *Bulletin of the American Meteorological Society,* 77, 437-472.

KARAGALI, I. & HØYER, J. 2013. Observations and modeling of the diurnal SST cycle in the North and Baltic Seas. *Journal of Geophysical Research: Oceans*.

KAWAI, Y. & KAWAMURA, H. 2000. Study on a platform effect in the in situ sea surface temperature observations under weak wind and clear sky conditions using numerical models. *Journal of Atmospheric and Oceanic Technology,* 17, 185-196.

KAWAI, Y. & WADA, A. 2007. Diurnal sea surface temperature variation and its impact on the atmosphere and ocean: A review. *Journal of Oceanography,* 63, 721-744.

KEELING, R. F. 1993. On the role of large bubbles in air-sea gas exchange and supersaturation in the ocean. *Journal of Marine Research,* 51, 237-271.

KITIDIS, V., HARDMAN-MOUNTFORD, N. J., LITT, E., BROWN, I., CUMMINGS, D., HARTMAN, S., HYDES, D., FISHWICK, J. R., HARRIS, C. & MARTINEZ-VICENTE, V. 2012. Seasonal dynamics of the carbonate system in the Western English Channel. *Continental Shelf Research,* 42, 30-40.

KOMORI, S., TAKAGAKI, N., SAIKI, R., SUZUKI, N. & TANNO, K. 2007. The effect of raindrops on interfacial turbulence and air-water gas transfer. *Transport at the Air-Sea Interface.* Springer.

KONDO, J., SASANO, Y. & ISHII, T. 1979. On wind-driven current and temperature profiles with diurnal period in the oceanic planetary boundary layer. *Journal of Physical Oceanography,* 9, 360-372.

KÖRTZINGER, A., MINTROP, L., WALLACE, D. W., JOHNSON, K. M., NEILL, C., TILBROOK, B., TOWLER, P., INOUE, H. Y., ISHII, M. & SHAFFER, G. 2000. The international at-sea intercomparison of fCO_2 systems during the R/V Meteor Cruise 36/1 in the North Atlantic Ocean. *Marine Chemistry,* 72, 171-192.

LAMPERT, W. 1989. The adaptive significance of diel vertical migration of zooplankton. *Functional Ecology,* 3, 21-27.

LANA, A., BELL, T., SIMÓ, R., VALLINA, S. M., BALLABRERA-POY, J., KETTLE, A., DACHS, J., BOPP, L., SALTZMAN, E. & STEFELS, J. 2011. An updated climatology of surface dimethlysulfide concentrations and emission fluxes in the global ocean. *Global Biogeochemical Cycles,* 25.

LARGE, W. & CARON, J. 2015. Diurnal cycling of sea surface temperature, salinity, and current in the CESM coupled climate model. *Journal of Geophysical Research: Oceans,* 120, 3711-3729.

LARGE, W. & POND, S. 1982. Sensible and latent heat flux measurements over the ocean. *Journal of Physical Oceanography,* 12, 464-482.

LARGE, W. G., MCWILLIAMS, J. C. & DONEY, S. C. 1994. Oceanic vertical mixing: A review and a model with a nonlocal boundary layer parameterization. *Reviews of Geophysics,* 32, 363-403.

LARGE, W. G. & YEAGER, S. G. 2004. Diurnal to decadal global forcing for ocean and sea-ice models: the data sets and flux climatologies.

LARUELLE, G. G., DÜRR, H., LAUERWALD, R., HARTMANN, J., SLOMP, C., GOOSSENS, N. & REGNIER, P. 2013. Global multi-scale segmentation of continental and coastal waters from the watersheds to the continental margins. *Hydrology and earth system sciences,* 17, 2029-2051.

LARUELLE, G. G., LAUERWALD, R., PFEIL, B. & REGNIER, P. 2014. Regionalized global budget of the CO2 exchange at the air-water interface in continental shelf seas. *Global Biogeochemical Cycles*, 2014GB004832.

LE QUÉRÉ, C., ANDREW, R. M., CANADELL, J. G., SITCH, S., KORSBAKKEN, J. I., PETERS, G. P., MANNING, A. C., BODEN, T. A., TANS, P. P. & HOUGHTON, R. A. 2016. Global carbon budget 2016. *Earth System Science Data,* 8, 605.

LEE, K., MILLERO, F. J. & CAMPBELL, D. M. 1996. The reliability of the thermodynamic constants for the dissociation of carbonic acid in seawater. *Marine chemistry,* 55, 233-245.

LENTZ, S. J. & LIMEBURNER, R. 1995. The Amazon River Plume during AMASSEDS: Spatial characteristics and salinity variability. *Journal of Geophysical Research: Oceans,* 100, 2355-2375.

LEWIS, E., WALLACE, D. & ALLISON, L. J. 1998. *Program developed for CO_2 system calculations*, Carbon Dioxide Information Analysis Center, managed by Lockheed Martin Energy Research Corporation for the US Department of Energy Tennessee.

LI, Y. H. & TSUI, T. F. 1971. The solubility of CO2 in water and sea water. *Journal of Geophysical Research,* 76, 4203-4207.

LISS, P. S., HEIMANN, M. & ROETHER, W. 1988. Tracers of Air-Sea Gas Exchange [and Discussion]. *Philosophical Transactions of the Royal Society of London. Series A, Mathematical and Physical Sciences,* 325, 93-103.

LISS, P. S. & MERLIVAT, L. 1986. Air-sea gas exchange rates: Introduction and synthesis. *The role of air-sea exchange in geochemical cycling.* Springer.

LISS, P. S. & SLATER, P. G. 1974. Flux of Gases across the Air-Sea Interface. *Nature,* 247, 181-184.

LITT, E. J., HARDMAN-MOUNTFORD, N. J., BLACKFORD, J. C., MITCHELSON-JACOB, G., GOODMAN, A., MOORE, G. F., CUMMINGS, D. G. & BUTENSCHÖN, M. 2010. Biological control of pCO2 at station L4 in the Western English Channel over 3 years. *Journal of plankton research,* 32, 621-629.

LLASAT, M. C. 2001. An objective classification of rainfall events on the basis of their convective features: application to rainfall intensity in the northeast of Spain. *International Journal of Climatology,* 21, 1385-1400.

LOOSE, B., STUTE, M., ALEXANDER, P. & SMETHIE, W. 2009. Design and deployment of a portable membrane equilibrator for sampling aqueous dissolved gases. *Water Resources Research,* 45.

LOVELY, A., LOOSE, B., SCHLOSSER, P., MCGILLIS, W., ZAPPA, C., PEROVICH, D., BROWN, S., MORELL, T., HSUEH, D. & FRIEDRICH, R. 2015. The Gas Transfer through Polar Sea ice experiment: Insights into the rates and pathways that determine geochemical fluxes. *Journal of Geophysical Research: Oceans,* 120, 8177-8194.

LUEKER, T. J., DICKSON, A. G. & KEELING, C. D. 2000. Ocean pCO calculated from dissolved inorganic carbon. *Marine chemistry,* 70, 105-119.

MAMMEN, T. C. & VON BOSSE, N. 1990. STEP—A Temperature Profiler for Measuring the Oceanic Thermal Boundary Layer at the Ocean–Air Interface. *Journal of Atmospheric and Oceanic Technology,* 7, 312-322.

MARANDINO, C. A., DE BRUYN, W. J., MILLER, S. D. & SALTZMAN, E. S. 2009. Open ocean DMS air/sea fluxes over the eastern South Pacific Ocean. *Atmos. Chem. Phys.,* 9, 345-356.

MARCOS, R., GONZÁLEZ-REVIRIEGO, N., TORRALBA, V., SORET, A. & DOBLAS-REYES, F. J. 2018. Characterization of the near surface wind speed distribution at global scale: ERA-Interim reanalysis and ECMWF seasonal forecasting system 4. *Climate Dynamics*, 1-13.

MARTIN, P. E. & BARKER, E. F. 1932. The infrared absorption spectrum of carbon dioxide. *Physical Review,* 41, 291.

MASKE, H., OCHOA, J., ALMEDA-JAUREGUI, C. O., RUIZ-DE LA TORRE, M. C., CRUZ-LÓPEZ, R. & VILLEGAS-MENDOZA, J. R. 2014. Near-surface temperature gradient in a coastal upwelling regime. *Journal of Geophysical Research: Oceans,* 119, 4972-4982.

MATTHEWS, A. J., BARANOWSKI, D. B., HEYWOOD, K. J., FLATAU, P. J. & SCHMIDTKO, S. 2014. The surface diurnal warm layer in the Indian Ocean during CINDY/DYNAMO. *Journal of Climate,* 27, 9101-9122.

MAYERS, K., POULTON, A., DANIELS, C., WELLS, S., WOODWARD, E., TARRAN, G., WIDDICOMBE, C., MAYOR, D., ATKINSON, A. & GIERING, S. 2018. Growth and mortality of coccolithophores during spring in a temperate Shelf Sea (Celtic Sea, April 2015). *Progress in Oceanography*.

MCGILLIS, W., EDSON, J., HARE, J. & FAIRALL, C. 2001. Direct covariance air-sea CO2 fluxes. *Journal of Geophysical Research: Oceans,* 106, 16729-16745.

MCGILLIS, W. R., EDSON, J. B., ZAPPA, C. J., WARE, J. D., MCKENNA, S. P., TERRAY, E. A., HARE, J. E., FAIRALL, C. W., DRENNAN, W., DONELAN, M., DEGRANDPRE, M. D., WANNINKHOF, R. & FEELY, R. A. 2004. Air-sea CO2 exchange in the equatorial Pacific. *Journal of Geophysical Research: Oceans,* 109, C08S02.

MCGILLIS, W. R. & WANNINKHOF, R. 2006. Aqueous CO< sub> 2</sub> gradients for air–sea flux estimates. *Marine chemistry,* 98, 100-108.

MCNEIL, C. L. & MERLIVAT, L. 1996. The warm oceanic surface layer: Implications for CO_2 fluxes and surface gas measurements. *Geophysical research letters,* 23, 3575-3578.

MEHRBACH, C., CULBERSON, C. H., HAWLEY, J. E. & PTKOWICZ, R. M. 1973. Measurement of the apparent dissociation constants of carbonic acid in seawater at atmospheric pressure. *Limnol. Oceanogr*, 897-907.

MELLOR, G. L. & YAMADA, T. 1982. Development of a turbulence closure model for geophysical fluid problems. *Reviews of Geophysics,* 20, 851-875.

MELVILLE, W. K. & MATUSOV, P. 2002. Distribution of breaking waves at the ocean surface. *Nature,* 417, 58-63.

MEMERY, L. & MERLIVAT, L. 1985. Modelling of gas flux through bubbles at the air-water interface. *Tellus B,* 37B, 272-285.

MILLER, L. A., BURGERS, T. M., BURT, W. J., GRANSKOG, M. A. & PAPAKYRIAKOU, T. N. 2018. Air-Sea CO2 Flux Estimates in Stratified Arctic Coastal Waters: How Wrong Can We Be? *Geophysical research letters*.

MILLER, S. D., MARANDINO, C. & SALTZMAN, E. S. 2010. Ship-based measurement of air-sea CO_2 exchange by eddy covariance. *Journal of Geophysical Research: Atmospheres,* 115.

MILLERO, F. J. 1995. Thermodynamics of the carbon dioxide system in the oceans. *Geochimica et Cosmochimica Acta,* 59, 661-677.

MILLERO, F. J. & POISSON, A. 1981. International one-atmosphere equation of state of seawater. *Deep Sea Research Part A. Oceanographic Research Papers,* 28, 625-629.

MINNETT, P. J., KNUTESON, R. O., BEST, F. A., OSBORNE, B. J., HANAFIN, J. A. & BROWN, O. B. 2001. The Marine-Atmospheric Emitted Radiance Interferometer: A High-Accuracy, Seagoing Infrared Spectroradiometer. *Journal of Atmospheric and Oceanic Technology,* 18, 994-1013.

MINNETT, P. J., SMITH, M. & WARD, B. 2011. Measurements of the oceanic thermal skin effect. *Deep Sea Research Part II: Topical Studies in Oceanography,* 58, 861-868.

MINNETT, P. J. & WARD, B. Measurements of near-surface ocean temperature variability—Consequences on the validation of AATSR on Envisat. Proc. ERS–ENVISAT Symp."Looking down to Earth in the New Millennium, 2000.

MONAHAN, A. H. 2006. The probability distribution of sea surface wind speeds. Part I: Theory and SeaWinds observations. *Journal of Climate,* 19, 497-520.

MONAHAN, E. C. & SPILLANE, M. C. 1984. The role of oceanic whitecaps in air-sea gas exchange. *Gas transfer at water surfaces.* Springer.

MONTEIRO, P., SCHUSTER, U., LENTON, A., TILBROOK, B., SABINE, C., WANNINKHOF, R., TAKAHASHI, T., HOOD, M., OLSEN, A. & BENDER, M. 2010. A global sea surface carbon observing system: Assessment of changing sea surface CO 2 and air-sea CO 2 fluxes. *Proceedings of the OceanObs,* 9.

MOORE, C. M., SUGGETT, D., HOLLIGAN, P. M., SHARPLES, J., ABRAHAM, E. R., LUCAS, M. I., RIPPETH, T. P., FISHER, N. R., SIMPSON, J. H. & HYDES, D. J. 2003. Physical controls on phytoplankton physiology and production at a shelf sea front: a fast repetition-rate fluorometer based field study. *Marine Ecology Progress Series,* 259, 29-45.

MOORE, C. M., SUGGETT, D. J., HICKMAN, A. E., KIM, Y.-N., TWEDDLE, J. F., SHARPLES, J., GEIDER, R. J. & HOLLIGAN, P. M. 2006. Phytoplankton photoacclimation and photoadaptation in response to environmental gradients in a shelf sea. *Limnology and Oceanography,* 51, 936-949.

MULLER-KARGER, F. E., VARELA, R., THUNELL, R., LUERSSEN, R., HU, C. & WALSH, J. J. 2005. The importance of continental margins in the global carbon cycle. *Geophysical Research Letters,* 32, L01602.

MÜLLER, R., PFEIFROTH, U., TRÄGER-CHATTERJEE, C., TRENTMANN, J. & CREMER, R. 2015. Digging the METEOSAT treasure—3 decades of solar surface radiation. *Remote Sensing,* 7, 8067-8101.

MURATA, A., SHIMADA, K., NISHINO, S. & ITOH, M. 2008. Distributions of surface water CO 2 and air-sea flux of CO 2 in coastal regions of the Canadian Beaufort Sea in late summer. *Biogeosciences Discussions,* 5, 5093-5132.

MURRAY, C. N. & RILEY, J. P. 1971. The solubility of gases in distilled water and sea water—IV. Carbon dioxide. *Deep Sea Research and Oceanographic Abstracts,* 18, 533-541.

NEZLIN, N. P., SUTULA, M. A., STUMPF, R. P. & SENGUPTA, A. 2012. Phytoplankton blooms detected by SeaWiFS along the central and southern California coast. *Journal of Geophysical Research: Oceans,* 117.

NICLÒS, R., CASELLES, V., COLL, C., VALOR, E. & RUBIO, E. 2004. Autonomous measurements of sea surface temperature using in situ thermal infrared data. *Journal of Atmospheric and Oceanic Technology,* 21, 683-692.

NIGHTINGALE, P. D., MALIN, G., LAW, C. S., WATSON, A. J., LISS, P. S., LIDDICOAT, M. I., BOUTIN, J. & UPSTILL-GODDARD, R. C. 2000. In situ evaluation of air-sea gas exchange parameterizations using novel conservative and volatile tracers. *Global Biogeochemical Cycles,* 14, 373-387.

NIXON, S., AMMERMAN, J., ATKINSON, L., BEROUNSKY, V., BILLEN, G., BOICOURT, W., BOYNTON, W., CHURCH, T., DITORO, D. & ELMGREN, R. 1996. The fate of nitrogen and phosphorus at the land-sea margin of the North Atlantic Ocean. *Nitrogen cycling in the North Atlantic Ocean and its Watersheds.* Springer.

NOH, Y., MIN, H. S. & RAASCH, S. 2004. Large eddy simulation of the ocean mixed layer: The effects of wave breaking and Langmuir circulation. *Journal of Physical Oceanography,* 34, 720-735.

OBERNOSTERER, I., CATALA, P., REINTHALER, T., HERNDL, G. J. & LEBARON, P. 2005. Enhanced heterotrophic activity in the surface microlayer of the Mediterranean Sea. *Aquatic Microbial Ecology,* 39, 293-302.

OHLMANN, J. C., SIEGEL, D. A. & GAUTIER, C. 1996. Ocean mixed layer radiant heating and solar penetration: A global analysis. *Journal of Climate,* 9, 2265-2280.

OSTLE, C., WILLIAMSON, P., ARTIOLI, Y., BAKKER, D. C., BIRCHENOUGH, S., DAVIS, C. E., DYE, S., EDWARDS, M., FINDLAY, H. S. & GREENWOOD, N. 2016. Carbon dioxide and ocean acidification observations in UK waters. Synthesis report with a focus on 2010–2015. University of East Anglia, UK.

PAINTER, S. C., HARTMAN, S. E., KIVIMÄE, C., SALT, L. A., CLARGO, N. M., BOZEC, Y., DANIELS, C. J., JONES, S. C., HEMSLEY, V. S. & MUNNS, L. R. 2016. Carbon exchange between a shelf sea and the ocean: The Hebrides Shelf, west of Scotland. *Journal of Geophysical Research: Oceans,* 121, 4522-4544.

PARVARESH, A., HASSANZADEH, S. & BORDBAR, M. Statistical analysis of wave parameters in the north coast of the Persian Gulf. Annales Geophysicae, 2005. 2031-2038.

PEARMAN, G. & HYSON, P. 1981. The annual variation of atmospheric CO2 concentration observed in the northern hemisphere. *Journal of Geophysical Research: Oceans,* 86, 9839-9843.

PEARRE JR, S. 1979. Problems of detection and interpretation of vertical migration. *Journal of Plankton Research,* 1, 29-44.

PEREIRA, R., ASHTON, I., SABBAGHZADEH, B., SHUTLER, J. D. & UPSTILL-GODDARD, R. C. 2018. Reduced air–sea CO 2 exchange in the Atlantic Ocean due to biological surfactants. *Nature Geoscience*, 1.

PEREIRA, R., SCHNEIDER-ZAPP, K. & UPSTILL-GODDARD, R. 2016. Surfactant control of gas transfer velocity along an offshore coastal transect: results from a laboratory gas exchange tank. *Biogeosciences,* 13, 3981-3989.

PFEIL, B., OLSEN, A., BAKKER, D. C., HANKIN, S., KOYUK, H., KOZYR, A., MALCZYK, J., MANKE, A., METZL, N. & SABINE, C. 2012. A uniform, quality controlled Surface Ocean CO2 Atlas (SOCAT). *Earth System Science Data Discussions,* 5, 735-780.

PINGREE, R. 1980. Physical oceanography of the Celtic Sea and English Channel. *Elsevier Oceanography Series,* 24, 415-465.

PINGREE, R., HOLLIGAN, P. & MARDELL, G. 1978. The effects of vertical stability on phytoplankton distributions in the summer on the northwest European Shelf. *Deep Sea Research,* 25, 1011-1028.

PINGREE, R., HOLLIGAN, P., MARDELL, G. & HEAD, R. 1976. The influence of physical stability on spring, summer and autumn phytoplankton blooms in the Celtic Sea. *Journal of the Marine Biological Association of the United Kingdom,* 56, 845-873.

PINGREE, R., MARDELL, G. & CARTWRIGHT, D. 1981. Slope turbulence, internal waves and phytoplankton growth at the Celtic Sea shelf-break [and discussion]. *Philosophical Transactions of the Royal Society of London A: Mathematical, Physical and Engineering Sciences,* 302, 663-682.

PINGREE, R. & NEW, A. 1989. Downward propagation of internal tidal energy into the Bay of Biscay. *Deep Sea Research Part A. Oceanographic Research Papers,* 36, 735-758.

POULTON, A. J., DAVIS, C. E., DANIELS, C. J., MAYERS, K. M., HARRIS, C., TARRAN, G. A., WIDDICOMBE, C. E. & WOODWARD, E. M. S. 2017. Seasonal phosphorus and carbon dynamics in a temperate shelf sea (Celtic Sea). *Progress in Oceanography*.

POULTON, A. J., STINCHCOMBE, M. C., ACHTERBERG, E. P., BAKKER, D. C. E., DUMOUSSEAUD, C., LAWSON, H. E., LEE, G. A., RICHIER, S., SUGGETT, D. J. & YOUNG, J. R. 2014. Coccolithophores on the north-west European shelf: calcification rates and environmental controls. *Biogeosciences,* 11, 3919-3940.

PRICE, J. F., MOOERS, C. N. & VAN LEER, J. C. 1978. Observation and simulation of storm-induced mixed-layer deepening. *Journal of Physical Oceanography,* 8, 582-599.

PRICE, J. F., WELLER, R. A., BOWERS, C. M. & BRISCOE, M. G. 1987. Diurnal response of sea surface temperature observed at the long-term upper ocean study (34° N, 70° W) in the Sargasso Sea. *Journal of Geophysical Research: Oceans (1978–2012),* 92, 14480-14490.

PRICE, J. F., WELLER, R. A. & PINKEL, R. 1986. Diurnal cycling: Observations and models of the upper ocean response to diurnal heating, cooling, and wind mixing. *Journal of Geophysical Research,* 91, 8411-8427.

PRYTHERCH, J., FARRAR, J. & WELLER, R. 2013. Moored surface buoy observations of the diurnal warm layer. *Journal of Geophysical Research: Oceans*.

QUINN, P. & BATES, T. 2011. The case against climate regulation via oceanic phytoplankton sulphur emissions. *Nature,* 480, 51-56.

REES, A. P., GILBERT, J. A. & KELLY-GERREYN, B. A. 2009. Nitrogen fixation in the western English Channel (NE Atlantic ocean). *Marine Ecology Progress Series,* 374, 7-12.

REVERDIN, G., MORISSET, S., BELLENGER, H., BOUTIN, J., MARTIN, N., BLOUCH, P., ROLLAND, J., GAILLARD, F., BOURUET-AUBERTOT, P. & WARD, B. 2013. Near–sea surface temperature stratification from SVP drifters. *Journal of Atmospheric and Oceanic Technology,* 30, 1867-1883.

REVERDIN, G., MORISSET, S., BOUTIN, J. & MARTIN, N. 2012. Rain-induced variability of near sea-surface T and S from drifter data. *Journal of Geophysical Research: Oceans,* 117.

RHODE, S. C., PAWLOWSKI, M. & TOLLRIAN, R. 2001. The impact of ultraviolet radiation on the vertical distribution of zooplankton of the genus Daphnia. *Nature,* 412, 69-72.

RIBAS-RIBAS, M., MUSTAFFA, N. I. H., RAHLFF, J., STOLLE, C. & WURL, O. 2017. Sea Surface Scanner (S3): A Catamaran for High-resolution Measurements of Biogeochemical Properties of the Sea Surface Microlayer. *Journal of Atmospheric and Oceanic Technology*.

RIBAS-RIBAS, M., REROLLE, V., BAKKER, D. C., KITIDIS, V., LEE, G., BROWN, I., ACHTERBERG, E. P., HARDMAN-MOUNTFORD, N. & TYRRELL, T. 2014. Intercomparison of carbonate chemistry measurements on a cruise in northwestern European shelf seas. *Biogeosciences,* 11, 4339-4355.

RIPPETH, T. P., WILES, P., PALMER, M. R., SHARPLES, J. & TWEDDLE, J. 2009. The diapcynal nutrient flux and shear-induced diapcynal mixing in the seasonally stratified western Irish Sea. *Continental Shelf Research,* 29, 1580-1587.

RISIEN, C. M. & CHELTON, D. B. 2008. A global climatology of surface wind and wind stress fields from eight years of QuikSCAT scatterometer data. *Journal of Physical Oceanography,* 38, 2379-2413.

ROBERTSON, J. & WATSON, A. 1992a. Thermal skin effect of the surface ocean and its implications for CO_2 uptake. *Nature,* 358, 738-740.

ROBERTSON, J. E., ROBINSON, C., TURNER, D. R., HOLLIGAN, P., WATSON, A. J., BOYD, P., FERNANDEZ, E. & FINCH, M. 1994. The impact of a coccolithophore bloom on oceanic carbon uptake in the northeast Atlantic during summer 1991. *Deep Sea Research Part I: Oceanographic Research Papers,* 41, 297-314.

ROBERTSON, J. E. & WATSON, A. J. 1992b. Thermal skin effect of the surface ocean and its implications for CO_2 uptake. *Nature,* 358, 738-740.

ROWE, G. T., CLIFFORD, C. H. & SMITH, K. 1975. Benthic nutrient regeneration and its coupling to primary productivity in coastal waters. *Nature,* 255, 215-217.

ROY, R. N., ROY, L. N., VOGEL, K. M., PORTER-MOORE, C., PEARSON, T., GOOD, C. E., MILLERO, F. J. & CAMPBELL, D. M. 1993. The dissociation constants of carbonic acid in seawater at salinities 5 to 45 and temperatures 0 to 45 C. *Marine Chemistry,* 44, 249-267.

ROYER, S.-J., GALÍ, M., SALTZMAN, E. S., MCCORMICK, C. A., BELL, T. G. & SIMÓ, R. 2014. Development and validation of a shipboard system for measuring high-resolution vertical profiles of aqueous dimethylsulfide concentrations using chemical ionisation mass spectrometry. *Environmental Chemistry,* 11, 309-317.

ROYER, S. J., GALÍ, M., MAHAJAN, A. S., ROSS, O. N., PÉREZ, G. L., SALTZMAN, E. S. & SIMÓ, R. 2016. A high-resolution time-depth view of dimethylsulphide cycling in the surface sea. *Scientific Reports,* 6, 32325.

SABBAGHZADEH, B., UPSTILL-GODDARD, R., BEALE, R., PEREIRA, R. & NIGHTINGALE, P. 2017. The Atlantic Ocean surface microlayer from 50° N to 50° S is ubiquitously enriched in surfactants at wind speeds up to 13 m s− 1. *Geophysical research letters,* 44, 2852-2858.

SABINE, C., HANKIN, S., KOYUK, H., BAKKER, D. C., PFEIL, B., OLSEN, A., METZL, N., KOZYR, A., FASSBENDER, A. & MANKE, A. 2012. Surface Ocean CO2 Atlas (SOCAT) gridded data products. *Earth System Science Data Discussions,* 5, 781-804.

SABINE, C. L., FEELY, R. A., GRUBER, N., KEY, R. M., LEE, K., BULLISTER, J. L., WANNINKHOF, R., WONG, C., WALLACE, D. W. & TILBROOK, B. 2004. The oceanic sink for anthropogenic CO2. *Science,* 305, 367-371.

SACKMANN, B. S., PERRY, M. J. & ERIKSEN, C. C. 2008. Seaglider observations of variability in daytime fluorescence quenching of chlorophyll-<i>a</i> in Northeastern Pacific coastal waters. *Biogeosciences Discuss.,* 2008, 2839-2865.

SALTER, M., UPSTILL-GODDARD, R., NIGHTINGALE, P., ARCHER, S., BLOMQUIST, B., HO, D., HUEBERT, B., SCHLOSSER, P. & YANG, M. 2011. Impact of an artificial surfactant release on air-sea gas fluxes during Deep Ocean Gas Exchange Experiment II. *Journal of Geophysical Research: Oceans,* 116.

SALTZMAN, E. S., DE BRUYN, W. J., LAWLER, M., MARANDINO, C. & MCCORMICK, C. 2009. A chemical ionization mass spectrometer for continuous underway shipboard analysis of dimethylsulfide in near-surface seawater. *Ocean Science,* 5, 537-546.

SANDWELL, D. T. & AGREEN, R. W. 1984. Seasonal variation in wind speed and sea state from global satellite measurements. *Journal of Geophysical Research: Oceans,* 89, 2041-2051.

SANTOS-GARCIA, A., JACOB, M. M., JONES, W. L., ASHER, W. E., HEJAZIN, Y., EBRAHIMI, H. & RABOLLI, M. 2014. Investigation of rain effects on Aquarius sea surface salinity measurements. *Journal of Geophysical Research: Oceans,* 119, 7605-7624.

SARMIENTO, J. & SUNDQUIST, E. 1992. Revised budget for the oceanic uptake of anthropogenic carbon dioxide. *Nature,* 356, 589-593.

SCANLON, B., WICK, G. & WARD, B. 2012. Near-surface diurnal warming simulations: validation with high resolution profile measurements. *Ocean Science Discussions,* 9, 3851-3878.

SCHUSTER, U., WATSON, A., BAKKER, D., DE BOER, A. M., JONES, E., LEE, G., LEGGE, O., LOUWERSE, A., RILEY, J. & SCALLY, S. 2014. Measurements of total alkalinity and inorganic dissolved carbon in the Atlantic Ocean and adjacent Southern Ocean between 2008 and 2010. *Earth System Science Data,* 6, 175-183.

SERRET, P., ROBINSON, C., ARANGUREN-GASSIS, M., GARCÍA-MARTÍN, E. E., GIST, N., KITIDIS, V., LOZANO, J., STEPHENS, J., HARRIS, C. & THOMAS, R. 2015. Both respiration and photosynthesis determine the scaling of plankton metabolism in the oligotrophic ocean. *Nature communications,* 6, 6961.

SHARPLES, J. & HOLLIGAN, P. M. 2006. Interdisciplinary studies in the Celtic Sea (19, E). *The global coastal ocean: interdisciplinary regional studies and syntheses,* 14, 1003.

SHARPLES, J., TWEDDLE, J. F., MATTIAS GREEN, J., PALMER, M. R., KIM, Y.-N., HICKMAN, A. E., HOLLIGAN, P. M., MOORE, C., RIPPETH, T. P. & SIMPSON, J. H. 2007. Spring-neap modulation of internal tide mixing and vertical nitrate fluxes at a shelf edge in summer. *Limnology and Oceanography,* 52, 1735-1747.

SHUTLER, J., LAND, P., BROWN, C., FINDLAY, H., DONLON, C., MEDLAND, M., SNOOKE, R. & BLACKFORD, J. 2013. Coccolithophore surface distributions in the North Atlantic and their modulation of the air-sea flux of CO 2 from 10 years of satellite Earth observation data. *Biogeosciences,* 10, 2699-2709.

SHUTLER, J. D., LAND, P. E., PIOLLE, J.-F., WOOLF, D. K., GODDIJN-MURPHY, L., PAUL, F., GIRARD-ARDHUIN, F., CHAPRON, B. & DONLON, C. J. 2016. FluxEngine: A Flexible Processing System for Calculating Atmosphere–Ocean Carbon Dioxide Gas Fluxes and Climatologies. *Journal of Atmospheric and Oceanic Technology,* 33, 741-756.

SIDDORN, J., ALLEN, J. & UNCLES, R. 2003. Heat, salt and tracer transport in the Plymouth Sound coastal region: a 3-D modelling study. *Journal of the Marine Biological Association of the United Kingdom,* 83, 673-682.

SIEMERING, B., BRESNAN, E., PAINTER, S. C., DANIELS, C. J., INALL, M. & DAVIDSON, K. 2016. Phytoplankton distribution in relation to environmental drivers on the North West European Shelf Sea. *PloS one,* 11, e0164482.

SIMPSON, J., CRISP, D. & HEARN, C. 1981. The shelf-sea fronts: Implications of their existence and behaviour [and discussion]. *Philosophical Transactions of the Royal Society of London. Series A, Mathematical and Physical Sciences,* 302, 531-546.

SIMPSON, J. H. & SHARPLES, J. 2012. *Introduction to the physical and biological oceanography of shelf seas*, Cambridge University Press.

SIMS, R. P., SCHUSTER, U., WATSON, A. J., YANG, M. X., HOPKINS, F. E., STEPHENS, J. & BELL, T. G. 2017. A measurement system for vertical seawater profiles close to the air–sea interface. *Ocean Science,* 13, 649.

SMYTH, T., FISHWICK, J., GALLIENNE, C., STEPHENS, J. & BALE, A. 2010a. Technology, design, and operation of an autonomous buoy system in the western English Channel. *Journal of Atmospheric and Oceanic Technology,* 27, 2056-2064.

SMYTH, T. J., FISHWICK, J. R., LISA, A.-M., CUMMINGS, D. G., HARRIS, C., KITIDIS, V., REES, A., MARTINEZ-VICENTE, V. & WOODWARD, E. M. 2010b. A broad spatio-temporal view of the Western English Channel observatory. *Journal of Plankton Research,* 32, 585-601.

SOLOMON, S., QIN, D., MANNING, M., AVERYT, K. & MARQUIS, M. 2007. *Climate change 2007-the physical science basis: Working group I contribution to the fourth assessment report of the IPCC*, Cambridge university press.

SOLOVIEV, A. & LUKAS, R. 1997. Observation of large diurnal warming events in the near-surface layer of the western equatorial Pacific warm pool. *Deep Sea Research Part I: Oceanographic Research Papers,* 44, 1055-1076.

SOLOVIEV, A. & LUKAS, R. 2006. *The near-surface layer of the ocean: structure, dynamics and applications*, Springer Science & Business Media.

SOLOVIEV, A. & VERSHINSKY, N. 1982. The vertical structure of the thin surface layer of the ocean under conditions of low wind speed. *Deep Sea Research Part A. Oceanographic Research Papers,* 29, 1437-1449.

SOLOVIEV, A., VERSHINSKY, N. & BEZVERCHNII, V. 1988. Small-scale turbulence measurements in the thin surface layer of the ocean. *Deep Sea Research Part A. Oceanographic Research Papers,* 35, 1859-1874.

SOUTHWARD, A. J., LANGMEAD, O., HARDMAN-MOUNTFORD, N. J., AIKEN, J., BOALCH, G. T., DANDO, P. R., GENNER, M. J., JOINT, I., KENDALL, M. A. & HALLIDAY, N. C. 2004. Long-term oceanographic and ecological research in the western English Channel. *Advances in marine biology,* 47, 1-105.

STEELE, M., ZHANG, J. & ERMOLD, W. 2010. Mechanisms of summertime upper Arctic Ocean warming and the effect on sea ice melt. *Journal of Geophysical Research: Oceans,* 115.

STUART-MENTETH, A. C., ROBINSON, I. S. & CHALLENOR, P. G. 2003. A global study of diurnal warming using satellite-derived sea surface temperature. *Journal of Geophysical Research: Oceans,* 108.

SUYKENS, K., DELILLE, B., CHOU, L., DE BODT, C., HARLAY, J. & BORGES, A. V. 2010. Dissolved inorganic carbon dynamics and air-sea carbon dioxide fluxes during coccolithophore blooms in the northwest European continental margin (northern Bay of Biscay). *Global Biogeochemical Cycles,* 24, GB3022.

SWEENEY, C., GLOOR, E., JACOBSON, A. R., KEY, R. M., MCKINLEY, G., SARMIENTO, J. L. & WANNINKHOF, R. 2007. Constraining global air-sea gas exchange for CO2 with recent bomb 14C measurements. *Global Biogeochemical Cycles,* 21.

TAKAHASHI, T., OLAFSSON, J., GODDARD, J. G., CHIPMAN, D. W. & SUTHERLAND, S. 1993. Seasonal variation of CO_2 and nutrients in the high-latitude surface oceans: A comparative study. *Global Biogeochemical Cycles,* 7, 843-878.

TAKAHASHI, T., SUTHERLAND, S. C., SWEENEY, C., POISSON, A., METZL, N., TILBROOK, B., BATES, N., WANNINKHOF, R., FEELY, R. A. & SABINE, C. 2002. Global sea–air CO< sub> 2</sub> flux based on climatological surface ocean< i> p</i> CO< sub> 2</sub>, and seasonal biological and temperature effects. *Deep Sea Research Part II: Topical Studies in Oceanography,* 49, 1601-1622.

TAKAHASHI, T., SUTHERLAND, S. C., WANNINKHOF, R., SWEENEY, C., FEELY, R. A., CHIPMAN, D. W., HALES, B., FRIEDERICH, G., CHAVEZ, F. & SABINE, C. 2009. Climatological mean and decadal change in surface ocean pCO< sub> 2</sub>, and net sea–air CO< sub> 2</sub> flux over the global oceans. *Deep Sea Research Part II: Topical Studies in Oceanography,* 56, 554-577.

TETT, P., JOINT, I., PURDIE, D., BAARS, M., OOSTERHUIS, S., DANERI, G., HANNAH, F., MILLS, D., PLUMMER, D. & POMROY, A. 1993. Biological consequences of tidal stirring gradients in the North Sea. *Phil. Trans. R. Soc. Lond. A,* 343, 493-508.

THOMAS, H., BOZEC, Y., ELKALAY, K. & DE BAAR, H. J. 2004. Enhanced open ocean storage of CO2 from shelf sea pumping. *Science,* 304, 1005-1008.

TSUNOGAI, S., WATANABE, S. & SATO, T. 1999. Is there a “continental shelf pump” for the absorption of atmospheric CO2? *Tellus B,* 51, 701-712.

TURK, D., ZAPPA, C. J., MEINEN, C. S., CHRISTIAN, J. R., HO, D. T., DICKSON, A. G. & MCGILLIS, W. R. 2010. Rain impacts on CO_2 exchange in the western equatorial Pacific Ocean. *Geophysical Research Letters,* 37.

UNCLES, R., STEPHENS, J. & HARRIS, C. 2015. Estuaries of southwest England: Salinity, suspended particulate matter, loss-on-ignition and morphology. *Progress in Oceanography,* 137, 385-408.

UNCLES, R. & TORRES, R. 2013. Estimating dispersion and flushing time-scales in a coastal zone: Application to the Plymouth area. *Ocean & coastal management,* 72, 3-12.

UPPSTRÖM, L. R. The boron/chlorinity ratio of deep-sea water from the Pacific Ocean. Deep Sea Research and Oceanographic Abstracts, 1974. Elsevier, 161-162.

UPSTILL-GODDARD, R., WATSON, A., LISS, P. & LIDDICOAT, M. 1990. Gas transfer velocities in lakes measured with SF6. *Tellus B,* 42, 364-377.

VAN HEUVEN, S., PIERROT, D., RAE, J., LEWIS, E. & WALLACE, D. 2011. MATLAB Program Developed for CO2 System Calculations. ORNL/CDIAC-105b. Carbon Dioxide Information Analysis Center, Oak Ridge National Laboratory, US Department of Energy, Oak Ridge, Tennessee. *cdiac. ornl. gov/ftp/co2sys/CO2SYS_calc_MATLAB_v1,* 1, l.

VAN SCOY, K. A., MORRIS, K. P., ROBERTSON, J. E. & WATSON, A. J. 1995. Thermal skin effect and the air-sea flux of carbon dioxide: A seasonal high-resolution estimate. *Global Biogeochemical Cycles,* 9, 253-262.

WALKER, C. F., HARVEY, M. J., SMITH, M. J., BELL, T. G., SALTZMAN, E. S., MARRINER, A. S., MCGREGOR, J. A. & LAW, C. S. 2016. Assessing the potential for dimethylsulfide enrichment at the sea surface and its influence on air-sea flux. *Ocean Science,* 12, 1033.

WALLACE, D. W. R. & WIRICK, C. D. 1992. Large air-sea gas fluxes associated with breaking waves. *Nature,* 356, 694-696.

WALSH, J. J. 1991. Importance of continental margins in the marine biogeochemical cycling of carbon and nitrogen. *Nature,* 350, 53-55.

WANNINKHOF, R. 1992. Relationship between wind speed and gas exchange over the ocean. *Journal of Geophysical Research: Oceans (1978–2012),* 97, 7373-7382.

WANNINKHOF, R. 2014. Relationship between wind speed and gas exchange over the ocean revisited. *Limnol. Oceanogr. Methods,* 12, 351-362.

WANNINKHOF, R., ASHER, W. E., HO, D. T., SWEENEY, C. & MCGILLIS, W. R. 2009. Advances in quantifying air-sea gas exchange and environmental forcing*. *Marine Science,* 1.

WANNINKHOF, R., DONEY, S. C., TAKAHASHI, T. & MCGILLIS, W. R. 2002. The Effect of Using Time-Averaged Winds on Regional Air-Sea CO~ 2 Fluxes. *GEOPHYSICAL MONOGRAPH-AMERICAN GEOPHYSICAL UNION,* 127, 351-356.

WANNINKHOF, R. & MCGILLIS, W. R. 1999. A cubic relationship between air-sea CO2 exchange and wind speed. *Geophysical Research Letters,* 26, 1889-1892.

WANNINKHOF, R., PARK, G.-H., TAKAHASHI, T., SWEENEY, C., FEELY, R. A., NOJIRI, Y., GRUBER, N., DONEY, S. C., MCKINLEY, G. A. & LENTON, A. 2013. Global ocean carbon uptake: magnitude, variability and trends.

WARD, B. 2006. Near-surface ocean temperature. *Journal of Geophysical Research: Oceans (1978–2012),* 111.

WARD, B. & DONELAN, M. 2006. Thermometric measurements of the molecular sublayer at the air-water interface. *Geophysical Research Letters,* 33, L07605.

WARD, B., FRISTEDT, T., CALLAGHAN, A. H., SUTHERLAND, G., SANCHEZ, X., VIALARD, J. & DOESCHATE, A. T. 2014. The Air–Sea Interaction Profiler (ASIP): An Autonomous Upwardly Rising Profiler for Microstructure Measurements in the Upper Ocean. *Journal of Atmospheric and Oceanic Technology,* 31, 2246-2267.

WARD, B., WANNINKHOF, R., MCGILLIS, W. R., JESSUP, A. T., DEGRANDPRE, M. D., HARE, J. E. & EDSON, J. B. 2004a. Biases in the air-sea flux of CO_2 resulting from ocean surface temperature gradients. *Journal of Geophysical Research: Oceans (1978–2012),* 109.

WARD, B., WANNINKHOF, R., MINNETT, P. J. & HEAD, M. J. 2004b. SkinDeEP: A profiling instrument for upper-decameter sea surface measurements. *Journal of Atmospheric and Oceanic Technology,* 21, 207-222.

WATSON, A. J., SCHUSTER, U., BAKKER, D. C., BATES, N. R., CORBIÈRE, A., GONZÁLEZ-DÁVILA, M., FRIEDRICH, T., HAUCK, J., HEINZE, C. & JOHANNESSEN, T. 2009. Tracking the variable North Atlantic sink for atmospheric CO2. *Science,* 326, 1391-1393.

WEBB, J. R., MAHER, D. T. & SANTOS, I. R. 2016. Automated, in situ measurements of dissolved CO_2, CH_4, and δ13C values using cavity enhanced laser absorption spectrometry: Comparing response times of air-water equilibrators. *Limnology and Oceanography: Methods,* 14, 323-337.

WEBSTER, P. J., CLAYSON, C. A. & CURRY, J. A. 1996. Clouds, radiation, and the diurnal cycle of sea surface temperature in the tropical western Pacific. *Journal of Climate,* 9, 1712-1730.

WEIHS, R. R. & BOURASSA, M. 2014. Modeled diurnally varying sea surface temperatures and their influence on surface heat fluxes. *Journal of Geophysical Research: Oceans,* 119, 4101-4123.

WEISS, R. & PRICE, B. 1980. Nitrous oxide solubility in water and seawater. *Marine Chemistry,* 8, 347-359.

WEISS, R. F. 1974. Carbon dioxide in water and seawater: the solubility of a non-ideal gas. *Marine chemistry,* 2, 203-215.

WENTZ, F., PETEHERYCH, S. & THOMAS, L. 1984. A model function for ocean radar cross sections at 14.6 GHz. *Journal of Geophysical Research: Oceans,* 89, 3689-3704.

WIDDICOMBE, C., ELOIRE, D., HARBOUR, D., HARRIS, R. & SOMERFIELD, P. 2010. Long-term phytoplankton community dynamics in the Western English Channel. *Journal of Plankton Research,* 32, 643-655.

WILLIAMS, P. L. B. 1998. The balance of plankton respiration and photosynthesis in the open oceans. *Nature,* 394, 55-57.

WIMMER, W., ROBINSON, I. S. & DONLON, C. J. 2012. Long-term validation of AATSR SST data products using shipborne radiometry in the Bay of Biscay and English Channel. *Remote sensing of environment,* 116, 17-31.

WOLF-GLADROW, D. A., ZEEBE, R. E., KLAAS, C., KÖRTZINGER, A. & DICKSON, A. G. 2007. Total alkalinity: The explicit conservative expression and its application to biogeochemical processes. *Marine chemistry,* 106, 287-300.

WOOLF, D. 1995. Energy dissipation through wave breaking and the air-sea exchange of gases. *Air-Water Gas Transfer*, 185-195.

WOOLF, D., LAND, P. E., SHUTLER, J. D., GODDIJN-MURPHY, L. & DONLON, C. J. 2016. On the calculation of air-sea fluxes of CO_2 in the presence of temperature and salinity gradients. *Journal of Geophysical Research: Oceans*.

WOOLF, D., LEIFER, I., NIGHTINGALE, P., RHEE, T., BOWYER, P., CAULLIEZ, G., DE LEEUW, G., LARSEN, S. E., LIDDICOAT, M. & BAKER, J. 2007. Modelling of bubble-mediated gas transfer: Fundamental principles and a laboratory test. *Journal of Marine Systems,* 66, 71-91.

WOOLF, D. K. 1997. Bubbles and their role in gas exchange. *The Sea*.

WRIGHT, J., COLLING, A. & PARK, D. 1999. *Waves, tides, and shallow-water processes*, Gulf Professional Publishing.

WURL, O., LANDING, W. M., MUSTAFFA, N. I. H., RIBAS-RIBAS, M., WITTE, C. R. & ZAPPA, C. J. 2018. The Ocean's Skin Layer in the Tropics. *Journal of Geophysical Research: Oceans*.

YANG, M., BEALE, R., SMYTH, T. & BLOMQUIST, B. 2013. Measurements of OVOC fluxes by eddy covariance using a proton-transfer-reaction mass spectrometer–method development at a coastal site. *Atmospheric Chemistry and Physics,* 13, 6165-6184.

YANG, M., BELL, T., HOPKINS, F., KITIDIS, V., CAZENAVE, P., NIGHTINGALE, P., YELLAND, M., PASCAL, R., PRYTHERCH, J. & BROOKS, I. 2015. Air-Sea Fluxes of CO2 and CH4 from the Penlee Point Atmospheric Observatory on the South West Coast of the UK. *Atmospheric Chemistry and Physics Discussions,* 2016, 1-30.

YOKOYAMA, R., TANBA, S. & SOUMA, T. 1995. Sea surface effects on the sea surface temperature estimation by remote sensing. *Remote Sensing,* 16, 227-238.

YOOL, A. & FASHAM, M. J. 2001. An examination of the "continental shelf pump" in an open ocean general circulation model. *Global Biogeochemical Cycles,* 15, 831-844.

ZAPPA, C., ASHER, W. & JESSUP, A. 2001. Microscale wave breaking and air-water gas transfer. *Journal of Geophysical Research: Oceans (1978–2012),* 106, 9385-9391.

ZAPPA, C., ASHER, W., JESSUP, A., KLINKE, J. & LONG, S. 2004. Microbreaking and the enhancement of air-water transfer velocity. *Journal of Geophysical Research,* 109, C08S16.

ZEEBE, R. E. & WOLF-GLADROW, D. 2001. *CO2 in Seawater: Equilibrium, Kinetics, Isotopes: Equilibrium, Kinetics, Isotopes*, Access Online via Elsevier.

ZENG, X. & BELJAARS, A. 2005. A prognostic scheme of sea surface skin temperature for modeling and data assimilation. *Geophysical research letters,* 32, L14605.

ZHAI, W., DAI, M., CAI, W.-J., WANG, Y. & WANG, Z. 2005. High partial pressure of CO2 and its maintaining mechanism in a subtropical estuary: the Pearl River estuary, China. *Marine Chemistry,* 93, 21-32.

ZHANG, X. & CAI, W. J. 2007. On some biases of estimating the global distribution of air-sea CO2 flux by bulk parameterizations. *Geophysical research letters,* 34.

ZISKA, F., QUACK, B., ABRAHAMSSON, K., ARCHER, S., ATLAS, E., BELL, T., BUTLER, J., CARPENTER, L., JONES, C. & HARRIS, N. 2013. Global sea-to-air flux climatology for bromoform, dibromomethane and methyl iodide. *Atmospheric Chemistry and Physics,* 13, 8915-8934.